The intricate interplay between protoplanetary disc winds, giant planets, and discs

Modelling photoevaporative winds and their observational tracers

Michael Lukas Weber

München 2024

The intricate interplay between protoplanetary disc winds, giant planets, and discs

Modelling photoevaporative winds and their observational tracers

Michael Lukas Weber

Dissertation
der Fakultät für Physik
der Ludwig-Maximilians-Universität
München

vorgelegt von
Michael Lukas Weber
aus Ochsenhausen

München, den 29.07.2024

Erstgutachter: Prof. Dr. Barbara Ercolano
Zweitgutachter: Prof. Dr. Til Birnstiel
Tag der mündlichen Prüfung: 16.09.2024

Zusammenfassung

Protoplanetare Scheiben sind entscheidend für das Verständnis der Planetenentstehung. Die Struktur und Entwicklung von Scheiben ist insbesondere geprägt durch die Wechselwirkungen mit ihren Planeten, aber auch durch Scheibenwinde. Riesenplaneten prägen ihre Scheibe durch die Bildung von Substrukturen wie Lücken und Spiralarmen, was weitreichende Auswirkungen auf die Dynamik des Gases und des Staubs innerhalb der Scheibe hat. Scheibenwinde tragen Material ab und begrenzen so die Lebensdauer der Scheiben sowie die verfügbare Zeit für die Planetenentstehung. Ihre genauen Antriebsmechanismen, vor allem die Rolle thermischer und magnetischer Prozesse, sind jedoch weitgehend ungeklärt. Diese Dissertation untersucht das Zusammenspiel zwischen einem durch Röntgen-Photoevaporation angetriebenen Scheibenwind mit den von einem Gasriesen erzeugten Substrukturen. Dabei werden beide Prozesse in einem umfassenden Modell kombiniert, um ihre Wechselwirkung im Detail zu untersuchen. Ein weiterer Schwerpunkt liegt auf der Simulation von Beobachtungen verschiedener Modelle von Scheibenwinden. Diese können mit echten Beobachtungen verglichen werden, um mehr über die realen Bedingungen zu erfahren, unter denen Scheibenwinde angetrieben werden.

Durch 3D-hydrodynamische Simulationen von Röntgen-bestrahlten protoplanetaren Scheiben, die einen Gasriesen beherbergen, quantifiziert diese Arbeit die Auswirkungen des Planeten auf den Wind und umgekehrt. Die Simulationen zeigen, dass eine von einem Riesenplaneten geformte Lücke die Struktur des Windes erheblich verändert. Innerhalb der Lücke kann kein Wind angetrieben werden. Stattdessen wird der Wind aus der Umgebung in die Lücke gelenkt und transportiert so eine große Menge Gas hinein, was erhebliche Auswirkungen sowohl auf den Planeten als auch auf die Scheibe hat: Die Lücke wird teilweise wieder aufgefüllt, der Planet kann dadurch deutlich mehr Masse aufnehmen und auch die Kräfte, die die Migration des Planeten vorantreiben, werden reduziert. Der verringerte Massenverlust durch den Wind und ein erhöhter Massentransport über die Lücke führt zu einer längeren Lebensdauer der inneren Scheibe. Die Berücksichtigung dieser Ergebnisse in Simulationen von Scheibenpopulation könnte deren Ausgang grundlegend verändern.

Die simulierten Beobachtungen zeigen, dass eine periodische Variabilität von Spektrallinienprofilen ein Hinweis auf in der Scheibe eingebettete Riesenplaneten sein kann. Die Beobachtungen des Röntgen-Photoevaporationsmodells stimmen gut mit räumlich und spektral aufgelösten Beobachtungen der [OI] 6300 Å Emissionslinie in TW Hya überein. Vorhersagen der Helligkeiten und Linienprofile von [OI] 6300 Å und [NeII] 12.81 µm aus magnetisch-thermisch angetriebenen Windmodellen sind mit den Beobachtungen vereinbar, wenn der magnetische Anteil des Winds schwach ist. Wenn der magnetische Anteil hingegen stark ist, sind manche [NeII] 12.81 µm Linienprofile nicht mehr mit den Beobachtungen kompatibel, allerdings können dann bestimmte [OI] 6300 Å- Beobachtungen reproduziert werden, die mit den anderen Modellen nicht reproduzierbar sind.

Abstract

Protoplanetary discs, as the birthplaces and nurseries of planets, are crucial to understanding planet formation. Disc winds and planet-disc interactions are fundamental mechanisms shaping the structure and evolution of protoplanetary discs and the planets within them. Massive planets can influence their discs by creating substructures such as gaps and spiral density waves, significantly impacting the dynamics of gas and dust within the disc. Winds can strip material from the disc, eventually dispersing it and setting an upper limit on both its lifetime and the timeframe available for planet formation. Despite their importance, the detailed mechanisms driving these winds – particularly the roles of thermal and magnetic processes at various locations and evolutionary stages – remain poorly constrained. This thesis investigates the intricate interplay between a thermal disc wind launched by X-ray photoevaporation and the substructures produced by giant planets. While previous detailed studies examined these processes separately, this work integrates them into one comprehensive model to investigate their interactions. Additional focus is put on producing synthetic observations of atomic forbidden emission lines in several disc wind models that can be compared to observational data and help constrain the launching conditions of disc winds.

This work quantifies the impact of planets on the wind and vice versa by conducting 3D hydrodynamic simulations of X-ray-irradiated protoplanetary discs hosting giant planets. The models show that a gap carved by a massive planet significantly alters the structure of a photoevaporative wind. Winds cannot be launched within or above the gap; Instead, the wind launched nearby is directed towards the gap, transporting substantial mass into it. This process creates a feedback mechanism with notable implications for the planet and disc, including partial refilling of the gap, increased mass accretion onto the planet, and reduced torque on the planet, which impacts its migration behaviour. Due to a partial recycling of the inner wind and an increased mass transport across the gap, inner disc lifetimes are prolonged. Considering these findings in synthetic disc population models could significantly alter their outcome.

The predicted spectral profiles of wind-tracing emission lines suggest that variable line profiles with periodically redshifted peaks could indicate the presence of embedded planets. The X-ray photoevaporation model aligns well with spatially and spectrally observed [OI] 6300 Å emission in TW Hya, supporting the idea of a predominantly X-ray photoevaporative wind in this system. The luminosities and spectral profiles of the [OI] 6300 Å and [NeII] 12.81 µm lines predicted by X-ray irradiated magnetothermal wind models are consistent with observations when the magnetic wind component is weak. However, stronger magnetic wind components sometimes produce higher blueshifts in the [NeII] 12.81 µm lines than observed. On the other hand, they can reproduce [OI] 6300 Å profiles with high blueshifts that the other models do not reproduce.

Contents

Chapter 1

Introduction

The origin of the earth and its neighbouring planets in the solar system is one of humanity's oldest questions, and the quest to find a natural explanation for the movements of celestial bodies has laid the foundation for modern astronomy. Since the Nobel Prize-winning discovery of the first extrasolar planet (in short, "exoplanet") around a solar-type star less than three decades ago (Mayor & Queloz, 1995), thousands of exoplanets have been discovered, many of which are in systems with multiple planets. These discoveries revealed a broad diversity of planets and planetary systems, sparking great new interest in the exoplanets and their formation history. It is generally accepted that planets form and evolve in protoplanetary discs composed of gas and solids in orbit around a star, which develop as a part of the star-formation process. Knowing the composition, structure, dynamics, and chemistry of protoplanetary discs, as well as their evolution, is essential to understanding the conditions in which planets form and evolve. It is one of the critical questions that must be answered to understand not only the formation history of our solar system but also the ubiquity and diversity of the many exoplanets and exoplanetary systems discovered in recent years. Among the most significant factors influencing the evolution of protoplanetary discs are disc winds and planet-disc interactions.

Disc winds, driven by thermal and magnetohydrodynamic processes, can effectively remove material from the disc, completely dispersing the disc over time. They are, therefore, responsible for setting an upper limit on the disc's lifetime and, with it, the timeframe within which planetesimals, the building blocks of planets, can form.

Planet-disc interactions can lead to substructures in the disc, as massive planets embedded within the disc can carve gaps and generate spiral density waves, drastically altering the disc's structure and subsequent evolution.

This work explores in detail the complex interplay between disc winds and the substructures generated by planet-disc interactions. By investigating how these two processes influence each other, one can gain deeper insights that will be valuable for future models of the combined evolution of discs and planets. Additional focus will be on producing synthetic observations of disc winds launched under various conditions in discs with and without planets. These synthetic observations can help interpret observational data and constrain the properties and launching mechanisms of the winds observed in actual protoplanetary discs.

The first chapter of this thesis provides a brief overview of the origin of protoplanetary discs and their most important properties relevant to this work. It also discusses some basic theoretical concepts that can be employed to describe discs mathematically and introduces protoplanetary disc winds.

1.1 Protoplanetary discs

1.1.1 The origin of protoplanetary discs

Protoplanetary discs are formed as a by-product of the star-formation process, which can occur in giant molecular clouds (GMCs), large, cold regions of enhanced density in the interstellar medium (ISM). GMCs can extend over several hundred pc (1 pc = $3.086 \cdot 10^{18}$ cm) and with densities exceeding $\sim 10^3\,\mathrm{cm}^{-3}$ they can contain masses up to $\sim 10^6\,\mathrm{M}_\odot$ (e.g. Larson, 1981; Williams & McKee, 1997; McKee & Ostriker, 2007, and references therein). Gas temperatures are on the order of ~10 K, and as the name indicates, the gas at these conditions is expected to be in the molecular form (e.g. review by Evans, 1999). Many GMCs are very inhomogeneous with filamentary structures that can fragment into several smaller, over-dense clumps and cores (e.g. André et al., 2014). Cores, often also called "prestellar cores", are regions with a typical size on the order of ~0.1 pc out of which individual stars can form (e.g. McKee & Ostriker, 2007). A core remains stable against collapse under its own gravity as long as it is in hydrostatic equilibrium, i.e. the gravitational force must be counteracted by the gas pressure gradient. If the core is massive and cool enough that small perturbations are no longer damped, it is unstable and will collapse. This concept is called the Jeans instability (e.g. Jeans, 1902).

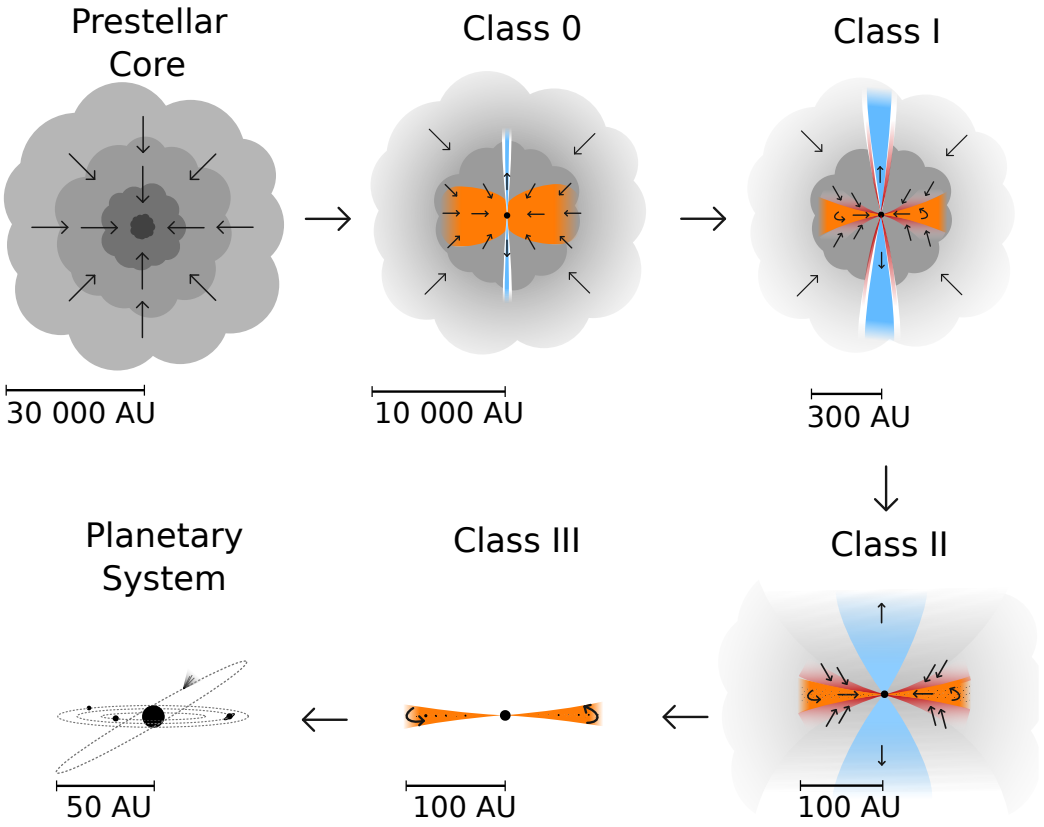

Figure 1.1: Sketch of the formation process from molecular clouds to stars with discs to a planetary system. Figure source: Persson (2014), licensed under CC BY 4.0.

Fig. 1.1 shows a sketch of the collapse from a prestellar core to a star with a protoplanetary disc.

For detailed reviews of this process, see, e.g. Evans (1999); McKee & Ostriker (2007); Young (2023). During the collapse, friction and collisions between the collapsing particles transform the gravitational potential into thermal energy, which initially is radiated away as thermal radiation at infrared (IR) wavelengths. However, as the density increases, the collapsing core becomes opaque to the thermal radiation. Consequently, the temperature and pressure rise and a first hydrostatic core (FHSC) is formed (Larson, 1969). The temperature continues to increase adiabatically until it reaches ~2000 K, at which point molecular hydrogen starts dissociating. H_2 dissociation is an endothermic reaction, i.e. it absorbs the energy released during the collapse, allowing further contraction of the FHSC until all H_2 is dissociated, which marks the formation of a protostar. At this point, the protostar has only reached a fraction of its final mass. It is still deeply embedded in an optically thick envelope from which it continues to accrete.

In general, clumps and cores in GMCs are rotating and therefore possess significant angular momentum (e.g. Goodman et al., 1993; Burkert & Bodenheimer, 2000). Because the collapse occurs over many orders of magnitude in radius, it follows from the conservation of angular momentum that there must be a significant increase in angular velocity. Consequently, the envelope that remains after the formation of the protostar does not fall directly onto the protostar but remains in orbital rotation around it. Considering that the collapse that led to the formation of the protostar with its envelope is an approximately spherically symmetric process, the envelope is also expected to be approximately spherically symmetric. Under this assumption, if a parcel of gas possesses a velocity component parallel to the rotation axis, it is expected to eventually collide with a gas parcel with an opposing velocity component close to the equatorial plane, such that the two components cancel each other. Therefore, over time, the envelope will flatten into a disc-like structure that is axisymmetric about the axis of rotation and symmetric with respect to the equatorial plane (typically called the midplane). Once the envelope has flattened enough that at least some radiation at near- or mid-IR wavelengths (λ < 25 µm) can escape the central regions, it is for the first time possible to observe direct evidence of the newly formed protoplanetary disc.

1.1.2 Observed properties of protoplanetary discs

1.1.2.1 Spectral energy distributions and classification

For a long time, until the advent of the Hubble Space Telescope (HST), it was impossible to detect protoplanetary discs in spatial observations. Instead, one of the most important tools for characterising young stellar objects (YSOs) and their discs was spectral energy distributions (SEDs). The SED describes the flux of an object F as a function of wavelength λ or frequency ν. Its shape, especially in the IR and mm wavelength range, can provide insight into the evolutionary stage of the YSO because this wavelength range is emitted mainly as thermal radiation by solids in the disc. Near- and mid-IR emission traces the dust in the hot and warm regions close to the star ($R \lesssim 1$ au), while far-IR and mm emission originates in the colder outer disc. With this relation, SEDs can be used to derive the presence of dust at different distances from the star, which has led to a classification scheme that was initially proposed by Lada (1987) (see also Fig. 1.2) and has since been refined multiple times. It is based on the IR spectral index, defined as

$$\alpha_{\mathrm{IR}} = \frac{d\log(\lambda F_\lambda)}{d\log(\lambda)}, \tag{1.1}$$

which is typically measured between two wavelength points in the near- to mid-IR, often between 2.2 and 14 µm. In this work, the following scheme will be adopted:

Class 0: $\alpha_{\rm IR}$ cannot be measured, as no near- or mid-IR is observed. The peak of the SED is in the far-IR or sub-millimetre. These objects are interpreted as a YSOs where the collapse phase is ongoing, and the protostar is deeply embedded in an opaque envelope. The lifetime of this phase is estimated to be ∼0.1 Myr (Evans et al., 2009).

Class I : $\alpha_{\rm IR} \gtrsim -0.3$, i.e. the SED has a rising slope in the near-IR. The peak lies in the mid- to far-IR. These objects are thought to be in the later stages of star and disc formation, but they still have a substantial envelope falling onto the disc. High-velocity outflows, such as jets, are often present (e.g. review by Frank et al., 2014). Evans et al. (2009) estimate a lifetime of ∼0.5 Myr for this phase.

Class II: $-1.6 \lesssim \alpha_{\rm IR} \lesssim -0.3$, i.e. the SED has a declining slope in the near- and mid-IR with significant excess emission over the clearly visible stellar photosphere. Class II objects are interpreted as pre-main sequence stars, where the envelope has been mostly accreted and settled into a well-defined protoplanetary disc. Excess emission in the ultraviolet (UV) or Hα is often observed, attributed to the disc-material accreted onto the star. Class II discs have been the main focus of the field of planet formation for a long time and are also the focus of this work. However, recent results deduced from the time evolution of observed disc masses (Manara et al., 2018; Williams et al., 2019; Testi et al., 2022) and observations of substructures in class I discs suggest that planets could form already at earlier stages (Hsieh et al., 2024). The class II phase usually lasts for a few million years until the disc is dispersed (e.g. Ribas et al., 2014).

Class III: $\alpha_{\rm IR} \lesssim -1.6$, i.e. the SED is essentially that of a pure photosphere with no IR or UV excess emission, indicating that the disc has mostly dispersed and accretion stopped in these objects. Consequently, planetesimals can no longer form. However, a small contribution at far infrared or millimetre wavelengths commonly indicates remaining dust that is typically thought to be produced and continuously replenished by colliding planetesimals (e.g. review by Williams & Cieza, 2011).

SEDs can also show characteristics of an evolutionary stage that lies between two classes. One important example is the class of transition discs. If the SED has reduced or no flux in the near- or mid-IR, while significant flux is present at longer wavelengths, the disc is assumed to have an inner dust cavity. Such objects are called transition discs because they are thought to be discs that are being dispersed from the inside out, thus transitioning between classes II and III. They are particularly interesting since they can provide insights into the disc dispersal process.

Although several factors can complicate the classification and its interpretation, such as the disc geometry or the size of dust grains in the disc (e.g. Williams & Cieza, 2011), SEDs have been extremely helpful in building large statistical samples of discs in multiple star-forming regions of different ages.

Throughout this work, unless specified otherwise, the term "discs" will refer specifically to class II discs around solar-type or lower-mass stars.

1.1.2.2 Lifetime

SED-based statistics made it possible to put constraints on the timescales over which protoplanetary discs are dispersed and set an upper limit for the timeframe over which planet formation has to occur. For a comprehensive review, see Ercolano & Pascucci (2017). To summarise the most important findings, the fraction of disc-bearing stars in very young clusters ($\lesssim$ 1 Myr) is close to 90 %, but decreases quickly with cluster age and reaches close to 0 after 10 to 20 Myr. Assuming an exponential

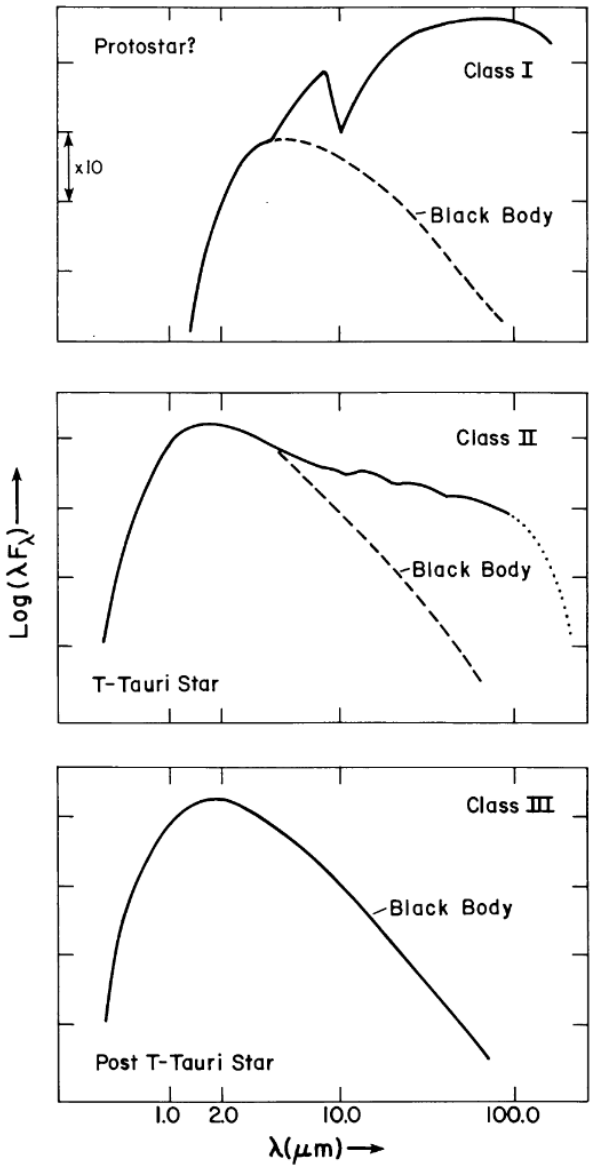

Figure 1.2: SED-based classification of YSOs as originally proposed by Lada (1987). Figure source: Lada (1987)

decline, Ribas et al. (2014) find an e-folding time for class II discs of 2 to 3 Myr at 3 to 12 µm and 4 to 6 Myr at 22 to 24 µm, hinting towards an inside-out dust clearing process or the production of second-generation dust by colliding planetesimals in the outer parts of the disc (Currie et al., 2008), but both could happen simultaneously. At the same time, the fraction of transition discs, i.e. discs with inner cavities, is on the order of 10 % and increases significantly with age, which suggests that the inside-out clearing process is acting on very short timescales of a few 10^5 years (Skrutskie et al., 1990; Balog et al., 2016).

1.1.2.3 Mass

In the optically thin limit, dust continuum emission can also be used to estimate the dust mass in a protoplanetary disc. If one assumes an average dust temperature $\bar{T}_d$ and dust opacity $\bar{\kappa}$ for the disc, the dust mass $M_{\rm dust}$ can be estimated from the total flux F_ν using the relation (Hildebrand, 1983; Miotello et al., 2023)

$$F_\nu = \frac{B_\nu\left(\bar{T}_d\right)\bar{\kappa}}{d^2} M_{\rm dust}, \tag{1.2}$$

where $B_\nu\left(\bar{T}_d\right)$ is the Planck function at the average disc temperature and d is the distance to the observed source.

Figure 1.3 shows the cumulative dust mass distribution for multiple star-forming regions with different ages (Tychoniec et al., 2018). The comparison reveals that the dust mass quickly declines with age, indicating that it is either lost in processes such as radial drift, where it accretes onto the star, or aggregates into planetesimals, which are much less efficient in emitting thermal radiation. The dust mass can be a proxy for the total disc mass if one assumes a specific dust-to-gas mass ratio ϵ. With the common assumption of $\epsilon = 0.01$, the value of the ISM (Bohlin et al., 1978), disc masses are typically found to be on the order of ∼1 % of the stellar mass (e.g. Andrews & Williams, 2005; Andrews et al., 2013). It should be noted, however, that these estimates are subject to significant uncertainties from the assumed average dust temperature and opacity and, in particular, the dust-to-gas ratio, which is much higher in some discs (e.g. Ansdell et al., 2016; Miotello et al., 2017) and is expected to evolve or vary with location in the disc (e.g. review by Birnstiel, 2023). Moreover, recent observations suggest that there may be a significant contribution of optically thick emission at the wavelengths typically used to determine the dust mass (Tripathi et al., 2017; Andrews et al., 2018a; see also reviews by Andrews, 2020; Miotello et al., 2023). If that is the case, the resulting disc masses are underestimated.

It is also possible to use gas tracers to obtain total disc masses independent of the dust mass measurements. However, a direct measurement is challenging since the main gaseous component is H_2, an extremely weak emitter due to its lack of a dipole moment. Instead, one has to rely on indirect gas mass tracers from other atomic or molecular species. The most abundant molecule after H_2 is carbon monoxide (CO), but it is so abundant that its emission, although easy to observe at (sub-)mm wavelengths, is mostly optically thick, limiting its usefulness as a mass tracer. Much better mass tracers are the CO isotopologues, especially ^{13}CO, C^{18}O or ^{13}C^{17}O, which in recent years have been used to survey many nearby star-forming regions, in particular with the Atacama Large Millimeter/Submillimeter Array (ALMA) (e.g. Ansdell et al., 2016; Pascucci et al., 2016; Eisner et al., 2016). Figure 1.4 shows the cumulative distribution of dust and gas masses compiled from various surveys by Andrews (2020). An essential result of the surveys is that the masses derived from CO emission are lower than expected, and the inferred dust-to-gas ratios are often much higher than the ISM value of 1 %. Moreover, most discs appear to possess much less dust and gas than would be required to form the planets in our solar system. However, as the dust continuum observations, the CO-based mass measurements are subject to their own uncertainties. For example, chemical processes

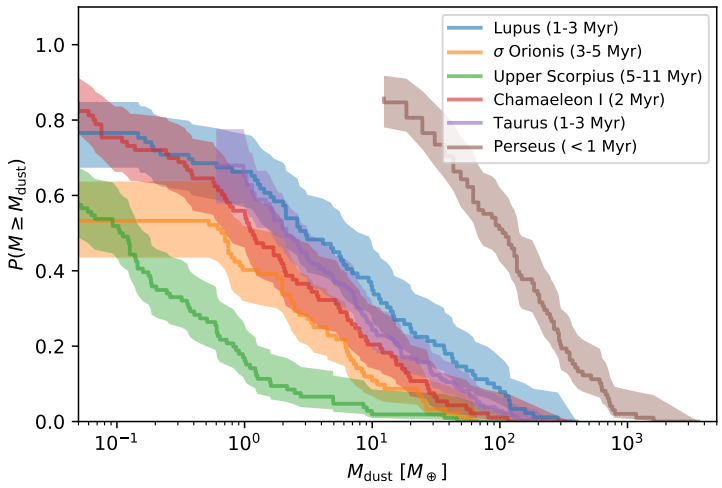

Figure 1.3: Cumulative distribution of dust disc masses in different star-forming regions. Data compiled by Tychoniec et al. (2018). Figure source: Miotello et al. (2023)

like the sequestration of carbon or oxygen-rich volatiles onto icy grains or organic molecules can remove CO from the gas phase, which would lead to a lower than expected C/H ratio and explain the low mass estimates (Favre et al., 2013, e.g.). Other tracers, such as hydrogen deuteride (HD), carbon monosulfide (CS) or the [OI] 63.2 µm line can be used as well, albeit within their own limitations (e.g. Andrews, 2020; Miotello et al., 2023, and references therein). At high disc-to-star mass ratios $M_{\rm disc}/M_* \gtrsim 0.1$, when the disc is sufficiently massive for self-gravity to become significant (Kratter & Lodato, 2016), the mass of the disc can also be constrained dynamically, by fitting its rotation curve obtained for example in CO observations. This has been initially proposed by Rosenfeld et al. (2013) and so far has been applied only to a few discs, Elias 2-27 (Veronesi et al., 2021), IM Lup and GM Aur (Lodato et al., 2023), and MWC 480 (Andrews et al., 2024). Despite the uncertainties, typical disc masses of class II objects appear to be on the order of ~1 % of their host star's mass and observations suggest that the mass fraction increases with stellar mass (Pascucci et al., 2016).

1.1.2.4 Mass accretion

One of the most important mechanisms contributing to the dispersal of protoplanetary discs is accretion onto the central star. For low-mass stars ($M_* \lesssim 1\,M_\odot$), it is generally expected that the disc is truncated at the stellar magnetosphere at a few stellar radii, from where it follows along magnetic field lines in accretion funnels onto the star, where it shocks near the stellar photosphere and produces strong emission that can be observed in the UV continuum or several emission lines such as Hα and other Balmer, Paschen or Brackett lines (see e.g. Hartmann et al., 2016, for a review). Under the assumption that the accreting material in the shock radiates away the entire kinetic energy it gained from the free-fall onto the star, the observed accretion luminosity $L_{\rm acc}$ can be converted into a mass accretion rate:

$$\dot{M}_{\rm acc} = \left(1 - \frac{R_*}{R_{in}}\right)^{-1} \frac{L_{\rm acc} R_*}{G M_*}, \tag{1.3}$$

where R_* and $R_{\rm in}$ are the stellar radius and the inner disc radius, respectively. A typically observed accretion rate for low-mass class II YSOs is $10^{-8}\,M_\odot\,{\rm yr}^{-1}$. However, the rates can range from 10^{-12}

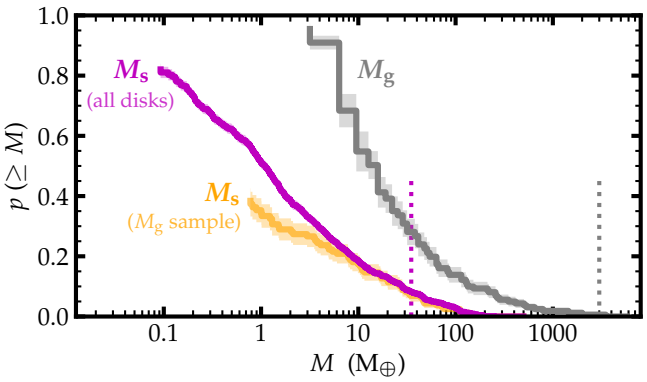

Figure 1.4: Cumulative distribution of dust/solid (M_s, purple) and gas (M_g, grey) masses compiled by Andrews (2020) from multiple surveys. Dust masses have been derived from mm continuum observations, gas masses from CO isotopologue emission, converted using the model by Miotello et al. (2017). The orange line shows the dust mass distribution in the subsample of those discs for which gas masses are available. The vertical dashed lines show the minimum dust (purple) and gas (grey) masses that would be required to produce the planets in our solar system (Weidenschilling, 1977). Figure used with permission of Annual Reviews, from Andrews (2020); permission conveyed through Copyright Clearance Center, Inc.

to $10^{-6}\,M_\odot\,yr^{-1}$, and the data suggests a positive correlation with stellar mass, as well as a negative correlation with age (e.g. Hartmann et al., 1998; Muzerolle et al., 2003; Hartmann et al., 2016; Manara et al., 2023).

Sustaining the accretion of mass is only possible if there is a radial mass flux from the outer to the inner disc, i.e., the accreting material's angular momentum must be either redistributed or removed from the disc. Some possible mechanisms that could drive accretion will be discussed in Sect. 1.1.3.4.

1.1.2.5 Size

Since protoplanetary discs do not have a well-defined, sharp boundary, their size is usually expressed in terms of an effective radius that encircles a fixed fraction of a given tracer's luminosity in spatially resolved observations. In a recent review, Andrews (2020) report dust disc sizes of approximately 200 objects ranging from ~10 to ~500 au (Tripathi et al., 2017; Andrews et al., 2018a; Hendler et al., 2020), measured as the 90 % fraction in mm continuum observations. Gas disc sizes derived in a similar fashion from CO line emission are in the range of ~100 to ~500 au and the effective CO-gas radius is universally larger than the dust radius, on average by a factor of ~ 2 (Ansdell et al., 2018).

1.1.2.6 Substructure

With the advent of ALMA, it has become possible to observe protoplanetary discs at high spatial resolution for the first time. The wealth of data it has provided led to significant new insights into planet formation. One of the most important discoveries is that most class II protoplanetary discs are highly sub-structured (e.g. ALMA Partnership et al., 2015; Zhang et al., 2016; Andrews et al., 2018b). A selection of discs that show various types of substructures is shown in figure 1.5. Since then, it has become apparent not only from mm continuum emission but also from optical/scattered light observations, e.g. with the Spectro-Polarimetric High-contrast Exoplanet Research (SPHERE) instrument on the Very Large Telescope (VLT), that substructures within discs are ubiquitous in both,

the gas and the dust (e.g. van der Marel et al., 2013; Zhang et al., 2016; Benisty et al., 2015, 2017, 2018; Andrews et al., 2018b; Long et al., 2018). When comparing different tracers within a single disc, however, substructures are not always present or identical at all tracers (e.g. Öberg et al., 2021). These discoveries made it clear that many discs do not have a simple smooth density profile, as often assumed in models, but are, in fact, much more complex, with many physical and chemical processes affecting their structure and evolution. For a comprehensive review of the morphological types of substructure and various processes that could be responsible for their presence, see Andrews (2020). The main categories are cavities, rings/gaps, spirals, and arcs. Many of these can be interpreted as signatures of embedded planets (c.f. Sect. 1.2) or disc winds (c.f. Sect. 1.3), but also many other processes could produce similar substructures, so linking them to the presence of planets is highly challenging (see, e.g. Pinte et al., 2022b, for a recent review).

1.1.2.7 Embedded planets

The overwhelming majority of exoplanets detected so far are very old, much older than the ∼10 Myr lifetime of protoplanetary discs. Observing young planets or protoplanets that are still in the process of forming is much more difficult because the optically thick protoplanetary disc blocks the view of the planet or the star, especially when viewed edge-on, which is what the most effective detection methods, transit photometry and radial velocity searches, rely on. Direct imaging of planets within discs remains difficult as well, as extinction along the line of sight can be high (e.g. Sanchis et al., 2020; Alarcón et al., 2024; Benisty et al., 2023). So far, the only direct detection that is generally undisputed is a planetary system in PDS70, where two planets were directly imaged inside the strongly depleted cavity of its transition disc (e.g. Keppler et al., 2018; Wagner et al., 2018; Haffert et al., 2019).

As mentioned in the previous section, substructures such as gaps, rings and spirals can be signatures of embedded planets. Massive planets perturb the density, pressure, and velocity structure in their disc (c.f. Sect. 1.2), creating gaps and spirals with characteristic deviations from a (sub-)Keplerian rotation profile. One of the most promising prospects for detecting forming planets is thus the detailed analysis of disc substructure, which has gained much attention in recent years. Teague et al. (2018) reported the first kinematic detection of embedded planets in the disc of HD 163296 and were able to constrain their mass and radius. In the same source, as well as in HD 97048, Pinte et al. (2018, 2019) found kinks in the isovelocity curves (i.e. the region where the projected velocity of the emitting surface is constant) of different ^{12}CO lines, consistent with the presence of a giant planet. Other observed signatures are, for example, spiral structures in the kinematics, which can be seen after subtracting a Keplerian disc model (e.g. Teague et al., 2019b; Wölfer et al., 2021; Teague et al., 2021). For a comprehensive review of the various types of signatures, see Pinte et al. (2022b).

1.1.3 Theoretical models of protoplanetary discs

The massive leap in observational capabilities within the last decade has provided a wealth of new data that is often difficult to interpret. Moreover, despite the remarkable advancements in the quality and quantity of observational data, many details remain concealed. To overcome these issues at least partially, observationally informed theoretical models that can be used for direct or indirect comparisons to the data are extremely valuable. Unfortunately, creating a single detailed model that includes all physical processes that may be relevant in protoplanetary discs is hugely challenging. Since many of these processes can only be solved numerically, it is too computationally expensive to be feasible today. Instead, models typically have to choose between focusing on selected details to study their effects within a particular system. Alternatively, they can include simplified approximations

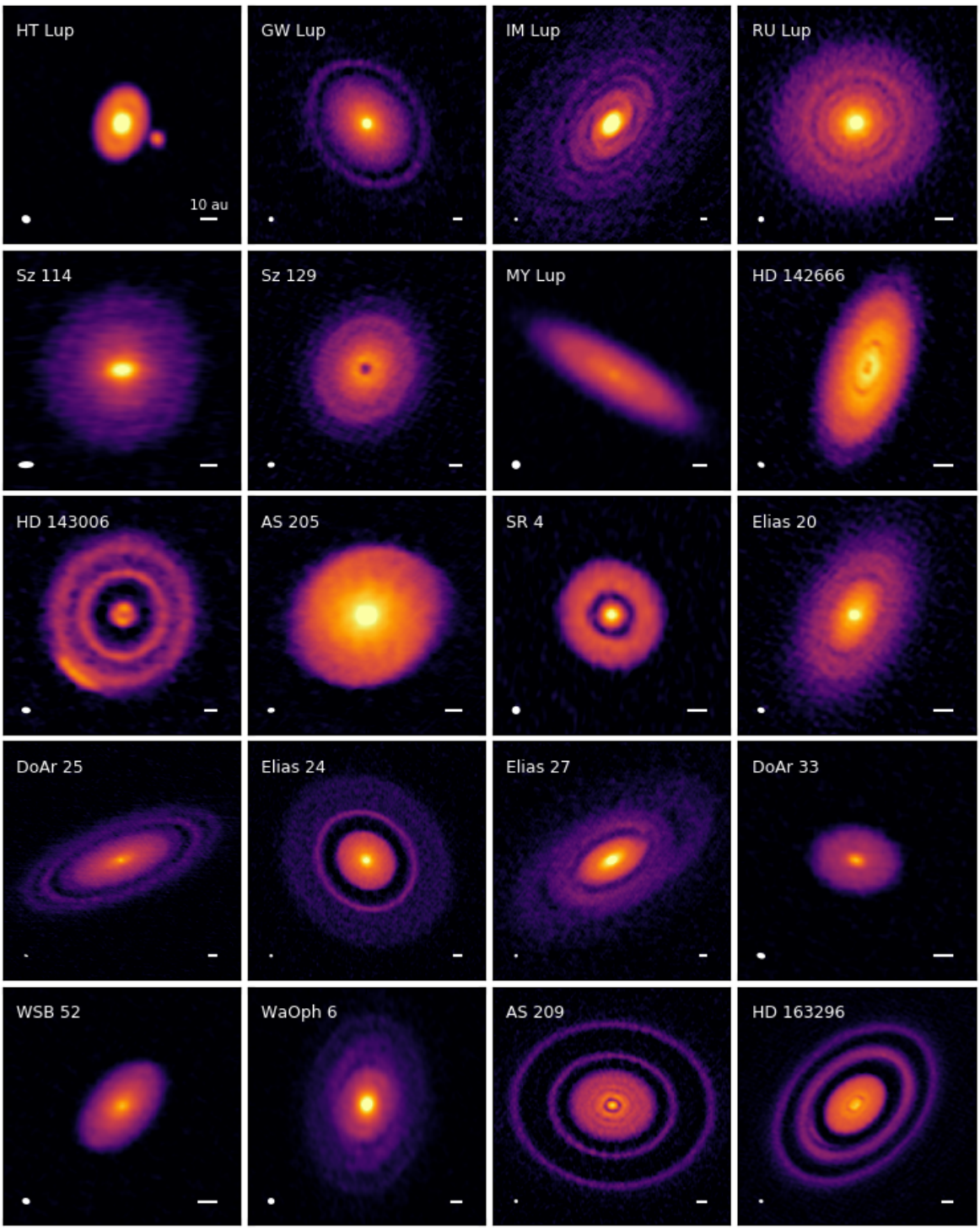

Figure 1.5: Gallery of 1.25 mm continuum emission images of the discs in the DSHARP sample. It is clear that (dust-) substructures are common. Image source: Andrews et al. (2018b), licensed under CC BY 4.0.

of many different processes to analyse their impact on general trends in large synthetic populations of discs. For most processes, an analytical description is only possible when simplifying assumptions are made. For example, a classical approach that has been initially derived for accretion discs around black holes but has become the widely adopted standard for describing protoplanetary discs treats the disc as vertically thin, axisymmetric, viscous, non-magnetised, rotationally supported low-mass disc (Shakura & Sunyaev, 1973; Lynden-Bell & Pringle, 1974). This approach is used even today as a starting point for many detailed models, including those presented in this thesis, to build upon. The details of this approach and its limitations will be discussed in the following sections.

Since protoplanetary discs consist mainly (~99 %) of gas, it is possible to use the concepts of fluid mechanics in order to describe their structure and evolution. As discussed in Sect. 1.1.2.4, discs are accreting, which requires that angular momentum is either redistributed within the disc or removed from the disc. While the latter may be the dominant process (see discussion in Sect. 1.3.2), in this work, it will be assumed that angular momentum is redistributed within the disc by viscous stresses. The disc can, therefore, be described by the continuity equation and the Navier-Stokes equation:

$$\frac{\partial \rho}{\partial t} + \nabla \cdot (\rho \boldsymbol{u}) = 0 \tag{1.4}$$

$$\frac{\partial \boldsymbol{u}}{\partial t} + \boldsymbol{u} \cdot \nabla \boldsymbol{u} = -\frac{\nabla P}{\rho} - \nabla \Phi + \frac{1}{\rho} \nabla \boldsymbol{T}, \tag{1.5}$$

where ρ is the mass density of the gas, $\boldsymbol{u}$ is the velocity vector, P the gas pressure, Φ the gravitational potential and $\boldsymbol{T}$ is the viscous stress tensor. If the mass of the disc is small compared to that of the star ($M_{\rm disc}/M_* < 0.1$), its self-gravity can be neglected (Kratter & Lodato, 2016), which is expected to be the case for most class II discs (c.f. Sect. 1.1.2.3). The gravitational potential at a distance r from the star can then be simplified to that of the star, $\Phi = -GM_*/r$. Another simplifying assumption is that the disc is axisymmetric. Moreover, as will be discussed later in Sect. 1.1.3.2, the disc orbits its star at close to Keplerian speed, such that in cylindrical coordinates (R, ϕ, z) the azimuthal velocity component $u_\phi \approx \sqrt{GM_*/R}$. This gives orbital timescales of days to years at the scales of protoplanetary discs, much shorter than the timescale for accretion, which is on the order of Myrs. It follows that $u_R \ll u_\phi$ and any velocity components that arise due to viscous stresses are small, and the disc can be considered to be in hydrostatic equilibrium.

1.1.3.1 Vertical disc structure

In the vertical direction, the vertical component of the gravitational force is balanced by the thermal pressure of the gas:

$$\frac{1}{\rho}\frac{\partial P}{\partial z} = -\frac{\mathrm{d}\Phi}{\mathrm{d}z}. \tag{1.6}$$

Suppose that the disc is thin, i.e. $z/r \ll 1$, then we can make the approximation

$$-\frac{\mathrm{d}\Phi}{\mathrm{d}z} \approx -\frac{GM_*}{R^3} z = -\Omega_K^2 z, \tag{1.7}$$

where Ω_K is the Keplerian angular velocity. When it is further assumed that the disc is locally isothermal, i.e. the speed of sound c_s is constant in the vertical direction (but see Sect. 1.1.3.3), eq. (1.6) can be expressed as

$$\frac{c_s^2}{\rho}\frac{\partial \rho}{\partial z} = -\Omega_K^2 z, \tag{1.8}$$

where we made use of the isothermal speed of sound $c_s^2 = \frac{\partial P}{\partial \rho}$. This can be directly integrated, and we find

$$\rho(z) = \rho_0 \exp\left(\frac{-z^2}{2H^2}\right), \tag{1.9}$$

where ρ_0 is the density at the midplane and H is the vertical disc scale height given by

$$H = \frac{c_s}{\Omega_K}, \tag{1.10}$$

which is a function of R. We can now calculate the disc's aspect ratio.

$$\frac{H}{R} = \frac{c_s}{v_K} \tag{1.11}$$

and find that our assumption of a thin disc is valid as long as $c_s \ll v_K$, where v_K is the Keplerian speed. For thin discs, it is often easier to work with the surface density instead of the volume density,

$$\Sigma(r) = \int_{-\inf}^{\inf} \rho(R, z) dz. \tag{1.12}$$

The midplane density can then be written as

$$\rho_0 = \frac{1}{\sqrt{2\pi}} \frac{\Sigma}{H}. \tag{1.13}$$

1.1.3.2 Radial disc structure

In the radial direction, an additional centripetal term arises in the force balance due to the rotation of the disc:

$$\frac{1}{\rho}\frac{\partial P}{\partial R} = -\frac{\mathrm{d}\Phi}{\mathrm{d}R} + \frac{u_\phi^2}{R}, \tag{1.14}$$

which, when expressed as

$$u_\phi^2 = v_K^2 + \frac{R}{\rho}\frac{\partial P}{\partial R}, \tag{1.15}$$

shows that the orbital velocity of the gas is different from the Keplerian speed. Since the pressure typically decreases with increasing R in discs without substructure, the second term on the right-hand side is negative, and the gas is expected to orbit with sub-Keplerian speed. If the pressure is described by a power law $P = R_0(R/R_0)^{-\beta}$, where $P_0 = \rho_0 c_s^2$ is the pressure at radius R_0, we find,

$$u_\phi = v_K \left(1 - \beta \frac{c_s^2}{v_K^2}\right)^{1/2}, \tag{1.16}$$

and we see that the deviation from the Keplerian speed is of order $O\left(\frac{H}{R}\right)^2$, which is small in a thin disc. Nevertheless, it has a very important consequence for the dust in the disc, which does not experience the additional pressure gradient force and is therefore orbiting at Keplerian speed. Consequently, the gas moves slower than the dust, leading to a drag force acting on the dust that depends on the gas density and the dust grain size. The drag forces give rise to complex dust dynamics with substantial implications on the formation of planetesimals, such as the radial drift of dust particles towards the star. For a recent comprehensive review on dust dynamics in protoplanetary discs, see Birnstiel (2023).

1.1.3.3 Radial temperature structure

A first approximation of the temperature structure can be made if it is assumed that the disc has a constant aspect ratio H/R and is in a thermal equilibrium where the intercepted stellar irradiation and the emitted thermal radiation set the balance. Since the irradiating flux at radius R scales with R^{-2} and the emitted thermal radiation scales with T^4, the radial profile of the temperature is expected to follow a power law profile $T(R) \propto R^{-1/2}$.

This simple estimate assumes that stellar irradiation is the only heating source and that the disc is optically thin. In reality, discs are optically thick so that towards the midplane, the heating is generally dominated by reprocessed radiation from the disc surface. Consequently, there will also be a vertical temperature gradient. The details depend strongly on the dust opacity, and the disc's geometry is also important. More sophisticated models show that discs are expected to flare, meaning their aspect ratio increases with radius, often following a power law $H/R \propto R^{\gamma}$. This leads to the disc's surface intercepting a higher fraction of the stellar radiation and, consequently, higher temperatures. Moreover, other processes, such as cosmic rays or viscous heating, can also contribute to the thermal balance. Taking all these factors into account requires detailed calculations with radiative transfer models (see, e.g. Dullemond et al., 2007, for a review).

1.1.3.4 Viscous evolution

So far, we have not considered the azimuthal direction, as any pressure gradients or gravitational forces vanish in axisymmetric discs. However, a non-vanishing force due to viscous stresses plays an essential role in mass diffusion. If bulk viscosity is neglected such that the viscosity is given only by shear stresses, which is usually a reasonable assumption in sub-sonic flows, the only non-zero component of the viscous stress tensor is

$$T_{R\phi} = \rho \nu R \frac{\mathrm{d}\Omega}{\mathrm{d}R}, \tag{1.17}$$

where ν is the kinematic viscosity, which will be discussed later in this section. Assuming further that $v_z = 0$ and approximating $v_\phi = v_K$, the azimuthal component of the Navier-Stokes equation (1.5) integrated in the vertical direction,

$$\Sigma \left(\frac{\partial u_\phi}{\partial t} + \frac{u_R u_\phi}{R} + u_R \frac{\partial u_\phi}{\partial R} \right) = \frac{1}{R^2} \frac{\partial}{\partial R} \left(R^2 T_{R\phi} \right), \tag{1.18}$$

can be combined with the continuity equation (1.4),

$$\frac{\partial}{\partial t}(\Sigma R u_\phi) + \frac{1}{R} \frac{\partial}{\partial R}(R u_R \Sigma R u_\phi) = \frac{1}{R} \frac{\partial}{\partial R} \left(R^2 T_{R\phi} \right), \tag{1.19}$$

to obtain the equation for the evolution of the surface density (Lynden-Bell & Pringle, 1974, see also, e.g. Frank et al., 2002; Lodato, 2008):

$$\frac{\partial \Sigma}{\partial t} = \frac{3}{R} \frac{\partial}{\partial R} \left[R^{1/2} \frac{\partial}{\partial R} \left(\nu \Sigma R^{1/2} \right) \right]. \tag{1.20}$$

This is a diffusion equation, so the viscous stresses lead to the diffuse transport of mass and angular momentum. As the disc spreads, angular momentum is transported outward, allowing the radial mass transport necessary for accretion onto the star. We have yet to specify the exact form of the viscosity,

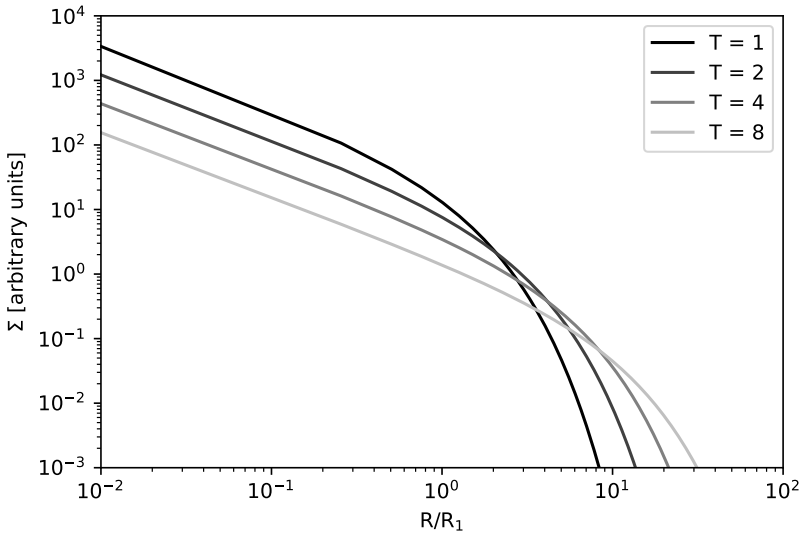

Figure 1.6: Evolution of the surface density in the self-similar solution at different scaled times T. The initial profile at $T = 1$ falls off exponentially beyond $R = R_1$, and the disc spreads with time.

but if we assume that it scales with a power law $\nu = \nu_1 (R/R_1)^\gamma$, eq. (1.20) can be solved and we find the well-known self-similar solution (Lynden-Bell & Pringle, 1974),

$$\Sigma(\tilde{R}, \tau) = \frac{C}{3\pi\nu_1 \tilde{R}^\gamma} \tau^{-(5/2-\gamma)/(2-\gamma)} \exp\left(-\frac{\tilde{R}^{(2-\gamma)}}{\tau}\right), \tag{1.21}$$

where $\tilde{R} = R/R_1$, R_1 is a characteristic radius that can be understood as an exponential cut-off length at $t = 0$, C is a normalisation constant, $\tau = t/t_s + 1$ and

$$t_s = \frac{1}{3(2-\gamma)^2} \frac{R_1^2}{\nu_1}. \tag{1.22}$$

Fig. 1.6 illustrates the evolution of the surface density profiles with this solution for typical protoplanetary disc parameters.

The timescale over which the self-similar solution evolves is set by the viscosity ν. However, the physical processes behind ν are still unclear. The viscosity that arises from random molecular collisions, which is the typical mechanism that is considered for fluids on earth, is estimated to be very small and would produce accretion rates that are too small by many orders of magnitude (e.g. Armitage, 2010). Instead, turbulence generated by various hydrodynamic instabilities has been proposed to generate an effective viscosity that drives accretion in protoplanetary discs (see Lesur et al., 2023, for a recent review). The effective viscosity conveniently abstracts its underlying physics, allowing us to model the viscous evolution without knowing the exact processes responsible for the angular momentum transport. It is traditionally expressed in terms of α, such that

$$\nu = \alpha c_s H. \tag{1.23}$$

This model is commonly referred to as the α-disc model. It was initially proposed by Shakura & Sunyaev (1973).

It is nevertheless essential to understand the mechanisms involved in driving viscous accretion through turbulence. For a long time, the most promising mechanism to create turbulence in discs was

the so-called magnetorotational instability (MRI) (Balbus & Hawley, 1991), a powerful magnetohydrodynamic (MHD) instability that can arise in a partially ionised differentially rotating disc when a (weak) magnetic field is present. However, more advanced studies that include non-ideal MHD effects have shown that the MRI is likely suppressed in the planet-forming regions of discs (e.g. Bai, 2015; Simon et al., 2018). As an alternative, several hydrodynamic turbulences have been investigated, most notably the vertical shear instability (VSI) (Arlt & Urpin, 2004; Nelson et al., 2013; see also Goldreich & Schubert, 1967; Fricke, 1968), the convective overstability (COS) (Klahr & Hubbard, 2014; Lyra, 2014) and the zombie vortex instability (ZVI) (Barranco & Marcus, 2005; Marcus et al., 2013; Lesur & Latter, 2016). The exact conditions at which these mechanisms operate, their strength and the efficiency of angular momentum transport are still an open research question. Still, current models often predict an effective $\alpha \sim 10^{-4}$, which cannot explain many of the observed accretion rates (Lesur et al., 2023). Nevertheless, the models are consistent with observational constraints on turbulence, which so far have only been able to provide an upper limit of $\alpha \lesssim 10^{-3}$ at the population level (e.g. review by Rosotti, 2023), which has been inferred from multiple indirect methods, as well as a minimal number of direct observations. In light of these results, the paradigm of wind-driven instead of viscous accretion has gained much attention. Specifically, magnetic disc winds can extract angular momentum from the disc, as will be discussed in Sect. 1.3.2.

1.2 Planet-disc interactions

If a planet is formed in a disc, its gravitational potential will induce feedback processes that act on the disc and vice versa. The most important process for the disc's evolution is the formation of density gaps in the presence of a massive planet. The other way around, gravitational torques from the disc can lead to the migration of planets. This section will briefly explain the most important concepts behind these two feedback mechanisms. For a detailed review of planet-disc interactions, see Kley & Nelson (2012); Baruteau et al. (2014) and Paardekooper et al. (2022).

1.2.1 Formation of gaps and spiral density waves

Due to the differential rotation of the Keplerian disc, a particle that is orbiting the star at a distance that is different from that of the planet will have a non-zero relative velocity with respect to the planet. Consider a particle that is closely passing the planet but sufficiently far away so that it experiences only a small deflection due to the planet's gravitational force. During deflection, the particle and the planet exchange angular momentum. The magnitude of this exchange can be roughly estimated using the so-called impulse approximation (Lin & Papaloizou, 1979). Assuming that the particle passes the planet with a relative velocity Δv at a distance b, which is the orbital separation between the particle and the planet, the change of the particle's angular momentum can be approximated as (Lin & Papaloizou, 1979)

$$\Delta j = \frac{2 a_p G^2 M_p^2}{b^2 \Delta v^3}, \tag{1.24}$$

where M_p and a_p are the planet's mass and orbital distance, respectively. Gas that orbits the star at a distance larger than the planet's will have a slower orbital velocity, so the angular momentum transfer will be positive. This leads to an increase in the orbital distance. Conversely, inside the planet's orbit, the gas is faster than the planet, so it will lose angular momentum and move towards the star. That way, the planet effectively pushes away the gas in its vicinity.

However, this is counteracted by viscous torques and pressure gradients in the disc so that only massive planets can effectively displace the gas in their orbit and open a gap. For the classical α-disc (c.f. Sect 1.1.3.4), it is possible to derive a criterion for gap formation by balancing the rate of angular momentum transfer with the the viscous torque (Lin & Papaloizou, 1993; Paardekooper et al., 2022):

$$q = \frac{M_p}{M_*} \gtrsim 5h^{5/2}\alpha^{1/2}, \tag{1.25}$$

where $h = H/R$ is the aspect ratio of the disc (typical values are 0.05 – 0.1). For a typical disc around a solar-mass star with aspect ratio $h = 0.05$ and $\alpha = 10^{-3}$ this criterion is fulfilled if $q > 8.8 \cdot 10^{-5}$, or $M_p \gtrsim 29\,\mathrm{M}_\oplus$.

1.2.2 Planet migration

A more detailed and accurate approach to the problem of angular momentum exchange is to do a Fourier analysis of the planet's perturbing gravitational potential. It can then be shown that the response of the disc to the planet's perturbation is the excitation of spiral density waves, which are a superposition of discrete resonances of the torques exerted by the planet (Goldreich & Tremaine, 1979, 1980). The first resonance is called the corotation resonance because it appears where the disc's angular velocity matches that of the planet $\Omega(R) = \Omega_p$. All other resonances are called Lindblad resonances. The sum of the torques exerted at all resonances yields the total amount of exchanged angular momentum. It will determine the direction and rate with which the planet changes its orbital distance, i.e. migrates. Generally, the resonances exterior to the planet's orbit exert a positive torque on the planet, which removes angular momentum from the planet and leads to inward migration. Torques exerted from inside the planet's orbital radius are negative, adding angular momentum to the planet and leading to outward migration.

Planet migration can be divided into different regimes. The type I migration regime is valid for less massive planets that do not significantly disturb the disc's density structure. Since the planet is not able to open a gap, the torques generated in its corotation region cannot be neglected. In a reference frame that corotates with the planet, the gas in the corotation region performs U-turns when it approaches the planet from either side. Gas from inside the planet's orbit moves outwards, and gas from outside the planet's orbit moves inward. This dynamic looks similar to a horseshoe, so the corotation region is often called the horseshoe region. The path the gas follows is called a horseshoe orbit (Ward, 1991). If the horseshoe orbits are asymmetric, for example, due to temperature or density gradients, there will be a net exchange in angular momentum called the horseshoe drag. Many numerical models accounting for many different effects have been developed, and depending on the assumptions, the resulting migration rates vary drastically, and even the direction can change to outward migration. However, under most conditions, inward migration is expected (e.g. Paardekooper et al., 2022).

Type II migration refers to the regime where the planet is massive enough to carve a gap in the disc. If the planet can perfectly separate the outer and the inner disc so that no gas can flow across the gap, the planet will be locked inside its own gap, and so it will migrate inwards together with the gap at the viscous rate (e.g. Lin & Papaloizou, 1986). However, many recent numerical models have shown that a significant amount of mass can flow across the gap and depending on the details, this can lead to faster or slower inward migration (e.g. Lubow & D'Angelo, 2006; Dürmann & Kley, 2015, 2017). Type II migration is the regime most relevant in this work, as the models containing a planet are all focused on giant planets.

The type III migration regime is relevant for intermediate-mass planets that can displace some material from their orbit but cannot open a deep gap. It is caused by an additional asymmetry that can

arise when the planet is radially moving and has first been described by Masset & Papaloizou (2003). For example, when the planet moves radially inwards, a fluid element passing by it can perform a single U-turn while it crosses the corotation region from the inside out. This removes angular momentum from the planet. If the corotation region is partially depleted, the resulting torque is not balanced out from the opposite direction, and the planet is accelerated in the direction it is already moving. This can lead to runaway migration.

1.3 Protoplanetary disc winds

As discussed in Sect. 1.1.2.2, most protoplanetary discs are relatively short-lived, often shorter than expected from the observed mass accretion rates. Moreover, evidence suggests that discs could disperse from the inside out. A possible explanation for both of these findings is the dispersal of protoplanetary discs by disc winds, i.e., outflows that carry away material from the upper layers of the disc a few scale heights above the midplane. Other than winds, outflows are often observed as jets, especially in early evolutionary stages during the class 0 and class I phases. Disc winds differ from jets in that jets are collimated, large-scale, often bipolar, high velocity $\gtrsim 100\,\mathrm{km\,s^{-1}}$ mass ejections that originate close to the star. In contrast, disc winds are radially extended outflows that arise from the disc surface and have velocities $\lesssim 30\,\mathrm{km\,s^{-1}}$. In this work, the focus will only be on disc winds. For more information on jets, see the reviews by Bally et al. (2007), Frank et al. (2014), Ray & Ferreira (2021), and Pascucci et al. (2022). Based on the underlying physical process driving them, disc winds can be divided into two main types: thermal winds (particularly photoevaporative winds) and magnetic winds. This section covers the basic concepts behind the most important types of winds and possible observational diagnostics that could help distinguish between them. For comprehensive reviews on the topic, see, e.g. Ercolano & Pascucci (2017); Ercolano & Picogna (2022), and Pascucci et al. (2022).

1.3.1 Photoevaporative winds

Photoevaporation is a thermal process that can operate when energetic photons irradiate the disc[1], which heats the surface layers to high temperatures ($\sim 10^3$–10^4 K). Since the gas density decreases exponentially in the vertical direction (c.f. Sect. 1.1.3.1), if the gas is heated to sufficiently high temperatures, a pressure gradient develops that can be strong enough to overcome the star's gravitational potential, leading to the hydrodynamic escape of gas away from the disc. The details of the resulting thermal wind, such as mass-loss rate, geometry, or composition, depend strongly on the different heating and cooling processes at play; hence, one of the first factors to consider is the irradiating spectrum.

1.3.1.1 Extreme-ultraviolet

The first self-consistent photoevaporation model in protoplanetary discs was developed by Hollenbach et al. (1994). This model considered photons with energy in the extreme-ultraviolet (EUV) range ($13.6 \leq h\nu < 100\,\mathrm{eV}$). EUV photons are highly efficient in directly ionising hydrogen atoms. The ejected electrons then thermalise the gas, providing the dominant heating process. The heating is balanced by cooling, dominated by the collisional excitation of heavier species and their subsequent emission of forbidden lines that can escape the disc. As a result, the irradiated column of gas has an

[1]Photoevaporation is not only relevant for protoplanetary discs but also for planetary atmospheres (see, e.g. Owen, 2019) or molecular clouds (e.g. Bertoldi, 1989; Dale, 2015).

approximately constant temperature of $T \sim 10^4$ K; the corresponding sound speed is $\sim$10 km s^{-1}. This can be used to define the radius at which the sound speed equals the Keplerian speed,

$$R_g = \frac{GM_*}{cs^2}, \tag{1.26}$$

the so-called gravitational radius. In a simplified picture, one can consider gas that is inside the gravitational radius to be bound in an extended "atmosphere" and gas that is at $R > R_g$ to escape at the rate

$$\dot{\Sigma}_{\rm EUV}(R) \simeq 2\rho_b(R)c_s, \tag{1.27}$$

where $\rho_b(R)$ is the density at the base of the ionised layer, which depends on the penetration depth of the EUV photons, which scales with the EUV flux. More sophisticated models later showed that mass-loss can already occur inside the gravitational radius, a critical radius $R_{\rm crit} \sim 0.2R_g$ (e.g. Liffman, 2003; Alexander, 2008) and the total mass-loss rate scales with the EUV flux $\Phi_{\rm EUV}$ according to (Font et al., 2004; Alexander et al., 2014)

$$\dot{M}_{\rm EUV} \simeq 1.6 \cdot 10^{-10} \left(\frac{\Phi_{\rm EUV}}{10^{41} s^{-1}}\right)^{1/2} \left(\frac{M_*}{\rm Msun}\right) {\rm M}_\odot \ {\rm yr}^{-1}. \tag{1.28}$$

If a radial (surface) mass-loss profile $\dot{\Sigma}(R)$ is known, it is possible to model the viscous evolution of a photoevaporating disc by including it as a sink term in the right-hand side of eq. (1.20). The advantage of such a one-dimensional evolution model is that it is much less computationally expensive than detailed 2D photoionisation and radiation-hydrodynamic simulations, which makes it possible to simulate the evolution of entire populations of discs over their entire lifetime. The general picture that emerged from the models (e.g. Clarke et al., 2001; Matsuyama et al., 2003; Alexander et al., 2006b) is the following: At early times, the mass-loss rate due to EUV-photoevaporation is negligible compared to the mass loss due to accretion. As the disc's mass slowly decreases, so does the accretion rate until the accretion rate is comparable to the wind mass-loss rate, which is when a gap will open close to the critical radius. The material radially inside the gap quickly drains onto the star, leaving a cavity behind. Once the cavity is opened, the edge of the inner disc is directly irradiated. Models have shown that this leads to an increase of the mass-loss rate by roughly an order of magnitude (e.g. Alexander et al., 2006a) so that the remaining disc is rapidly ($\sim 10^5$ yr) dispersed from the inside-out (Alexander et al., 2006b). This behaviour is sketched in Fig. 1.7; although it includes an X-ray and an inner magnetic wind component, the behaviour is qualitatively the same. Fig. 1.8 shows the surface density evolution modelled by Alexander et al. (2006b). The model could provide a natural explanation for the existence of transition discs and the observed "two-timescale" behaviour with a long phase of viscous evolution followed by rapid inside-out dispersal (c.f. Sect. 1.1.2.2), but there are multiple caveats that undermine its plausibility: Although EUV fluxes from young stars are poorly constrained, they are likely too low ($\Phi_{\rm EUV} \lesssim 10^{42}$ s^{-1}) for being able to drive the mass-loss rates that would be necessary to explain the observed disc lifetimes. Moreover, due to their high photoionisation cross-section for neutral hydrogen, EUV photons reach an optical depth of order unity already at a column of $N_{\rm H} \sim 10^{17}$–10^{18} cm^{-2} (e.g. Hollenbach & Gorti, 2009). Therefore, most of the mass loss occurs close to the critical radius. At larger radii, the disc is primarily heated by a diffuse EUV field generated by recombinations in the extended atmosphere close to the star (Hollenbach et al., 1994; Alexander et al., 2006a). Another important consequence is that for the EUV photons to reach the disc's surface, the EUV flux must be high enough to keep the base of the wind fully ionised. Fully ionised winds, however, are not supported by observational constraints, as will be discussed in Sect. 1.3.4.

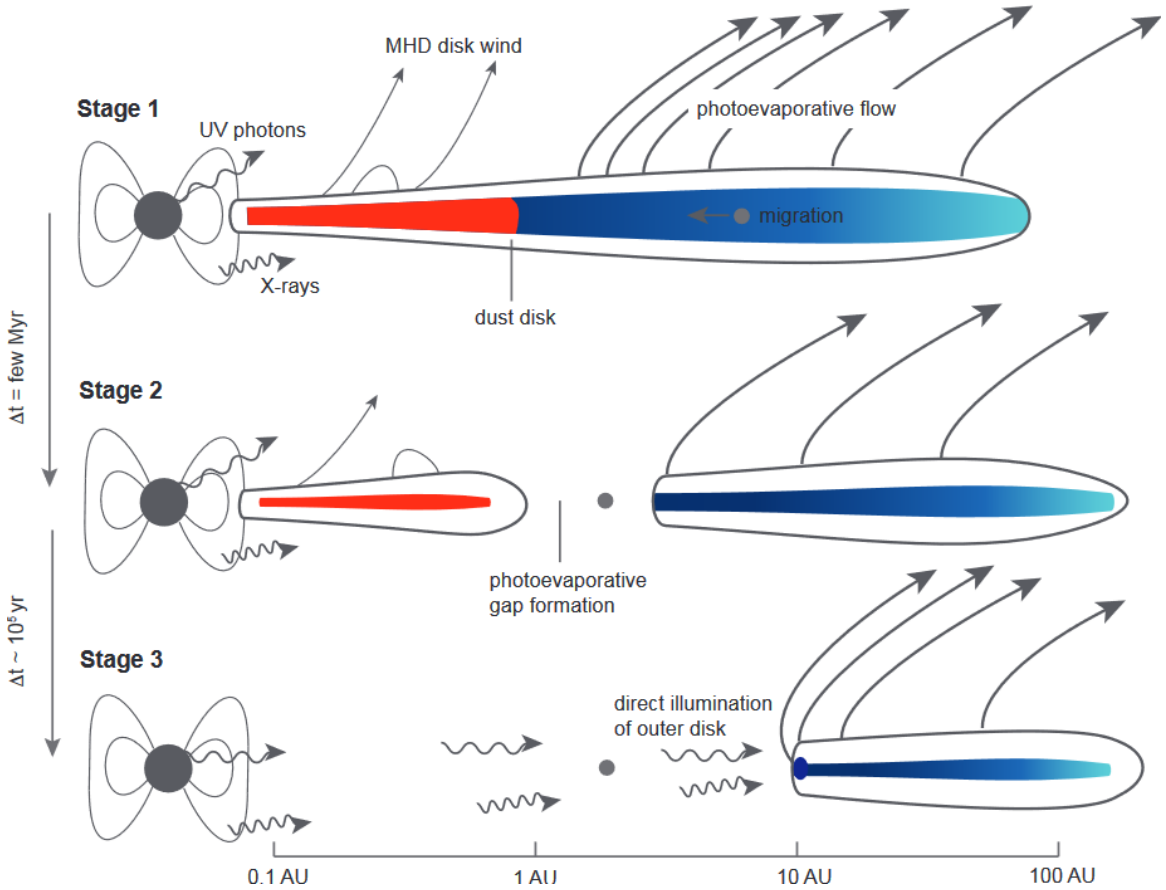

Figure 1.7: Sketch of the two-timescale disc dispersal process driven by photoevaporation. Magnetic processes can launch a wind in the inner disc. Image adapted from Ercolano & Pascucci (2017), originally licensed under CC BY 4.0.

1.3.1.2 X-ray

It is observationally established that young stars exhibit much more magnetic activity than main-sequence stars, producing consistently high levels of energetic X-ray radiation during their first few million years after their formation (e.g. Bouvier et al., 1993; Feigelson & Montmerle, 1999; Preibisch et al., 2005; Getman et al., 2022). Their luminosity in the X-ray band typically lies between 10^{28} to $10^{31}\,\mathrm{erg\,s^{-1}}$ with a median around $L_X \simeq 2 \cdot 10^{30}\,\mathrm{erg\,s^{-1}}$ (Preibisch et al., 2005). This raises the question of whether or not X-ray irradiation can drive photoevaporative winds. The primary X-ray heating process is not the photoionisation of hydrogen but of the inner electron shells of heavier elements and molecules. The ejected electrons can then cause secondary ionisations of atoms and eject more electrons, which thermalise their kinetic energy as well (Alexander et al., 2014).

Alexander et al. (2004) first estimated the impact of X-rays in this context with a simple heating model and found that they cannot drive stronger winds than EUV photons. However, Ercolano et al. (2008b) estimated mass-loss rates on the order of $\sim 10^{-8}\,\mathrm{M_\odot\,yr^{-1}}$ with an irradiating spectrum that combined EUV + X-ray employing a photoionisation and dust radiative transfer model of a fixed-structure disc that was calculated with the MOCASSIN Monte Carlo radiative transfer code (Ercolano et al., 2003, 2005, 2008a). After revising this model by self-consistently updating the vertical density structure of the disc to maintain hydrostatic equilibrium, they found mass-loss rates on the order of

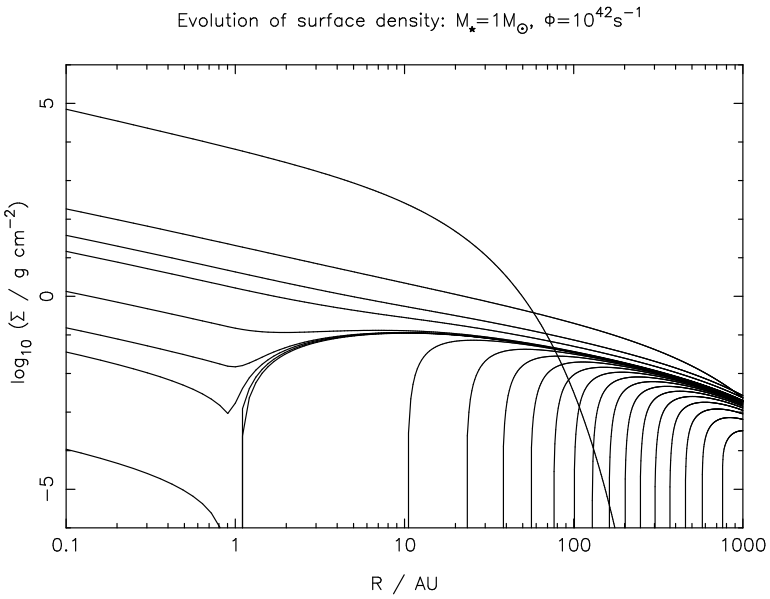

Figure 1.8: Surface density evolution in the EUV-photoevaporation model by Alexander et al. (2006b) for a disc around a $1\,M_\odot$ star and $\Phi_{EUV} = 10^{42}\,s^{-1}$. The lines show snapshots at times $t = 0, 2, 4, 5.9, 6.0, 6.01, 6.02, ..., 6.18$ Myr. Figure source: Alexander et al. (2006b)

$\sim 10^{-9}\,M_\odot\,yr^{-1}$ and that soft X-ray ($0.1 \leq h\nu < 1\,keV$) are by far the dominant heating source in the surface layers of the disc (Ercolano et al., 2009). They further showed that the maximum penetration depth for soft X-ray photons is of order $N_H \sim 10^{22}\,cm^2$ (Ercolano et al., 2009), so they can penetrate much deeper than EUV photons and heat the disc at larger radii, leading to more extended disc winds. In different models that included EUV, X-ray, and far-ultraviolet (FUV) (c.f. Sect. 1.3.1.3), however, Gorti & Hollenbach (2009) and Gorti et al. (2009) found that X-rays play only a minor role. However, their models used a simplified input spectrum with hard X-rays that inefficiently heat the gas.

For more detailed models, it is necessary to couple the photoionisation and dust radiative transfer models with the hydrodynamics, which was first done by Owen et al. (2010, 2011, 2012). To make this computationally viable, they parametrised the results of the hydrostatic equilibrium calculations by Ercolano et al. (2009) to find the temperature in the 2D grid as a function of the ionisation parameter (Tarter et al., 1969)

$$\xi = \frac{L_X}{nr^2}, \tag{1.29}$$

where L_X is the X-ray luminosity, n the local number density and r the spherical radius. This is the so-called $\xi - T$ parametrisation. This approach's disadvantage is that it requires the assumption of radiative equilibrium and cannot account for adiabatic cooling. Owen et al. (2010) verified the validity of the former with an a posteriori comparison of the thermal and dynamical timescales. The winds launched in these models reach a temperature up to a few $\sim 1000\,K$ and are predominantly neutral. Their surface mass-loss profile peaks at $R < 10\,au$. The models were later refined to use an updated temperature parametrisation that additionally depends on the column density (Picogna et al., 2019) and observationally derived spectra that depend on the X-ray luminosity (Ercolano et al., 2021). Since heavy elements like C and O are essential contributors to the X-ray opacity Ercolano & Clarke (2010), a decrease in metallicity means that deeper layers of the disc will be heated and mass-loss rates will be higher (Ercolano et al., 2018; Wölfer et al., 2019).

Models by Wang & Goodman (2017) that include EUV, X-ray, and FUV solve the radiative transfer

alongside the hydrodynamics. Additionally, they include thermochemistry with a simple chemical network. Their results differ drastically from those found in models using the $\xi - T$ parametrisation in that their wind is much hotter, highly ionised and driven by EUV rather than X-ray. In a recent detailed investigation, Sellek et al. (2022) concluded that the discrepancy is primarily due to their choice of the irradiating spectrum that was sampled on only a few frequency points and due to missing important cooling processes. The efficiency with which X-ray photons can heat the gas at the disc surface is a strong function of their frequency, so choosing a realistic spectrum in the models is very important. Moreover, they found that cooling from molecules, which is missing in the $\xi - T$ model, could be somewhat relevant, but it is unlikely that this strongly affects the launching of the wind. Adiabatic cooling, also missing in these models, was found to play no significant role. Conversely, based on a new analytical model tailored for EUV photoevaporation, Nakatani et al. (2024) recently argued that in X-ray heated regions, cooling from hydrodynamical effects cannot be neglected, considering the finite timescales of photoheating and photoionisation compared to the dynamical timescales of the wind.

Nakatani et al. (2018b) found in other models that included all three spectral ranges that FUV was predominantly driving the wind, similar to the results of Gorti & Hollenbach (2009) and Gorti et al. (2009). They found that X-ray mainly aids in the launching of the FUV-driven wind by raising the ionisation layers, resulting in more efficient FUV-heating, an effect that becomes particularly important at very low metallicities ($Z \lesssim 10^{-1.5}$). The source of this discrepancy still needs to be clarified. It could be a combination of factors, including their X-ray spectrum, simplified treatment of X-ray heating and choice of a very high FUV luminosity (Sellek et al., 2022; Pascucci et al., 2022).

1.3.1.3 Far-ultraviolet

FUV photons ($6 \leq h\nu < 13.6\,\mathrm{eV}$) are not energetic enough to ionise hydrogen, but they can dissociate simple molecules like H_2 or CO. However, the primary FUV heating mechanism is the photoelectric heating of small dust grains and very efficiently of polycyclic aromatic hydrocarbons (PAHs). Modelling the temperature in FUV-heated discs thus requires a detailed knowledge of the dust evolution and chemistry, making it a much more complex problem, which naturally leads to higher uncertainties, not least because PAHs are rarely detected in discs around solar-type stars and their abundance is still poorly constrained (e.g. Ercolano et al., 2022). Due to these complicating factors, FUV will not be considered in this work, and the photoevaporation models presented in this work will only include EUV and X-ray.

Gorti & Hollenbach (2009) and Gorti et al. (2009) developed the first photoevaporation models that included FUV (besides EUV and X-ray) for discs in hydrostatic equilibrium and incorporating a chemical network. They later refined the model (Gorti et al., 2015) to include a dust evolution scheme following Birnstiel et al. (2011). Their results suggest that when PAHs are present, FUV-irradiation can be the primary driver of winds (but see the discussion on their choice of X-ray spectrum in the previous section) with mass-loss rates on the order of $\sim 10^{-8}\,\mathrm{M_\odot\,yr^{-1}}$. While their surface mass-loss profile exhibits a local peak near $R \lesssim 10\,\mathrm{au}$, the global peak lies outside $R \gtrsim 100\,\mathrm{au}$, which is where most of the mass is lost in their wind. Nakatani et al. (2018a,b) find similar results in their models that include hydrodynamics. Moreover, they find an increasing mass-loss rate for decreasing metallicity due to reduced opacity until $Z \sim 10^{-1.5}$.

In contrast, Wang & Goodman (2017) found that FUV and X-ray only play a minor role and help the EUV by raising the thickness of the warm surface layer of the disc so that it intercepts more EUV photons that then launch a wind (but see the discussion on this model in the previous section). Moreover, their computational domain did not extend beyond 100 au, where most FUV-driven mass loss arises in other FUV models.

1.3.1.4 External photoevaporation

Besides being irradiated by their host star, protoplanetary discs can also be exposed to high-energy irradiation from their environment. This is particularly important for discs near massive OB stars with very high FUV and EUV luminosities. Famous, impressive examples of externally photoevaporating discs are the proplyds in the Orion Nebular Cluster (ONC), which exhibit long tails of outflowing gas directed towards their neighbouring massive stars with mass-loss rates as high as $\sim 10^{-6}\,\mathrm{M_\odot\,yr^{-1}}$ (Churchwell et al., 1987, review by Winter & Haworth, 2022). However, even if there are no massive stars in the direct neighbourhood, external photoevaporation could play a crucial role in the evolution of protoplanetary discs. Most stars are formed in clusters, where they are expected to experience FUV fluxes in the range of $\sim 10^3$ to $10^4\,\mathrm{G_0}$ if extinction is neglected (Fatuzzo & Adams, 2008; Winter et al., 2020). This could be enough to drive a wind from the outermost parts of large discs, where the gravitational potential is low (e.g. Haworth et al., 2017). Nevertheless, since the models in this work all focus on the inner ~ 10 au, where internal photoevaporation is expected to dominate, the effects of external photoevaporation will be ignored throughout this work.

1.3.2 Magnetic winds and wind-driven accretion

Another essential component for understanding the evolution of protoplanetary discs is the effect of magnetohydrodynamics (MHD). The most striking evidence of MHD operating in YSOs is the launching of high-velocity jets that are often observed in YSOs (e.g. Ray & Ferreira, 2021). Protoplanetary discs are generally expected to be threaded by a large-scale magnetic field (e.g. reviews by Koenigl & Ruden, 1993; McKee & Ostriker, 2007); however, the strength and geometry of the field are essentially unconstrained. Suppose the gas in the disc is sufficiently ionised, for example, due to cosmic rays or high-energy irradiation. In that case, it can couple to the magnetic field, giving rise to MHD effects. One such effect, the MRI (Balbus & Hawley, 1991), has long been believed to be the dominant source of turbulent viscosity, but as discussed in Sect. 1.1.3.4, it is no longer believed to operate in the planet-forming regions of discs because non-ideal effects suppress it. With purely hydrodynamical instabilities unlikely to generate the effective viscosity required to explain the observed distribution of accretion rates, MHD has gained even more attention, particularly winds driven by magnetic processes, as they can extract angular momentum from the disc, hence driving accretion. Consequently, multiple magnetic wind models incorporating non-ideal MHD effects (Ohmic resistivity, ambipolar diffusion, hall effect) were developed in the recent past, demonstrating the importance of magnetic processes on the evolution of protoplanetary discs (see reviews by Hartmann et al., 2016; Lesur et al., 2023).

Two main launching mechanisms have been identified based mainly on the strength and geometry of the magnetic field.

If the field lines are anchored below the disc surface, they can force well-coupled gas at higher heights to corotate with the field at speeds higher than the local Keplerian speed. If the field lines are sufficiently inclined from the rotation axis (by $\gtrsim 30°$), the gas can get flung out along the field lines due to the resulting centrifugal force. Such a magnetocentrifugal wind was first modelled by Blandford & Payne (1982), originally applied to jets launched in accretion discs around black holes; however, they noted that the model should also be applicable to stars. This can launch strong winds ($\dot{M}_{\mathrm{MC}} \sim 10^{-8}\,\mathrm{M_\odot\,yr^{-1}}$) that typically extend to $R \lesssim 10$ au and since the launching mechanism extracts angular momentum it can create thin layers of fast accretion flows on the order of $\dot{M}_{\mathrm{acc}} \sim 10^{-8}\,\mathrm{M_\odot\,yr^{-1}}$ (e.g. Bai & Stone, 2013; Gressel et al., 2015, reviews by Hartmann et al., 2016; Lesur et al., 2023).

If the magnetic field and the gas are not coupled sufficiently, the field cannot force the gas to corotate. In that case, the field tends to wind up and develop a strong toroidal field that is strongest at

some height above the midplane but well below the surface of the disc (e.g. Lynden-Bell, 1996; Bai, 2017). The resulting vertical gradient has two important consequences: Towards the disc surface, the gradient in magnetic pressure can drive a radially extended disc wind. At the same time, it can drive a radial flow, according to (Bai & Stone, 2013)

$$-\frac{1}{2}\rho\Omega_K v_R \approx -\frac{B_z}{4\pi}\frac{\mathrm{d}B_\phi}{\mathrm{d}z}, \tag{1.30}$$

where v_R is the radial velocity of the flow and B_z and B_ϕ the vertical and toroidal components of the magnetic field, respectively. The resulting wind mass-loss rates and the mass-accretion rates are comparable and can be as high as $\sim 10^7\ \mathrm{M_\odot\ yr^{-1}}$ (Béthune et al., 2017). However, Béthune et al. (2017) found that whether or not accretion and winds are driven depends on the configuration of the magnetic field. Moreover, the winds in their model can also be asymmetric, launching only on one side of the disc, and under some circumstances, axisymmetric density and pressure bumps can develop, which could be observed as substructure.

1.3.3 Magneto-thermal winds

To better understand the coupling between the gas and the magnetic field lines, it is important to know the gas's detailed thermal structure and ionisation state. Furthermore, when high-energy radiation is present, it is almost inevitable that there is also a contribution from a thermal pressure gradient in the wind-launching mechanisms unless an inner magnetic wind is strong enough to effectively screen the disc from X-ray and FUV already at the critical radius. Thus, the wind-launching process should not be viewed merely as an isolated magnetic phenomenon; thermal processes should also be incorporated into the models. To this end, Bai (2017) developed a model including the approximate treatment of ionisation chemistry and FUV-heating, While they found the wind to be launched predominantly by the magnetic toroidal pressure gradient, the mass-loss rates did correlate with FUV luminosity. They argued that "magneto-thermal" winds are the expected outcome in any protoplanetary disc. They identified two critical scenarios where thermal effects are significant: Firstly, in a case where the wind is launched in regions where the magnetic pressure is not much larger than the thermal pressure, suggesting that thermal pressure aids the loading of mass onto the magnetic field lines. Secondly, even if the wind is launched magnetically, thermal pressure can subsequently accelerate it.

Wang et al. (2019) and Gressel et al. (2020) later developed models that included self-consistent (FUV-based) thermochemistry. Wang et al. (2019) found a wind mainly launched by the toroidal magnetic pressure that is relatively insensitive to radiative heating, with only a dependence of the mass-loss rate on FUV-luminosity, which helps to increase the ionisation fraction in the wind launching region. X-ray irradiation does not contribute to their wind mass loss but helps increase the accretion rate, although it should be noted that they included only hard (3 keV) X-ray photons. In contrast, Gressel et al. (2020) found a wind launched predominantly magnetocentrifugally. Their wind does not depend strongly on the thermal pressure, but their thermochemistry is mainly FUV-based.

Rodenkirch et al. (2020) developed a model that implements the $\xi - T$ approach by Picogna et al. (2019) to treat heating by EUV + X-ray. The model includes Ohmic resistivity as the only non-ideal MHD term. Nevertheless, they found that the wind is predominantly thermally driven if the magnetic field is weak ($\beta \gtrsim 10^7$), where β is the dimensionless plasma parameter, defined as the ratio of thermal over magnetic pressure,

$$\beta = \frac{2\mu_0 p}{B^2}. \tag{1.31}$$

Here, p is the thermal pressure, B is the magnetic field strength, and μ_0 is the magnetic constant. β is commonly used to express the magnetic field strength, especially in magneto-thermal winds.

Sarafidou et al. (2024) subsequently refined the model by Gressel et al. (2020) by implementing the same $\xi - T$ parametrisation as well as all three non-ideal MHD effects. They found that photoevaporation generally dominates the mass loss at radii $R \gtrsim 1.5au$ unless the magnetic field is very strong ($\beta \gtrsim 10^3$), or the X-ray luminosity very low ($L_X \lesssim 2 \cdot 10^{29}\,\mathrm{erg\,s^{-1}}$). Moreover, they find that the accretion rate is sensitive to the inclusion of the hall effect if the initial magnetic field is aligned to the rotation axis of the disc. In that case, the accretion rate increases approximately an order of magnitude to $\sim 10^{-7}\,\mathrm{M_\odot\,yr^{-1}}$. The wind mass-loss rate remains unaffected.

A common result shared between the models is that they can reproduce mass-accretion and wind-mass loss rates that are at least $\sim 10^8\,\mathrm{M_\odot\,yr^{-1}}$, consistent with the majority of the observed disc lifetimes and mass-accretion rates.

1.3.4 Observational constraints on disc winds

1.3.4.1 Wind-tracing emission lines

One of the few observable direct signatures of disc winds are emission lines from atomic or molecular species. The most useful lines are optical and infrared forbidden emission lines that are emitted in low-density, high-temperature regions and are, therefore, not, or only to a small degree, contaminated by emission from the disc itself. Commonly observed lines are, for example, [OI] 6300 Å, [OI] 5577 Å, [SII] 4068 Å, and the [NeII] 12.81 µm line. These observations establish the constraints which any realistic wind model must adhere to. As an example, purely EUV-driven photoevaporation models have the fundamental problem that they fail to reproduce the observed [OI] line luminosities because their heating mechanism naturally leads to highly ionised winds, such that neutral oxygen is not sufficiently abundant to produce the observed emission (e.g. Font et al., 2004; Ercolano & Owen, 2016). Most other wind models are compatible with the typically observed luminosities, so it is important for observations to provide more details.

Spatially resolved lines Spatially resolving these lines is challenging, and most spatially resolved observations of outflows to date trace large-scale jets e.g. Ray et al., 1996, 2007. However, more recent ALMA observations show that they can be accompanied by slower wide-angle outflows (e.g. Klaassen et al., 2016; Louvet et al., 2018; Lee et al., 2021) that could trace swept-up material or disc winds (see, e.g. Pascucci et al., 2022, for a recent review). Nevertheless, recent efforts made use of new observational capabilities in an attempt to image also disc winds in class II objects. Fang et al. (2023) reported the first spatially resolved observation of the [OI] 6300 Å emission in TW Hya and concluded, based on the compactness of the emission, that it must trace an inner disc wind. However, as will be shown in chapter 4, the observations are also entirely consistent with the newer EUV+X-ray photoevaporation models by Picogna et al. (2019). In recent observations of T Cha with the MIRI-MRS instrument on the James Webb Space Telescope (JWST), Bajaj et al. (2024) detected extended emission of [NeII], [NeIII], [ArII], and [ArIII] lines. Sellek et al. (2024) subsequently modelled these emission lines using their self-similar thermal wind model (Sellek et al., 2021). The III/II line ratios of Ne and Ar emission suggest a low degree of ionisation, so they rule out that EUV dominates the ionisation. Instead, they find, based on the Ne fluxes, that the [NeII] emission likely traces a dense wind that is irradiated by X-ray that extends to at least ∼12 au. To reproduce the more compact and fainter [ArII] emission, they require a column of $\gtrsim 3 \cdot 10^{20}\,\mathrm{cm^{-2}}$ to screen EUV and soft X-ray beyond ∼12 au. This would suggest a wind with a mass-loss rate $\sim 3 \cdot 10^8\,\mathrm{M_\odot\,yr^{-1}}$ that extends to small inner radii $\lesssim 0.1$ au, consistent with the $\xi - T$ X-ray photoevaporation models or the FUV-dominated model by Nakatani et al. (2018b), but also an inner MHD wind could contribute to the required column

density.

Spatially resolved observations with JWST/MIRI that detect signatures that could trace disc winds are becoming more common. Some authors suggest to have found evidence for a MHD disc wind based on the compactness of the launching region and the outflow angle (e.g. Arulanantham et al., 2024) and some reporting possible evidence for small dust grains entrained in a photoevaporative wind (e.g. Duchêne et al., 2024), which is consistent with photoevaporative or magnetothermal wind models (Hutchison et al., 2016; Hutchison & Clarke, 2021; Booth & Clarke, 2021; Franz et al., 2022; Rodenkirch & Dullemond, 2022).

Spectrally resolved lines Much more observational data is available in the form of emission line spectra, which can be used to derive the kinematical properties of an outflow. If the line is observed with sufficiently high spectral resolution ($\Delta v \sim$ few km s^{-1}), it becomes possible to get insights into the kinematics of the wind. A typical sign of disc winds are emission lines that are blueshifted by several km s^{-1}. Significantly redshifted emission is rarely observed, as would be expected if the emission from the side of the disc facing away from the observer is blocked by the optically thick disc. Statistical analysis of large observational samples of [OI] 6300 Å emission has revealed several interesting links to other disc properties, such as the accretion luminosity/rate, inclination or the evolutionary stage of the disc as traced by the spectral index (c.f. Sect. 1.1.2.1). To facilitate the analysis of spectral line profiles, they are usually decomposed into multiple components by performing a multi-Gaussian fit and classifying the resulting Gaussian components based on their centroid velocity v_c and their Full Width at Half Maximum (FWHM). Components with $v_c > 30\,\mathrm{km\,s^{-1}}$ are called high-velocity components (HVCs) and are usually attributed to fast jets, while components with $v_c \leq 30\,\mathrm{km\,s^{-1}}$ are called low-velocity components (LVCs) and are generally believed to trace disc winds. (Hamann, 1994; Hartigan et al., 1995). LVCs are often fit best when they are further divided into two Gaussian components, a narrow low-velocity component (NLVC) that fits a narrow peak and a broad low-velocity component (BLVC) that fits wider wings of the profile. The distinction between NLVC and BLVC is based on a FWHM-threshold that is often set to $40\,\mathrm{km\,s^{-1}}$ (Rigliaco et al., 2013; Simon et al., 2016). If the NLVC is better fit by a single Gaussian, it is usually called a single component (SC), or SCJ, if a jet/HVC is also present (Banzatti et al., 2019). An example is illustrated in Fig. 1.9 for the case of DG Tau.

If it is assumed that the emission region is rotating with Keplerian velocity and that the broadening of the line is dominated by Keplerian rotation (requires a sufficiently large inclination), the FWHM of a component can be used to estimate the cylindrical radius at which its emission originates. The emission radii that are derived for BLVCs are typically between 0.05 to 0.5 au and for the NLVCs between 0.5 to 5 au (e.g. Simon et al., 2016; Banzatti et al., 2019). This implies that BLVCs cannot trace a photoevaporative wind since those can only be launched at larger radii (c.f. Sect 1.3.1). However, Weber et al. (2020) caution that the components found by Gaussian decomposition do not necessarily trace physically distinct regions, as velocity gradients in different parts of the flow can lead to overlapping emission in the spectrum, especially if a high-velocity component is also present. Banzatti et al. (2019) found that the centroid velocities, FWHMs and luminosities of the BLVCs correlate with those of the NLVCs in a large sample of [OI] 6300 Å observations and argued that these correlations suggest a common wind origin, i.e. a magnetic wind, as the BLVCs cannot trace a photoevaporative wind. On the other hand, Weber et al. (2020) post-processed the EUV+X-ray photoevaporation model by Picogna et al. (2019), as well as a simple analytical model of a magnetocentrifugal wind (Milliner et al., 2019), and showed that all three correlations are also expected when the components are produced in two different winds, because the centroid velocity, FWHM and luminosity of BLVCs and NLVCs

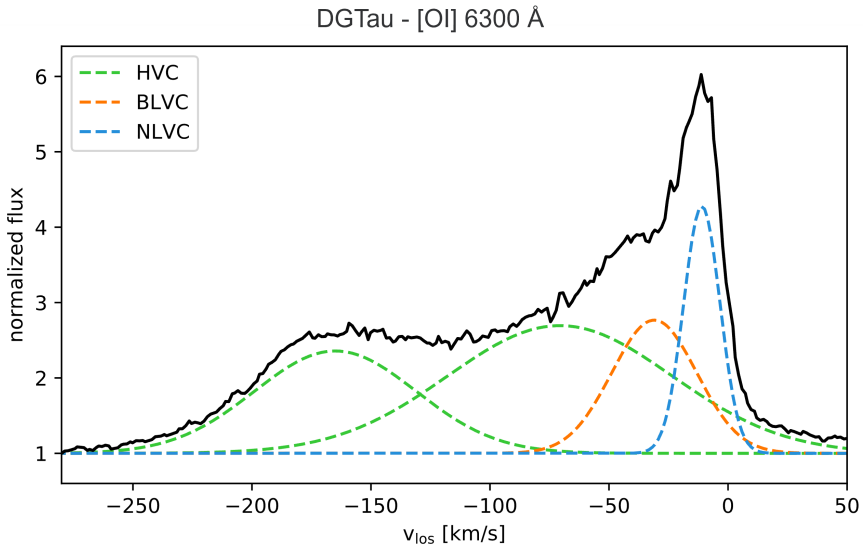

Figure 1.9: Multi-Gaussian decomposition of the [OI] 6300 Å spectral profile of DG Tau. The black solid line shows the observed profile from Banzatti et al. (2019), the green dashed line is the HVC, and the orange and blue dashed lines show the BLVC and NLVC, respectively.

all share a common correlation with a third variable, the accretion luminosity. The correlation of line luminosities with L_{acc} has been demonstrated earlier by Ercolano & Owen (2016), who found that the lines are primarily collisionally excited, and it is the EUV component of the accretion luminosity that dominates the heating and consequently the line excitation in the wind. The photoevaporation model used by Weber et al. (2020) reproduces the centroid velocities, FWHMs, and luminosities of NLVCs and SCs remarkably well. In contrast, the simple MHD wind model has difficulties reproducing the observed centroid velocities for both the NLVCs and BLVCs due to pronounced Keplerian double peaks in the synthetic profiles, which are rarely observed. This can be seen in figure 1.10, where the NLVCs of their models are plotted. Further, they show that combining their MHD wind model with an X-ray photoevaporation model could alleviate this issue, as the Keplerian trough is filled by the NLVC that traces the photoevaporative part of the wind.

Another interesting correlation identified in observations is with the spectral index, which can be understood as a proxy for the disc's evolutionary stage. HVC, NLVC and BLVC are predominantly observed in sources that have optically thick inner discs (full discs) and high accretion rates, whereas SCs are mainly found in discs with inner cavities (McGinnis et al., 2018; Fang et al., 2018; Banzatti et al., 2019). SCs usually are less blueshifted (see also Nisini et al., 2024), which is well reproduced with transition discs models that undergo X-ray photoevaporation, as found by Ercolano & Owen (2010) and Picogna et al. (2019), who argue that the line appears more symmetric due to a superposition with redshifted emission that reaches the observer through the cavity in the disc.

Lines other than the [OI] 6300 Å are less well studied but can nevertheless provide valuable insights. In particular, the [NeII] 12.81 µm line is interesting, as it shows a different behaviour than the [OI] 6300 Å line. Pascucci et al. (2020) found that this line is lacking in most full discs, and there is a trend of increasing luminosity when the inner disc is depleted, opposite to the [OI] 6300 Å line. Ionisation of Ne requires hard X-ray photons (Pascucci et al., 2014), Pascucci et al. (2020) proposed an evolutionary scenario where in full discs, an inner magnetic wind is screening the hard X-rays until the inner disc is depleted and the magnetic wind weakened. This scenario would require that

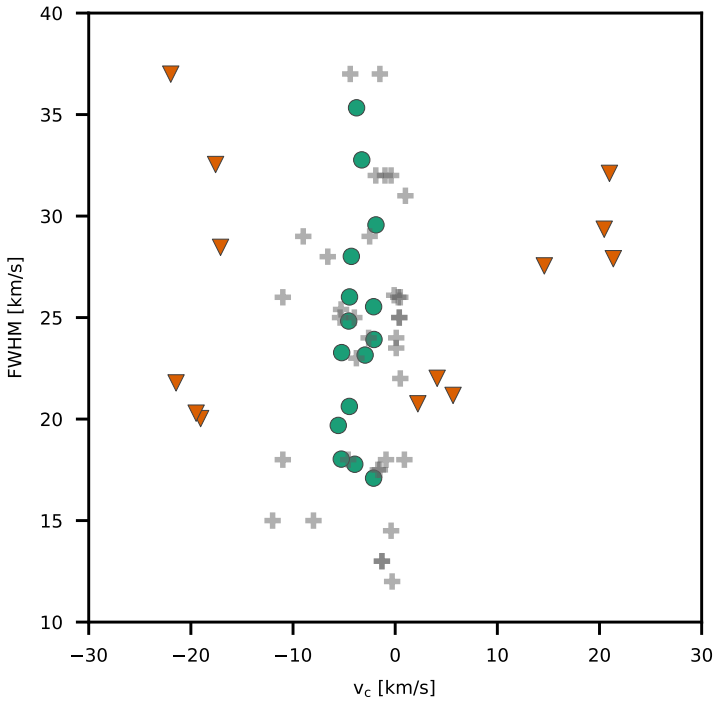

Figure 1.10: Overview of the NLVC properties of the EUV+X-ray photoevaporation (green points) and magnetocentrifugal (red triangles) models presented by Weber et al. (2020). The grey plusses represent the NLVCs in the observational sample by Banzatti et al. (2019).

the inner disc is mainly molecular and efficiently cooled, such that Ne is not efficiently ionised, while the [OI] 6300 Å can still be excited. Indeed, molecular wind signatures have been detected in CO and potentially water vapour emission and appear to originate in a relatively compact region around ($R \sim 1$ au) (Banzatti et al., 2022, 2023). Gangi et al. (2020) presented a larger sample of [OI] 6300 Å lines simultaneously observed with the ortho-H_2 2.12 µm molecular line (hereafter o$-H_2$ 2.12 µm) and compared their properties. In the sources where both lines are detected, they find that the FWHMs and centroid velocities of the two lines correlate tightly with each other and that the o$-H_2$ 2.12 µm line is tracing regions between 2 to 20 au, while the [OI] 6300 Å line traces regions between 0.05 to 20 au. They conclude that the two lines likely trace the same wind. Rab et al. (2022) subsequently modelled both lines by post-processing the X-ray photoevaporation models presented in Weber et al. (2020) and found that the models are consistent with the NLVCs in the data. They show that o$-H_2$ 2.12 µm traces significantly more extended regions than [OI] 6300 Å. However, the FWHM of the components fitted to the profiles are similar due to the complex velocity field in the emitting regions. They conclude that the assumption of purely Keplerian broadening is not well suited to derive the physical emitting region from the FWHM and no conclusions on the launching mechanism can be derived from these observations.

While none of the direct observational tracers discussed in this section allow for a conclusive distinction between the different wind types, they demonstrate that magnetic and photoevaporative winds could both play an essential role, and their relative importance may vary with location in the disc or evolutionary stage. The interpretation of disc wind diagnostic lines requires the comparison to detailed theoretical models that account for their combined effects. To this end, in chapter 5, spectrally resolved synthetic observations will be presented, calculated from the EUV+X-ray heated non-ideal

magnetothermal wind models by Sarafidou et al. (2024).

1.3.4.2 Indirect constraints on disc winds

Besides matching direct observational signatures, wind models should also be compatible with observed evolutionary trends of protoplanetary discs that disc winds might influence. Tests of this kind can be done with population synthesis models by simulating a large population of discs over an observationally informed parameter space for long timescales and comparing the outcome to the observed population. Due to the computational cost this entails, it is unfeasible to do this with detailed hydrodynamic wind models. Instead, population synthesis models typically rely on one-dimensional wind mass-loss profiles derived from more detailed wind models.

One prediction that can readily be tested in a population synthesis model is the disc lifetime (c.f. Sect. 1.1.2.2). Photoevaporation models driven by X-ray or FUV can reach high mass-loss rates sufficient to disperse even relatively massive discs within only a few Myrs (c.f. Sect. 1.3). In particular, the X-ray models following the $\xi - T$ approach have been tested extensively with population synthesis models. They are very successful in reproducing the observed lifetimes and the two-timescale behaviour described in Sect. 1.1.2.2 and 1.3.1.1 (Owen et al., 2011). The two timescale behaviour, however, is also consistent with models that combine magnetic and photoevaporative winds, where magnetic winds dominate at early times (e.g. Kunitomo et al., 2020).

Another test is the comparison to the distribution of discs with cavities that are still accreting (e.g. Ercolano & Pascucci, 2017). $\xi - T$ based X-ray photoevaporation models can provide a natural explanation for many of these observations. However, they cannot reproduce the parameter space populated by discs with large holes and very high accretion rates (Owen et al., 2011; Picogna et al., 2019). Moreover, they over-predict a population of relic discs, i.e. discs with cavities that do not accrete. The former, discs with large holes and high accretion rates, have traditionally been explained as discs with a gap carved by giant planets (see also Sect. 1.2). The problem of relic discs could be alleviated, e.g. by considering chemical effects that reduce the metallicity in the gas phase, such as the freeze-out of C and O onto dust grains, which leads to higher wind mass-loss rates at larger radii due to the reduction in opacity for the X-ray photons (Ercolano et al., 2018; Wölfer et al., 2019). Alternatively, adding FUV or external photoevaporation could help disperse the remaining outer disc. However, when combining the $\xi - T$ based photoevaporation models with external photoevaporation models, disc lifetimes become too short in population synthesis models (e.g. Emsenhuber et al., 2023). Conversely, Weder et al. (2023) show that the combination of MHD winds that dominate at early times with internal EUV photoevaporation and external photoevaporation can reproduce the expected lifetimes.

Ercolano et al. (2023) tested whether EUV, FUV and X-ray photoevaporation models can reproduce recently observed stars with very low accretion rates (Thanathibodee et al., 2023). They find the $\xi - T$ based X-ray driven models (Ercolano et al., 2021; Picogna et al., 2021) to be consistent and reproduce the observed distribution best out of the three models. Additionally, (Picogna et al., 2021) show that their models match well the observed dependence of inner disc lifetimes on the stellar mass (Picogna et al., 2021). However, this can also be reproduced with the model by Komaki et al. (2021), based on the FUV+EUV+X-ray photoevaporation model by Nakatani et al. (2018b).

It is clear that none of the wind models can provide a definite answer that explains all observed constraints. More theoretical and observational research is needed to determine which type of wind will dominate at what location and evolutionary stage of the disc. With improved quality and quantity of observational data, more methods will become available to tighten the constraints on these questions. As an example, one prospective method that could help distinguish between viscously evolving discs

and wind-driven discs is the analysis of the evolution of properties such as the disc radius or mass over time or the evolution of the spread of the $M_{\rm disc}/\dot{M}_{\rm acc}$ ratio (Rosotti, 2023; Somigliana et al., 2023). However, Coleman et al. (2024) pointed out that including effects caused by photoevaporation could complicate such an analysis.

1.4 Research questions

The preceding discussions clearly show the impact that photoevaporation has on the evolution of protoplanetary discs and their embedded planets. Many studies have employed theoretical models to investigate the long-term effects of disc winds, often also in the context of planet formation and migration (see also Sect. 3.1). However, all long-term evolution models of photoevaporative winds to date rely on one-dimensional wind mass-loss profiles derived from models of smooth discs without planets. Consequently, they cannot account for any additional effects that may arise from the interaction between the planet and the wind, e.g., due to planet-induced substructures in the disc.

Moreover, it is still impossible to conclusively distinguish between different wind models from observational data. In particular, the distinction between thermal and magnetic winds would provide highly desirable insights, as the latter are promising candidates for replacing the long-established standard picture of viscous accretion with a picture of wind-driven accretion. The interpretation of observations requires detailed models of all possible wind types. However, numerical limitations have made producing synthetic observables from detailed magnetic wind models challenging.

This work aims to address some of these outstanding questions. Chapter 2 explores how the presence of a giant planet and its substructures affects the structure and dynamics of a photoevaporative wind and its observables. Chapter 3 addresses the resulting feedback, i.e. the impact of the wind on the planet and the disc if the wind is affected by the presence of a giant planet. Chapter 4 seeks to answer whether the first spatially resolved observation of compact [OI] 6300 Å emission, which has been interpreted as evidence for a magnetic wind (Fang et al., 2023), is also consistent with photoevaporation models. Chapter 5 is focused on producing synthetic observables from the most complete X-ray-irradiated non-ideal magnetohydrodynamic wind model to date (Sarafidou et al., 2024). Finally, chapter 6 brings this thesis to a close with a summary and concluding remarks.

Chapter 2

Impact of giant planets on photoevaporative winds and their observational signatures

The content of this chapter was published in Weber et al. (2022)[1]:

Michael L. Weber, Barbara Ercolano, Giovanni Picogna, Christian Rab: "The interplay between forming planets and photoevaporating discs I: forbidden line diagnostics",
Monthly Notices of the Royal Astronomical Society, Volume 517 Issue 3 (2022), 3598-3612

Abstract

Disc winds and planet formation are considered to be two of the most important mechanisms that drive the evolution and dispersal of protoplanetary discs and in turn define the environment in which planets form and evolve. While both have been studied extensively in the past, we combine them into one model by performing three-dimensional radiation-hydrodynamic simulations of giant planet hosting discs that are undergoing X-ray photo-evaporation, with the goal to analyse the interactions between both mechanisms. In order to study the effect on observational diagnostics, we produce synthetic observations of commonly used wind-tracing forbidden emission lines with detailed radiative transfer and photo-ionisation calculations. We find that a sufficiently massive giant planet carves a gap in the gas disc that is deep enough to affect the structure and kinematics of the pressure-driven photo-evaporative wind significantly. This effect can be strong enough to be visible in the synthetic high-resolution observations of some of our wind diagnostic lines, such as the [OI] 6300 Å or [SII] 6730 Å lines. When the disc is observed at inclinations around 40° and higher, the spectral line profiles may exhibit a peak in the redshifted part of the spectrum, which cannot easily be explained by simple wind models alone. Moreover, massive planets can induce asymmetric substructures within the disc and the photo-evaporative wind, giving rise to temporal variations of the line profiles that can be strong enough to be observable on timescales of less than a quarter of the planet's orbital period.

[1]The work presented in this chapter resulted from a collaboration with my co-authors, which I led. I was responsible for conducting all the simulations and analysis, as well as composing the manuscript. My co-authors provided advice on the interpretation of the results. Giovanni Picogna provided the underlying photoevaporation model, which I adapted for implementation in 3D models with a planet.

2.1 Introduction

As the birth sites of planets, protoplanetary discs (PPDs) provide not only the material out of which planets form, but also the environmental conditions in which they form and then evolve. Observations suggest that PPDs typically disperse over timescales of only a few million years (e.g. Haisch et al., 2001; Fedele et al., 2010; Ribas et al., 2014) and the observed disc fractions at different wavelengths hint at an inside-out dispersal of discs (see also Koepferl et al., 2013; Ercolano et al., 2015). Understanding the processes that drive this evolution and dispersal is essential to understand the formation and evolution of the many diverse planets and planetary systems that have been discovered in recent years.

While several mechanisms have been proposed to be contributing to the evolution of PPDs, it remains difficult to constrain their relative importance. Angular momentum transport through turbulence, induced by magnetorotational instability (MRI) (Balbus & Hawley, 1991), has long been believed to be the dominant process for driving viscous accretion, but viscous accretion by itself cannot explain the inside-out dispersal of discs. Moreover, advancements in theoretical models have brought the effectiveness of MRI into question, as it became clear that MRI-driven turbulence is greatly reduced at several disc locations when non-ideal magnetohydrodynamical (MHD) effects are considered (Bai, 2015; Simon et al., 2018). It is very likely that the main mechanism responsible for driving accretion varies with the location in the disc and possibly its evolutionary stage. Growing evidence suggests that magnetic disc winds play an important role by extracting angular momentum from the disc (Gressel et al., 2015; Bai, 2017; Béthune et al., 2017; Wang et al., 2019; Gressel et al., 2020). Thermal disc winds, while unable to drive accretion, contribute directly to disc dispersal by carrying away material from the disc surface with mass-loss rates on the order of 10^{-8} $M_\odot$/yr that can lead to fast inside-out dispersal of a disc (see Ercolano & Pascucci, 2017; Pascucci et al., 2022, for recent reviews). With these considerations, both thermal and magnetic disc winds appear to play one of the most important roles in disc evolution.

Another important mechanism is the interaction between the disc and massive planets within. A sufficiently massive planet that is embedded in a PPD will exert enough gravitational torque on the surrounding material that a gap is opened along the planet's orbit (Papaloizou & Lin, 1984) and spirals are generated in the disc (Ogilvie & Lubow, 2002), perturbing its gas and dust structure. Many spatially resolved observations of PPDs show detailed substructures such as gaps, rings and spirals (ALMA Partnership et al., 2015; Andrews et al., 2018b) and often planet-disc interactions are proposed as their most likely origin. In fact, some of the substructures have recently been associated to kinematic detections of planets (e.g. review by Pinte et al., 2022a, and references therein). Planet-disc interactions are also the driver for planet migration and therefore crucial to understand the evolution of newly formed planets and the architecture of planetary systems. Numerical models show that planet migration can strongly be affected by disc dispersal via photo-evaporative winds (Alexander & Armitage, 2009; Ercolano & Rosotti, 2015; Jennings et al., 2018; Monsch et al., 2021b) and in an observational study of the semi-major axis a of exoplanets and the X-ray luminosity L_X of their host stars Monsch et al. (2019) found a void in the $L_X - a$ plane that may hint towards the parking of giant planets close to where a wind launched by X-ray photo-evaporation would open a gap. Alexander & Armitage (2009) and Rosotti et al. (2013) have found numerically that a planetary gap may reduce the mass inflow into the inner disc and in consequence accelerate dispersal of the inner disc by a photo-evaporative wind. The effect is referred to as planet-induced photo-evaporation (PIPE). This demonstrates the importance that the interplay between disc winds and planet-disc interactions has for the evolution of PPDs.

While in the recent years spatial observations of discs and the substructures within them have become increasingly more detailed, direct observations of disc winds remain challenging. One of

the most important observational tools for studying the structure and kinematics of disc winds are forbidden emission lines (FEL). These are usually lines from neutral or lowly ionized elements, such as the [OI] 6300 Å or [NeII] 12.8 µm lines, but also molecular low-velocity outflows from the inner disc regions have been detected in CO emission (e.g. Bast et al., 2011; Pontoppidan et al., 2011) or H_2 emission (Gangi et al., 2020). The lines often show complex spectral profiles that are blueshifted with respect to the stellar velocity, indicating an outflow that is approaching the observer. The profiles can provide insight into the structure of the outflow and its origin. To this end, they are often decomposed into one or multiple Gaussian components and classified according to the centroid velocity and width of the components. It should be noted that a single component does not necessarily trace the emission from a specific physically closed volume of the wind (see also Weber et al., 2020), but they are nevertheless useful to build statistics and study kinematic links. High-velocity components (HVC) with blueshifts $\gtrapprox$ 30km/s are usually attributed to fast-flowing jets, while less blueshifted low-velocity components (LVC) are believed to have their origin in slower winds (Hamann, 1994; Hartigan et al., 1995). The LVCs can be further decomposed into broad components (BC) with FWHM $\gtrapprox$ 40km/s and narrower components (NC) (Rigliaco et al., 2013; Simon et al., 2016; McGinnis et al., 2018; Fang et al., 2018; Banzatti et al., 2019). Under the assumption of Keplerian-broadening, BCs are often believed to trace winds within the inner 0.5 au of the disc and thus to have their origin in a magnetic wind (Simon et al., 2016), while narrow components (NC) are attributed to outflows at larger radii and are consistent with both, MHD winds (Banzatti et al., 2019) and theoretical models of PE winds (Ercolano & Owen, 2010; Weber et al., 2020; Ballabio et al., 2020). Pascucci et al. (2020) suggest an evolution in time, where inner MHD winds are dominating at early stages of disc evolution and outer winds could become more important at later stages. On short timescales (∼1 decade) the overall structure of the LVC remains mostly stable within the limits of the available spectral resolution (Simon et al., 2016), but for a few objects there exist multiple spectra with comparable resolution (∼6 km/s) that were observed a few years apart and show small variations in the LVC (e.g. UX Tau in Simon et al., 2016; Fang et al., 2018).

To understand and interpret the observed line profiles, synthetic observations of theoretical models that can be compared to real observations have proven useful. While it is still numerically challenging to calculate synthetic line profiles for MHD wind models, extensive work in that direction has been done on hydrodynamical models of PE winds. Font et al. (2004) modelled spectral profiles and fluxes of various optical forbidden lines emitted in an EUV-driven photo-evaporative wind and found good agreement with observational data for lines of ionized species, but their models could not account for the luminosities of neutral oxygen lines. Alexander (2008) extended this work by modelling the mid-infrared [NeII] 12.8 µm line and found encouraging results, too. Ercolano & Owen (2010) used the X-ray+EUV photo-evaporation models by Owen et al. (2010) to predict many optical and mid-infrared lines and found good agreement with the observed line luminosities, including that of the [OI] 6300 Å neutral oxygen line and subsequently Ercolano & Owen (2016) showed that the observed correlation between line intensity and accretion luminosity can be well reproduced by adding an additional accretion luminosity component to the irradiating spectrum. Later Picogna et al. (2019) introduced a new generation of X-ray photo-evaporation models that improved on the model by Owen et al. (2010). With those, Picogna et al. (2019) and Weber et al. (2020) showed that many of the observed NC can be reproduced, as well as their correlations with the observed BC although the BC is not present in a PE wind and is likely to have a different origin.

This paper is the first of a series in which we aim to connect two important drivers of disc evolution – disc winds and planet-disc interactions – and study their interplay by means of three-dimensional radiation-hydrodynamic simulations of X-ray photo-evaporating protoplanetary discs that host a giant planet. In this paper, we present synthetic forbidden emission line profiles calculated with these

Table 2.1: Model parameters for the hydrodynamical models. We name the 2D reference model with no planet REF, the other two models that include a planet are named MJ1 and MJ5, according to the planet's mass.

Parameter	Value	Model-ID
M_{planet}	0	REF
	1 M_J	MJ1
	5 M_J	MJ5
M_*	0.7 $M_\odot$	
M_{disc}	≈ 0.1 M_*	
α (viscosity parameter)	10^{-3}	
γ (adiabatic index)	1.4	
μ (mean molecular weight)	1.37125	
L_X [erg/s]	$2 \cdot 10^{30}$ erg/s	

models and study the effects that the presence of the giant planet has on the wind and on the forbidden emission lines that are emitted in it.

2.2 Methods

2.2.1 Hydrodynamical models

2.2.1.1 2D r-θ model of a disc with X-ray photo-evaporation

As a first step, we have rerun the two-dimensional model of an X-ray photo-evaporating primordial protoplanetary disc with a 0.7 $M_\odot$ host star by Picogna et al. (2019). This model uses a temperature parametrisation that is derived from detailed radiative-transfer calculations performed with the gas and dust radiative transfer code MOCASSIN (Ercolano et al., 2003, 2005, 2008a). The radiative transfer calculations used the X-ray + EUV spectrum presented by Ercolano et al. (2008b, 2009) with a luminosity of $L_X = 2 \cdot 10^{30}$ erg/s and solar abundances from Asplund et al. (2005), depleted according to Savage & Sembach (1996). The resulting parametrisation depends on the local ionisation parameter $\xi = L_X/nr^2$ and the gas column number density N_H along the line of sight towards the star, both of which are easily accessible in the hydrodynamical simulation, allowing for very efficient temperature updates at each hydrodynamical time step, while retaining good accuracy to the full radiative-transfer calculations (Picogna et al., 2019, fig. 1). The parametrisation is applied up to a gas column number density of $2.5{\cdot}10^{22}$ cm^{-2}, beyond which thermal coupling between gas and dust is assumed and the temperature is set to the dust temperatures from the models of D'Alessio et al. (2001). The initial density and temperature distribution is taken from the hydrostatic equilibrium models of Ercolano et al. (2008b, 2009). To reduce computational cost, the disc is assumed to be symmetric with respect to the disc midplane. We reran this model using the PLUTO code (Mignone et al., 2007) for 500 orbits at 5.2 au, after which a steady state has been reached. It serves as a starting point for our 3D models with a planet, as well as a reference model for a disc with no planet. The parameters for this and all other models are listed in table 2.1. The details of the numerical grids used in the hydrodynamical simulations are listed in table 2.2.

Table 2.2: Grid composition for the hydrodynamical simulations. The intervals in the radial dimension are given in code units (1 c.u. = 5.2 au).

	Step 1: 2D polar			Step 2: 3D spherical			Step 3: 3D spherical, extended		
Dim.	Interval	N Points	Type	Interval	N Points	Type	Interval	N Points	Type
r	412	[0.06, 115]	logarithmic	[0.28, 0.846]	60	uniform	[0.077, 0.846]	80	uniform
				[0.846, 1.154]	40	uniform	[0.846, 1.154]	40	uniform
				[1.154, 2.5]	60	logarithmic	[1.154, 2.5]	60	logarithmic
θ	160	[0.005, $\frac{\pi}{2}$]	uniform	[0.3, 1.417]	68	uniform	[0.088, 1.417]	82	uniform
				[1.417, $\frac{\pi}{2}$]	20	uniform	[1.417, $\frac{\pi}{2}$]	20	uniform
Φ				[0, 0.154]	20	uniform	[0, 0.154]	20	uniform
				[0.154, 6.130]	355	uniform	[0.154, 6.130]	355	uniform
				[6.130, 2π]	20	uniform	[6.130, 2π]	20	uniform

2.2.1.2 3D model of a disc with X-ray photo-evaporation and a giant planet

In a second step, we extended the 2D model into a three-dimensional spherical grid, assuming azimuthal symmetry around the polar axis. After verifying that the 3D-model yields exactly the same results as the 2D-model, we introduced an additional gravitational potential at $(R_p, \theta_p, \phi_p) = (1, \frac{\pi}{2}, 0)$ which we adopted from Klahr & Kley (2006):

$$\Phi_{\mathrm{P}} = \begin{cases} -\frac{G\,M_p}{d}\left[\left(\frac{d}{r_{sm}}\right)^4 - 2\left(\frac{d}{r_{sm}}\right)^3 + 2\frac{d}{r_{sm}}\right], & \text{if } d \le r_{sm} \\ -\frac{G\,M_p}{d}, & \text{if } d > r_{sm} \end{cases}. \tag{2.1}$$

This models the gravitational potential of a planet with mass M_p, that is smoothed with a cubic polynomial if the distance d from the planet is less than the smoothing length r_{sm}. Following Kley et al. (2009) we chose a smoothing length of 0.5 $\mathrm{R_{Hill}}$. Converted from code units, $R_p = 1$ corresponds to a planet with an orbital distance of 5.2 au, comparable to Jupiter in the solar system. To prevent strong disturbances of the disc, we used a sinusoidal function to slowly increase the planet mass from 0 to its final value M_p over 20 planetary orbits. In order to more accurately capture the planet-disc interactions, we used a nested, rotating grid, to achieve a higher resolution of 0.1 $\mathrm{R_{Hill}}$ within a region extending $\approx$ 2 $\mathrm{R_{Hill}}$ around the planet's location (see table 2.2). The planet's orbit was held fixed. At the radial boundaries we employed reflective conditions, in the polar direction we used a mirror condition at the disc midplane and an open boundary in the disc wind. In the azimuthal direction periodic boundary conditions were applied. We note that the choice of a reflective boundary at the midplane greatly reduces computational cost, but has the disadvantage that the planet is placed directly on the domain boundary. In theory, this could lead to numerical problems that could affect the density structure close to the planet or the propagation of the planet-induced spiral waves. However, it is unlikely that this has strong effects with the massive planets considered in this work and we do not expect it to have a significant effect on the depth and width of the gap or the disc surface, which is the most relevant aspect when studying the interaction between the planet-induced substructures and the wind. To prevent reflections of the spiral waves, we implemented wave-killing damping regions in the radial intervals [0.280, 0.376] and [2.308, 2.5] in code units, similar to those of De Val-Borro et al. (2006). Inside these intervals the density and the radial and polar velocities are damped towards their respective initial values on a damping timescale of 3% of the orbital period at the boundary.

We evolved the model until the planet-induced substructures reached a sufficiently steady state everywhere outside the planet-induced cavity, where the wind is launched. Figure 2.1 shows the surface density evolution of the models. The model with a Jupiter-like planet (MJ1) reached a sufficiently steady state after approximately 150 orbits. We ran the simulation for 216 orbits, after which we

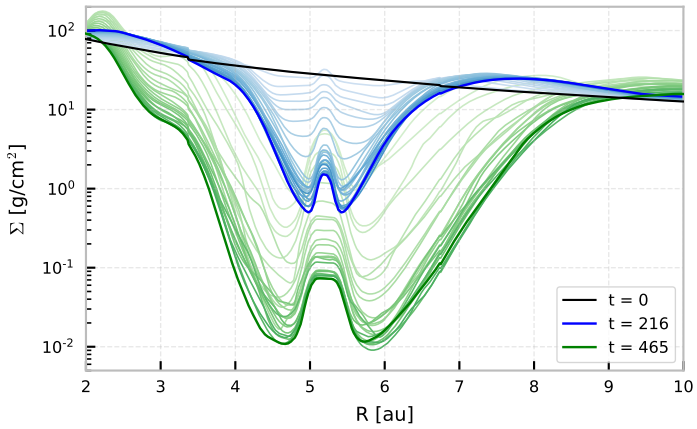

Figure 2.1: Surface density in steps of 10 orbits starting at the time of planet insertion (t = 0), which is represented by the lightest blue line. The dark blue line at t = 216 orbits represents the surface density of the MJ1 model. At the same time, it serves as the starting point for the MJ5 model (green lines), which was evolved for another 249 orbits until t = 465.

gradually increased the planet mass over 20 orbits to 5 M_J for the MJ5 model. The MJ5 model was then run for another 249 orbits until t = 465. We note that there are still small variabilities in the surface density profile at the outer edge of the gap. However, these are mainly caused by hydrodynamical instabilities that lead to asymmetric features such as vortices, which are strongest close to the disc-midplane and not at the disc surface, where the wind is launched.

As a third step, we then extended the grid in the radial and polar directions by reducing the inner boundary to $R_{in} = 0.077$ (corresponding to 0.4 au) and $\theta_{in} = 0.088$ and mapping the grid from the 2D model into the newly opened space. The interval of the inner damping region was adjusted to [0.077, 0.135]. The model was then evolved for another 10 planetary orbits, which corresponds to ≈ 470 orbits at the new inner boundary. This is done to ensure that the domain includes the inner disc atmosphere which may have a small contribution to the line profiles, as well as partially screen irradiation from the central star, reducing the amount of irradiation that reaches the outer disc regions.

2.2.2 Forbidden emission lines with MOCASSIN

We post-processed snapshots of the density and velocity grids by remapping them to a three-dimensional cartesian grid with 196 points in x- and y-direction and 86 points in the vertical z-direction, all spaced according to a power law with exponent $q = \frac{3}{4}$. Converted from code units, the remapped grid extends from -12 to 12 au in x- and y- direction and 0 to 10 au in z-Direction, however inside a radius of 0.4 au all cells are set to 0. We do not expect this region to contribute to the total line flux in a significant way, because the volume of this region is small. For our 2D model, the third dimension is not necessary, which allowed us to verify that the resolution is sufficiently high, by rerunning the 2D-calculations with a resolution that was increased by more than a factor of 6. The resulting line profiles were not affected, as the differences are not significant enough to be recognisable after the artificial degradation of the spectrum, which we employ to simulate a realistically achievable spectral resolution.

Furthermore, all cells with a column number density $> 10^{23}$ cm^{-2} are set to 0 in order to reduce computational demand. This is possible, because this condition is only met within the bound disc, where the lines that we are interested in are not emitted.

We used the remapped cartesian grids to calculate the photo-ionisation structure and line emission with MOCASSIN, following Ercolano & Owen (2010), Ercolano & Owen (2016) and Weber et al. (2020), where we updated the atomic database to CHIANTI version 9 (Dere et al., 1997, 2019). The irradiating spectrum is the same as in model PE-1 of Weber et al. (2020). It consists of a soft X-ray component with a luminosity of $2 \cdot 10^{30}$ erg/s and a blackbody component at a temperature of 12000 K with a bolometric luminosity $L_{acc} = 2.6 \cdot 10^{-2}$ $L_{\odot}$, which corresponds to an ionising EUV luminosity ($h\nu > 13.6$ eV) of $8.56 \cdot 10^{28}$ erg/s. This accretion component is used to model a spectrum that could be emitted by material that is accreting onto the central star. It plays an important role for the forbidden line emission along the inner edge of the wind. Since the wind is optically thick to EUV photons, it is absorbed quickly along that edge, where it dominates the ionization and heating process, but it has a negligible effect on the wind dynamics, because it is unable to penetrate the wind and to reach the wind-launching region at the disc surface (Owen et al., 2012).

2.2.3 Line profile calculations

As our set of synthetic forbidden emission lines, we chose the commonly observed [OI] 6300 Å, [SII] 4068 Å, [SII] 6730 Å and [NeII] 12.8 µm lines, as well as the [FeII] 17.2 µm line and created luminosity grids using the post-processing tools that are provided with MOCASSIN. Due to the nature of Monte-Carlo simulations, the results typically contain several individual zones that are undersampled after the simulation and thus yield unrealistic values for the line luminosity. We filtered out these outliers by calculating for each zone the local mean value using the 3 nearest-neighbours in all directions and setting its value to the local median, if it exceeds the mean by 3 standard deviations.

With the luminosity grids we were then able to calculate spectral line profiles, following the work of Ercolano & Owen (2010), Ercolano & Owen (2016) and Weber et al. (2020):

For each volume element in the grid, we calculated the gas-velocity projected along the line of sight v_{los} and the thermal rms velocity $v_{th} = \sqrt{k_B T/m}$ of the emitting element, where m is the mass of the element. We then calculated the total luminosity that can be observed along the line of sight with velocity u by summing the contribution of the individual zones of the 3D-grid $l(\boldsymbol{r})$:

$$L(u) = \int d\boldsymbol{r} \frac{l(\boldsymbol{r})}{\sqrt{2\pi} v_{th}(\boldsymbol{r})} exp\left(- \frac{[u - v_{los}]^2}{2 v_{th}(\boldsymbol{r})^2} \right), \tag{2.2}$$

where $\boldsymbol{r}$ is the vector pointing to the node. This way, we created spectral line profiles by calculating the total line luminosity at a range of velocity bins spaced 0.25 km/s apart. The profiles were then convolved with a Gaussian of width $\sigma = c/R$, to simulate a finite resolving power R. For the optical forbidden emission lines, we chose a resolving power of $R = 50000$, which is comparable to currently available high resolution spectral observations and $R = 100000$ for profiles that are more representative of potential future observations. For the lines in the mid-infrared we used $R = 30000$ and $R = 60000$. Upcoming instruments such as ANDES on the ELT could realistically achieve a comparable resolution for the optical lines. Unfortunately, it is unlikely that the lines in the mid-infrared will be observable with such high resolution in the near future. Nevertheless, we include the profiles for completeness.

We assumed that only the disc midplane is optically thick to the lines and neglected scattering and absorption processes of the forbidden line emission which should be negligible along most lines of sight that do not cross the midplane of the disc. This approximation is rendered necessary by the limited extent of our computational domain that does not allow for an accurate calculation of the optical depth through the wind. We created fits to our profiles using the multi-Gaussian decomposition method described in (Weber et al., 2020). This produces fits that are similar to the ones typically used for real observations. It works by adding an additional Gaussian component only if it improves the

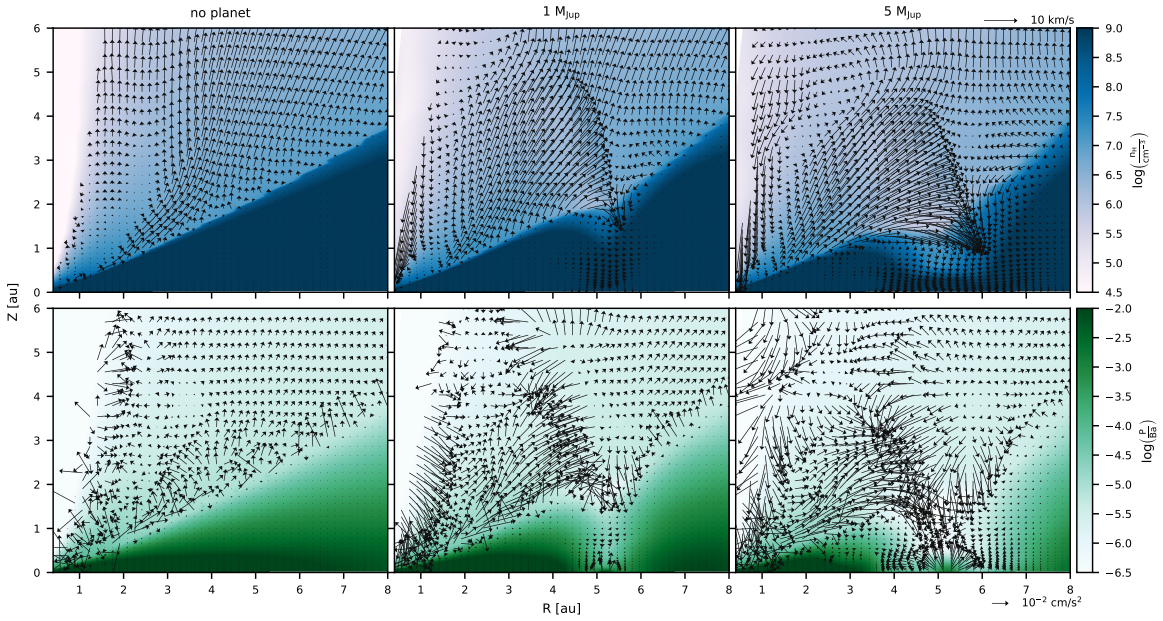

Figure 2.2: Top panels: Azimuthally averaged hydrogen number density (background color) and velocity field (black arrows). Bottom panels: Azimuthally averaged gas pressure (background color) and the effective acceleration as the sum of the gravitational acceleration towards the central star, the acceleration caused by the pressure-gradient force and the centrifugal acceleration. The velocity and acceleration fields are only plotted where the number density exceeds $2 \cdot 10^5$ cm^{-3}.

χ^2-value by at least 20%. Moreover, it includes an additional exit-condition $\chi^2 < \frac{2}{3} y_{max}^2$, where y_{max} is the flux at the peak of the profile, in order to account for the fact that our synthetic profiles are much smoother and therefore generally better fitted by Gaussian components than it is the case with real spectra.

2.3 Results & Discussion

2.3.1 Wind structure and kinematics

A photo-evaporative wind is a thermal wind that is driven away from the surface of the bound protoplanetary disc by a pressure gradient. Its kinematics are therefore dependent on the density and temperature structure of the disc surface. Since massive planets interact strongly with the gas in the disc, opening up a deep gas-cavity around the entire azimuth, they could also indirectly influence a thermal disc wind. The top panels of Figure 2.2 show the gas density structure, as well as the velocity field of the wind in our three different models. The bottom panels show the gas pressure and the effective acceleration field that we calculated by summing the three major contributing components: the gravitational acceleration towards the star, the acceleration by the pressure-gradient force and the centrifugal acceleration due to Keplerian rotation, which we have to consider in our frame of reference. The gravitational acceleration by the planet can be neglected, as in the wind regions it is much weaker than that of the star. Even in the y=0 plane at the disc surface directly above the 5 M_J planet, the vertical component caused by the planet reaches only $\approx 18\%$ of the stellar value. The left panels show our model without a planet, where the wind is launched consistently along the disc surface. Inside R

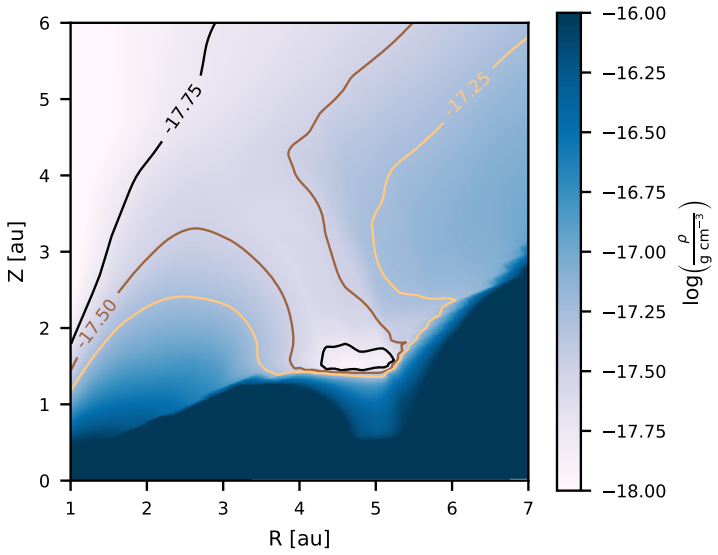

Figure 2.3: Azimuthally averaged gas density of the 5 M_J model.

$\approx$ 3 au, the pressure gradient is not strong enough for the wind to overcome the gravitational potential, except for a thin layer directly above the disc surface, where material can flow radially outwards, where it can later be vertically driven away from the disc. In terms of the gravitational radius r_g, this corresponds to a minimum launching radius of $\approx 0.1 - 0.3 r_g$, which is consistent with the critical radius found in previous studies (e.g. Liffman, 2003; Dullemond et al., 2006).

Comparing this to the models that include a planet-induced gap in the disc, it becomes evident that at the position of the cavity, the pressure gradient is inverted and no material is launched into the wind. This, in consequence, leads to an under-density at the location of the cavity that is perpendicular to the disc surface and reaches several au into the wind. Instead of being driven vertically farther away from the disc, material that crosses this under-density can fall back into the cavity or onto the outer edge of the gap. This effect is stronger in the model with a 5 M_J planet, which is able to create a much deeper cavity. In Figure 2.3 we visualize the under-density of model MJ5. The Figure shows the azimuthally averaged gas density, where a region above the gap, spanning approximately 2 au in the radial and 4 au in the vertical direction, is apparent, within which the density is reduced by up to a factor $\approx$ 3 compared to the surrounding environment.

Apart from the under-density, Figure 2.2 shows an additional effect: In the region inside R $\approx$ 3 au, where in the REF model the material is mostly gravitationally bound, in the models with a planet the pressure gradient is increased towards the under-density, allowing the wind to be launched from slightly closer in but with a less steep angle. This, in turn, modifies the pressure gradients along the inner vertical edge of the wind, which is especially evident in the MJ5 model, where material at z$\approx$5 au reverses direction and falls back down towards the disc along the inner edge of the wind.

We note again that these effects are a consequence of the modified pressure gradient that drives the wind and are not caused by the additional gravitational potential, as discussed earlier in this section. It is not yet known whether a wind that is not dominantly driven by a pressure gradient (i.e. a magnetically driven wind), would experience similar effects on its velocity structure. Detailed numerical models would be required in order to investigate how the presence of a massive planet can affect a magnetic wind.

2.3.2 Forbidden line diagnostics

2.3.2.1 Emission regions

One of the most important diagnostic tools that exist for analysing protoplanetary disc winds are optical forbidden emission lines. These collisionally excited lines are particularly well suited to study disc winds, because they depend strongly on the temperature through the Boltzmann term $\exp(-\Delta k_B T)$, but also on the density. In the bound protoplanetary disc, the temperature is usually low and the density high enough for collisional de-excitation to dominate, which means that the forbidden line emission is suppressed in the disc itself. However, disc-winds can have the right conditions to allow for significant emission. The ideal conditions vary from line to line, opening up the possibility to study different regions of a wind by analysing different emission lines. Figure 2.4 shows the temperature that is resulting from our photo-ionisation calculations of the wind models as well as the 85% emission regions of the lines in our sample, namely the optical [OI] 6300 Å, [SII] 4068Å and [SII] 6730 Å lines and in the mid-infrared the [NeII] 12.8 µm fine structure emission line and the [FeII] 17.2 µm line. When the model includes a planet the left panel shows the azimuthal average and the right panel the emission region in the y=0 plane, where the planet is situated. We include this comparison in order to illustrate the typical magnitude of the deviation from the mean, which we expect to be strongest at the azimuthal position of the planet. Generally the averaged emission regions are in good agreement with the emission in the y=0 plane, although in the latter all lines show a higher vertical extent along the inner edge and both show reduced emission inside the under-density above the planetary gap, but the void that this creates in the emission region is larger in the y=0 plane, which is expected, as asymmetries within the disc would wash out the feature in the average. The low emission inside this region can be interpreted as a consequence of less efficient collisional excitation at lower densities. It is possible that this could to a degree be compensated when material accretes onto the planet and forms strong shocks, emitting additional EUV-radiation that could reach and heat the wind. In that case the forbidden lines would trace the under-density better and the effect on the line profile would be even stronger. We note that the emission regions show the contours within which 85% of the emission is originating and do not indicate the absolute luminosity. This means that the two phenomena, the reduced emission inside the under-density and the increased vertical extent, are likely to be linked, as taking away emission from one part of the wind will result in the 85% contours being shifted towards another part.

Of the lines in our sample only the [SII] 6730 Å, the [NeII] 12.8 µm and the [FeII] 17.2 µm lines reach far enough into the wind to cover the region above the gas cavity, however, as the emission is strongly reduced inside the under-density, these lines do not trace that region very well, either. Nevertheless, as the velocity structure of the wind is modified far beyond the under-density, even reaching to the innermost parts of the wind, all lines do trace parts of the wind that are in some way affected by the planet. At larger radii, the models that include a planet experience a smoother transition between low and high temperatures at the disc-wind interface outside the cavity. As a result, the line emission is suppressed close to the disc surface, and the emission region pushed to higher heights above the disc surface. The [FeII] 17.2 µm line is the least affected by this, such that in model MJ1 its 85% emission region reaches down to the disc surface. It is also the line that with least emission along the inner edge of the wind, making it a promising diagnostic line for tracing the actual launching region of extended disc winds.

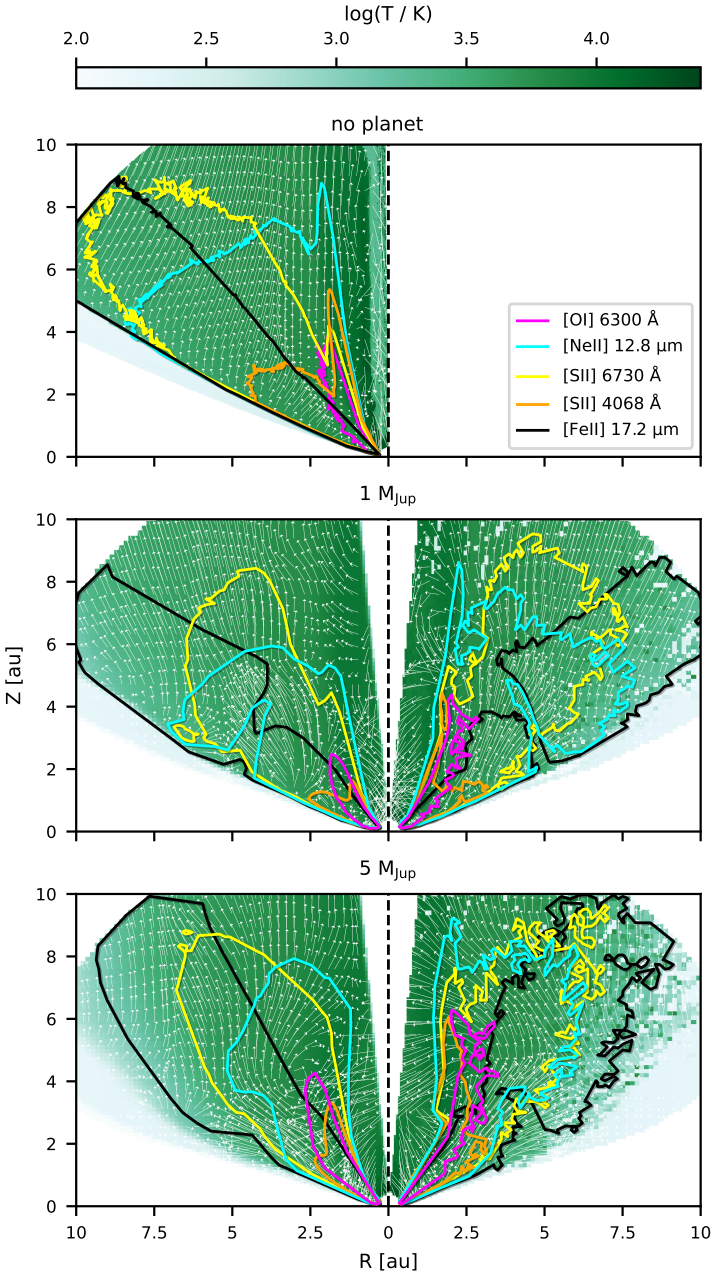

Figure 2.4: 85% emission regions of our chosen diagnostic lines. The left halves show the azimuthal average, the right halves show a cut through the y=0 plane, where the planet is located. The background colour indicates the temperature that was calculated with MOCASSIN. The white arrows indicate the velocity field of the wind.

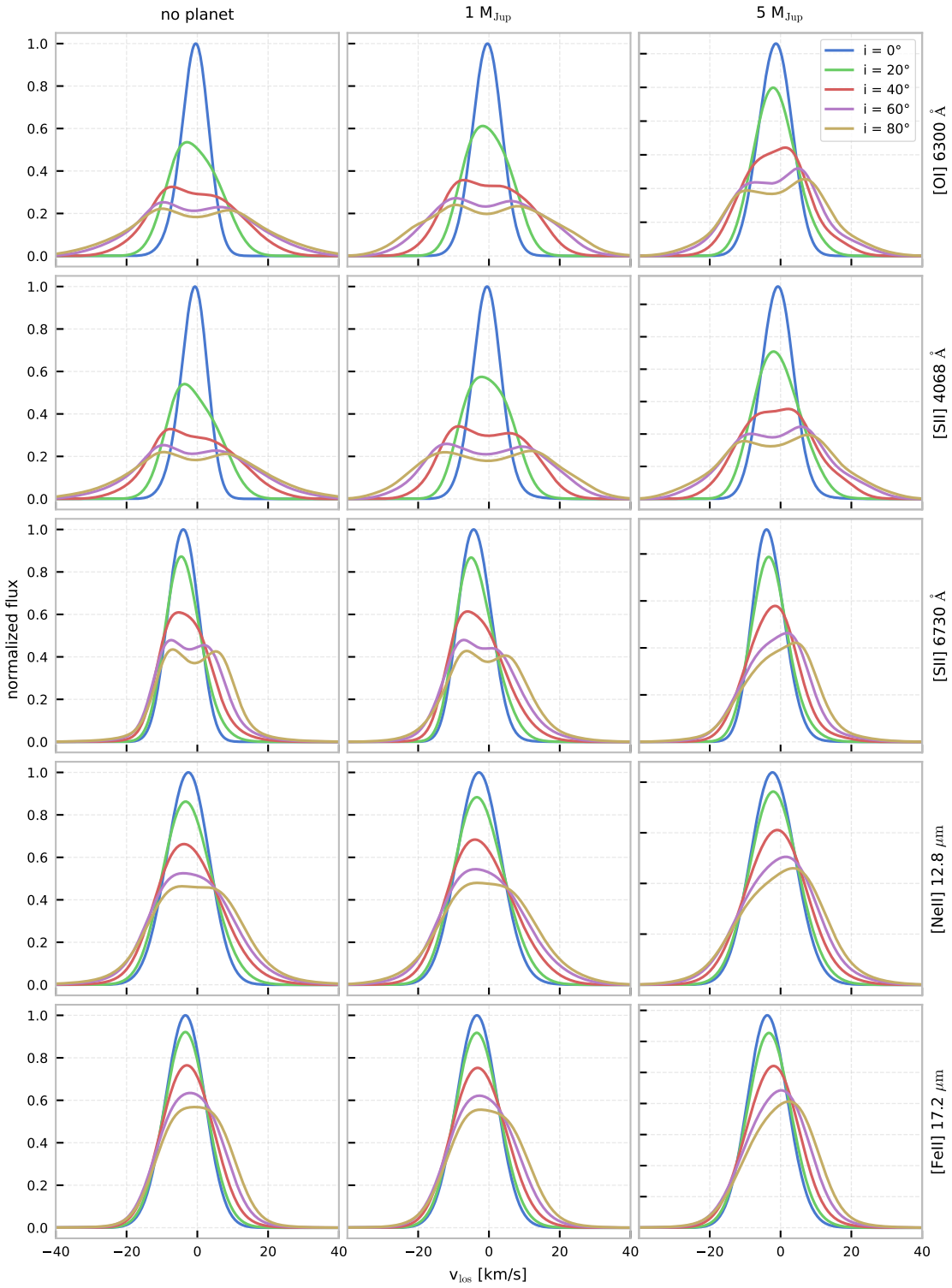

Figure 2.5: Synthetic spectral profiles of the optical lines viewed at inclination i and azimuth angle ϕ = 0. The profiles were artificially degraded to a spectral resolution corresponding to R = 100000 (optical) and R = 60000 (mid-infrared) and normalised to the peak of the face-on profile with i = 0°.

2.3.2.2 Line profiles

To study the structure and kinematics of protoplanetary disc winds it is useful to analyse the spectral line profiles of the emission lines. We have calculated artificial line profiles from our models as described in section 2.2.3 and convolved them with a Gaussian function, in order to simulate a finite spectral resolution that would be the limiting factor in real observations. Figure 2.5 shows the resulting profiles. The line profiles are artificially degraded to a resolving power of R = 100000 and R = 60000 for the optical lines and mid-infrared lines, respectively. We show profiles with half the resolution in appendix 2.5.1. Since the line profiles always trace an extended region of the disc wind that covers a range of wind velocities, changes in the flow structure in one region of the wind are not easily distinguishable from a change of the luminosity in a different region of the wind. In order to be able to observe a difference between models, the affected region must either be very large, or very luminous with a drastically different flow structure.

In our model MJ1 the wind is affected by the gas-gap only to a limited extent. Although the emission regions extend over wind regions where the outflow is affected, no significant difference in the line profiles can be seen, when comparing them to the reference model without a planet. When not observed face-on, the [OI] 6300 Å line and the very similar [SII] 4068 Å line are slightly less blueshifted, but it would be difficult to draw any conclusions from such a small effect. As an example, the Gaussian fit for the [OI] 6300 Å profile observed at i=40° and Φ=0° yields a centroid velocity of -0.66 km/s compared to -1.16 km/s in the reference model (see table 2.3 in the appendix). Since the majority of the line emission originates from close-in, the contribution to the line profile that traces parts of the wind that are the most affected by the presence of a planet is small.

In the MJ5 model, however, the perturbations of the flow structure are much stronger, as already seen in Figure 2.2. Not only is the gap and with it the affected volume of the wind much larger, but also the wind-launching region in the inner disc is affected much more. The effects are sufficiently strong to make an impact on the line profiles. The profiles show less blueshift when observed at small inclinations while at higher inclinations the peak is shifted into the redshifted part of the spectrum. All of the modelled optical lines have their peak at velocities > 0 when observed at inclinations of 60° or more. Although the redshift is small (only few km/s), it is a notable observation, as it requires a significant portion of the wind to move away from the observer. Such a scenario cannot easily be explained by a simple wind model alone. Even in transition disc models, where a portion of the receding wind on the other half of the disc can be observed through the large inner gas cavity, the profiles only show enhanced symmetry and less blueshift, but cannot exhibit a redshifted peak (Picogna et al., 2019).

The [SII] 6730 Å line is the only optical line in our model that features a single peak even at high inclinations. With its large emission region, it's profile is not dominated by the regions close to the star that are subject to strong Keplerian broadening. Instead, it traces much of the wind-region that is most affected by the planetary gap. As a result the line is strongly skewed towards the red with a peak in the red part of the spectrum at i≥60°. The [OI] 6300 Å and [SII] 4068 Å lines both start to exhibit a redshifted peak already at i=40°. At higher inclinations, their profiles show clear Keplerian double peaks with the dominant peak in the red. This indicates that the red part of the profiles not only traces the region above the gap, but the presence of a massive planet farther out also affects the inner parts of the wind, as was already discussed in section 2.3.1. The lines in the mid-infrared trace a similarly extended region as [SII] 6730 Å, but are degraded to a lower spectral resolution. Nonetheless, they behave very similarly with redshifted peaks at i≥60° ([NeII] 12.8 µm) and i≥80° ([FeII] 17-2 µm).

In a typical analysis, where the profiles are decomposed into multiple Gaussian components, the features described above would easily be missed. Because the profiles are skewed or exhibit a Keplerian

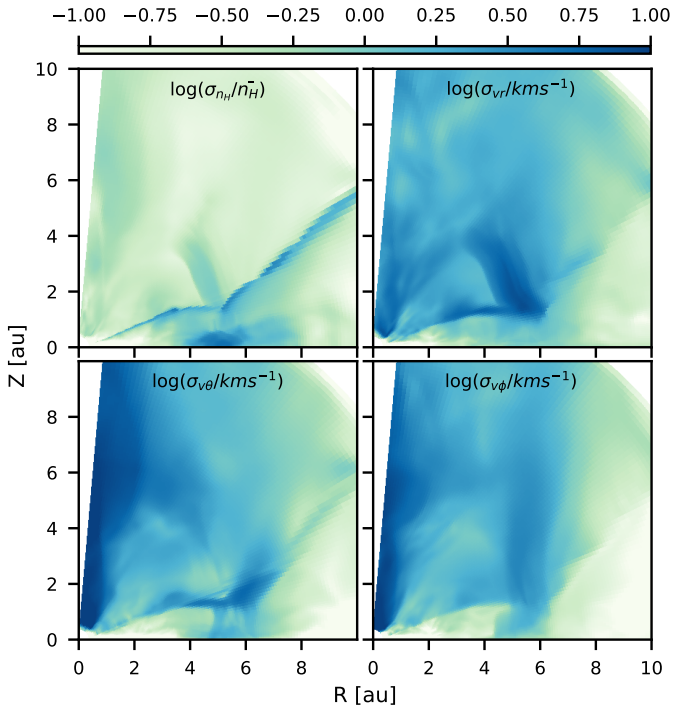

Figure 2.6: Maps of the standard deviation σ along the azimuthal direction for the hydrogen number density and the three velocity components in spherical coordinates. For the number density, the map is weighted by the local azimuthal mean $\bar{n_H}$.

double-peak feature, it is clear that with increasing spectral resolution, most are not well represented by Gaussian components, especially when observed at intermediate to high inclinations. With upcoming instruments that will allow for observations with higher resolution, it becomes worthwhile to study the detailed shape of the profiles. To show this, we list the results of the Gaussian decomposition of the [OI] 6300 Å line profiles as well as the velocity of the actual peak in table 2.3. The results for the other lines are available as online supplementary material. When the decomposition yields only a single component, the centroid velocity is almost always in the blueshifted part of the spectrum, even if the peak is clearly redshifted. At higher inclinations, starting at $\approx 40°$, the decomposition often yields two narrow components that fit to the Keplerian double peaks. Such a decomposition does not allow for a clear identification of a redshifted peak either, as it often fails to produce a fit that accurately matches the peaks of the high-resolution profiles.

For reference, we also show profiles calculated with half the spectral resolution, comparable to currently available observations, in appendix 2.5.1. It is clear that the effects of the planet on the wind cannot be unambiguously observed in currently available spectra. Forbidden line diagnostics of disc winds will greatly benefit from the anticipated high resolution spectra.

2.3.2.3 Profile variability

Simon et al. (2016) compared their high-resolution (~6 km/s) [OI] 6300 Å profiles to the slightly lower-resolution (~12 km/s) profiles that were observed earlier by Hartigan et al. (1995). While they found that the general structure of the LVC remains mostly stable over the timescale of one or two

decades, they did find objects that had variations between the different epochs. Two of the objects in their high-resolution sample, UX Tau A and IP Tau, were observed twice, ~6 years apart. The profile of IP Tau evolved so strongly that the LVC vanished from the decomposition of the later profile. UX Tau A experienced significant variations, too.

In our three-dimensional models, the substructures such as the spiral waves and instabilities that are induced by the planet in the disc do have an impact on the azimuthal symmetry of the wind. We show the extent of the asymmetries in Figure 2.6, were we plot a map of the standard deviation along the azimuth. Since the number density spans a large range of values of several orders of magnitude, we weighted its standard deviation with the local azimuthal mean value of the number density. The deviation inside the wind reaches up to ~30% of the mean. The velocity components show a deviation of several km/s. This is sufficient to lead to variations in our synthetic line profiles on timescales shorter than the planet's orbit. Figure 2.7 shows the variations that would be observed with a high spectral resolution (R = 100000) when the disc is observed at an inclination of 60° and from different azimuth angles. This crude approximation of the variations that would be observed during an orbit of the planet neglects the wind dynamics. The resulting variations should therefore be considered a lower limit. However, we expect the influence of the wind dynamics to be small, because the hydrodynamical timescales over which variations in the wind structure propagate far enough to cover a significant portion of the line emission region are of the order of years (at a typical speed of 5 km/s high up in the wind, it takes ≈ 1 year to travel 1 au).

Variability is observable in the [OI] 6300 Å and [SII] 4068 Å profiles of the MJ1 model and it is even more evident in the MJ5 model, which shows significant variations in all other lines, too. The profiles experience observable shifts of the peak velocity on a timescale of less than a quarter of the planet's orbital period, which corresponds to ≈3.5 years in our models. Around the location of the peak the flux varies by 10 – 20 %. A signal to noise ratio between 25 and 50 should therefore be sufficient to detect the variability at the simulated spectral resolution. For model MJ5 we also show synthetic profiles that were calculated from a time-average of the hydrodynamical grid taken from 850 snapshots over ≈5 orbits of the planet. This is to show that the presented profiles, which are individual snapshots, are reasonably scattered around the average and are not an edge-case.

In the MJ5 model the average shows that the redshifted peak is dominating most of the time in the [OI] 6300 Å line profile, but not in the profiles of the other lines. Given that the overall wind structure is in an approximately steady state with only minor dynamical fluctuations over multiple orbits, the variations shown here should be periodic in nature with a period that increases with the planet's separation. Due to the high computational cost of the simulations, however, we did not explore models with different separations.

One caveat may be that the planet-induced variability could be overshadowed by variability of the stellar accretion luminosity that is mainly responsible for the heating of the wind and drives the emission of our modelled lines. As was shown e.g. by Weber et al. (2020), the line profile properties correlate with the accretion luminosity. Although they find that this correlation is strongest for the line luminosity, they do find that it correlates with the width and centroid-velocity of the fitted Gaussian components and can slightly affect the line profile shape. Even though the effect on the shape of the line profile appears small, it could complicate the interpretation of profile variations, especially since variability of the accretion luminosity has been observed over much shorter timescales on the order of days (Manara et al., 2021).

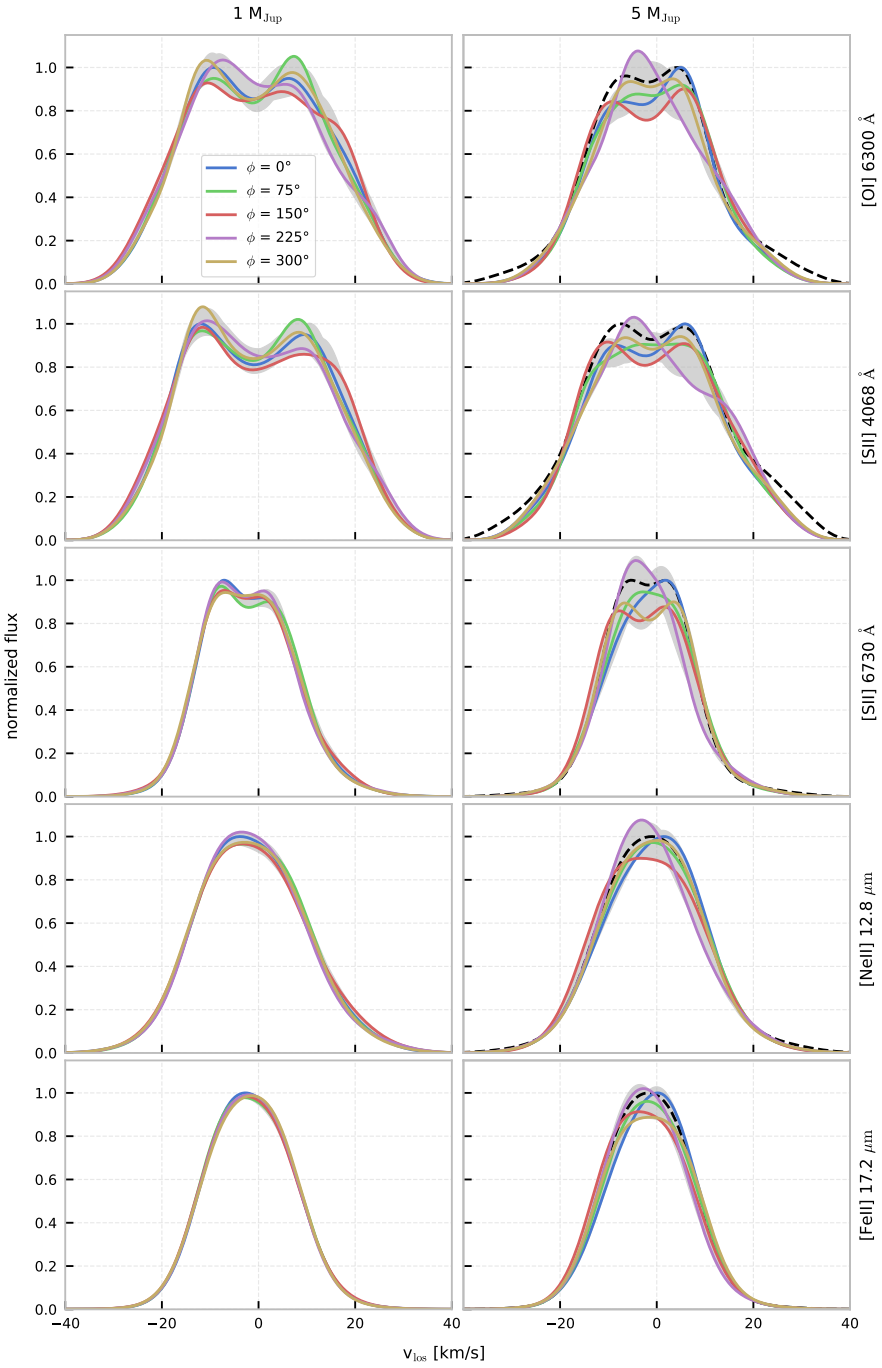

Figure 2.7: Synthetic spectral profiles viewed at 60° inclination but at different azimuth angles ϕ. The grey shaded area encloses the minimum and maximum flux at a certain velocity that can be observed during one orbit of the planet. The profiles were degraded to a resolving power of R = 100000 and normalised to the peak flux of the $\phi = 0$ profile.

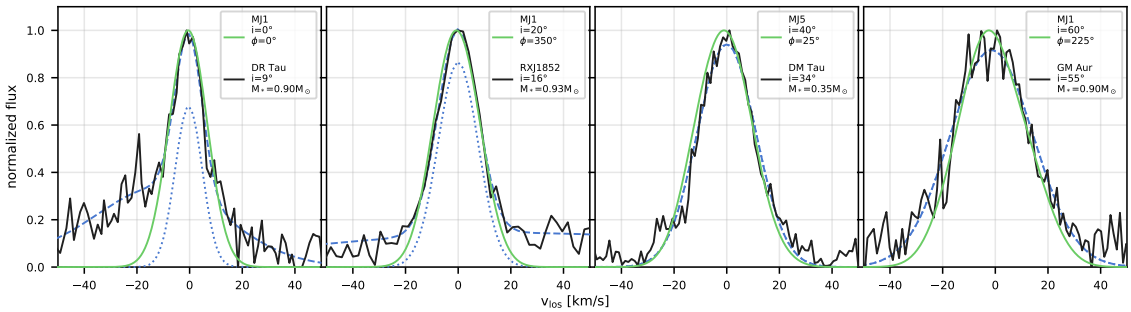

Figure 2.8: Comparison of our synthetic [OI] 6300 Å profiles with selected observations. The black solid line shows the observed line profiles taken from Banzatti et al. (2019). The inclinations and stellar masses are taken from Banzatti et al. (2019, table 1). The blue dashed line shows the fit to the observed profile, the blue dotted line shows the NC of the fit. The green solid line shows the modelled profile that matches best between all profiles from all three models.

2.3.2.4 Comparison with observations

In Figure 2.8 we show for inclinations of 0°, 20°, 40° and 60° a well-matching pair of a modelled and an observed [OI] 6300 Å profile. The observations were selected from the combined observational sample of Fang et al. (2018) and Banzatti et al. (2019). In these works, the authors also list references for the inclinations of most objects, which we used to limit the comparisons to objects with an inclination that deviates not more than 10° from that of the model. Due to the lack of near edge-on observations, we do not include a comparison at 80°. We use the [OI] 6300 Å line, because it is the line with the most available observations. To find a good match, we degraded the synthetic profiles to a resolving power R = 45000, comparable to that of the observations and then chose the model-observation pair that minimises χ^2 in the intervals [-15, 15], [-19, 19], [-23, 23] and [-26, 26] km/s for i=0°, 20° 40° and 60°, respectively. We extend the intervals with increasing inclination in order to account for the broadening that is expected due to Keplerian rotation and we ignore everything outside the intervals, because our models can reproduce only narrow low-velocity components and not the broad or high-velocity components that are often additionally observed and usually attributed to magnetic winds. We note that this method will favour observations that have a distinct, isolated narrow component. However, it is not possible to unambiguously extract the narrow component from more complex line profiles that are likely to contain additional emission that traces a magnetic wind. Moreover, the noise of the observed profiles is often larger than the difference between our synthetic profiles at the available resolution. With the currently available data our approach is therefore not suitable for a quantitative comparison between different models, or to distinguish between models with and without planets, as for example also a model of a photo-evaporating transition disc without a planet but with a completely depleted inner gas cavity typically leads to profiles with lower blueshifts. Nevertheless, we consider this comparison to be a good demonstration that our models can reproduce the often observed narrow low-velocity components very well.

The resulting matches are all between one of the models that contains a planet and an object with a clear narrow component in it's line profile that is only slightly blueshifted (v_c = -0.16, -0.21, -0.16 and -1.77 for DR Tau, RX J1852, DM Tau and GM Aur, respectively). Due to the limited resolution, neither the models nor the observations exhibit any Keplerian double peaks or obviously skewed profiles where a single redshifted peak could be identified. At that resolution, profiles with similarly

low blueshifts could possibly be also reproduced with a model of a photo-evaporating transition disc without a planet, as a completely depleted inner gas cavity typically leads to profiles with lower blueshifts (Picogna et al., 2019). However, it is remarkable that although none of our models have been tuned to reproduce any of the observations, they match the observations very well across all available inclinations and across different types of discs. DR Tau is considered a very active classical T Tauri star with a complex line profile that can be decomposed into high-velocity and broad and narrow low-velocity components. Mesa et al. (2022) detected a compact and elongated structure in its disc at a separation of 303±10 mas, corresponding to ≈ 59 au, which they suggest could hint at the presence of an embedded forming planet with a few M_J in mass. In contrast, RX J1852, DM Tau and GM Aur, are all known accreting transition discs with simpler line profiles and with observed gaps that could be caused by planets. DM Tau and GM Aur have been particularly well studied. Bosman et al. (2021) found evidence for a strongly depleted gas cavity inside R ≈ 15 au in the disc around GM Aur. Kudo et al. (2018) detected a dust ring at R ≈ 4 au in the 1.3mm dust continuum emission and ^{12}CO J = 2 → 1 emission of DM Tau that could potentially indicate the presence of a planetary gap at a location that is similar to that in our models. But even then a direct comparison to our model would not be possible, because DM Tau has only half the stellar mass of the star in our models. We will discuss in the following section how our results may be affected by different model parameters such as the location of the planetary gap and the stellar mass.

2.3.3 Dependence on model parameters

Although the high computational cost of the simulations prevent us from doing an extensive parameter study, we can nevertheless apply theoretical considerations to get insight on the influence of the key parameters in our models. Kanagawa et al. (2016) found a relation for the gap width Δ_{gap}:

$$\frac{\Delta_{gap}}{a_p} = 0.41\left(\frac{M_p}{M_*}\right)^{\frac{1}{2}}\left(\frac{h_p}{a_p}\right)^{-\frac{3}{2}}\alpha^{-\frac{1}{4}}, \tag{2.3}$$

where a_p is the orbital radius of the planet, h_p the scale height of the disc at the location of the planet and α is the viscosity parameter. Since the width of the gap determines the size of the affected wind-region, we can use this to investigate how our results depend on an individual parameter, while keeping the others constant.

2.3.3.1 Dependence on the planetary mass

We have already seen in section 2.3.1 that an increase in planet mass leads to a wider gap, which leads to stronger effects on the wind structure and on the line profiles. We have also shown that the gravitational potential of the planet is negligible in the wind regions. From relation (2.3) we would therefore expect the gap width to increase by a factor $\sqrt{5} \approx 2.24$ between the models MJ5 and MJ1. When measured between the points at the gap edges, where the azimuthally averaged 1D surface density profile reaches half of the unperturbed value at the location of the planet, we find a factor 2.69 increase in our models, which is in reasonably good agreement.

2.3.3.2 Dependence on the stellar mass

According to equation (2.3), the dependence of the gap-width on the stellar mass is inverse to that of the planet. The combination of a 0.14 $M_\odot$ star with a Jupiter-like planet should give a similar gap width as we find in model MJ5. However the stellar mass has a strong impact on the structure of the

photo-evaporative wind, because it not only defines the gravitational potential that the wind has to overcome, but it also affects the irradiating spectrum and luminosity that is driving the wind (Ercolano et al., 2021; Picogna et al., 2021). A lower stellar mass allows the wind to be launched at radii closer to the star, but it is also less extended. In such a scenario it is possible that the EUV radiation that heats the wind and drives the forbidden line emission will to some degree be screened by the inner wind and not reach the region that is the most affected by the presence of the planet. In that case the distinctive features in the line profiles would be weaker, but detailed models are required in order to determine how the lower wind-launching radius affects the wind dynamics and the forbidden emission lines.

2.3.3.3 Dependence on the viscosity

We do not expect the viscosity to have a significant effect on the dynamics of the wind, however since the gap width scales with $\alpha^{-\frac{1}{4}}$, we should be able to reproduce effects similar to that of increasing the planet mass, when we decrease the viscosity, instead. As an example, a model with $\alpha = 4 \cdot 10^{-5}$ and $M_p = M_J$ should be comparable to our model MJ5.

2.3.3.4 Dependence on the orbital radius

Assuming a constant aspect ratio of the disc, if the orbital radius of the planet is larger, the gap will be proportionally wider (see eq. (2.3)). However since the forbidden line emission is generally dominated in the wind-regions close to the star, most lines will not be able to trace the regions above the gap if the planet is outside $\approx$ 10 au. Although our models show that the presence of the gap modifies the wind dynamics even in the inner parts of the disc, it is unclear whether this would happen with a gap at a larger orbital radius. Because the photo-evaporative wind is weaker at larger radii, the pressure difference between the under-density and the wind at the inner gap-edge will be smaller, too, which will lead to smaller horizontal components in the pressure gradient. A lower orbital radius would shift the gap closer to the star and closer to the wind-launching region that dominates the emission. In that case, we expect the effect on the line-profiles to become stronger and the timescales of the profile-variability to become shorter, as long as the gap does not reach the critical launching radius of the wind ($\approx$ 2 au, see Figure 2.2). When measuring the width of the gap as described in section 2.3.3.1, we can get the estimation from Figure 2.2 that no wind is launched inside the inner $\approx$75 % of the gap. Assuming that this ratio is constant, we find with eq. (2.3) an estimated threshold orbital radius of $\approx$ 2.5 au and $\approx$ 3.3 au for $M_p = M_J$ and $M_p = 5\ M_J$, respectively. If the orbital radius was lower than the threshold, a photo-evaporative wind could only be launched outside the gap. The emission would then likely shift outwards, too, which would lead to narrower lines and less variability, due to the slower Keplerian rotation at higher radii.

2.3.3.5 Dependence on the X-ray luminosity

The X-ray luminosity is the main driver of the photo-evaporative wind in our model. A higher X-ray luminosity leads to a more vigorous wind with a higher total mass loss. With a denser wind we expect the contrast between the under-density and the wind to be stronger, leading to stronger pressure gradients, which could amplify the features that we observed in the line profiles of the MJ5 model. In contrast to that, while Ercolano & Owen (2016) have shown that there is no significant correlation between the luminosity of forbidden lines and the X-ray luminosity, we do expect the emission regions to be less extended when the wind is denser, because the EUV-radiation is more efficiently absorbed. Again, detailed models would be required to quantify these competing effects.

2.3.3.6 Dependence on the accretion luminosity

Although the accretion luminosity has no significant impact on the disc or wind structure, its EUV component is the main driver for the line emission (Ercolano & Owen, 2016). Weber et al. (2020) have shown that when the accretion luminosity is higher, the size of the emission regions increases. That way, the forbidden lines could potentially trace more of the region that is affected by the presence of the planet, leading to stronger features in the line profiles with higher accretion luminosity.

2.4 Conclusions

We have created three-dimensional numerical models of photo-evaporating, viscous ($\alpha = 10^{-3}$) protoplanetary discs hosting a giant planet with the goal of studying the interplay between planet-disc interactions and photo-evaporation. In order to predict the imprint on forbidden emission line diagnostics, we have performed detailed photo-ionisation and radiative transfer simulations and created synthetic spectral line profiles from the results. The models show that

- A massive, gap-opening planet can significantly alter the photo-evaporative wind structure at and inside the radial location of the gap. Above the gap, the pressure gradient that drives the wind is inversed, pointing downwards. As a result, a region of reduced density develops above the gap and wind-material that enters this region from the inner disc wind or from above the outer gap-edge can fall back down and into the gap. It is unclear whether winds that are not driven by a pressure gradient (e.g. magnetic winds) would experience similar effects.

- A gap carved by a 5 M_J planet can show an imprint on the spectral line profiles of forbidden line emission in high resolution (R $\approx$ 100000) spectra. In all of our synthetic emission lines the peak of the profile could be shifted to the red part of the spectrum by several km/s, when the disc is observed at an inclination of 40°– 60° or more. These details are lost in a multi-Gaussian decomposition, demonstrating the need for more detailed analyses of line profiles with increasing spectral resolution. A much less massive planet (1 M_J) cannot affect the wind-structure enough to have an observable effect on the line profiles, unless the viscosity in the disc is much lower than in our models.

- Asymmetric substructures that are generated by the planet within the disc leave a signature in the photo-evaporative wind. This gives rise to temporal variations of the line profile shape that can be strong enough to be observable on timescales of less than a quarter of the planet's orbital period.

- Our synthetic line profiles compare well to a subset of observations of objects with different inclinations and stellar masses. However, the resolution of currently available observations is not sufficient to allow for an identification of the distinctive features that our models would predict in the presence of a planetary gap. Future observations with about twice the currently available spectral resolution could provide enough detail for this to become possible.

Acknowledgements

We are grateful to the anonymous referee, whose comments helped improve this work. This research was supported by the Excellence Cluster ORIGINS which is funded by the Deutsche Forschungsgemeinschaft (DFG, German Research Foundation) under Germany´s Excellence Strategy – EXC-2094-

390783311. BE, GP and CHR acknowledge the support of the Deutsche Forschungsgemeinschaft (DFG, German Research Foundation) - 325594231. CHR is grateful for support from the Max Planck Society. The simulations have been partly carried out on the computing facilities of the Computational Center for Particle and Astrophysics (C2PAP).

Data Availability

The data underlying this article are available from the authors upon request.

2.5 Appendix

2.5.1 Line profiles and fits

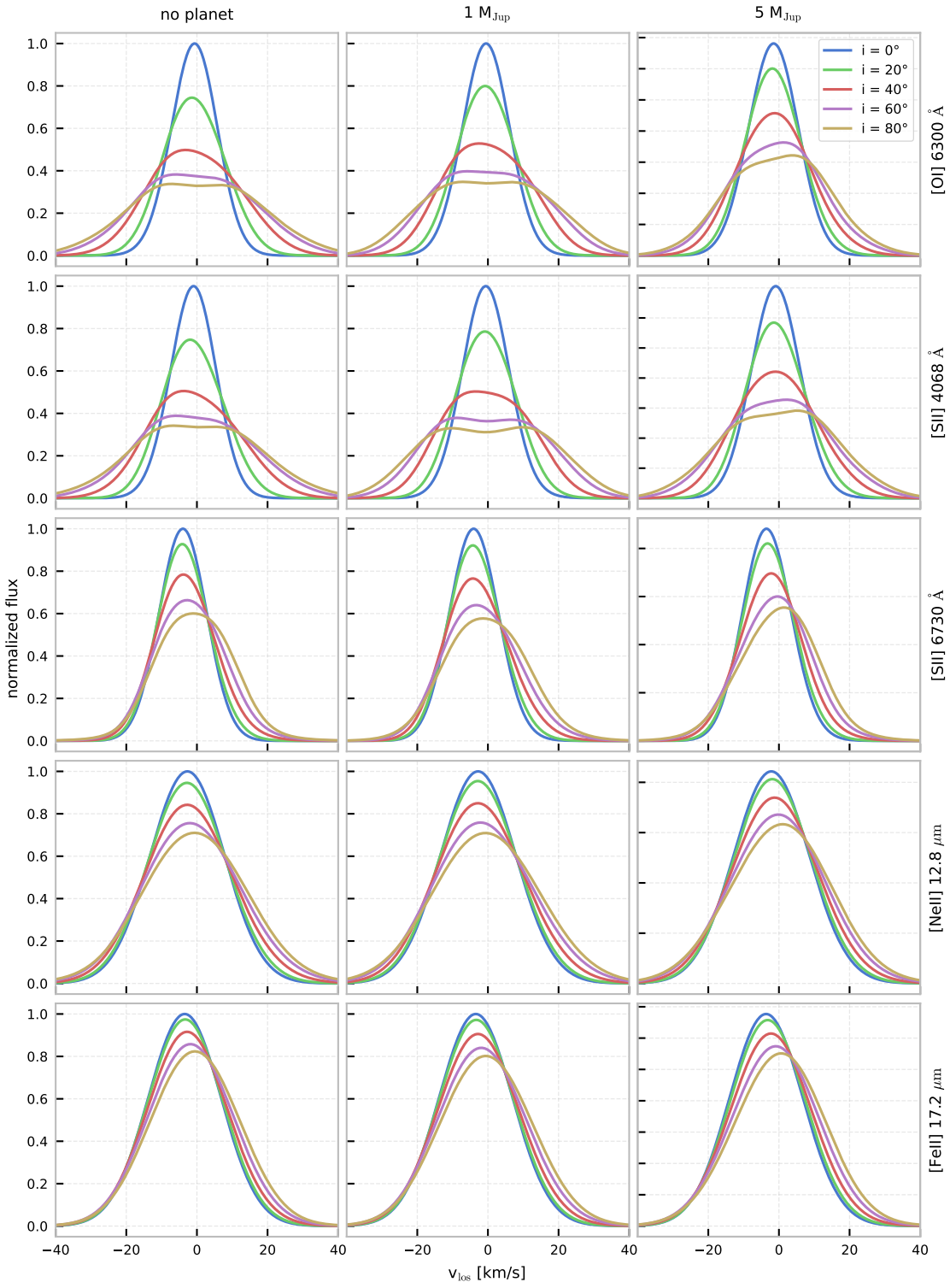

Figure 2.9: Synthetic spectral profiles viewed at inclination i and azimuth angle $\phi = 0$. The profiles are normalised to the peak of the face-on profile with i = 0°. The profiles were artificially degraded to a resolving power R = 50000 and R = 30000 for the optical and mid-infrared lines, respectively. This is comparable to currently available high-resolution observations.

Table 2.3: Results of the Gaussian decomposition of the [OI] 6300 Å high-resolution (R=100000) line profiles. We also list the velocity of the actual peak of the profile v_p in addition to the centroid velocity v_c. The velocities and FWHM are given in units of km/s. The results of all lines are available as online supplementary material.

		MJ1				MJ5				REF			
i[°]	phi [°]	v_c	v_p	FWHM	log(L/L$_\odot$)	v_c	v_p	FWHM	log(L/L$_\odot$)	v_c	v_p	FWHM	log(L/L$_\odot$)
0	0	-0.50	-0.38	9.82	-5.04	-1.50	-1.38	11.16	-4.88	-0.62	-0.38	9.42	-4.94
20	0	-0.66	-1.63	16.14	-5.03	-1.81	-2.13	14.09	-4.88	-1.15	-2.88	17.19	-4.94
	25	-0.71	-1.88	16.30	-5.03	-1.66	-1.88	14.25	-4.88				
	50	-0.70	-2.13	16.80	-5.03	-1.55	-1.63	14.71	-4.88				
	75	-0.64	-1.88	17.54	-5.03	-1.54	-1.63	15.42	-4.88				
	100	-0.61	-1.88	18.29	-5.04	-1.58	-2.13	16.02	-4.88				
	125	-0.64	-2.38	18.81	-5.03	-1.62	-2.38	16.40	-4.88				
	150	-0.78	-2.88	18.78	-5.03	-1.64	-2.38	16.70	-4.88				
	175	-1.01	-2.88	18.07	-5.03	-1.68	-2.38	16.77	-4.88				
	200	-1.23	-2.63	17.15	-5.03	-1.76	-2.63	16.26	-4.88				
	225	-1.31	-2.63	16.27	-5.03	-1.86	-2.38	15.46	-4.88				
	250	-1.19	-2.13	15.67	-5.03	-1.94	-2.13	14.90	-4.88				
	275	-0.96	-1.38	15.63	-5.03	-2.00	-2.13	14.52	-4.88				
	300	-0.75	-1.38	15.81	-5.03	-2.04	-2.38	14.26	-4.88				
	325	-0.64	-1.38	16.03	-5.03	-2.00	-2.38	14.11	-4.88				
	350	-0.64	-1.63	16.13	-5.03	-1.87	-2.13	14.07	-4.88				
40	0	-0.66	-7.14	27.84	-5.03	-1.45	1.38	21.77	-4.88	-1.16	-7.14	28.53	-4.94
	25	-0.66	-6.39	28.13	-5.03	-1.25	0.63	21.66	-4.88				
	50	-0.57	1.88	28.50	-5.04	-1.19	0.88	22.18	-4.88				
	75	4.91	4.39	19.81	-5.21	-1.29	1.63	23.72	-4.88				
		-10.45	4.39	12.86	-5.52								
	100	6.85	-7.64	17.61	-5.28	-1.43	-6.14	24.71	-4.88				
		-9.36	-7.64	14.68	-5.39								
	125	8.33	-7.39	16.83	-5.35	-1.48	1.63	25.35	-4.88				
		-8.42	-7.39	16.87	-5.32								
	150	8.65	-7.64	17.57	-5.36	-1.49	2.13	25.14	-4.88				
		-8.21	-7.64	17.69	-5.30								
	175	-0.97	-6.89	29.88	-5.03	-1.55	1.88	25.22	-4.88				
	200	-1.29	-6.14	28.25	-5.03	-1.74	-3.88	23.27	-4.87				
	225	-1.43	-5.39	27.11	-5.03	-1.87	-2.63	21.71	-4.88				
	250	-1.29	-5.39	26.73	-5.03	-1.84	-1.63	20.70	-4.89				
	275	-1.00	-6.39	26.98	-5.03	-1.81	-1.13	20.61	-4.88				
	300	-0.77	-6.89	27.41	-5.03	-1.82	-1.13	20.79	-4.88				
	325	-0.66	-7.14	27.77	-5.03	-1.72	0.38	21.21	-4.88				
	350	-0.66	-7.14	27.77	-5.03	-1.53	1.38	21.67	-4.88				

Table 2.4: Results of the Gaussian decomposition of the [OI] 6300 Å line profiles.

		MJ1				MJ5				REF			
i [°]	phi [°]	v_c	v_p	FWHM	log(L/L$_\odot$)	v_c	v_p	FWHM	log(L/L$_\odot$)	v_c	v_p	FWHM	log(L/L$_\odot$)
60	0	8.79	-9.40	23.55	-5.27	-0.77	4.89	28.08	-4.87	-0.76	-9.65	37.20	-4.94
		-11.60	-9.40	18.33	-5.41								
	25	8.37	-9.15	24.33	-5.26	-0.53	3.63	27.75	-4.87				
		-11.61	-9.15	18.94	-5.42								
	50	-0.14	5.39	36.44	-5.03	-0.49	3.38	27.70	-4.87				
	75	7.81	7.39	23.14	-5.24	-0.70	4.89	29.40	-4.88				
		-12.54	7.39	17.40	-5.46								
	100	10.00	8.90	20.19	-5.32	-0.88	5.64	30.63	-4.88				
		-11.09	8.90	19.10	-5.36								
	125	12.42	-9.65	18.24	-5.41	5.20	5.14	20.51	-5.07				
		1.82	-9.65	10.08	-6.39	-11.42	5.14	14.09	-5.34				
		-10.39	-9.65	21.10	-5.31								
	150	11.00	-10.65	21.95	-5.34	5.29	5.64	20.14	-5.08				
		-10.83	-10.65	21.79	-5.32	-11.60	5.64	13.97	-5.33				
	175	9.89	-9.15	24.06	-5.31	5.90	-7.64	19.99	-5.11				
		-11.33	-9.15	21.17	-5.35	-10.76	-7.64	15.51	-5.28				
	200	-0.99	-8.15	36.85	-5.02	-1.35	-4.64	28.98	-4.87				
	225	-1.16	-7.39	35.69	-5.03	-1.49	-3.88	27.28	-4.88				
	250	-1.10	-8.15	34.81	-5.02	-1.36	-1.38	26.48	-4.88				
	275	7.82	-9.65	22.81	-5.27	-1.22	2.13	27.42	-4.88				
		-11.58	-9.65	17.37	-5.42								
	300	8.18	-10.65	22.61	-5.27	-1.19	3.38	28.26	-4.88				
		-11.95	-10.65	16.89	-5.42								
	325	8.63	-10.90	23.02	-5.27	-1.10	4.14	27.90	-4.87				
		-11.92	-10.90	17.63	-5.41								
	350	8.94	-9.40	23.12	-5.28	-0.88	4.89	28.12	-4.87				
		-11.60	-9.40	18.13	-5.40								
80	0	11.15	-9.40	25.08	-5.30	-0.01	6.89	32.20	-4.87	11.04	-9.90	25.84	-5.23
		-12.40	-9.40	22.49	-5.37					-12.11	-9.90	23.72	-5.28
	25	10.88	7.89	25.43	-5.30	0.27	4.89	31.38	-4.87				
		-12.05	7.89	23.33	-5.37								
	50	0.42	7.39	40.23	-5.02	0.32	4.64	30.70	-4.87				
	75	10.09	9.15	23.89	-5.28	0.06	6.14	31.77	-4.88				
		-12.67	9.15	21.24	-5.40								
	100	12.08	11.15	20.68	-5.35	-0.13	6.89	32.77	-4.88				
		-11.27	11.15	22.26	-5.33								
	125	13.47	-10.15	20.53	-5.39	-0.19	7.14	33.06	-4.87				
		-10.58	-10.15	24.69	-5.28								
	150	16.52	-11.40	17.93	-5.52	8.25	7.64	19.09	-5.16				
		5.23	-11.40	12.75	-5.98	-10.21	7.64	17.10	-5.23				
		-10.89	-11.40	24.87	-5.28								
	175	11.88	8.40	24.63	-5.33	9.62	-7.64	18.12	-5.22				
		-12.04	8.40	24.00	-5.33	-8.85	-7.64	18.81	-5.16				
	200	7.68	-8.65	29.48	-5.21	-0.73	-5.14	31.98	-4.87				
		-9.54	-8.65	11.65	-5.89								
		-19.97	-8.65	17.27	-5.74								
	225	-0.70	-7.89	40.25	-5.02	-0.86	-4.64	30.58	-4.88				
	250	-0.70	-8.90	39.68	-5.02	-0.66	-5.39	30.68	-4.88				
	275	10.45	-10.90	23.39	-5.31	-0.46	5.39	31.78	-4.88				
		-12.22	-10.90	19.96	-5.37								
	300	10.04	-12.66	24.73	-5.28	-0.41	-7.14	32.25	-4.88				
		-13.35	-12.66	19.18	-5.41								
	325	10.54	10.65	25.41	-5.28	-0.33	6.89	32.34	-4.87				
		-13.31	10.65	20.78	-5.39								
	350	11.23	-9.15	24.83	-5.30	7.50	7.14	18.62	-5.14				
		-12.52	-9.15	22.12	-5.37	-10.51	7.14	16.56	-5.26				

Chapter 3

Impact of photoevaporative winds on discs hosting embedded giant planets

The content of this chapter was published in Weber et al. (2024)[1]:

Michael L. Weber, Giovanni Picogna, Barbara Ercolano: "The interplay between forming planets and photoevaporating discs II: Wind-driven gas redistribution",
Astronomy & Astrophysics, Volume 686 (2024), A53

Abstract

Context. Disc winds and planet-disc interactions are two crucial mechanisms that define the structure, evolution and dispersal of protoplanetary discs. While winds are capable of removing material from discs, eventually leading to their dispersal, massive planets can shape their disc by creating substructures such as gaps and spiral arms.
Aims. We study the interplay between an X-ray photoevaporative disc wind and the substructures generated due to planet-disc interactions to determine how their mutual interactions affect the disc's and the planet's evolution.
Methods. We perform three-dimensional hydrodynamic simulations of viscous ($\alpha = 6.9 \cdot 10^{-4}$) discs that host a Jupiter-like planet and undergo X-ray photoevaporation. We trace the gas flows within the disc and wind and measure the accretion rate onto the planet, as well as the gravitational torque that is acting on it.
Results. Our results show that the planetary gap takes away the wind's pressure support, allowing wind material to fall back into the gap. This opens new pathways for material from the inner disc (and part of the outer disc) to be redistributed through the wind towards the gap. Consequently, the gap becomes shallower, and the flow of mass across the gap in both directions is significantly increased, as well as the planet's mass-accretion rate (by factors $\approx$ 5 and $\approx$ 2, respectively). Moreover, the wind-driven redistribution results in a denser inner disc and less dense outer disc, which, combined with the recycling of a significant portion of the inner wind, leads to longer lifetimes of the inner

[1]The work presented in this chapter resulted from a collaboration with my co-authors, which I led. I was responsible for conducting all the simulations and analysis, as well as composing the manuscript. My co-authors provided advice on the interpretation of the results. Giovanni Picogna provided the underlying photoevaporation model, which I adapted for implementation in 3D models with a planet.

disc, contrary to the expectation in a planet-induced photoevaporation (PIPE) scenario that has been proposed in the past.

3.1 Introduction

The extensive diversity of exoplanets and exoplanetary systems discovered in recent years highlights the importance of understanding the many different processes involved in the formation and evolution of planets in protoplanetary discs. Two of the most important processes that can affect the structure, evolution, and dispersal of protoplanetary discs are planet-disc interactions and disc winds.

Through the gravitational influence on its surrounding material, a newly formed planet that is still embedded in a protoplanetary disc can generate complex substructures in the disc that can influence both the planet's and the disc's evolution (see e.g. Paardekooper et al., 2022, for a recent review). A planet excites spiral density waves at Lindblad resonances, and if the planet is massive enough, the torque that the spiral waves exert on the disc can become strong enough to overcome the viscous torque, at which point a gap will open in the disc along the planet's orbit (Goldreich & Tremaine, 1979, 1980; Papaloizou & Lin, 1984). Numerical simulations show that at the edges of such gaps, the gas follows meridional flows, circulating between the lower and upper layers of the protoplanetary disc (e.g. Morbidelli et al., 2014; Fung & Chiang, 2016). The disc, on the other hand, also has a gravitational influence on the planet and asymmetric substructures in the disc can result in a net torque that acts on the planet, changing its angular momentum, which will lead to its migration through the disc, either radially inward or outward (e.g. Kley & Nelson, 2012, and references therein). Recent observations, e.g. with the Atacama Large Millimeter/submillimeter Array (ALMA), have revealed that most discs are indeed highly substructured, including, among other features, gaps, spirals and meridional flows that may be linked to the presence of planets (see e.g. review by Pinte et al., 2022b). These observations present an excellent testbed for theoretical models of planet-disc interactions. Interpreting them, however, requires a complex understanding of all the different processes at play.

During the last decades, observational campaigns spanning multiple star-forming regions have shown that most protoplanetary discs have a lifetime of only a few million years (Haisch et al., 2001; Mamajek et al., 2009; Fedele et al., 2010; Ribas et al., 2014). Moreover, the observed disc fractions at different wavelengths suggest that most discs disperse from the inside-out (see also Koepferl et al., 2013; Ercolano et al., 2015). While many physical processes have been proposed to drive the dispersal of discs, it is still mostly unconstrained which process is dominant at a given location and time. It is clear that accretion onto the star plays a major role in the disc's evolution, but the mechanism that is responsible for the necessary transport of angular momentum is still uncertain and could be either turbulence driven by various types of instabilities or magnetic winds or a combination of both (e.g. Lesur et al., 2022, for a recent review). Very likely, the dominant process varies with the location in the disc and its evolutionary stage. In recent years, magnetically driven disc winds have been shown to be able to drive mass-loss and accretion at rates compatible with observations (e.g. Gressel et al., 2015; Bai et al., 2016; Béthune et al., 2017; Wang et al., 2019; Gressel et al., 2020; Lesur, 2021), adding to a growing body of evidence that they play an important role in disc evolution, especially at early stages, while later in the disc's life, thermal winds may become the dominant dispersal mechanism (see also Ercolano & Pascucci, 2017; Pascucci et al., 2020, 2022). Models of thermal winds, in particular those driven by internal photoevaporation, have been very successful in explaining the lifetimes and fast inside-out dispersal of protoplanetary discs (e.g. Alexander et al., 2006b; Gorti & Hollenbach, 2009; Owen et al., 2010; Picogna et al., 2019), as well as numerous other observables, including some of the observed spectra of wind-tracing emission lines (Ercolano & Owen, 2010, 2016; Weber et al., 2020;

Rab et al., 2022), the spatially resolved [OI] 6300 Å spectral line in TW Hya (Rab et al., 2023) or stars with low accretion rates (Ercolano et al., 2023). We refer to Ercolano & Pascucci (2017); Ercolano & Picogna (2022); Pascucci et al. (2022) for recent reviews on the topic.

Disc winds not only play an essential role in the disc's dispersal, but they can also strongly affect the evolution of planets and vice versa. Multiple theoretical works have shown that photoevaporative winds can strongly affect the orbital migration and final semi-major axis distribution of planets (Alexander & Armitage, 2009; Alexander & Pascucci, 2012; Ercolano & Rosotti, 2015; Jennings et al., 2018; Monsch et al., 2021a). Additionally, in an observational study, Monsch et al. (2019) have constructed a catalogue of the X-ray luminosities and stellar and planetary properties of stars hosting giant planets and found a void in the distribution of giant planets in the plane of semi-major axis versus X-ray luminosity, which could point towards the parking of giant planets close to the location of a gap that is opened by X-ray photoevaporation (Monsch et al., 2021b).

Moreover, an accreting planet that is massive enough to carve a gap can significantly reduce the mass flux across the gap, effectively starving the inner disc of material (e.g. Lubow & D'Angelo, 2006). As a result, the wind-driven dispersal of the disc interior to the gap can be significantly accelerated, leading to the start of the transition disc phase, where the inner disc is depleted, and the then directly illuminated outer disc is quickly photoevaporated from the inside out (Alexander & Armitage, 2009; Rosotti et al., 2013). This effect is sometimes referred to as planet-induced photoevaporation (PIPE). In a companion work (Weber et al., 2022), we showed that a massive, gap-opening planet strongly affects the kinematics of a photoevaporative wind, an effect that could potentially be observed in emission line diagnostics as periodic variations in the spectral line profile with peaks in the redshifted part of the spectrum that trace the asymmetries generated by the planet in the wind.

In recent years, multiple theoretical works have shown that magnetic winds, too, can strongly influence the gap-opening, planet migration and accretion onto planets (e.g. Kimmig et al., 2020; Lega et al., 2021; Elbakyan et al., 2022; Nelson et al., 2023). Kimmig et al. (2020) found that a planet's migration behaviour can differ strongly depending on the radial density gradients in the disc, with rapid type-III-like outward migration being possible under certain circumstances. Lega et al. (2021) showed that migration can be fast or slow, depending on whether or not the torque from the planet is strong enough to block the accretion flow and in a similar study Nelson et al. (2023) demonstrated that accretion rates onto the planet itself also depend on this criterion. Elbakyan et al. (2022) found that it is easier to open deep gaps in discs with magnetised winds than in a standard viscous disc. Aoyama & Bai (2023) carried out global three-dimensional non-ideal magnetohydrodynamic (MHD) simulations of planet-disc interactions, including magnetic winds and found that the magnetic flux concentrates in the corotation region of the planet, leading to a strongly enhanced angular momentum extraction from the gap region and an outflow that primarily originates from the disc surface outward of the gap. Moreover, their gaps are wider and deeper than in the purely viscous or inviscid models, reducing the torque acting on the planet. With a different 3D global non-ideal MHD model, Wafflard-Fernandez & Lesur (2023) recently found that the planet deflects magnetic field lines at the disc surface, resulting in a more efficient wind at the outer edge of the gap and less efficient wind at the inner edge, which creates an asymmetric gap and consequently an asymmetric torque acting on the planet, leading to slower or potentially even outward migration.

This highlights the importance of understanding planet-disc interactions and disc winds not just as two separate physical processes but as an intertwined system with feedback processes that play a crucial role in the evolution of newly formed planets. In this work, we aim to study the interplay between planet-disc interactions and photoevaporative disc winds, expanding upon prior work in this field by conducting global, three-dimensional radiation-hydrodynamic simulations of a protoplanetary disc hosting a Jupiter-like planet and undergoing X-ray photoevaporation.

In Sect. 3.2, we describe the details of our numerical model and the assumptions made. In Sect. 3.3, we present our results, followed by a discussion in Sect. 3.4 and a summary in Sect. 3.5.

3.2 Methods

3.2.1 Model strategy and initial conditions

To reduce the computational cost of our simulations, we divide our models into three stages. In stage I, we start with a two-dimensional model of a purely viscously evolving protoplanetary disc in the midplane ($R-\Phi$ plane), to which we add a Jupiter-like planet that is held fixed on its circular orbit. The model is then evolved until the substructures that are generated by the planet have reached a steady state in the gas density. In stage II, we extend the model into three-dimensional space by adding a vertical dimension extending to about six disc scale heights to capture the planet-disc interactions fully. Again, the model is evolved until a quasi-steady state has been reached. In stage III, we activate the accretion of gas onto the planet and extend the 3D grid in the vertical direction to about 29 disc scale heights to prepare for the inclusion of a disc wind. Moreover, we branch off the model. In the first branch, we switch on the temperature parametrisation by Picogna et al. (2019) to model the temperature structure of the disc's upper layers in the presence of EUV and X-ray irradiation from the central star, which results in a photoevaporative wind. In the second one, we keep evolving the disc purely viscously, which is achieved by turning off the temperature parametrisation by setting the X-ray luminosity L_X to zero. All other physical parameters of the model remain the same across all stages. This allows us to directly compare the effect of a thermal wind on the disc and planet evolution. From now on, we will refer to the purely viscous model (without wind) as NOWIND and to the model with the temperature parametrisation enabled as PEWIND. An extensive list of parameters and their values can be found in table 3.1 and we list here only the most important ones, namely the stellar mass $M_* = 0.7\ M_\odot$, the viscosity parameter $\alpha = 6.9 \cdot 10^{-4}$, the planet mass $M_P = M_J$ and the semi-major-axis $a = 5.2\ au$. The details for the individual stages are described in the following subsections.

3.2.2 2D setup

To carry out our initial two-dimensional simulations of the planet-disc interactions, we use the hydrodynamics version of the FARGO3D code (Benítez-Llambay & Masset, 2016) with the orbital advection algorithm of Masset (2000). We use a polar grid with 776 uniformly spaced zones in the azimuthal and 512 logarithmically spaced zones in the radial direction between 0.364 au and 26 au, centred on the star with $M_* = 0.7\ M_\odot$. An overview of all grids used in the different stages is given in table 3.2. In the initial setup, the surface density Σ is set by the profile

$$\Sigma(R) = \Sigma_0(R) \left(\frac{R}{R_0} \right)^{-p} . \tag{3.1}$$

For the initial surface density, we choose $\Sigma_0 = 30\ g\ cm^{-2}$ at the base length unit $R_0 = 5.2\ au$ and a slope $p = 1$. Further, the setup assumes an isothermal, mildly flaring disc with flaring-index $f = 0.25$ that sets the aspect ratio according to $h(R) = H/R = 0.05\ (R/R_0)^f$. We include viscosity using the well-known α parametrisation by Shakura & Sunyaev (1973) with $\alpha = 6.9 \cdot 10^{-4}$. In the azimuthal direction, periodic boundary conditions are applied. In the radial direction, the azimuthal velocity and density are extrapolated using a Keplerian profile and the initial surface density profile, respectively, and an antisymmetric boundary condition is used for the radial velocity. To prevent oscillations at the boundary, we apply the wave-dampening method by De Val-Borro et al. (2006) with the timescale

Table 3.1: Parameters for the hydrodynamic models. Common parameters are shared between all models.

Model	Parameter	Value	Description
Common	M_*	0.7 $M_\odot$	stellar mass
	M_P	1 M_J	planet mass
	a_P	5.2 au	semi-major axis
	α	$6.9 \cdot 10^{-4}$	viscosity parameter
	γ	1.67	adiabatic index
	μ	2.35	mean molecular weight
	τ_{damp}	0.3	damping timescale
Stage I	Σ_0	30 g cm^{-2}	initial surface density
	p	1.0	surface density slope
	h	0.05	aspect ratio
	f	0.25	flaring index
	s	0.6	smoothing length
	t_{taper}	20	mass tapering time
	l_{damp}	1.15	damping zone width
Stage II & III	w_{damp}	0.4 au	damping zone width
	r_{sm}	0.5 R_H	smoothing length
	ρ_{floor}	10^{-21} g cm^{-3}	floor density
Stage III	τ_{acc}	0.5	accretion timescale
PEWIND	L_X	$2 \cdot 10^{30}$ erg s^{-1}	X-ray luminosity

$\tau_{\text{damp}} = 0.3$ and a width parameter l_{damp} (DampingZone) of 1.15, roughly corresponding to 10 per cent of the radius at the boundary.

The planet is modelled by including an additional gravitational potential of the form

$$\Phi_P = \sqrt{\frac{GM_P}{R^2 + s^2}}, \tag{3.2}$$

with a smoothing length defined by $s = 0.6\, h(R)\, R$ (ThicknessSmoothing). Since we use a reference frame that is corotating with the planet, we also include the indirect term that arises from the star's acceleration by the planet. We assume a circular orbit with a fixed semi-major axis $a_P = 5.2\ au$ and fixed mass $M_P = M_J$. To prevent shocks from inserting a massive planet into an unperturbed disc, we slowly increase its mass to its final value during the first 20 orbits. The model is run for 1000 orbits until a steady state is achieved.

3.2.3 3D setup

We use the results of our initial 2D simulation to inform the setup of our 3D model by mapping the density and azimuthal velocity information from the 2D model into a 3D spherical grid. For the density, we assume hydrostatic equilibrium, while the azimuthal velocity is set according to

$$v_\phi = v_K \left[(-p - q) \left(\frac{H}{R} \right)^2 + (1 - q) - \frac{-qR}{\sqrt{R^2 + Z^2}} \right]^{1/2}, \tag{3.3}$$

Table 3.2: Grids used in the hydrodynamic models. Radii are given in code units where the unit length is 5.2 au.

	Stage I			Stage II			Stage III		
Dim.	Interval	N Points	Type	Interval	N Points	Type	Interval	N Points	Type
r	[0.07, 5]	512	logarithmic	[0.280, 0.846]	60	uniform	[0.280, 0.846]	60	uniform
				[0.846, 1.154]	80	uniform	[0.846, 1.154]	80	uniform
				[1.154, 2.500]	60	logarithmic	[1.154, 2.500]	60	logarithmic
θ				[1.274, 1.417]	15	uniform	[0.600, 1.040]	26	uniform
				[1.417, $\frac{\pi}{2}$]	40	uniform	[1.040, 1.416]	29	uniform
							[1.416, $\frac{\pi}{2}$]	40	uniform
Φ	[-π, π]	776	uniform	[0, 2.988]	244	uniform	[0, 2.988]	244	uniform
				[2.988, 3.295]	80	uniform	[2.988, 3.295]	80	uniform
				[3.295, 2π]	244	uniform	[3.295, 2π]	244	uniform

which takes into account the force balance in the radial and vertical directions (e.g. Nelson et al., 2013). Here, R and Z are the cylindrical radius and height above the midplane, respectively, and $q = 0.5$ defines the slope of the temperature profile $T(R) = T_0(R/R_0)^{-q}$ and can also be expressed as $q = 1 - 2f$. The radial and polar velocities are set to zero. Although this does not take into account local deviations due to the planet and its substructures, it is sufficiently accurate for reducing the time required for the substructures in the 3D model to reach a quasi-steady state in the gas-density, compared to a start from a smooth disc without any substructure.

We perform all three-dimensional simulations using a modified version of the PLUTO code (Mignone et al., 2007). The code switch is merely for convenience, as our photoevaporation model is already implemented in PLUTO, whereas the 2D model was quicker to set up in FARGO3D. The 3D models are run in a spherical grid, spanning in the radial direction from $r = 1.456\ au$ to $r = 13\ au$ and in stage II (stage III) from $\theta = 1.274$ (0.6), corresponding to ≈ 6 (29) scale heights at the location of the planet, to $\theta = \frac{\pi}{2}$ (the disc midplane). We use a nested static grid to achieve a resolution of $\approx 0.05 R_H$ inside two Hill radii R_H from the planet. The details of the grids are listed in table 3.2. To further reduce the computational cost, we assume symmetry with respect to the midplane, which allows us to model only half of the disc. To do this, we choose our boundary conditions in the polar direction to be reflective at the midplane. On the other side, we use a reflective boundary in stage II and an open boundary in stage III to allow the wind to escape the domain. We note that the open boundary may cause reflections when the outflowing gas is subsonic, which is indeed the case in most parts of the simulation domain. However, we verified that the structure of the wind does not differ in a significant way from that in the previous generation of models presented in Weber et al. (2022). In that work, the focus lay on the inner regions of the wind, thus a much larger domain with the upper polar boundary very close to the polar axis was used. In the radial directions, we again extrapolate the azimuthal velocity component using a Keplerian profile and choose an open boundary condition for the other quantities. At the azimuthal boundary, periodic conditions are applied. As in the 2D model, we apply the wave-dampening method by De Val-Borro et al. (2006) with a width $w_{\mathrm{damp}} = 0.4$ au and timescale $\tau_{\mathrm{damp}} = 0.3$. Viscosity is implemented using PLUTO's default implementation with zero bulk viscosity. This means that the stress tensor is calculated according to:

$$\boldsymbol{\tau} = \rho\nu \left[\nabla \boldsymbol{v} + (\nabla \boldsymbol{v}^{\mathrm{T}}) - \frac{2}{3}(\nabla \cdot \boldsymbol{v})\boldsymbol{I} \right],$$

where $\boldsymbol{I}$ is the identity matrix and $\nu = \alpha c_s^2 \Omega_K^{-1}$ is the kinematic viscosity with c_s being the sound speed and Ω_K the Keplerian angular velocity.

As in the 2D model, the planet is implemented as an additional gravitational potential, where we adopt the potential from Klahr & Kley (2006), which, in 3D, is more accurate than the classical smoothed potential that we used for the 2D model:

$$\Phi_P = \begin{cases} -\frac{G\,M_P}{d}\left[\left(\frac{d}{r_{sm}}\right)^4 - 2\left(\frac{d}{r_{sm}}\right)^3 + 2\frac{d}{r_{sm}}\right], & \text{if } d \leq r_{sm} \\ -\frac{G\,M_P}{d}, & \text{if } d > r_{sm} \end{cases}. \tag{3.4}$$

Here, d is the distance from the planet and r_{sm} the smoothing length, which we set to 0.5 R_H, such that the potential will be smoothed if the distance to the planet is less than 0.5 Hill radii. Again, we use a rotating reference frame and add the indirect term $\Phi_{Ind,P} = -GM_P/a_P$ to the potential to account for the acceleration of the star due to the planet. The planet is fixed on its circular orbit and does not accrete in stage II.

We run the model in stage II for 444 orbits, after which we extend the grid in the vertical direction to that of stage III. This will allow us to include a significant portion of the disc wind that will be launched in stage III. After another 40 orbits, we activate the accretion onto the planet, which is detailed in Sect. 3.2.3.2, and branch off the model into the two branches with photoevaporation turned on or off. Photoevaporation is implemented via the temperature parametrisation by Picogna et al. (2019). The details for it are explained in the following subsection. The two branches are then run for another 200 orbits. To trace gas flows in the disc and wind, we add passive scalar tracers after the first 100 orbits of stage III; the details for those are described in Sect. 3.2.3.3.

3.2.3.1 Temperature structure and photoevaporation model

When modelling thermal winds, it is important to accurately determine the temperatures in the wind and at the disc-wind interface. To this end, we implement the temperature parametrisation by Picogna et al. (2019) for a photoevaporative wind driven by EUV + X-ray irradiation from the central star. The parametrisation is derived for a 0.7 $M_\odot$ star that irradiates the disc with the synthetic EUV + X-ray spectrum presented by Ercolano et al. (2008b, 2009) with an X-ray luminosity of $L_X = 2 \cdot 10^{30}$ erg/s. The disc is assumed to have solar abundances (Asplund et al., 2005), depleted according to Savage & Sembach (1996) to account for the gas locked in dust grains. With this setup Picogna et al. (2019) carried out detailed radiative transfer calculations with the gas photoionisation and dust radiative transfer code MOCASSIN (Ercolano et al., 2003, 2005, 2008a), which includes all relevant microphysical processes to self-consistently solve the ionisation and thermal balance of the gas and dust. From the result, they then created a temperature parametrisation that depends only on parameters that are easily accessible during the hydrodynamic simulation: the column number density N_H along the line-of-sight towards the star and the local ionisation parameter $\xi = L_X/nr^2$, where n is the local number density and r the distance to the star. It is applied where the column density is less than $2.5 \cdot 10^{22}$ cm^{-2}, which is the maximum penetration depth of X-rays Ercolano et al. (2009), and it covers the wind and disc-wind interface. At higher column densities, it is assumed that the irradiation from the star is screened and the gas temperatures are coupled to the dust temperatures, which are adopted from D'Alessio et al. (2001). For more details, we refer to Picogna et al. (2019).

The advantage of this parametrisation is that it enables efficient temperature updates during every hydrodynamic timestep while maintaining high accuracy to the full radiative transfer calculation. The disadvantage is that it neglects any additional heating by the planet or its substructures, which could have implications on the gas dynamics, especially close to the planet, e.g. for material that is accreting onto the planet. However, since our Jupiter-mass planet is well in the regime of runaway gas accretion, where the accretion rate is only limited by the amount of gas the disc can supply, the

exact temperature structure and gas dynamics close to the planet are less important. We therefore approximate the temperature in the vicinity of the planet using a simple 1D radial power-law profile with an exponential cut-off that is similar to the profile found by Szulágyi (2017) for a Jupiter-mass planet with a temperature of 4000 K:

$$T(d) = max\left\{ T_{\rm dust},\ 230\ K \cdot \left(\frac{d}{R_H}\right)^{-0.62} \left(1 - \frac{1}{exp(2 - \frac{2d}{R_H}) + 1}\right)\right\}, \tag{3.5}$$

where d is the distance to the planet. Another shortcoming of this approach is that it neglects heating in shaded regions from a diffuse EUV or X-ray field that could change the temperature structure in the planetary gap. To verify that this effect is not strong enough to affect our results significantly, we post-processed our model a posteriori with MOCASSIN to find the temperature structure in the shaded gap region when the diffuse field is accounted for. We present the details of this test in appendix 3.6.1.

3.2.3.2 Gas accretion by the planet

To model the accretion of gas onto the planet, we use a simple method that is similar to the approaches described by D'Angelo & Lubow (2008) and Dürmann & Kley (2017). At each hydrodynamic time step Δt, we remove an amount of gas within 0.5 R_H of the planet, which is given by $\frac{\Delta t}{\tau_{\rm acc}} \int \rho dV$, where $\tau_{\rm acc}$ can be understood as an accretion timescale. We choose $\tau_{\rm acc} = 0.5\ \Omega_P^{-1}$ inside 0.5 R_H and $\tau_{\rm acc} = 0.25\ \Omega_P^{-1}$ inside 0.25 R_H, which means that the accretion is twice as efficient in the inner quarter of the Hill sphere. For simplicity, we only remove the accreted mass from the disc without adding it to the planet, which is justified considering that our simulation will be evolved only for short timescales and the total accreted mass will be small compared to the planet's mass.

This accretion method, while simplistic, is sufficient to estimate accretion rates in the runaway gas accretion scenario that we want to model here. It is not our focus to study the detailed dynamics of accretion flows but to estimate the influence that a wind can have on the accretion rate due to the redistribution of disc material. More accurate modelling would require higher resolution and more sophisticated treatment of the heating and cooling processes in the vicinity of the planet. However, this would be too computationally demanding for our global model.

3.2.3.3 Gas tracers

To trace and quantify the radial redistribution of gas in the models, we add multiple passive scalars Q_k as tracer variables. They obey the advection equation

$$\frac{\delta \rho Q_k}{\delta t} + \nabla \cdot (\rho Q_k \boldsymbol{v}) = 0, \tag{3.6}$$

where k is the index of the tracer, ρ the gas density and $\boldsymbol{v}$ the velocity vector. The tracers are placed between 2 and 10 au in radial bins of width 0.5 au that span the entire vertical and annular domain. This is done by setting $Q_k = 1$ within the radial bin and $Q_k = 0$ elsewhere so that each tracer initially traces 100 per cent of the mass in its bin. We add the tracers only after the first 100 orbits of stage III to ensure that the photoevaporative wind is fully established at their introduction. As a result, the initial amount of mass that they trace differs between the models. To address this problem, we present in our results also a version where we perform our analysis after weighing the PEWIND model with the fraction of the initially traced mass,

$$w_k = \frac{M_{k,\rm NOWIND}}{M_{k,\rm PEWIND}}. \tag{3.7}$$

3.3 Results

In this section, we present the results of our simulations. Unless stated otherwise, or unless we present a temporal evolution, we show averaged quantities calculated from 100 snapshots during the last ten orbits of the simulation (orbit 190 to 200 for the NOWIND and PEWIND models). When mentioning a radius or radial components, we refer to the cylindrical radius (capital R) unless we explicitly refer to the spherical radius (lowercase r).

3.3.1 Surface density structure and evolution

Fig. 3.1 shows the one-dimensional gas surface density evolution for all model stages. It can be seen that in stage one (the initial 2D model), the planet opens up a deep gap over the course of a few hundred orbits. In the middle of the gap, where the planet is located, remains a bump in the surface density from gas accumulating in the circumplanetary region. The surface density reaches a steady state after 600 – 800 orbits.

After 1000 orbits, we extend the model into three dimensions and start stage II. During the first $\approx$ 40 orbits, the surface density adjusts to the new 3D structure before it, too, reaches a steady state. The width and depth of the gap in the 2D and 3D models are similar. After 444 orbits in stage II (marked by the white vertical line in the second panel of Fig. 3.1), we again extend the domain in the vertical direction to allow the disc wind to be included in the next stage. Since the newly created space is virtually empty with the gas density set to the floor density, the model does not need to adjust, which we verify by running it for another 40 orbits.

In stage III, we activate the gas accretion onto the planet and start another model branch, where the temperature parametrisation described in Sect. 3.2.3.1 is also active. We refer to the models with and without photoevaporation by the identifiers PEWIND and NOWIND, respectively. In both models, the surface density bump at the planet's location very quickly disappears as the planet undergoes runaway gas accretion. While there is no change in the width of the gap in either model, in the PEWIND model, the depth of the gap reduces by more than an order of magnitude within less than 30 orbits after the start of stage III.

We present the two-dimensional structure of the stage III models in Fig. 3.2, where it is visible that the reduction of the depth of the gap in the PEWIND model is relatively uniform, almost around the entire azimuth. Only close to the planet, where the gas is following horseshoe orbits, the surface density is lower than in the rest of the gap. Outside the gap, the models remain comparable in their overall disc structure, including the width of the gap and the geometry of the spirals.

In Fig. 3.3, we present the initial 1d gas surface density profile and the azimuthally averaged surface density profiles at the end of every stage in detail. Comparing the profile of the PEWIND model with that at the end of stage III confirms that the gap has become shallower by a factor of $\approx$ 10 and even more when we compare it to the NOWIND model, where the gap has been depleted further by the accreting planet. The width of the gap is not affected. Outside the gap, the surface density stays similar between the 3D models, but the PEWIND model exhibits a slightly reduced surface density between approximately 6.5 and 8 au.

Fig. 3.4 shows a three-dimensional representation of the density in the PEWIND model, overlain by gas streamlines in the disc and wind (white), as well as streamlines that show example paths along which gas can be transported into the planet's Hill sphere (green).

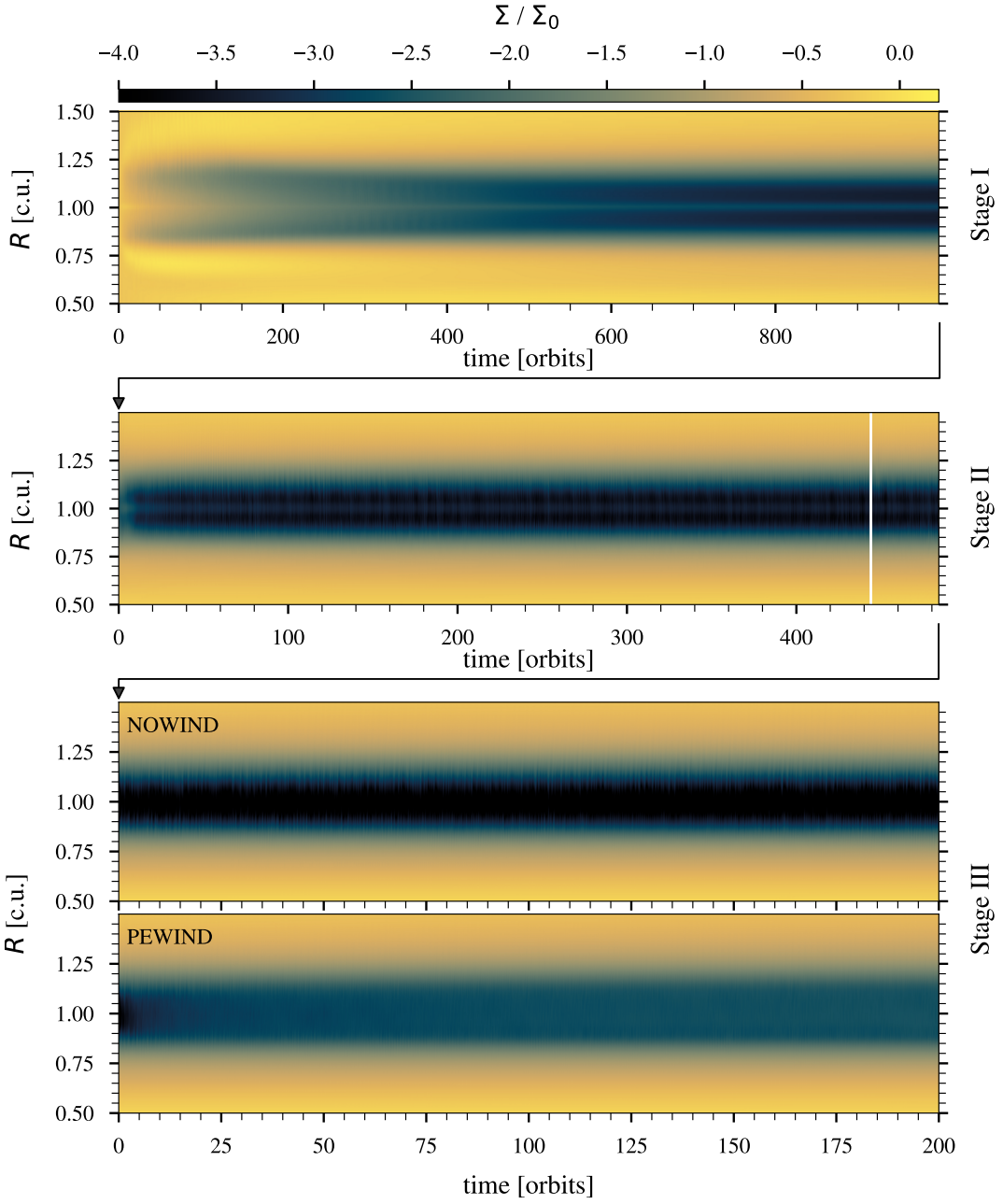

Figure 3.1: Surface density evolution during the different model stages, normalized by the initial surface density profile. From top to bottom: stage I (2D model), stage II (start of 3D model), and stage III with NOWIND and PEWIND model, respectively. The white vertical line in the second panel indicates the time at which the model was vertically extended to the final 3D grid (see Sect. 3.2.3 for details). A black arrow between two panels means that the following stage was started from the end of the previous stage. We note that the scale of the time axis varies between the panels.

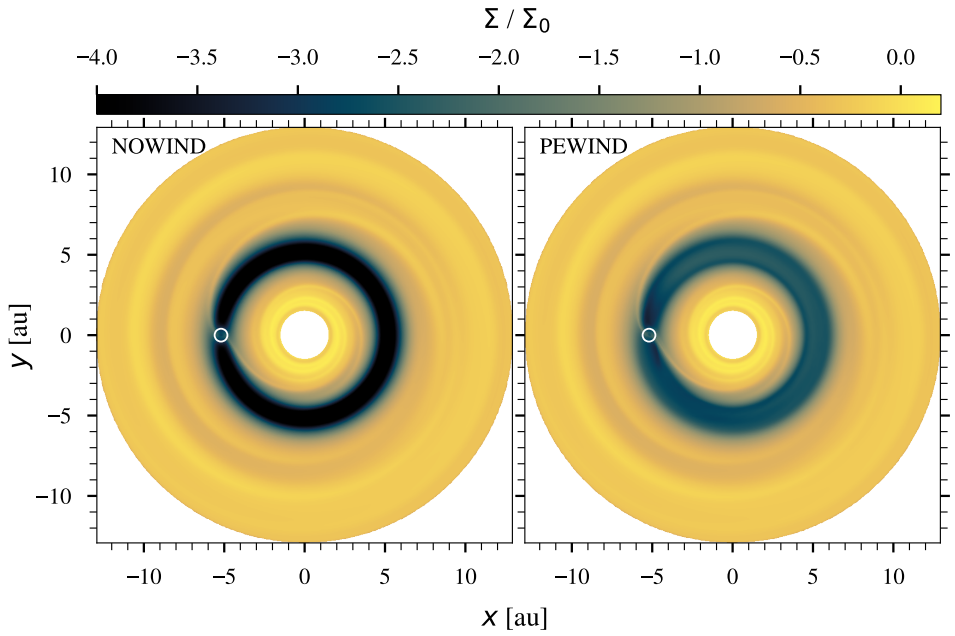

Figure 3.2: Surface density maps of the NOWIND (top panel) and PEWIND (bottom panel) models, normalized by the initial surface density profile. The white dashed circle indicates the Hill sphere of the planet.

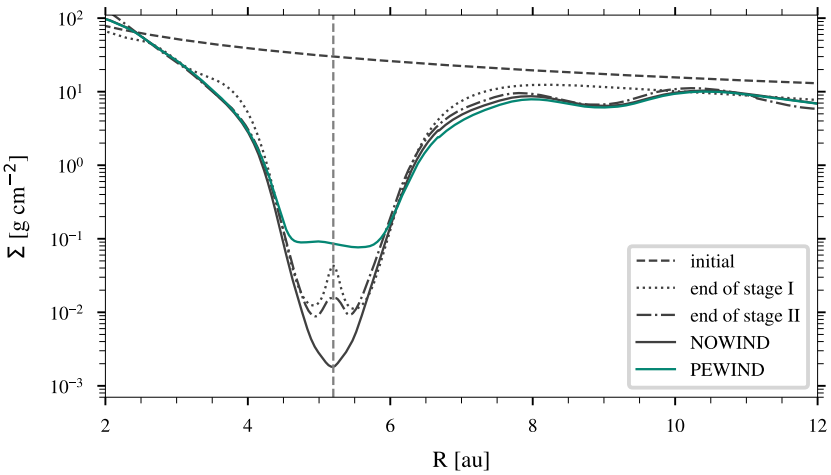

Figure 3.3: Azimuthally averaged 1D surface density profiles. The grey dashed line indicates the location of the planet.

3.3.2 Disc structure

In previous work (Weber et al., 2022), we have found that the planetary substructures, especially a gap in the disc gas, can profoundly affect the structure and kinematics of a photoevaporative wind. In the presence of a gap, the pressure gradient in the wind-launching region and even beyond the gap is significantly altered, and since a photoevaporative wind is a thermal wind driven by pressure gradient forces, the wind itself is strongly affected, too, which we can also observe in our PEWIND model. In this work, we are mainly interested in the implications of this for the disc and the planet. We will only

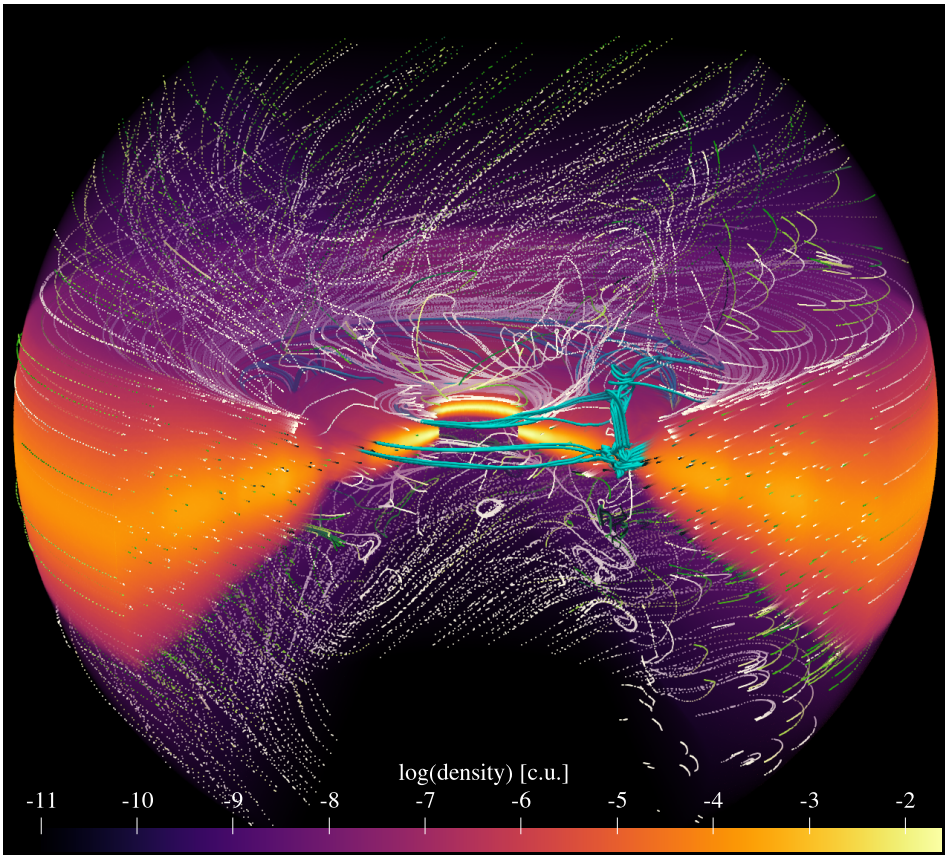

Figure 3.4: 3D visualization of the density in the PEWIND model created from a snapshot a t = 100 orbits. The dotted lines are gas streamlines. Their colour represents the integration time, which is useful for understanding the direction gas follows along the streamline (from white to green). The cyan tubes are gas streamlines traced back from within the planet's Hill sphere and indicate example paths that the gas can take towards the planet.

briefly touch upon the impact on the wind and direct readers to our previous work for more details.

In Fig. 3.5, we show the azimuthally averaged density, pressure and gas temperature structure of the stage III models. The panels in the top row show the density structure, overlain by density contours that indicate the gap profile. The crucial difference between the models is the heating by EUV + X-ray irradiation from the central star that is applied in the PEWIND model via the temperature parametrisation. The panels in the third row show the resulting temperature structure, overplotted by column density contours up to $2.5 \cdot 10^{22}$ cm^{-2}, which is the maximum penetration depth of the X-rays. At the heated surface layers of the disc, the PEWIND model experiences a sharp temperature rise (third row), accompanied by a sharp drop in the gas density, which is in contrast to the NOWIND model, where the density falls off exponentially in the vertical direction. The transition from cold to hot gas can be understood as the transition from the bound disc to the wind-launching region, which happens at column number densities between $2.5 \cdot 10^{21}$ and $2.5 \cdot 10^{22}$ cm^{-2}. A strong pressure gradient develops in this region, pointing away from the disc surface (second row), which can launch a dense wind. However, at the location of the planetary gap, where the density and temperature of the bound disc are low, the pressure is also low. As a result, the pressure gradient is pointing into the gap and no wind is launched from the location of the gap. We will discuss the structure of the wind in more detail in the

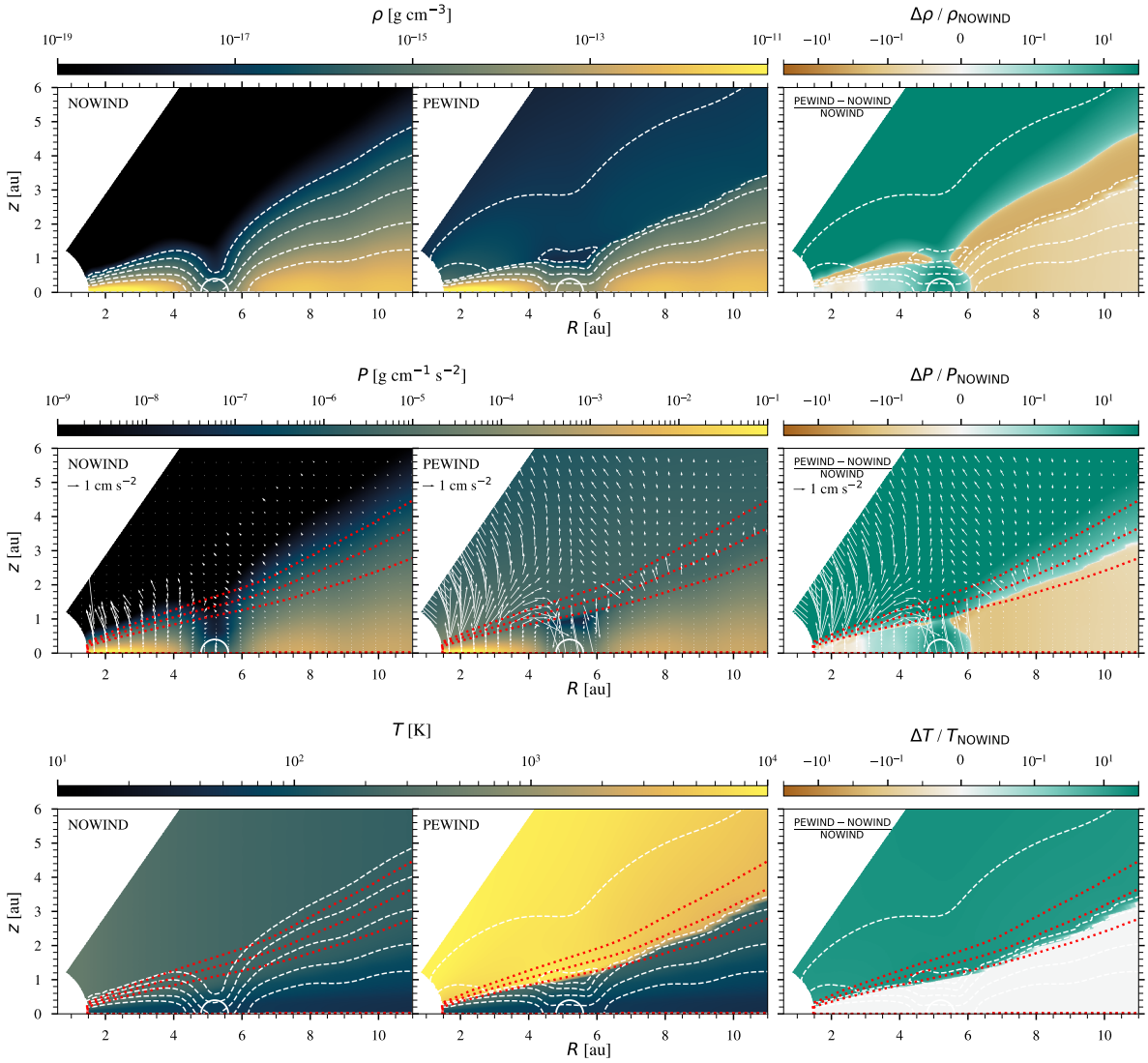

Figure 3.5: From top to bottom: Azimuthally averaged gas density, gas pressure and gas temperature. From left to right: NOWIND model, PEWIND model, and their relative difference. White dashed lines are density contours for (from top to bottom) 10^{-17} to 10^{-13} g cm^{-3} in increments of one order of magnitude. Red dotted lines are column density contours for (from top to bottom) $2.5 \cdot 10^{20}$, $2.5 \cdot 10^{21}$, and $2.5 \cdot 10^{22}$ cm^{-2}. The arrows in the second row represent the pressure gradient force. In the right column, only the contours of the PEWIND model are shown. The white circles indicate the extent of the planet's Hill sphere.

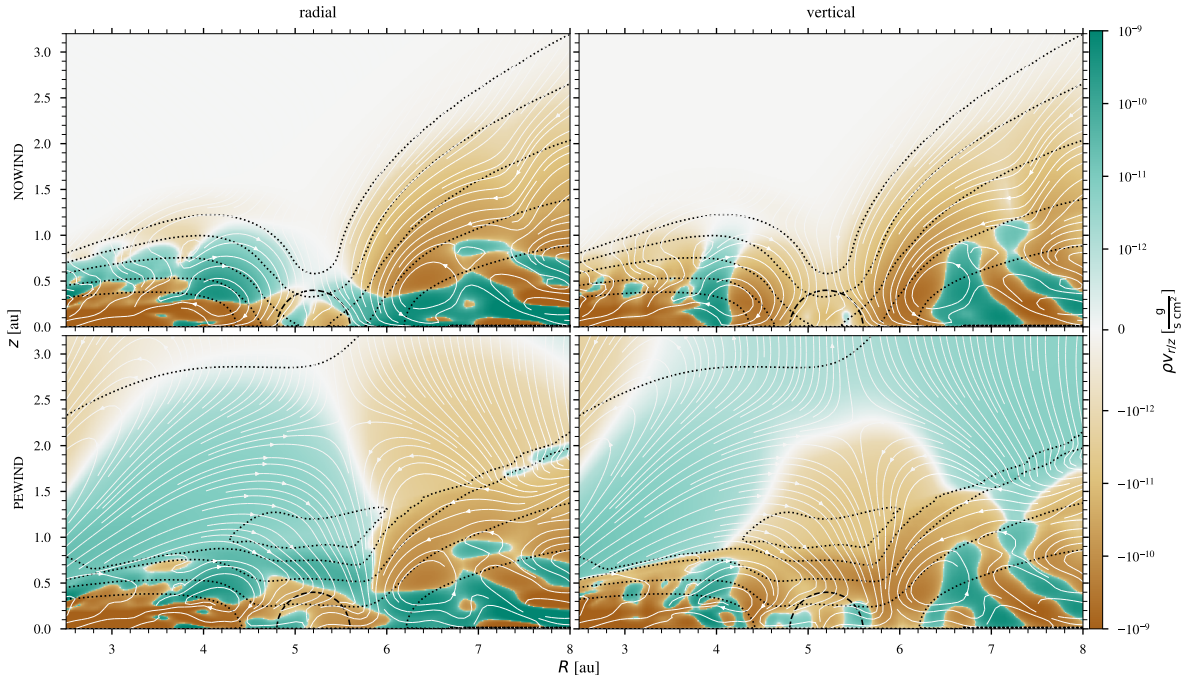

Figure 3.6: Azimuthally averaged radial and vertical mass flux. The dotted black lines are density contours for (from top to bottom) 10^{-17} to 10^{-13} g cm^{-3} in increments of one order of magnitude. The dashed black circles show the Hill sphere of the planet. The white solid lines are streamlines of the gas.

next section.

As seen in the top-right panel, the disc in the PEWIND model has a slightly lower density (by a few per cent) radially outside the gap. This can be explained by the mass that has been redistributed or lost due to the wind during the simulation. We can confirm this with a quick estimation: The measured mass-loss rate due to the wind inside the domain is $\approx 5 \cdot 10^{-9}\ M_\odot\ yr^{-1}$ (see Sect. 3.3.7 for details). If the mass-loss rate were constant, we would expect to have lost $\approx 1.42 \cdot 10^{-5} M_\odot$ during our simulation. The difference in total disc mass between the two models is $\approx 1.37 \cdot 10^{-5} M_\odot$, which corresponds to $\approx$ 2.5 per cent of the mass at the start of stage III, consistent with the percent-level difference in the density in the outer disc. Radially inside of the gap, as already noted in the previous section, the gas density is enhanced, and a region of increased density extends radially towards the star into the inner disc down to $R \approx 3$ au. A possible explanation could be that a fraction of the surplus gas inside the gap is viscously transported radially inward. In that case, the planetary gap would be less efficient in blocking the accretion flows towards the star in a model that includes a photoevaporative wind. We will study the details of this gas redistribution and its implications in the following sections.

3.3.3 Wind structure and gas redistribution

In Fig. 3.6, we present the radial and vertical components of the azimuthally averaged mass flux overlain by the gas streamlines. The kinematic structure of the bound disc is very similar between the models, in agreement with our findings in the previous section that the wind has no significant impact on the bound disc outside of the gap, aside from slight differences in the density. Particularly noteworthy are the meridional circulations that can be seen at the edges of the gap in both models.

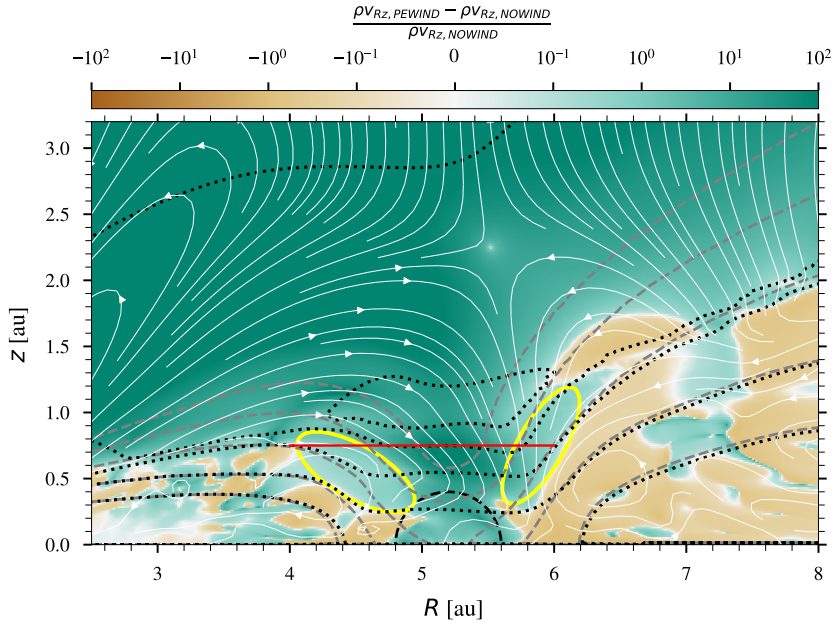

Figure 3.7: Relative difference of the azimuthally averaged mass flux magnitude in the meridional plane. The dotted black lines are density contours of the PEWIND model for (from top to bottom) 10^{-17} to 10^{-13} g cm^{-3} in increments of one order of magnitude. The dashed grey lines are the same contours for the NOWIND model. The red line defines the ring surface through which we calculate the vertical mass flux into the gap. The solid yellow ellipses highlight the gap edges with increased mass-flux in the PEWIND model. The dashed black circle shows the Hill sphere of the planet. The white solid lines are streamlines of the gas in the PEWIND model.

The only exception is inside the gap above the planet's Hill sphere, where the PEWIND model has a lot of additional momentum directed radially outward and downward towards the midplane. This momentum is delivered to the gap by the wind. The streamlines demonstrate that the wind is launched from the disc surface everywhere except at the location of the planetary gap. This leads to a zone of low density and pressure in the wind above the gap, causing the pressure gradient in the surrounding wind to point towards that zone. As a result, material that is launched into the wind from the inner disc is driven towards this zone, where it then falls back into the gap, and the same is true for material launched close to the outer edge of the gap. The two flows then collide above the gap's outer edge, followed by the infall of wind material into the gap. The collision of the opposing flows prevents the direct delivery of gas through the wind across the gap from the inner to the outer disc and vice versa. Instead, mass transport across the gap happens only after the gas is delivered to the gap and subsequently pushed towards the edges by the planet's torque.

It is important to notice that this effect is entirely dominated by the presence of the gap and its implications on the pressure field and not due to the gravitational potential of the planet, which is negligible at the height of the disc surface. This means that the described behaviour is similar around the entire azimuth and not limited to locations close to the planet.

Above the gap, at heights $z \approx 2$ au, is a turning point where the wind turns vertically upwards again, which is further reassuring that the wind structure in this region is not significantly affected by reflections at the open polar boundary.

In addition to the gas that is delivered to the gap through the wind, the PEWIND model also has

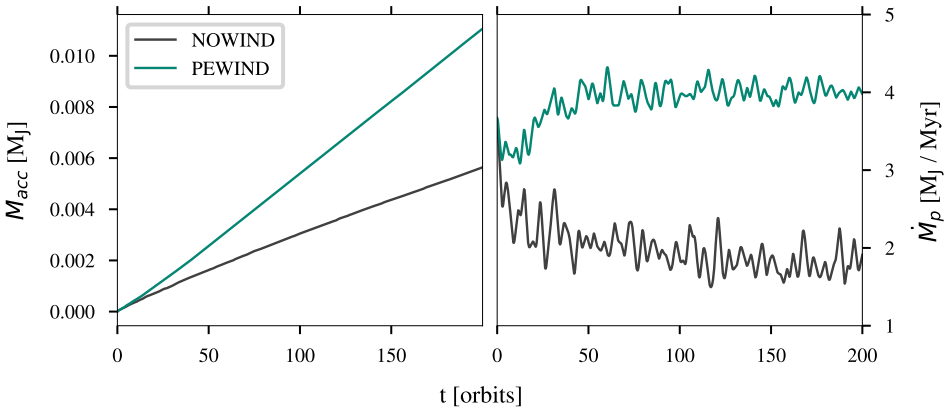

Figure 3.8: Amount of mass accreted by the planet (left) and mass accretion rates onto the planet (right).

an increased radial and vertical mass flux directly at the gap edges. This can be seen better in the relative difference of the mass flux magnitude within the meridional plane, which we show in Fig. 3.7, where we marked these regions with yellow ellipses. The increased flux in these regions is likely due to a combination of additional gas delivered by the wind and increased acceleration towards the gap by thermal pressure from the heated disc surface. Moreover, as discussed in the previous section, the gas density is increased in the PEWIND model radially interior to the gap. Consequently, the inner meridional flow carries more mass than in the NOWIND model, which is delivered into that region. At the outer gap, the opposite effect would be expected, but the decrease in mass is outweighed by the mass delivered through the wind and the enhanced acceleration.

These delivery paths combined result in a significant flux directly above the planet's corotation region, that flows towards the outer edge of the gap and vertically towards the midplane. To quantify the amount of extra mass that is delivered through these pathways, we calculate the mass-flux through a ring surface defined by the red line in Fig. 3.7. This surface spans across the gap, starting and ending where the 10^{-15} g cm^{-3} density contours of both models meet, which roughly coincides with the borders of the region of enhanced mass-flux in the PEWIND model. For the PEWIND model, we find a rate of $\dot{m}_{\mathrm{gap,v}} \approx 10.7\ M_J\, Myr^{-1}$ ($\approx 1.0 \cdot 10^{-8}\ M_\odot\, yr^{-1}$) flowing through this surface into the gap, compared to $\approx 2.1 M_J\, Myr^{-1}$ ($\approx 2.0 \cdot 10^{-9}\ M_\odot\, yr^{-1}$) in the NOWIND model. We list the most important quantities measured in our models in table 3.3. We note that this measurement does not give an accurate picture of the total mass that flows into and out of the gap in both models, as it does not account for flows below this surface. Instead, it serves to estimate the amount of gas delivered from the vertical direction.

3.3.4 Accretion onto the planet

As discussed in the previous sections, the depth of the planetary gap is reduced in the PEWIND model by more than an order of magnitude. Therefore, the amount of mass available for accretion onto the planet is significantly increased. In Fig. 3.8, we present the temporal evolution of the accreted mass and the accretion rates onto the planet in both models, measured as the amount of mass removed from inside the Hill sphere, as described in Sect. 3.2.3.2. After 200 orbits, the planets have accreted $5.6 \cdot 10^{-3}\ M_J$ and $11.1 \cdot 10^{-3}\ M_J$ in the NOWIND and PEWIND models, respectively. For the mean accretion rate during the last 50 orbits, we measure $M_P \approx 1.8\ M_J Myr^{-1}$ and $4.0\ M_J Myr^{-1}$, showing that the accretion rate in the PEWIND model is more than twice the rate in the NOWIND model. While

significant, this increase in the accretion rate is much lower than the order of magnitude increase of the surface density in the gap. However, as discussed in Sect. 3.3.1, the density in the gap is not constant along the entire azimuth. It can be seen in Fig. 3.2 that very close to the planet, the density is lower than far away from the planet. This is because the gas within the coorbital region follows horseshoe orbits and does not necessarily reach the planet's Hill sphere. In fact, the majority of the gas that reaches the Hill sphere usually does so from the vertical direction (D'Angelo et al., 2003), but the specific dynamics close to the planet and the structure of the circumplanetary disc depend strongly on the thermodynamics in the circumplanetary region (e.g. Szulágyi et al., 2016), which we model only in the very basic manner described in Sect. 3.2.3.1. Our measured accretion rates can, therefore, only provide a rough approximation. It is nevertheless clear that photoevaporation increases the amount of mass available for accretion.

In the right panel in Fig. 3.8, it can be seen that the planets in both models accrete with the same rate at the start of stage III, but while in the NOWIND model, the rate quickly drops after the initially available circumplanetary material is accreted, in the PEWIND model, photoevaporation can sustain the initial accretion rate already after only a few orbits before the accretion rate increases to its final value which is reached after $\approx$ 50 orbits.

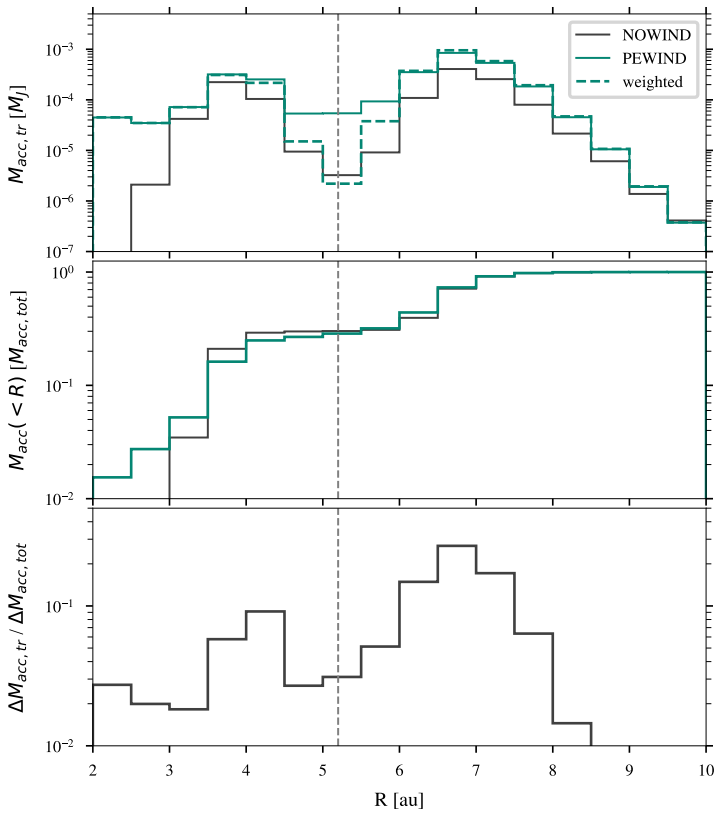

Figure 3.9: Top panel: Contribution of the radial bins to the mass accreted by the planet, traced with passive scalars introduced at t=100 and evaluated at t=150 orbits. The dashed line shows the profile of the PEWIND model, weighted to account for the discrepancy in the initial amount of mass traced in each bin. Middle panel: Cumulative radial profile. Bottom Panel: Contribution fraction of each radial bin to the additionally accreted mass in the PEWIND model. The grey vertical lines indicate the location of the planet.

To study which parts of the disc contribute most to the mass that the planet accretes, we added passive scalars to our simulations, allowing us to trace gas flows and determine the origin of the accreted gas. Starting at orbit 100, we placed 16 passive scalars as tracers in radial bins of 0.5 au width between 2 and 10 au. The bins span the entire verticle extent of the disc. Fig. 3.9 shows the contribution of each radial bin to the accreted mass, the cumulative radial profile, and the fraction that each tracer contributes to the difference of total accreted mass between the models, all evaluated at orbit 150. Since we place the tracers starting only at orbit 100, where there are already density differences between the models, the tracers do not trace the exact same amount of mass between the models. However, this is only significant inside the gap, where the density difference is considerable. To show this, we also present the contribution of the radial bins in the PEWIND model after weighting them by the initially traced mass, which represents the most extreme case and can be considered a limiting case. This is shown as the dashed line in the top panel of Fig. 3.9. As is evident from the figure, the planet in the PEWIND model can accrete more material than in the NOWIND model from all radial bins up until 9.5 au, beyond which it accretes slightly less than in the NOWIND model. This is consistent with the wind being less efficient in delivering material towards the gap from larger radii outside of the gap because, at large radii, the influence of the gap decreases up until the point where the wind is launched radially outward again, as would be expected if there was no gap.

A particularly notable difference between the models is the contribution of the bins at $R < 3\ au$: It can be seen from the cumulative profile that in the PEWIND model, ≈ 3 per cent of the total accreted mass originates inside three au, in contrast to the NOWIND model where there is no significant contribution from inside that radius.

3.3.5 Planet Migration

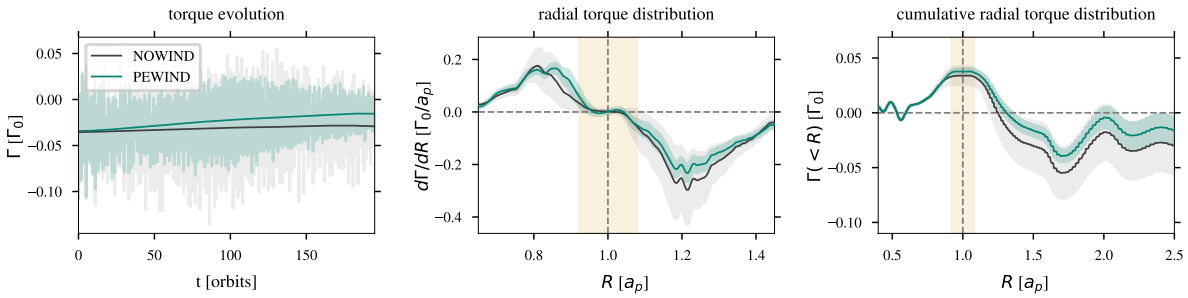

Figure 3.10: Torque evolution (left panel), radial torque distribution (middle panel) and cumulative radial torque (right panel). The temporal evolution was smoothed with a Gaussian kernel over ten orbits to make the plot more readable, and the shaded area indicates the spread of the actual samples. In the other panels, the shaded area indicates the standard deviation from the mean, calculated from 1000 samples between orbit 190 and 200. The yellow vertical band marks the extent of the planet's Hill sphere, and horizontal and vertical dashed lines indicate the zero point and the planet's location, respectively.

During our simulations, we also calculate the disc's gravitational torque that is acting on the planet by integrating over the entire disc, where we follow Crida et al. (2008) and Kley et al. (2009) to apply a tapering function

$$f_\Gamma(d) = \left[exp\left(-\frac{d/R_H - b}{b/10} \right) \right], \tag{3.8}$$

with d being the distance from the planet and $b = 0.8$ a torque cut-off radius in units of R_H. This ensures that contributions from gas that is gravitationally bound to the planet are ignored, which is important because, in a more realistic model that does not neglect self-gravity, this gas should experience the same torque as the planet and therefore be considered a part of it.

During our analysis of the torques, we use the standard normalization (Paardekooper et al., 2010)

$$\Gamma_0 = \Sigma_p \Omega_p^2 a_p^4 \left(\frac{M_P}{M_*}\right)^2 h^{-2}. \tag{3.9}$$

The left panel of Fig. 3.10 shows the temporal evolution of the torque. Initially, the magnitude of the torques decreases over time in both models, but the decrease is faster in the PEWIND model. After ≈ 100 orbits, the torque appears to reach a steady state in the NOWIND model, while it decreases further in the PEWIND model, albeit at a slightly reduced rate. At the end of stage III, the torque in the PEWIND model is reduced almost by a factor of 2. If we assume that the torque remains constant in the NOWIND model, we can estimate the migration timescale

$$\tau_M = \frac{a_p}{|\dot{a}|} = \frac{J_p}{2\Gamma} = \frac{M_p a_p^2 \Omega_p}{2\Gamma}, \tag{3.10}$$

where J_p is the planet's angular momentum. Evaluating the timescale for the NOWIND model, we find $\tau_{M,\text{NOWIND}} \approx 5.3 \cdot 10^5\ yr$. For the PEWIND model, we find $\tau_{M,\text{PEWIND}} \approx 9.9 \cdot 10^5\ yr$; however, the torque will likely continue to decrease in this model, slowing down the migration even more.

As is best visible in the cumulative torque and the radial torque distribution, most of the difference between the models arises between 0.8 and 1.4 a_p, which corresponds to 4.16 and 7.28 au, but only a minor contribution comes from inside the corotation region, defined by the extent of the Hill sphere (marked yellow in the figure). The difference can likely be explained by the enhanced density observed radially interior to the gap in the PEWIND model (see Sect. 3.3.2), leading to a higher positive torque around $R = 0.9\ a_p$. The same argument holds the other way around: Radially outside the gap, the density is smaller, leading to a weaker negative torque around $R = 1.2\ a_p$.

3.3.6 Mass transport across the gap

The transport of mass across a deep planetary gap can significantly be reduced by an accreting planet, depending on how efficient the planet is in accreting the gas that is supplied from disc (e.g. Lubow & D'Angelo, 2006). It was proposed in the past that this could lead to the starvation of the inner disc, resulting in an accelerated dispersal of the inner disc, which could start the transition disc phase, where a photoevaporative wind quickly evaporates away the then fully exposed inner edge of the gas cavity (Alexander & Armitage, 2009; Rosotti et al., 2013). This process is often called planet-induced photoevaporation (PIPE). Using our three-dimensional models, we can investigate this scenario in full detail, taking into account not only the mass loss but also the redistribution of gas by the wind.

In Fig. 3.11, we present the mass rates crossing the gap either from the outside in or vice versa. The rates are calculated using our radially binned passive scalar tracers. Gas originating in a particular bin is considered to have crossed the gap if transported across the bin between 5.0 and 5.5 au (shaded in grey in the figure). In the NOWIND model, the total rates of inward and outward transport are $\dot{m}_{\text{cross,in}} \approx 2.0 \cdot 10^{-10}\ M_\odot\ yr^{-1}$ and $\dot{m}_{\text{cross,out}} \approx 6.1 \cdot 10^{-11}\ M_\odot\ yr^{-1}$, respectively. The PEWIND model has increased rates by factors of 5.4 and 5.1 with $9.9 \cdot 10^{-10}\ M_\odot\ yr^{-1}$ and $3.3 \cdot 10^{-10}\ M_\odot\ yr^{-1}$, respectively. If we use the simple estimation for the steady state accretion rate onto the star in an unperturbed disc, $\dot{m}_{acc} = 3\pi\nu\Sigma$ with $\nu = \alpha c_s H$ and $H = \frac{c_s}{\Omega}$, we find $\dot{m}_{acc} \approx 6.6 \cdot 10^{-10} M_\odot\ yr^{-1}$.

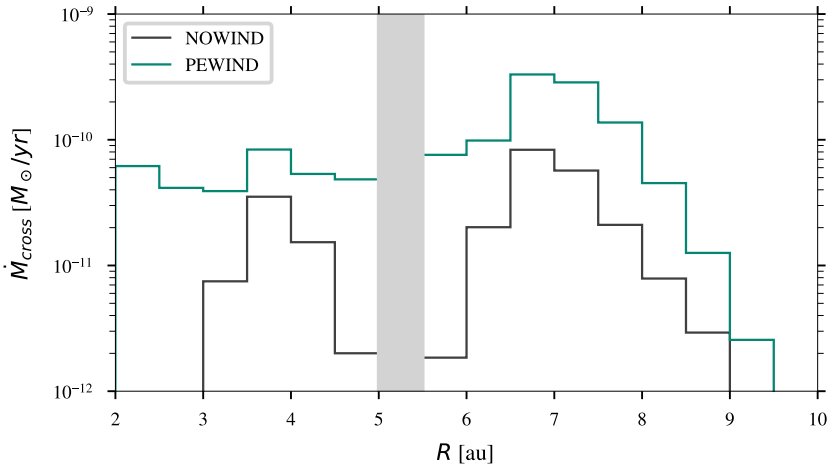

Figure 3.11: Contribution of the radial bins to the rate of mass crossing the gap either outward (if to the right of the grey shaded area) or inward (if to the left of it).

This rate is exceeded in the PEWIND model, while in the NOWIND model, only $\approx$ 30 per cent of it can be sustained. Moreover, we note that our reported values should be considered lower limits because our tracers are only placed between 2 and 10 au and mass further inside or outside is ignored in this calculation. In particular, this could affect the outward transport rates of the PEWIND model, as the rates are still high for the innermost radial bin between 2 and 2.5 au. Photoevaporation usually cannot launch a wind very close to the star ($R \lessapprox 2$ au) because the pressure gradients are not strong enough for the resulting force to overcome the strong gravitational force in the innermost regions of the disc. However, it is nevertheless possible for gas from the inner disc to be pushed outward along the disc surface and later be picked up by the wind, a process that is facilitated by the presence of a gap that increases the pressure gradient in the radial direction (see also Weber et al., 2022).

In Sect. 3.3.3, we have seen that the wind cannot deliver material across the gap directly, because it collides with the opposing wind from the other side of the gap, leading to the infall of wind material into the gap. However, the material delivered into the gap can indirectly cross the gap, when the torque from the planet pushes the material towards the edges of the gap, from where it can subsequently diffuse viscously. To provide a more intuitive picture, we visualized the two flows from the outer and inner disc in appendix 3.6.2, where we show three different snapshots of the innermost tracer in Fig. 3.15 and of a tracer near the outer gap edge in Fig. 3.16. Since the disc is viscously accreting onto the star, gas at the outer edge of the gap is not effectively transported farther outwards. Instead, it accumulates at the edge of the gap. In Fig. 3.12, we show the gas density traced by the tracer originating in our innermost radial bin between 2 and 2.5 au. Between R = 6.5 and 7.5 au, at the location of the meridional flow, the traced gas appears to accumulate, with the tracer density quickly falling off at larger radii.

3.3.7 Wind mass-loss rate and profile

In Fig. 3.13, we show the azimuthally averaged surface mass-loss profile in the PEWIND model. The profile was calculated from the mass flux measured through the surface that is 0.4 au above the surface where the temperature gradient reaches its maximum (the transition from blue to yellow in Fig. 3.5). Consistent with the streamlines discussed in the previous section, the profile shows an infall of mass between 4 and 6.4 au. For comparison, we also show the surface mass-loss profile of the unperturbed

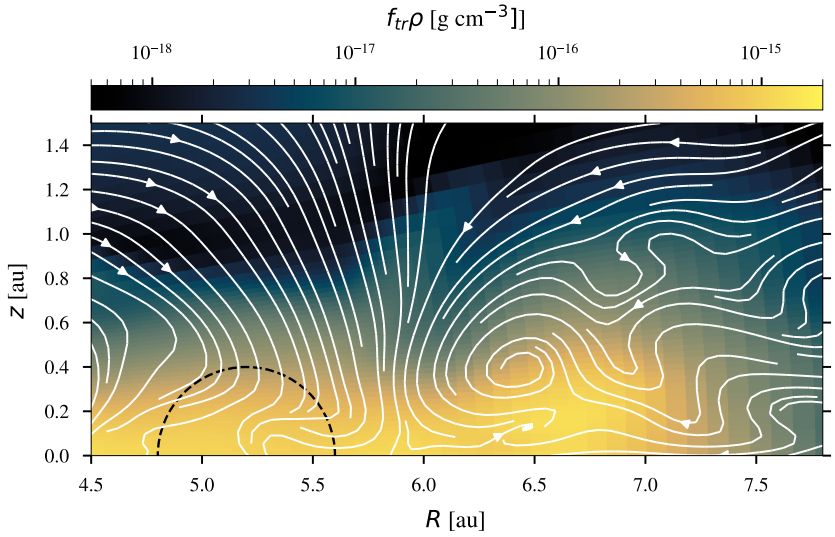

Figure 3.12: Closeup view of the outer gap edge, showing the density of gas traced by the innermost tracer, i.e. of gas that originated between $R = 2$ and 2.5 au and was transported across the gap. Solid white lines are streamlines, and the black dashed circle indicates the extent of the planet's Hill sphere.

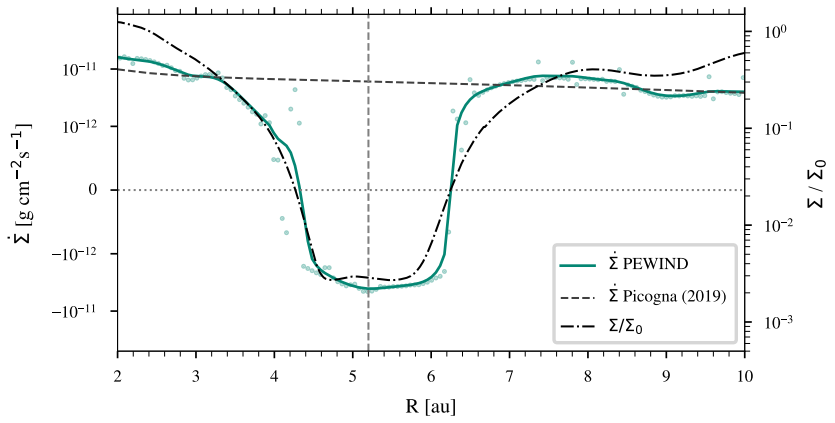

Figure 3.13: Azimuthally averaged surface mass-loss profile of the PEWIND model. The coloured circles indicate the individual samples and the green solid line is obtained by smoothing the samples using a Gaussian kernel with $\sigma = 3$. The black dashed line shows the surface mass-loss profile of the primordial disc by Picogna et al. (2019), which does not have any substructures; the vertical dashed line indicates the planet's location. The black dashed-dotted line shows the 1d surface density profile.

Table 3.3: Overview of the most important quantities measured in the models.

Quantity	Description	NOWIND	PEWIND	Unit
$\dot{M}_P$	accretion rate onto the planet	$1.8 \cdot 10^{-6}$	$4.0 \cdot 10^{-6}$	$M_J yr^{-1}$
$\dot{m}_{\mathrm{gap,v}}$	mass-flow vertically into the gap	$0.2 \cdot 10^{-8}$	$1.0 \cdot 10^{-8}$	$M_\odot yr^{-1}$
$\dot{m}_{\mathrm{cross,in}}$	mass-flow inwards across the gap	$2.0 \cdot 10^{-10}$	$9.9 \cdot 10^{-10}$	$M_\odot yr^{-1}$
$\dot{m}_{\mathrm{cross,out}}$	mass-flow outwards across the gap	$0.6 \cdot 10^{-10}$	$3.3 \cdot 10^{-10}$	$M_\odot yr^{-1}$
$\dot{m}_{\mathrm{wind}}(2\ au \leq R \leq 10\ au)$	wind mass-loss rate between 2 and 10 au		$4.1 \cdot 10^{-9}$	$M_\odot yr^{-1}$
$\dot{m}_{\mathrm{wind}}(R < 5.2\ au)$	wind mass-loss rate inside 5.2 au		$1.1 \cdot 10^{-9}$	$M_\odot yr^{-1}$
τ_M	migration timescale	$5.3 \cdot 10^5$	$9.9 \cdot 10^5$	yr

primordial disc in Picogna et al. (2019). Although there are differences in the initial conditions between their setup and ours (primarily in disc mass and viscosity), and they use a different method to calculate the mass-loss profiles, the profiles should be robust against these differences since the wind mass-loss profile is mainly dependent on the X-ray spectrum and luminosity, the stellar mass and the disc aspect ratio, all of which we adopted from their model. Indeed, the two profiles reach similar mass-loss rates far away from the planetary gap. The total rate for mass that is lost through this surface (and not falling back) is $\dot{m}_{\mathrm{wind}} \approx 5.2 \cdot 10^{-9}\ M_\odot yr^{-1}$. However, since the mass-loss close to the domain boundaries can be affected by the wave-dampening we apply, we limit our analysis to the radial range between 2 and 10 au, where the model experiences a wind mass-loss rate of $\approx 4.1 \cdot 10^{-9}\ M_\odot yr^{-1}$. Of that, $\approx 1.1 \cdot 10^{-9}\ M_\odot yr^{-1}$ is lost inside the planet's orbit. In the same radial range, the surface mass-loss profile of Picogna et al. (2019) yields a rate of $\approx 6.4 \cdot 10^{-9}\ M_\odot yr^{-1}$ of which $\approx 2.5 \cdot 10^{-9}\ M_\odot yr^{-1}$ are lost inside 5.2 au. The total rate for mass falling back into the gap is $\approx 7.4 \cdot 10^{-10}\ M_\odot yr^{-1}$. We note that this infall rate only includes gas lifted by at least 0.4 au from the surface and does not include material transported into the gap while staying below that threshold. It is therefore much lower than the rate we found in Sect. 3.3.3.

3.4 Discussion

3.4.1 Inner disc lifetime and PIPE

As shown in the previous sections, a significant fraction of the wind launched from the inner disc is recycled by falling back into the gap and then transported inwards again. In consequence, the wind mass-loss rate in the inner disc is reduced by a factor ≈ 2.5 to $\approx 1.1 \cdot 10^{-9}\ M_\odot yr^{-1}$ (see Sect. 3.3.7). Additionally, due to the increase of mass that is loaded into the gap from outside of the planet's orbit and then pushed by the planet's torque towards the edges of the gap, an inward mass transport across the gap is sustained at a rate of $\approx 10^{-9}\ M_\odot yr^{-1}$ (see Sect. 3.3.6). This rate is about 50 per cent higher than the viscous accretion rate in the unperturbed disc despite the presence of a strongly accreting planet. If we assume that all rates remain constant and that the star always accretes gas at the viscous rate, $\dot{m}_{\mathrm{visc}}$, we can make a simple estimate of the lifetime of the inner disc, τ_{inner}:

$$\tau_{\mathrm{inner}} = \frac{M_{\mathrm{inner}}}{\dot{m}_{\mathrm{visc}} + \dot{m}_{\mathrm{wind}}(R < 5.2\ au) - \dot{m}_{\mathrm{cross,in}}}.$$

M_{inner} is the mass of the inner disc. This is, of course, not an accurate estimate. In reality, the rates will not remain constant over the entire lifespan. For example, the accretion rate decreases with decreasing density. But it is still useful for a comparison between the different models. In the case without a planet, we assume that $\dot{m}_{\mathrm{cross,in}} = \dot{m}_{\mathrm{visc}}$, so that the mass accretion rate onto the star balances the

resupply from the outer to the inner disc and the inner disc mass decreases with the wind mass-loss rate. The inner disc would then be dispersed after only 80 kyr. In the PEWIND model, the lifetime would be extended by more than a factor of 3 to 260 kyr. In the NOWIND model, the inner disc would be accreted by the star within 455 kyr. If the planetary gap acts as a filter for the dust in the disc, the increased lifetime of the inner gas disc could potentially explain the higher-than-expected occurrence rate of observed accreting transitions discs with large dust cavities (e.g. Ercolano & Pascucci, 2017).

The prolonged lifetime of the PEWIND model compared to a model with no planet is opposite to the expectation in the proposed planet-induced photoevaporation (PIPE) scenario (Alexander & Armitage, 2009; Rosotti et al., 2013), which is based on the assumption that a gap-opening planet reduces the rate of viscous mass-transport to the inner disc. Hydrodynamic simulations show that planets typically reduce the mass flow across the gap to 10 – 25 per cent of the viscous steady-state accretion rate (Lubow & D'Angelo, 2006). Considering the wind recycling and the additional mass-loading across the gap, PIPE can only operate if this reduction exceeds the effects of the wind-driven redistribution, which could be the case for more viscous discs with higher accretion rates.

The effects of the gap on the photoevapoative wind depend primarily on the width of the gap, which increases with increasing orbital radius and decreasing planet-to-star mass ratio, disc scale height and viscosity (Kanagawa et al., 2015). We therefore expect the effects to be more substantial if the disc is less viscous, the planet more massive, or the orbit larger. However, the exact relation between the width of the gap and the size of the affected wind region is unclear because the latter also depends on the temperature and density gradients in the wind itself, which are not scale-invariant so that more models would have to be run to make accurate predictions.

3.4.2 Observational signatures

In a companion work Weber et al. (2022) have studied the effect that the modified wind structure has on the spectral line profiles of forbidden emission lines that are commonly used as disc wind tracers (e.g. OI 6300 Å). They found that while the region above the gap, where the kinematics of the wind is affected the most, is not very well traced by the wind, the asymmetric substructures that are generated by the planet do leave an imprint in the wind that can cause variations in the line profiles that could be observed with high spectral resolution ($R \approx 100\,000$). Most notably, the peak of the line profiles can move between the blue- and the redshifted parts of the spectrum on timescales of less than a quarter of the planet's orbit.

In recent years, molecular line observations with ALMA have very successfully been used to detect kinematic signatures of planets via the distortion of the disc's gas flow (e.g. Pinte et al., 2018; Teague et al., 2019a; Wölfer et al., 2023; review by Pinte et al., 2022b). In particular, it has become possible to map the 3D gas flow in the vicinity of the planet and, by doing so, to reveal exciting signatures, for example, of meridional flows (e.g. Teague et al., 2019a; Yu et al., 2021). Galloway-Sprietsma et al. (2023) even found evidence for an upward flow arising from the location of the gap of AS 209, which could be evidence for a disc wind. In light of these new possibilities, investigating our photoevaporative wind's effect on these observations would be extremely interesting. Unfortunately, the spatial resolution of the observations currently limits this kind of analysis to planets at larger separations than that in our model. However, we will present in a future work synthetic observations of our model with a planet at a larger distance from the star to investigate the effect that photoevaporation has on the kinematic signatures of the planet.

One of our main findings in this work is that the photoevaporative wind refills the gap, reducing its depth by more than an order of magnitude. This possibility should be considered when inferring disc or planet properties, such as the viscosity parameter α or the planet's mass from observed gap depths

(e.g. Kanagawa et al., 2015; Liu et al., 2018).

3.4.3 Mixing and reprocessing of disc material

Our results show that a photoevaporative wind can redistribute material from the inner disc towards the gap and the circumplanetary region, from where it can be accreted by the planet or accumulate near the meridional flows at the gap edges. This could have significant consequences on the gas composition near the gap or in the planet's atmosphere because the gas in the inner disc is expected to have a different composition than that in the outer disc. For example, inward-drifting and evaporating pebbles can significantly enrich the inner disc with volatile vapour (e.g. H_2O inside the water snowline) (Booth et al., 2017; Schneider & Bitsch, 2021). If it is then transported through the wind towards the planet, this could enrich the planet's atmosphere with heavy elements, even if the planet is located beyond the respective snowlines of the volatiles. Such enrichment is not only observed for most hot-Jupiters (Thorngren et al., 2016) but also for the giant planets in the solar system, which all have an enhanced heavy element mass-fraction compared to the solar value (e.g. review by Guillot et al., 2022).

It should also be considered that when gas or dust is transported through the wind or along the disc surface, it is subject to a high-temperature environment with highly energetic EUV or X-ray irradiation from the central star. This allows for a reprocessing of the material that is impossible in the disc's interior. One such process is isotope selective photodissociation, an essential mechanism for isotope fractionation, especially for oxygen and nitrogen isotopes (Visser et al., 2009; Furuya & Aikawa, 2018; review by Nomura et al., 2022). Isotopic ratios are valuable tools for tracing the chemical evolution and origin of objects in our solar system. However, to link them to planetary formation theories, it is necessary to take into account the environment that the gas and dust were already subject to in the protoplanetary disc.

Besides the gas, photoevaporation could also help redistribute small dust grains in the disc. Using the same photoevaporation model as in our model, Franz et al. (2020, 2022) have shown that the photoevaporative wind can entrain dust grains with a size of up to $\approx 11\ \mu m$. This depends strongly on the amount of small grains that are available on the disc surface, thus on the degree of vertical mixing in the disc, for example, by the vertical shear instability (VSI) (e.g. Flock et al., 2017, 2020). In Sect. 3.3.3, we have also seen that the meridional flows, where some of the redistributed material accumulates, contribute significantly to mass delivery into the gap. They could also stir up dust grains from the midplane towards the surface, where they could undergo further reprocessing.

Addressing the above points will require the detailed post-processing of our model to calculate the chemical evolution of the gas and, ideally, the dust. While this is out of scope for this work, the model presented here can serve as the basis for future investigations.

3.4.4 Comparison with magnetic wind models

Several studies that have been published recently have investigated the interplay between planet-hosting discs and magnetic winds. In particular, Aoyama & Bai (2023) and Wafflard-Fernandez & Lesur (2023) independently found that the magnetic field lines concentrate in the gap and are deflected by the planet such that a magnetic wind is driven most dominantly from the outer edge of the gap. This is in contrast to our findings with a photoevaporative wind, which promotes a vertical infall into the gap also at the outer edge. As we find in our model, Wafflard-Fernandez & Lesur (2023) report reduced migration rates of the planet in the presence of an MHD wind, a result of their gap becoming asymmetric with the outer gap being deeper radially outside of the planet than inside. Aoyama & Bai (2023) also found that the gaps become deeper and wider in their MHD simulations.

It is likely that, in reality, disc winds are not either purely magnetic or purely thermal, but both mechanisms operate simultaneously, and their relative importance may vary with the evolutionary stage of the disc (e.g. Pascucci et al., 2020). In that case, a magnetic wind could act against the infall of a thermal component in the wind if it is strong enough to overcome the inverted thermal pressure gradient and sustain the wind above the gap. However, if the magnetic wind cannot completely prevent the infall, some of the effects observed in both models could amplify each other. For instance, the reduced migration rate is observed with both types of winds. It is also expected that with wider gaps, a larger volume of the wind is affected. Wind models that combine both (non-ideal) magnetohydrodynamic effects and photoevaporation currently exist only for 2D axisymmetric discs without planets, but they still provide very useful insights into the wind-launching processes.

Wang et al. (2019) developed non-ideal MHD disc wind models including self-consistent thermochemistry. They found that their magnetothermal wind is predominantly launched by the magnetic toroidal pressure gradient and that radiative heating affects the wind launching only weakly, although the mass-loss rate of their wind depends on the ionisation fraction near the wind base and is thus moderately affected by the luminosity of high-energy radiation, mainly soft-FUV and Lyman-Werner photons. In their model, the X-ray luminosity affects the accretion rate rather than the wind mass-loss rate. However, they only include 3 keV X-ray photons, and as was shown by Ercolano et al. (2009), the heating in the wind-launching region is by far dominated by the soft X-ray band (< 1 keV). In a similar model with more complete radiation physics (but still mainly focused on FUV-driven processes), Gressel et al. (2020) found a wind that is launched magnetocentrifugally rather than by magnetic toroidal pressure, so the mass loss is also only moderately affected by thermochemical effects. In both cases, the dynamics of the magnetic wind do not depend strongly on the thermal pressure, and its behaviour in the presence of a gap would depend on the impact of the gap on the magnetic field.

Other models indicate that thermal pressure may play an important role even in the presence of a magnetothermal wind: Rodenkirch et al. (2020) modelled a wind that includes ohmic diffusion as a non-ideal MHD effect and implements the same temperature and ionisation parametrisation by Picogna et al. (2019) that is used in this work. They found that photoevaporation is the dominant launching mechanism for weak magnetic fields with a plasma parameter $\beta > 10^7$. With a different model that includes all non-ideal MHD effects and again the same temperature parametrisation, Sarafidou et al. (2024) recently found that while the inner regions of the disc ($R \leq 1.5$ au) are always dominated by magnetic winds, photoevaporation can dominate the mass loss at larger radii for stronger magnetic fields ($\beta \geq 10^5$ or even stronger), depending on the X-ray luminosity. Moreover, they found that beyond the footpoint of the wind, it is generally sustained thermally rather than magnetically. In that case, the thermal pressure may dominate over the magnetic field in the region above the gap where the pressure gradient is inverted, such that the infall is sustained against the magnetic wind, especially from the inner disc, considering the magnetic wind is expected to be weaker at the inner edge of the gap. However, without detailed models of non-ideal magnetothermal winds in protoplanetary discs with gaps, the outcome of this scenario remains unclear.

3.5 Summary

We have performed three-dimensional radiation-hydrodynamic simulations of a photoevaporating, viscous ($\alpha = 6.9 \cdot 10^{-4}$) protoplanetary disc hosting a Jupiter-like planet. We studied the interplay between the photoevaporative wind and the substructures generated by the planet, particularly the gap, and traced the redistribution of the gas and its accretion onto the planet. For comparison, we have also run the model with photoevaporation switched off. We refer to the model with and without

photoevaporation with the identifiers PEWIND and NOWIND, respectively. Our results show that:

- At the location of the gap carved by the planet, a photoevaporative wind cannot be supported. In the vicinity of the gap, the pressure gradient in the wind is inverted, and the wind is falling back into the gap. Consequently, the depth of the gap is reduced by more than an order of magnitude. The same mechanism is at work not only in the wind but also at the hot, uppermost layers of the disc surface at the inner and outer edge of the gap.
- The continuous resupply of gas into the gap significantly increases the amount of mass the planet has available for accretion. In our simplified accretion model, this leads to a factor 2 increase in the planet's accretion rate. Most of the additionally accreted gas originates from a radius up to ≈ 8 au, beyond which the wind structure is not significantly affected by the presence of the gap. It is particularly noteworthy that ≈ 3 percent of the accreted mass originates inside $R < 3$ au if photoevaporation is operating. In the NOWIND model, this region does not contribute to the accreted mass in a significant amount.
- The modified density structure of the disc leads to a reduction of the torque that is acting on the planet. After 200 orbits, the migration timescale is already reduced by almost a factor of 2 compared to the case without photoevaporation, and the torque is expected to continue to decrease.
- After being delivered to the gap, the material that is not accreted by the planet is pushed towards the edges of the gap by the gravitational torque of the planet, from where it viscously diffuses in the bound disc. This leads to an increase of the gap-crossing rates by a factor of ≈ 5 in both directions compared to the NOWIND model. Consequently, the mass rate crossing the gap from the outer disc to the inner disc in the PEWIND model is higher than the viscous accretion rate that would be expected in an unperturbed disc without a planet.
- The increased inwards-crossing rate, in combination with the recycling of a significant portion of the wind that is falling back to the gap, results in a slower dispersal and, therefore longer lifetime of the inner disc compared to a model without a planet. This is opposite to the planet-induced photoevaporation (PIPE) scenario that has been proposed in the past.

We have discussed that the wind-driven redistribution of gas could potentially influence the chemical and isotopic composition of the planet's atmosphere and the material in the vicinity of the gap. In future work, we will present an adapted model more suitable for creating synthetic observations of molecular (CO) emissions and compare them to actual observations. It is unclear how a magnetic wind would change our results. Models of non-ideal magnetothermal winds in protoplanetary discs with gaps will be valuable for determining whether an infall would also happen in the presence of magnetic fields.

Acknowledgements

We would like to thank the anonymous referee for a constructive report that improved the manuscript. This research was supported by the Excellence Cluster ORIGINS, which is funded by the Deutsche Forschungsgemeinschaft (DFG, German Research Foundation) under Germany´s Excellence Strategy – EXC-2094-390783311. GP and BE acknowledge the support of the Deutsche Forschungsgemeinschaft (DFG, German Research Foundation) - 325594231. The simulations have been carried out on the computing facilities of the Computational Center for Particle and Astrophysics (C2PAP).

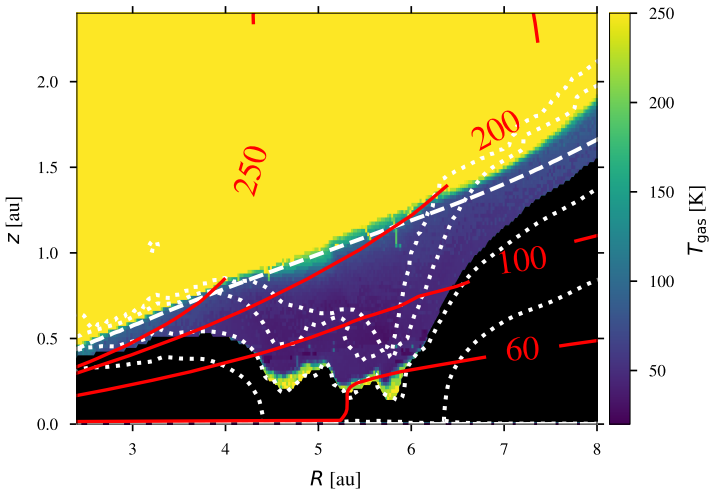

Figure 3.14: Temperature structure of a density slice at $\Phi = 0$ post-processed with MOCASSIN. The white dashed line shows the contour for a column number density of $2.5 \cdot 10^{22}$ cm^{-2}, above which the temperature is fixed to the dust temperature. The red solid lines are contours of the dust temperature. The dotted white lines are density contours for (from top to bottom) 10^{-16} to 10^{-13} g cm^{-3} in increments of one order of magnitude and indicate the structure of the gap. The black region is too far inside the disc to receive any energy packets in the radiative transfer calculation, which means it is shielded from stellar radiation or the diffuse field.

3.6 Appendix

3.6.1 Influence of the diffuse EUV and X-ray field on the temperature structure of the gap

A shortcoming of the temperature parametrisation used in our models is that any heating by diffuse EUV or X-ray radiation is neglected. To verify that this effect is not strong enough to affect our result significantly, we took a density slice of our model at $\Phi = 0$ in the $R\theta$-plane and post-processed it with MOCASSIN, using the same configuration as was used by Picogna et al. (2019) to derive the parametrisation. We present the resulting temperature structure inside the gap in Fig. 3.14. Most of the gap is not significantly heated by the diffuse field, and the temperature remains below the dust temperature. In our model, the dust temperature is assumed where the column number density exceeds $2.5 \cdot 10^{22}$ cm^{-2}. Hence, the diffuse field has only an effect if it can heat the gas beyond the dust temperature. This is the case only deep inside the gap, close to the 10^{-14} g cm^{-3} density contour, where the temperature reaches up to ≈ 250 K. However, this temperature and the resulting pressure gradient are more than an order of magnitude lower than the opposing gradient at the surface of the disc and not sufficient to launch a photoevaporative wind inside the gap. We can illustrate this using the basic concept of the gravitational radius (Liffman, 2003),

$$R_g = \frac{\gamma - 1}{2\gamma} \frac{GM_* \mu m_p}{k_B T}, \tag{3.11}$$

which is often used to approximate the radius outside which a photoevaporative wind can be launched. Here, m_p is the proton mass, k_B is the Boltzmann constant, and T is the gas temperature. For $T = 250$ K, we find $R_g \approx 100$ au, much larger than the radius of the gap.

3.6.2 Snapshots of gas tracers

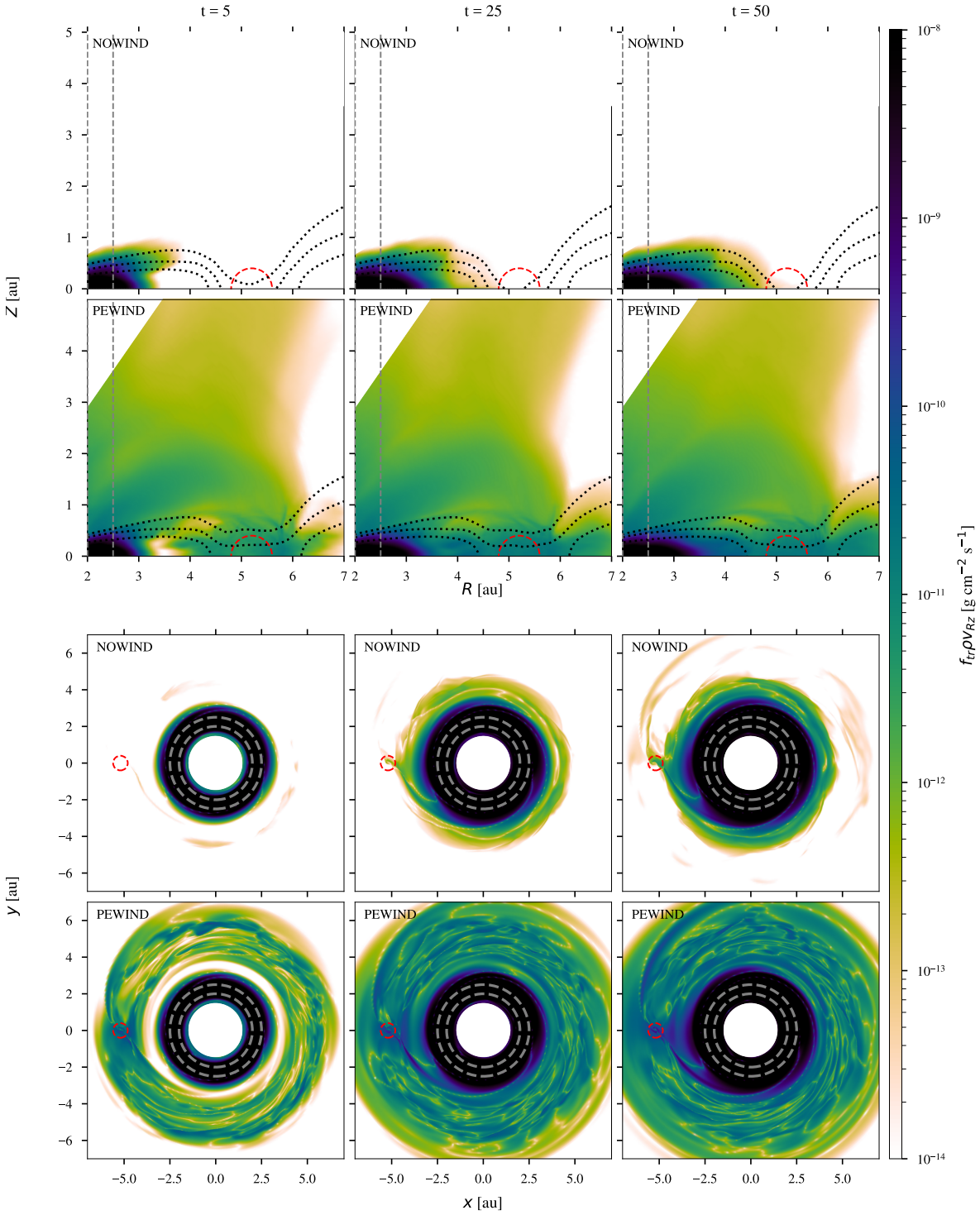

Figure 3.15: Poloidal mass flux of the gas originating in the innermost radial tracer-bin between $R = 2$ and 2.5 au at t = 5, 25 and 50 orbits. The top panels show the azimuthal average, and the bottom panels show the traced mass flux in the midplane. The black dotted lines are density contours for (from top to bottom) 10^{-17} to 10^{-13} g/cm^3 in increments of one order of magnitude. The red circle indicates the extent of the planet's Hill sphere. The grey dashed lines show the boundaries of the radial bin, inside which the tracer was originally distributed.

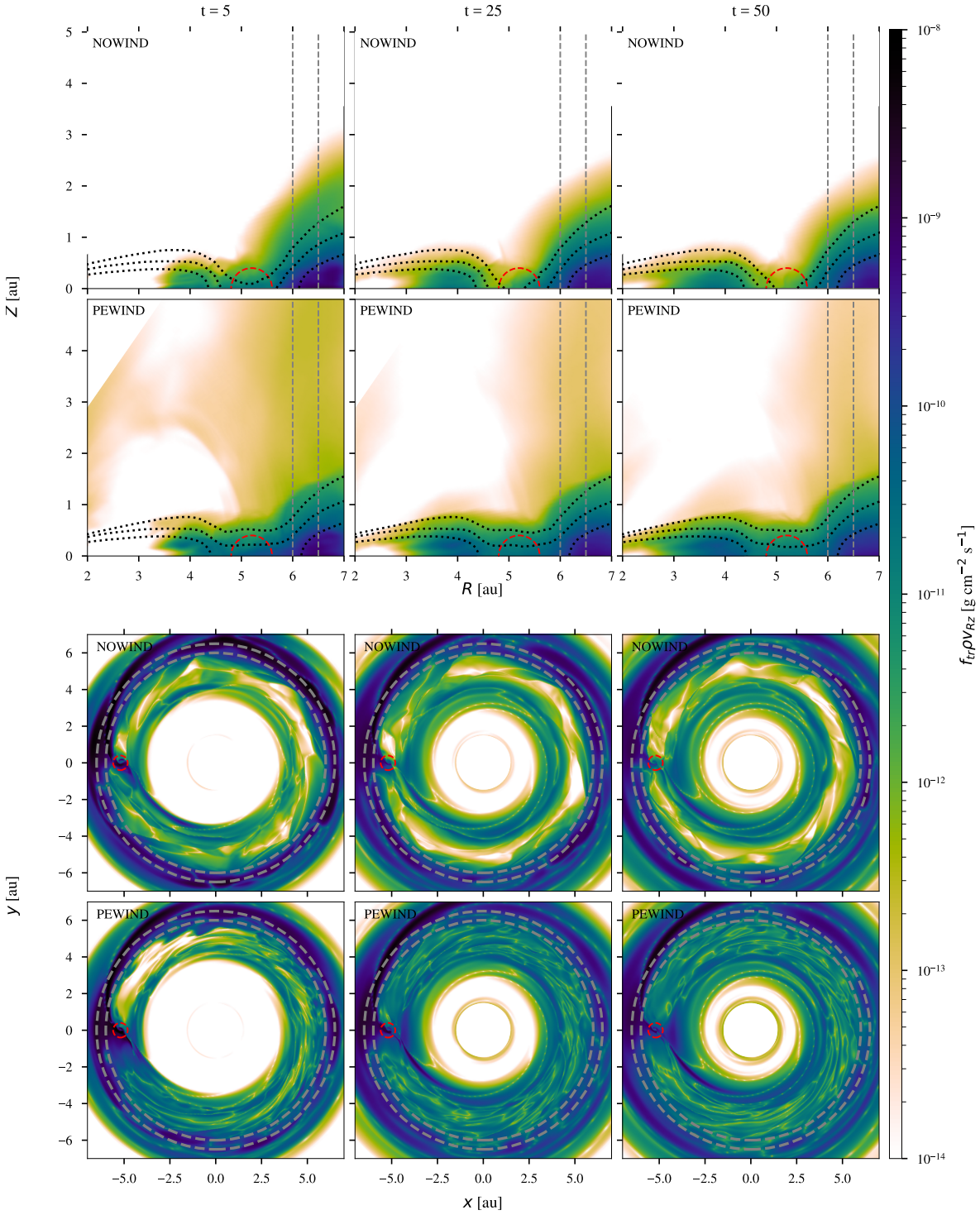

Figure 3.16: As Fig. 3.15 but for the tracer that originates in the radial bin between R = 6 and 6.5 au

Chapter 4

Reproducing spatially resolved [OI] emission in TW Hya with photoevaporation models

The content of this chapter was published in Rab et al. (2023)Weber et al. (2024)[1]:

Christian Rab, **Michael Weber**, Giovanni Picogna, Barbara Ercolano, James Owen: "High-resolution [OI] line spectral mapping of TW Hya consistent with X-ray driven photoevaporation",
The Astrophysical Journal Letters, Volume 955 Issue 1 (2023), L11

Abstract

Theoretical models indicate that photoevaporative and magnetothermal winds play a crucial role in the evolution and dispersal of protoplanetary disks and affect the formation of planetary systems. However, it is still unclear what wind-driving mechanism is dominant or if both are at work, perhaps at different stages of disk evolution. Recent spatially resolved observations by Fang et al. (2023) of the [OI] 6300 Å spectral line, a common disk wind tracer, in TW Hya revealed that about 80% of the emission is confined to the inner few au of the disk. In this work, we show that state-of-the-art X-ray driven photoevaporation models can reproduce the compact emission and the line profile of the [OI] 6300 Å line. Furthermore, we show that the models also simultaneously reproduce the observed line luminosities and detailed spectral profiles of both the [OI] 6300 Å and the [NeII] 12.81 µm lines. While MHD wind models can also reproduce the compact radial emission of the [OI] 6300 Å line they fail to match the observed spectral profile of the [OI] 6300 Å line and underestimate the luminosity of the [NeII] 12.81 µm line by a factor of three. We conclude that, while we cannot exclude the presence of an MHD wind component, the bulk of the wind structure of TW Hya is predominantly shaped by a photoevaporative flow.

[1]The work presented in this chapter resulted from a collaboration with my co-authors, led by Christian Rab (CR). I was responsible for computing the synthetic observables and emission maps using MOCASSIN and composing the corresponding parts of the manuscript. CR computed the observables with PRODIMO and composed the remainder of the manuscript. The analysis of the results was a collaborative effort between CR and myself, with advice from the other co-authors.

4.1 Introduction

The evolution and final dispersal of protoplanetary disks is thought to strongly affect the formation and evolution of planetary systems. Disk winds are considered to be significant contributors to the evolutionary processes occurring within protoplanetary disks (Lesur et al., 2023; Pascucci et al., 2022). Thermal winds can be launched through photoevaporation (PE) from the central star (e.g. Gorti & Hollenbach, 2009; Nakatani et al., 2018a; Picogna et al., 2021; Ercolano et al., 2021) and are efficient at removing material at rates comparable to the observed accretion rates of T-Tauri stars (e.g. Ercolano & Pascucci, 2017). Thermal winds do not remove angular momentum from the disk, and, when combined with viscous accretion models, they are successful in reproducing the observed two-timescale behavior, evidenced by the evolution of disk colors (e.g. Koepferl et al., 2013; Ercolano et al., 2015) and several observational correlations such as the observed accretion rates and the mass of the central star (Ercolano et al., 2014) or inner disk life times (Picogna et al., 2021).

The inclusion of non-ideal magneto-hydrodynamical effects in weakly ionized protoplanetary disk has shown that magnetorotational instability (MRI) (Balbus & Hawley, 1991), hypothesized to drive viscosity in disks, is suppressed in most regions of the disk (see e.g. Lesur et al., 2022, for a recent review), except the very inner regions where thermionic emission from dust dominates (Desch & Turner, 2015; Jankovic et al., 2021). Vigorous, magnetically supported, disk winds (from now on MHD winds), are a solid prediction of most recent simulations (e.g. Gressel et al., 2015; Bai, 2016; Wang et al., 2019; Lesur, 2021; Gressel et al., 2020) and they replace MRI in most disk regions by removing angular momentum from the disk, allowing material to flow inward.

Which type of wind might dominate at different times and different locations in a disk is an important question, which directly affects planet formation models. The current picture emerging from the careful analysis of spectroscopic diagnostics is that both types of winds operate in disks, with MHD winds stronger in young objects and thermal winds dominating the final evolution and eventual dispersal of disks (Ercolano & Pascucci, 2017; Weber et al., 2020).

Currently used spectroscopic wind diagnostics, particularly the [OI] 6300 Å collisionally excited spectral line, have complex line profiles (e.g. Simon et al., 2016; Fang et al., 2018; Banzatti et al., 2019; Gangi et al., 2020), often preventing important wind parameters, like the wind launching radius, to be directly determined (see discussion in Weber et al. 2020). Rab et al. (2022) find that a combination of [OI] 6300 Å and molecular hydrogen observations are consistent with thermal winds driven by X-ray photoevaporation, but alternative models cannot be ruled out.

In order to break the degeneracies hidden in the interpretation of non-spatially resolved line profiles, high-resolution spectral mapping of wind diagnostics represent an attractive option. This has recently been done for the [OI] 6300 Å line from TW Hya by Fang et al. (2023), using the multi-unit spectroscopic explorer (MUSE) at the Very Large Telescope, who showed that about 80% of the [OI] emission is confined to within 1 au radially from the star. In this paper we show that state-of-the-art thermal wind models driven by X-ray photoevaporation (e.g. Picogna et al., 2019; Ercolano et al., 2021; Picogna et al., 2021) are consistent with the observations recently published by Fang et al. (2023). In Section 4.2 we briefly describe the used photoevaporative disk wind models and our approach to produce synthetic observables. In Section 4.3 we show our results in particular the comparison to the observational data. We discuss our results in context to previous works and MHD disk wind models and present our conclusions in Section 4.4.

4.2 Methods

In this section, we describe the physical models used in this work and how we produce synthetic observables from those models that can be directly compared to observational data.

4.2.1 Photoevaporative disks wind models

To model a photoevaporative disk wind we follow the approach by Picogna et al. (2019, 2021); Ercolano et al. (2021)[2], to which we refer for details. This model uses a modified version of the PLUTO code (Mignone et al., 2007; Picogna et al., 2019) to perform radiative-hydrodynamic simulations of a disk irradiated by a central star. The temperatures in the wind and the wind-launching regions, i.e. the upper layers of the disk, where the column number density towards the central star is in the range between 5×10^{20} and 2.5×10^{22} cm^{-2}, are determined by parameterizations that are derived from detailed radiative transfer calculations with the gas photo-ionization code MOCASSIN (Ercolano et al., 2003, 2005, 2008a). For a given column number density the respective parameterization yields the gas temperature dependent on the ionization parameter $\xi = \frac{L_X}{nr^2}$, where L_X is the X-ray luminosity of the star, n the volume number density and r the spherical radius. In this work, we use a stellar mass $M_* = 0.7 M_\odot$ and the parametrizations derived from the spectrum labeled as Spec29 in Ercolano et al. (2021) with $L_X = 2 \times 10^{30}$ erg s^{-1}, which is appropriate considering observational constraints on TW Hya (Robrade & Schmitt, 2006; Ercolano et al., 2017). The computational grid was centered on the star. Spherical polar coordinates were adopted with 512 logarithmic spaced cells in the radial direction from 0.33 au to 600 au, and 512 uniform spaced cells in the polar one from 0.005 to $\pi/2$. Outflow boundaries were adopted in the radial directions, while special reflective boundaries were used to treat the regions close to the polar axis and the disk mid-plane. A periodic boundary was assumed in the azimuthal direction. The influence of the inner boundary was tested by decreasing the inner radial boundary to 0.1 au, while keeping the same radial resolution outside 0.33 au.

4.2.2 Disk model without a wind

Additionally to the PE disk wind models, we use an existing radiation thermo-chemical disk model for TW Hya from the DIANA (DIsc ANAlysis[3]) project presented in Woitke et al. (2019). This model does not include a wind component but was made to reproduce existing (mostly spatially unresolved) observational data including the spectral energy distribution and about 50 spectral lines (i.e. line fluxes are matched within a factor of two to three). With this model we show how a pure disk model compares with the spatially resolved [OI] 6300 Å observations. As at the time of the publication of this model no spatially resolved observables for the [OI] 6300 Å were produced, we rerun the model with a more recent version of the radiation thermo-chemical code ProDiMo (PROtoplanetary DIsk MOdel[4], Woitke et al. 2009; Kamp et al. 2010; Thi et al. 2011; Woitke et al. 2016) to produce line cubes and images that can be compared to the spatially resolved data.

4.2.3 Synthetic observables

To produce synthetic observables we use two different approaches to post-process the PE disk wind model. Similar to Weber et al. (2020) we use the MOCASSIN Monte Carlo radiative transfer code

[2]X-ray PE models and data from Picogna et al. (2021) are available here `https://cutt.ly/lElY9JI`

[3]`https://diana.iwf.oeaw.ac.at`

[4]`https://prodimo.iwf.oeaw.ac.at` revision: 66efbd75 2023/06/27

that allows to model spectral line emission for atomic species in the optical and infrared (Ercolano et al., 2003, 2005, 2008a). Furthermore we use the radiation thermo-chemical code ProDiMo that was recently applied in Rab et al. (2022) to produce synthetic observables for atomic and molecular species that are supposed to trace disk winds. We use both approaches to show that our results, in particular the spatial extent of the [OI] 6300 Å, are robust and do not strongly depend on the details of the post-processing method (e.g. chemistry, heating-cooling, line excitation).

For both approaches, we use the same physical structure (density and velocity field), the same X-ray/stellar spectrum, and the same dust properties. To account for the accretion luminosity we add to the X-ray spectrum a black body spectrum with $T_{\rm eff} = 12000$ K normalized to $L_{\rm acc} = 2.95 \times 10^{-2}\ L_{\odot}$ (Fang et al., 2018). For the dust we assume a gas-to-dust ratio of 100 and an ISM size distribution (see Weber et al. 2020 for details). Quantities such as temperatures, line populations, chemical abundances and the synthetic observables are self-consistently calculated within each post-processing framework. For a more detailed discussion on these different post-processing approaches and a comparison see Rab et al. (2022).

At first we use the line radiative transfer modules of MOCASSIN and ProDiMo to produce synthetic model images for the [OI] 6300 Å emission assuming a distance of 60 pc (Gaia Collaboration et al., 2021) and a disk inclination of 7° (Qi et al., 2004), consistent with Fang et al. (2023). For the produced model images we use an oversampling factor of seven (0.003615 arcsec) compared to the pixel scale of the observations. Following Fang et al. (2023) we downsample the model images to the pixel scale of the MUSE data before convolving it with the PSF. For these model images and for the observed image we produce azimuthally averaged radial profiles using the corresponding pixel scale as the width for the radial bins. Additionally we also produce radial profiles for the unconvolved model images to better show the real extend of the emission. We also produce synthetic images in the same way for the toy model (power-law model) presented in Fang et al. (2023) and the thermo-chemical model without a wind. We note that the used oversampling factor is not enough to fully resolve the toy model of Fang et al. (2023) but we found that it is sufficient to reproduce the observation after convolution of the toy model image (mainly because a downsampling to the pixel size of the observations is anyway required). We also note that a higher resolution spatial grid is used for the radiative transfer step, but as we are not aiming for a detailed fitting of the observational data we use the oversampling factor of all model images for consistency (e.g. between the two different post-processing methods) and efficiency.

We also compare our model with the observations of the [NeII] 12.81 µm line presented in Pascucci et al. (2011). For this line we simply produce spectral line profiles again using both post-processing approaches.

4.3 Results

Here, we compare our modeling results to the observational data. As we do not present newly developed PE models we focus only on the observables. In Sect. 4.3.1 we present normalized azimuthally averaged radial profiles for [OI] 6300 Å in a similar fashion as Fang et al. (2023) and in Sect. 4.3.2 we compare our PE wind models to the observed spectral profiles for the [OI] 6300 Å and [NeII] 12.81 µm spectral lines.

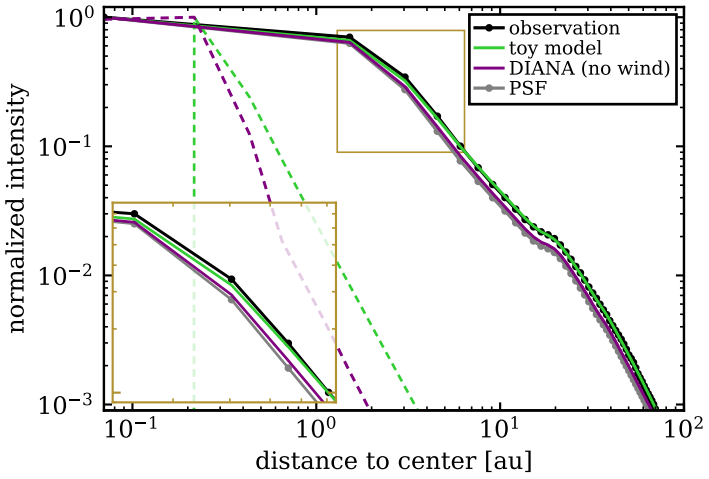

Figure 4.1: The toy (power-law) model (green) from Fang et al. (2023) compared to results from a radiation thermo-chemical disk model (purple) without a wind that fits a large set of observational data for TW Hya (Woitke et al., 2019). The dashed and solid colored lines show the radial profiles for the unconvolved and convolved images, respectively. The gray solid line shows the radial profile of the PSF and the black solid line for the [OI] 6300 Å MUSE observations (Fang et al., 2023). The inset shows a zoom-in to the region marked by the brown box ($r = 1.3 - 6.4$ au) in the main panel.

4.3.1 Radial profiles

4.3.1.1 Disk only model

In Fig. 4.1, we show the toy model from Fang et al. (2023) in comparison to the disk-only model from Woitke et al. (2019). The thermo-chemical disk model shows a similar radial profile for the [OI] 6300 Å emission, in particular the steep slope, but is slightly more compact and hence does not match the data (i.e. it remains unresolved). We note that the model of Woitke et al. (2019) uses a parameterized disk structure, which is quite different to the disk wind models used in this work or in Fang et al. (2023), in particular, it has a dust and gas depleted (optically thin but not empty) inner hole extending up to almost 3 au. Although it is possible to adapt this model to achieve a better match to the spatially resolved data, such a disk only model, by construction, cannot match the blue-shifts seen in the observed line profiles of the [OI] 6300 Å and [NeII] 12.81 µm lines. Nevertheless, it is interesting to see that such a model is almost in agreement with the spatially resolved data, although such constraints were not included in the modeling. Furthermore, this model indicates that a disk only solution seems to produce an even more compact emission region for the [OI] 6300 Å compared to the wind models presented here or in Fang et al. (2023) and also that the contribution from a disk itself can be significant in the case of TW Hya.

4.3.1.2 Photoevaporative disk wind models

In Fig. 4.2 we compare the [OI] 6300 Å radial intensity profiles of our PE wind model at an inclination of 7° to the observation by Fang et al. (2023). As can be seen in the unconvolved radial profiles, both, the MOCASSIN and ProDiMo models yield very similar results, with the ProDiMo model having slightly more emission at very low ($\lesssim 0.4$ au) and at extended radii, and MOCASSIN showing enhanced emission at intermediate radii between ≈ 0.5 and 3 au. In both models, the emission peaks well inside of 1 au with a steep decrease in intensity at larger radii. Computing the cumulative integral,

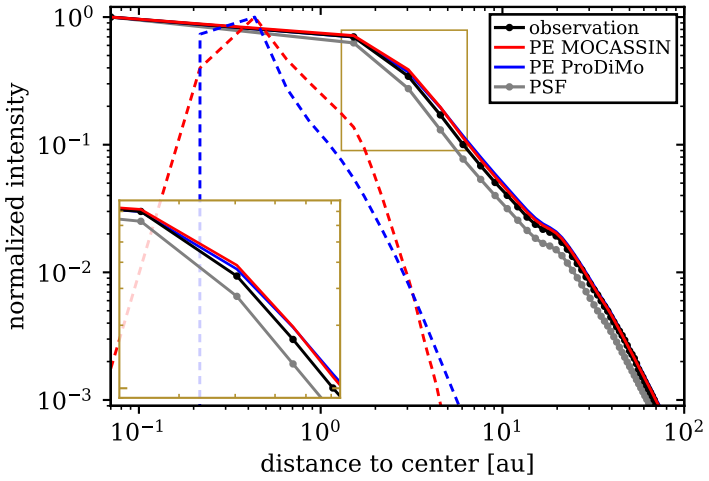

Figure 4.2: Comparison of the photoevaporative disk wind model with the observed normalized radial intensity profiles of the [OI] 6300 Å line. The black solid line shows the observation, the gray solid line the PSF (both from Fang et al. 2023. The colored solid and dashed lines show the model results, convolved with the PSF and at the resolution of the model image, respectively. In red, we show the results from the MOCASSIN and in blue from the ProDiMo post-processing. The inset shows a zoom-in to the region marked by the brown box ($r = 1.3 - 6.4$ au) in the main panel.

we find that 80% of the emission originates inside 2 au of the central star, compared to 1 au for the toy model that Fang et al. (2023) derived as a fit to the data. This is also visible in Fig. 4.3, where we show 2D emission maps overlain by contours showing the 80% regions. It is worth pointing out that although the 80% regions extend to ≈ 2 au and ≈ 14 au for the [OI] 6300 Å and [NeII] 12.81 µm lines, respectively, the emission inside this region is not uniform but has a strong gradient with the peak close to the star. Comparing the profiles after convolution with the PSF, it can be seen that the radial profiles of the PE wind model are in very good agreement with the observations. This shows that current state-of-the-art photoevaporative disk models produce compact emission consistent with the spatially resolved observations of TW Hya.

Figure 4.3 shows significant emission originating from the inner 1 au, which is inside the gravitational radius of the X-ray photoevaporation models shown here (∼ 3.5 au). The emitting material close to the star is thus bound to the inner disk and not affected by photoevaporation. This implies that our main result would not qualitatively change in the case of a "gapped" inner disk as suggested by the observations of a dark annulus in mm-wave dust emission at ≈ 1 au (Andrews et al., 2016). Indeed, the presence of gas close to the central star of TW Hya, which shows clear accretion signatures, justifies the employment of primordial disk models in this case. While we do not expect significant changes to the wind structure due to the gap and hence on the main picture of having compact emission, a detailed hydrodynamical model would be required to assess potential differences in the detailed spectroscopic line profiles emitted from this region (see also Sect. 4.4). Such a model is, however, outside the scope of this study and would also require higher spatial resolution in the observations of the inner disc, which is not possible with current instrumentation.

4.3.2 Spectral line profiles

In Fig. 4.4 we compare the modelled spectral line profiles to the observations of the [OI] 6300 Å and [NeII] 12.81 µm spectral lines. For [OI] 6300 Å we show three different observed spectra representing

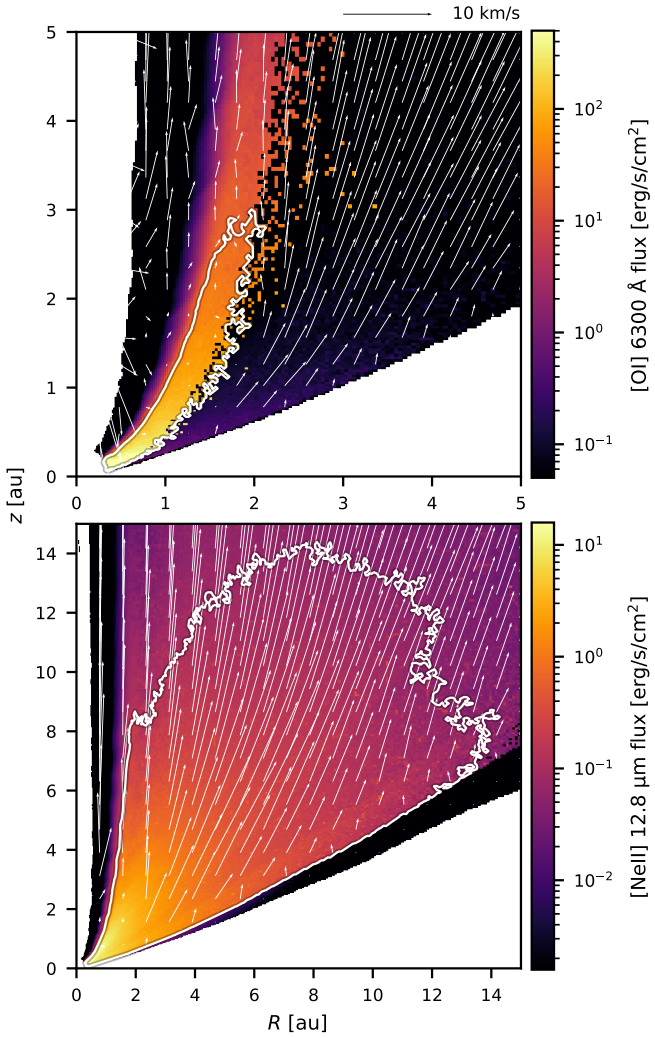

Figure 4.3: [OI] 6300 Å (top) and [NeII] 12.81 µm (bottom) line flux of our photoevaporation disk wind model obtained by multiplying the emissivity with $2\pi R$ in order to illustrate the origin of the emission. White solid contour lines indicate the regions where the top 80 % of emission originates. White arrows represent the velocity field in the PE model.

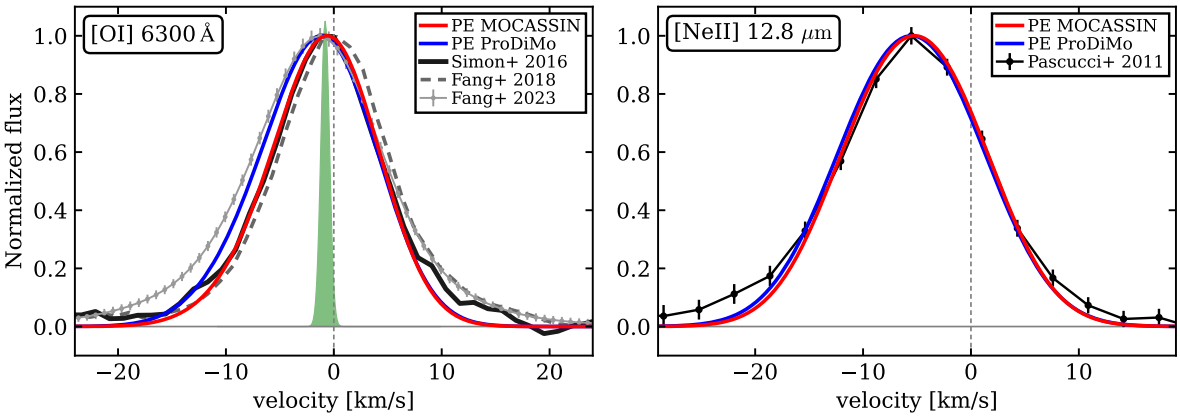

Figure 4.4: Comparison of observed [OI] 6300 Å (Simon et al., 2016; Fang et al., 2018, 2023) and [NeII] 12.81 µm (Pascucci et al., 2011) spectral line profiles to synthetic line profiles of photoevaporative disk wind models. The [OI] line profiles from the models and that observed by Fang et al. (2023) have been degraded to a resolving power $R = 40000$, comparable to the resolution in the observation by Simon et al. (2016). For the Fang et al. (2023) data the error bars correspond to 3σ uncertainties (for visibility). The Gaussian distribution shown in green represents the derived mean centroid shift of $-0.8\,\mathrm{kms}^{-1}$ with a standard deviation of $0.4\,\mathrm{kms}^{-1}$ as derived by Fang et al. (2023) from various observations of [OI] 6300 Å. The [NeII] model profile has been degraded to $R = 30000$ and the error bars in the observed profile indicate 1σ uncertainties.

the scatter observed in the measured centroid velocities v_c with a mean of $v_c = -0.8\,\mathrm{kms}^{-1}$ and a standard deviation of $0.4\,\mathrm{kms}^{-1}$ (Fang et al., 2023). Both models are in good agreement with the observations. In particular the MOCASSIN ($v_c \approx -0.8\,\mathrm{kms}^{-1}$) model matches the profile of (Simon et al., 2016), that shows $v_c \approx -0.8\,\mathrm{kms}^{-1}$, exceptionally well. The ProDiMo profile is slightly broader in the blue part of the spectrum and therefore appears more blue-shifted ($v_c \approx -1.5\,\mathrm{kms}^{-1}$). Nevertheless this is still consistent with observations as for example the profile of Fang et al. (2023) shows a similar behavior with $v_c \approx -1.5\,\mathrm{kms}^{-1}$, for the spectrum downgraded to R=40000. The [OI] 6300 Å line fluxes from the models are $1.2 \times 10^{-5}\,L_\odot$ (MOCASSIN) and $5.5 \times 10^{-6}\,L_\odot$ (ProDiMo), in good agreement with the observed values of $1.0 - 1.5 \times 10^{-5}\,L_\odot$ (Simon et al., 2016; Fang et al., 2018, 2023).

The difference in the shape of the two model spectra can be explained by the slightly more extended [OI] 6300 Å emission of the ProDiMo model (see Fig.4.2), which traces slightly faster velocities of the PE wind compared to the MOCASSIN model. We tested this by simply removing all emission for $r > 4$ au in the synthetic observables of the ProDiMo model and find that for this case the MOCASSIN and ProDiMo line profiles become almost identical. As the density structure and velocity fields in both models are the same; the differences arise from different radial temperature gradients and differences in the line excitation calculations. However, our results indicate that detailed models for TW Hya, fully considering the stellar properties and possibly also details of the disk structure (i.e. a gap in the disk structure; see Owen 2011) are required for a comprehensive interpretation of the [OI] 6300 Å line profile.

For [NeII] 12.81 µm the modeled profiles are very similar and match very well the observed spectral profile. As [NeII] 12.81 µm traces regions further out and higher up (up to r ≈ 10 au) in the disk/wind with respect to [OI] 6300 Å, it traces higher velocities of the photoevaporative flow (see Fig. 4.3), consistent with the observed $v_c \approx -5\,\mathrm{kms}^{-1}$. The line luminosity of the models is $3.4 \times 10^{-6}\,L_\odot$

(MOCASSIN) and $5.1 \times 10^{-6}\,L_{\odot}$ (ProDiMo) which are in excellent agreement with the observed range of luminosities of $\approx 3.5 - 6.2 \times 10^{-6}\,L_{\odot}$ (Pascucci et al., 2011; Pascucci & Sterzik, 2009; Najita et al., 2010b).

4.4 Discussion and Conclusions

Our results show that current state-of-the-art PE disk wind models are consistent with the observational data presented in Fang et al. (2023). We want to emphasize that for this work, we did not use any new developments or adaptations to the PE wind modeling approach already presented and used in Picogna et al. (2019); Weber et al. (2020); Picogna et al. (2021); Ercolano et al. (2021); Rab et al. (2022); Weber et al. (2022). The only difference between this work and previously published work is the choice of an appropriate X-ray spectrum for TW Hya.

Fang et al. (2023) compared the spatially resolved [OI] 6300 Å emission to very low resolution early photoevaporation models (Owen et al., 2010; Ercolano & Owen, 2010) which present a more extended emission profile for the [OI] 6300 Å. Based on this comparison, they concluded that a magneto-thermal driven wind is necessary to explain the spatially resolved [OI] 6300 Å line data. We show here, however, that, compared to the fiducial magneto-thermal wind model presented in Fang et al. (2023), modern PE models produce only very slightly more extend [OI] 6300 Å emission but are still fully consistent with the data. Apart from the higher inner grid resolution, an important difference between the "old" PE models (Owen et al., 2010; Ercolano & Owen, 2010) and the newer PE models (Picogna et al., 2019; Weber et al., 2020; Picogna et al., 2021; Ercolano et al., 2021) is the temperature parameterization. The new models take into account the detailed column density distribution (attenuation) in the simulation regions, yielding a more accurate temperature (and thus density) profile. More specifically, the density in the inner disk is higher for the new models, resulting in a more compact emission region.

The new PE models can match the observed line luminosity and the shape of the [OI] 6300 Å profile very well, in particular the small observed blue-shift of $v_c \approx -0.8\,\mathrm{km/s}$. As noted by Fang et al. (2023) the [OI] 6300 Å spectral profile of their MHD model is too blue-shifted compared to observations, which is likely caused by the higher wind velocities in the inner regions compared to our PE model. Fang et al. (2023) argue that the discrepancy could be caused by the lack of an inner hole in their primordial disk model and that the presence of such a hole would allow for red-shifted emission from the back side of the disk to contribute to the line profile, reducing its blue-shift. However, in order to zero the velocity center by this effect, the line would then result broadened by the blue-shifted value (Ercolano & Owen, 2010, 2016), which would then again be in tension with the observations. Additionally, as TW Hya is seen almost face-on, the contribution from the back-side of the disk will be limited unless an unsuitable large inner hole (several au) is assumed. More quantitatively speaking, our model has an inner radius of $r_{\mathrm{in}} = 0.33\,\mathrm{au}$ (i.e. larger than the MHD model), but still the back side of the disk contributes to less than 2% to the total flux and does not have any significant impact on the centroid velocity. We also tested a PE wind model with $r_{\mathrm{in}} = 0.1\,\mathrm{au}$ and found no significant differences. In any case, for a more thorough interpretation of the [OI] 6300 Å spectral profile of TW Hya, a more detailed disk structure model for the inner few au is required. In particular constraints from ALMA observations (gap at $\approx$ 1 au and unresolved emission from $r < 0.5\,\mathrm{au}$; Andrews et al. 2016) and VLT/SPHERE (marginal detection of emission from the inner few au; van Boekel et al. 2017) indicate that there is likely still some dust in the inner $1 - 2\,\mathrm{au}$ (see also Ercolano et al., 2017) that would reduce [OI] 6300 Å emission from the backside of the disk.

As already noted in Pascucci et al. (2011) and also discussed in Fang et al. (2023) the [NeII] 12.81 µm

line observation points towards a thermally driven wind. This is supported by the models presented in this work, as the agreement of the PE wind model with the spectral line profile and the observed line fluxes (which is under-predicted by a factor of three by the MHD model of Fang et al. 2023) is excellent, indicating that at least for the radii larger than a few au, traced by the [NeII] 12.81 µm line, the disk wind structure of TW Hya is predominantly shaped by a PE flow.

We conclude that, while the currently available spatially resolved data does not allow to clearly distinguish a pure thermally driven wind from a magneto-thermal wind, the simultaneous agreement of the PE wind models with the spatially resolved data and the spectral profiles of [OI] 6300 Å and [NeII] 12.81 µm strongly indicates that at least large parts of the disk wind seen in TW Hya are driven by X-ray photoevaporation.

Acknowledgments

We thank the anonymous referee for a quick and constructive report. We thank Min Fang for providing their reduced observational data for the [OI] 6300 Å line including the PSF. We acknowledge the support of the Deutsche Forschungsgemeinschaft (DFG, German Research Foundation) Research Unit "Transition discs" - 325594231. This research was supported by the Excellence Cluster ORIGINS which is funded by the Deutsche Forschungsgemeinschaft (DFG, German Research Foundation) under Germany's Excellence Strategy - EXC-2094 - 390783311. CHR is grateful for support from the Max Planck Society. This research has made use of NASA's Astrophysics Data System.

Software

This research made use of Astropy, a community-developed core Python package for Astronomy (Astropy Collaboration et al., 2013, 2018). This research made use of Photutils, an Astropy package for detection and photometry of astronomical sources (Bradley et al., 2022). matplotlib version 3.7.0 (Hunter, 2007); scipy (Virtanen et al., 2020); numpy (Harris et al., 2020).

Chapter 5

Modelling forbidden emission lines in X-ray-irradiated non-ideal magnetothermal winds

5.1 Motivation

While the previous chapters explored purely EUV+X-ray-driven photoevaporative winds, it is clear that magnetic winds can play a vital role. Especially with the long-established model of viscous disc evolution having fallen out of favour in preference for magnetic wind-driven disc evolution models (see Sect. 1.1.3.4 and 1.3.2), it is more important than ever to gain observational constraints that can shed light on the launching mechanisms of winds. As discussed in Sect. 1.3.4.1 and the previous chapters, the most commonly used wind-tracers are spectrally resolved forbidden emission lines from neutral or lowly ionised atoms, such as [OI], [SII], or [NeII]. Their luminosities, line ratios, and spectral line profiles can provide valuable insights into the properties and kinematics of the wind regions they trace. The analysis of line ratios, however, is only accurate if both lines are tracing the same regions. While the spectral line profile can inform to a limited extent about the inner radius of the emission, its radial and vertical extent is often uncertain. Moreover, the complex shapes that line profiles may exhibit are believed to result from the superposition of emission in multiple regions, which complicates their interpretation. The comparison to theoretical models is, therefore, invaluable for correctly understanding and interpreting the observations.

Many photoevaporation models have been used to produce synthetic observables (e.g. Font et al., 2004; Alexander, 2008; Ercolano & Owen, 2010, 2016; Picogna et al., 2019; Weber et al., 2020; Ballabio et al., 2020; Rab et al., 2022; see also chapter 2, 4), and while they are typically able to reproduce many of the observed narrow low-velocity components (NLVCs) (see Sect. 1.3.4.1 for a definition), they cannot reproduce broad low-velocity components (BLVCs). BLVCs are generally thought to be dominantly broadened by Keplerian rotation, i.e. they have to trace a radially compact wind launched close to the star, where photoevaporation cannot operate. Only a few studies so far have attempted to reproduce forbidden emission line profiles with models that incorporate magnetic winds. Gressel et al. (2020) computed [OI] 6300 Å profiles, and while they find blueshifted profiles in their predominantly magnetocentrifugal wind, they would still be classified as NLVCs. However, the inner boundary of their model is at 0.75 au, whereas the BLVCs are believed to be launched at smaller radii ($0.05 \lesssim R \lesssim 0.5$ au). Other detailed numerical models of magnetic winds have

similar limitations (e.g. Wang et al., 2019; Rodenkirch et al., 2020). Despite the lack of the innermost regions, the magnetothermal wind model by Rodenkirch et al. (2020) would be an excellent candidate for synthetic observations, as they also find a radial extended thermal wind component for weaker magnetic fields. However, the models have another limitation in that they employ a numerical floor density that is high enough to produce significant flux in the wind-tracing forbidden emission lines, contaminating the results (Weber et al., 2020). In a different approach, Weber et al. (2020) predicted several optical forbidden emission lines using the analytical magnetic wind model by Milliner et al. (2019), which is based on the magnetocentrifugal wind model by Blandford & Payne (1982). They find that the model can predict well the BLVCs and even the high-velocity components (HVCs) but fail to reproduce the NLVCs. Moreover, they could reproduce the complex line profiles with all three components by combining the magnetic profiles with those predicted from the X-ray photoevaporation model by Picogna et al. (2019). Nemer & Goodman (2024) recently post-processed an analytical magnetothermal wind model based on the model by Bai et al. (2016) and predicted several wind-tracing lines. They find complex [OI] 6300 Å and [NeII] 12.81 µm line shapes with long tails on the blueshifted side that can be fitted with a BLVC and NLVC. However, the predicted luminosity of the [NeII] 12.81 µm is an order of magnitude lower than typically observed.

This chapter will focus on post-processing the non-ideal magnetothermal wind model recently developed by Sarafidou et al. (2024) to predict synthetic forbidden emission lines. In these models, the wind is usually magnetically assisted in the launching region and thermally sustained beyond it. Moreover, the authors find that when using the median X-ray luminosity, photoevaporation can dominate the wind-launching already at magnetic field strengths $\beta \gtrsim 10^5$, much stronger than previous models suggest (Rodenkirch et al., 2020). This makes them a promising choice for probing the transition between a magnetically and a thermally dominated wind. To this end, particular focus will be given to the [OI] 6300 Å and [NeII] 12.81 µm lines. While [OI] 6300 Å is the most commonly observed wind-tracer and mainly traces the hot directly irradiated inner parts of the wind, the [NeII] 12.81 µm line is a promising line to trace radially extended disc winds (e.g. Pascucci et al., 2020). Their combined study has the potential to offer insights into the evolution of disc winds, specifically by revealing whether and how disc winds transition from an inner magnetic wind to a radially extended photoevaporative wind (Pascucci et al., 2020).

5.2 Methods

5.2.1 Magnetothermal wind model

The underlying model this chapter will be based on is the magnetothermal wind model recently presented by Sarafidou et al. (2024), where it is described in detail. In short, it is based on the non-ideal MHD setup presented in Gressel et al. (2020) with two major adaptions. The first adaption is the inclusion of the Hall effect via the framework developed by Krapp et al. (2018) as an additional non-ideal MHD effect, such that the model includes all three non-ideal MHD effects (c.f. Sect. 1.3.2). The second adaption is that the FUV-based thermochemistry is replaced by the $\xi - T$ parametrisation for X-ray irradiated discs presented in Picogna et al. (2019). The temperature during the simulation is thus given by the ionisation parameter $\xi = L_X/(nr^2)$ and the local column number density N_H (see also Sect. 1.3.1.2). Additionally, they include the effects of collisional ionisation following (Desch & Turner, 2015).

In order to avoid the numerical problems discussed in the previous section, Sarafidou et al. (2024) re-ran the models on a different numerical grid with a smaller inner radial boundary, as well as a lower density floor, making them more suitable for producing synthetic forbidden emission lines. The 2D-

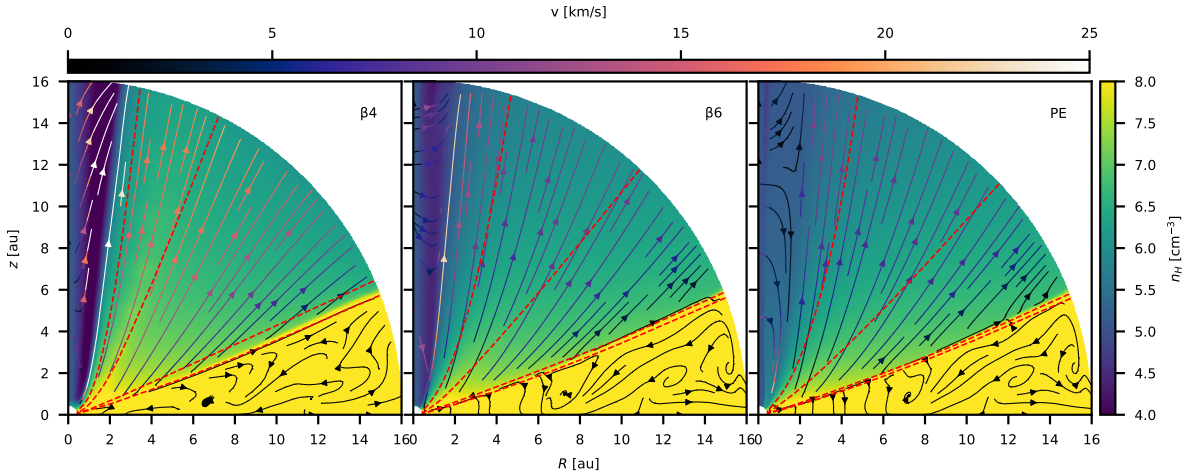

Figure 5.1: Number density maps of the (from left to right) $\beta4$, $\beta6$ and PE wind models. The streamlines represent the velocity structure, and their colour represents the speed. Red dashed lines are column density contours for the values (from top to bottom) 10^{20}, 10^{21}, 10^{22}, $2.5 \cdot 10^{22}$ cm^{-2}.

axisymmetric spherical-polar grid has a resolution of $N_r = 457$ and $NC_\theta = 289$ in the radial and polar direction, respectively. The radial direction is modelled within $r \in [0.45, 16]$ au and the polar direction within $\theta \in [0, \pi/2]$. The minimum density is limited to a floor value $\rho_{\rm floor} \approx 1.25 \cdot 10^{-19}$ g cm^{-3}. Moreover, when re-running the models, the Hall effect was switched off to reduce computational cost. As discussed in Sarafidou et al. (2024), the Hall effect mainly operates in the disc's interior, and the wind mass-loss rates do not depend on it. However, in the Hall anti-aligned case, where the initial magnetic field is antiparallel to the disc's rotation axis, the wind-launching is suppressed in the innermost regions ($R \lesssim 1.4$ au). Conversely, in the Hall-aligned case, the wind is launched from slightly smaller radii than in the Hall-free case ($R \lesssim 1$ au vs $R \lesssim 1.2$ au). Therefore, investigating the different cases presents an intriguing avenue for future research. Nevertheless, the computationally less costly Hall-free models can offer meaningful initial insights.

By post-processing three different models, the impact of the magnetic field strength on the observables can be investigated. The first model (hereafter referred to as model $\beta4$) has a strong initial magnetic field with $\beta = 10^4$. The second model (hereafter $\beta6$) has a weaker magnetic field with $\beta = 10^6$, and the third model is a pure photoevaporation model with no magnetisation, referred to as model PE. In all models, the X-ray luminosity is $2 \cdot 10^{30}$ erg s^{-1}. The density and velocity structure of the wind models is shown in Fig. 5.1

5.2.2 Prediction of forbidden emission lines

Line fluxes and spectral line profiles of forbidden emission lines are produced following the method described in Sect. 2.2.2 (see also Ercolano & Owen, 2016; Weber et al., 2020). To summarise, the models are post-processed with MOCASSIN, using the EUV+X-ray spectrum presented in Ercolano et al. (2009), complemented by an additional component to model the UV emission produced by accretion onto the star. This accretion component is approximated with a blackbody at $T = 12000$ K and a luminosity that is converted from the mass accretion rate measured in the models, using the relation (1.3) in Sect. 1.1.2.4,

$$L_{\rm acc} = \left(1 - \frac{R_*}{R_{\rm in}}\right) \frac{G M_* \dot{M}_{\rm acc}}{R_*} \approx 0.8 \frac{G M_* \dot{M}_{\rm acc}}{R_*}, \tag{5.1}$$

Table 5.1: Wind mass-loss rates and mass accretion rates measured in the models, as well as the accretion luminosities resulting from the mass-accretion rate conversion.

Model	$\dot{M}_{\rm wind}$ [$M_\odot\,{\rm yr}^{-1}$]	$\dot{M}_{\rm acc}$ [$M_\odot\,{\rm yr}^{-1}$]	$L_{\rm acc}$ [$L_\odot$]
$\beta4$	$4.20 \cdot 10^{-8}$	$3 \cdot 10^{-8}$	0.26
$\beta6$	$1.90 \cdot 10^{-8}$	$1 \cdot 10^{-9}$	$8 \cdot 10^{-3}$
PE	$1.67 \cdot 10^{-8}$	–	$8 \cdot 10^{-3}$

where $R_{\rm in} = 5R_*$ is assumed. The measured mass-accretion rates and the resulting accretion luminosities are listed in table 5.1, assuming $R_* = 2R_\odot$. Note that since the model is inviscid and accretion is purely driven by magnetic stresses, the PE model has no measured accretion rate. However, if magnetic winds are generally not operating, it is likely that discs are viscously evolving. Therefore, in the PE model, the accretion luminosity is assumed to be the same as in the weakly accreting $\beta6$ model. Note that the mass loss due to the photoevaporative wind is independent of the accretion rate or luminosity, as it is primarily driven by X-ray irradiation. The accretion luminosity component is only important for the excitation of the wind-tracing forbidden emission lines. It is thus reasonable to assume that the structure of the wind does not change when introducing the accretion component to the irradiating spectrum.

Before processing the models with mocassin, they are remapped onto a cartesian grid that extends in both directions from 0 to 16 au on 600 quadratically spaced grid points. Moreover, inside $r < 0.6$ au, the gas density is set to zero. This was necessary in order to avoid a screening effect from an unphysical pile-up of gas, which is present at radii close to the inner radial boundary of the domain, due to the numerical damping that is applied at the boundary. Another unphysical flow can be seen near the polar axis, which is especially visible as downward-pointing streamlines in Fig 5.1 in the PE model. This is also believed to be a numerical effect (Gressel et al., 2020; Sarafidou et al., 2024) and to avoid contamination of the synthetic spectra with emission from this region, the gas density is set to zero when either $R < 0.45$ au, $n < 10^5\,{\rm cm}^{-3}$, or ($n < 10^7\,{\rm cm}^{-3}$ and $v_z < 0$) is fulfilled, where n is the local number density. This ensures that the problematic regions are removed without affecting the wind regions or the bound disc.

The grid is then processed with MOCASSIN to calculate the line fluxes and two-dimensional emissivity maps of the [OI] 6300 Å, [NeII] 12.81 µm, [NeIII] 15.55 µm, and [SII] 6730 Å lines. To generate the spectral profiles predicted from a synthetic observation at an inclination angle i, first, the 2D velocity and emissivity grids are rotated onto 256 uniformly spaced azimuthal grid points, creating a 3D axisymmetric cylinder. It is assumed that the disc-midplane is completely optically thick, such that no emission from the other side of the disc can reach the observer. Next, for each grid cell, the projected line-of-sight velocity $v_{\rm los}$ and the thermal root mean square velocity $v_{\rm th}$ are calculated. By summing the contributions of the thermal broadened line-of-sight velocities from all grid cells onto 800 velocity bins uniformly spaced $0.25\,{\rm km\,s}^{-1}$ apart, the spectral line profile is obtained (see Sect. 2.2.3 for details). Finally, to simulate realistic observational conditions, the spectral profile is artificially degraded to a limited resolution by convolving it with a Gaussian of width FWHM = $c/R_{\rm spec}$, where c is the speed of light and $R_{\rm spec}$ represents the simulated resolving power of the observational instrument. For the optical lines, a resolving power of $R_{\rm spec,opt} = 50000$ is used, comparable to the resolution of most available data. The IR lines are degraded to $R_{\rm spec,IR} = 30000$. Spectral line profiles with double the resolution will be presented in appendix 5.4.

Table 5.2: Luminosities of selected forbidden emission lines, given as $log_{10}(L_{\rm line}/L_{\odot})$. For reference, [ArII] 6.98 µm and [ArIII] 8.99 µm lines are included, although no emission maps or spectral profiles were calculated for them and they are not studied in detail in this work.

Model	[OI] 6300 Å	[NeII] 12.81 µm	[NeIII] 15.55 µm	[ArII] 6.98 µm	[ArIII] 8.99 µm	[SII] 6730 Å
β4	-4.37	-5.35	-5.28	-4.49	-5.89	-7.27
β6	-5.05	-5.69	-6.48	-5.72	-6-74	-7.54
PE	-5.03	-5.67	-6.53	-5.69	-6.75	-7.53

5.3 Results & Discussion

5.3.1 Temperature structure and ionisation

Fig. 5.2 presents the thermal and ionisation structure of the models, obtained after processing them with MOCASSIN. It is clear from the panels in the second row and also from Fig. 5.1 that the β4 model exhibits a much denser inner wind with a narrow but dense outflow channel close to the inner edge of the wind, which emanates from a "puffed-up" inner atmosphere at $R < 2$ au. This channel significantly raises the column density to values $\sim 10^{21}$ cm^{-2}, as seen from the contours in Fig. 5.1. As a result, this inner outflow channel screens a significant fraction of the soft X-ray irradiation. EUV is already absorbed in much smaller neutral columns. The hot ($T > 8000$ K) ionisation front visible in the leftmost panels in the top and bottom row of Fig. 5.2 corresponds approximately to the location of the 10^{20} cm^{-2} column number density contour.

The β6 model with a weaker magnetic field does not exhibit the same well-defined dense inner channel, which is also reflected in the (column) density contours that reach deeper into the wind than in the β4 model, as well as in the temperature and ionisation fraction, that are sustained to higher values deeper in the wind, due to less severe absorption in the inner regions. Overall, the wind density at small radii is smaller and drops off much more quickly in the vertical direction. Nevertheless, the model still exhibits an inner "puffed-up" atmosphere that is slightly more extended in the vertical direction than in the PE model. A comparison of the wind mass-loss rates (see 5.1) reveals a $\sim$ 13 % higher mass-loss in the β6 model compared to the PE model, suggesting that this magnetic contribution to the wind-launching is small. Apart from this, the PE model is very similar to the β6 model.

5.3.2 Line luminosities & emission regions

Fig. 5.4 shows the luminosities of selected forbidden emission lines, and in Fig. 5.3, emission maps are presented. The values of the luminosities are listed in table 5.2. Model β4 has the highest luminosities in all selected lines. It has been shown in multiple studies that the [OI] 6300 Å luminosity positively correlates with the accretion luminosity (e.g. Simon et al., 2016; Banzatti et al., 2019). This effect can be explained by the size of the EUV-heated region (Ercolano & Owen, 2016; Weber et al., 2020). [OI] 6300 Å emission is very strongly dependent on the temperature, such that the line traces the hottest regions where neutral oxygen is still present, which is a vertically extended layer close to the EUV ionisation front (see also Fig. 5.3). Since the accretion luminosity contains an EUV component, increasing the accretion luminosity also increases the size of this region, and the line gets brighter. Given that the β4 model has a much higher accretion luminosity, a brighter [OI] 6300 Å is thus expected [OI] 6300 Å. However, the increase in EUV also pushes the ionisation front marginally farther out in the radial direction. This can be seen from the inner edge of the [OI] 6300 Å emission region, which is at slightly larger radii in the β4 model than in the other models.

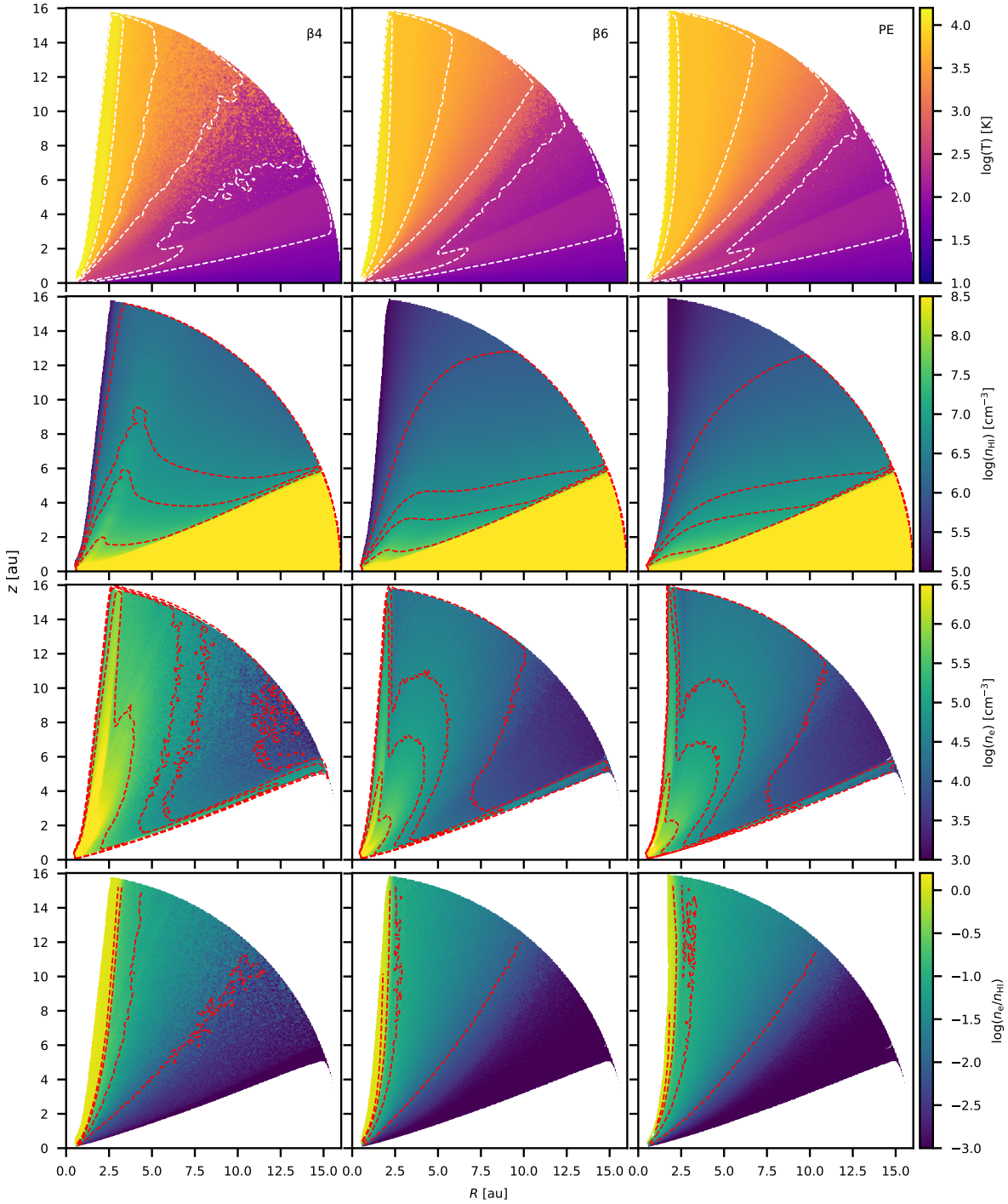

Figure 5.2: Thermal and ionisation structure after post-processing the models with MOCASSIN. First row: Temperature. The contours represent values of (from bottom to top) 100, 200, 1000, 4000, and 8000 K, obtained after applying a Gaussian filter with $\sigma = 4$ to filter Monte-Carlo noise. Second row: Neutral hydrogen number density $n_{\rm HI}$ and contours for values of (from bottom to top) 10^6, $5 \cdot 10^6$, 10^7, and $5 \cdot 10^7$ cm^{-3}. Third row: Electron number density $n_{\rm e}$ and contours for values of (from right to left) 10^4, $5 \cdot 10^4$, 10^5, and $5 \cdot 10^5$ cm^{-3} obtained with a Gaussian filter with $\sigma = 2$. Last row: Ionisation fraction $n_{\rm e}/n_{\rm HI}$ and contours for values of (from right to left) 10^{-2}, 10^{-1}, 0.5, and 1 obtained with a Gaussian filter with $\sigma = 2$.

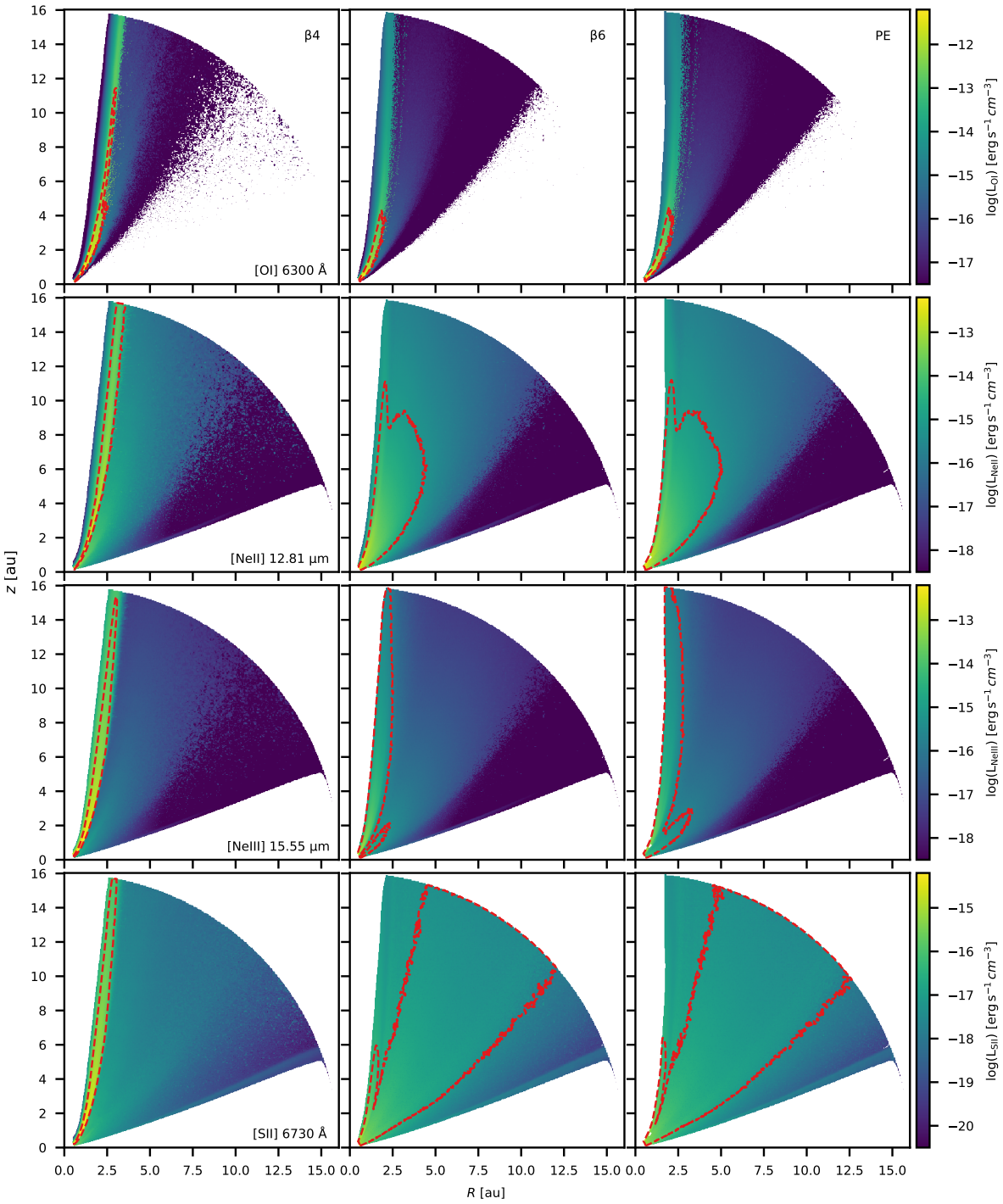

Figure 5.3: Emissivity maps of the selected lines in the $\beta 4$ (left column), $\beta 6$ (middle column) and PE (right column) models. The red dashed lines are contours enclosing the region where 80% of the total line flux is emitted in a 3D axisymmetric disc.

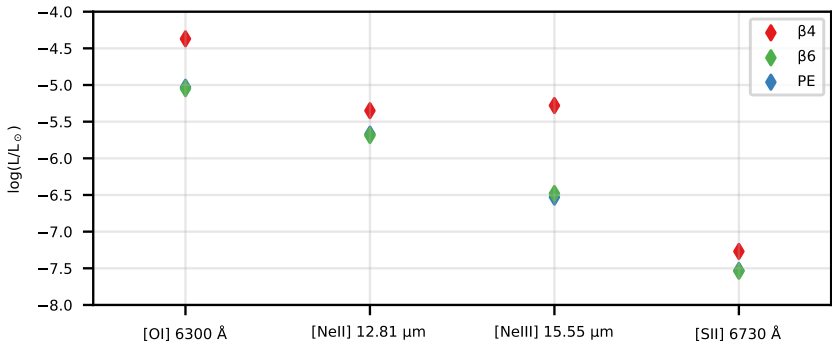

Figure 5.4: The luminosities of selected forbidden emission lines. Note that the markers of the PE model are hidden behind those of the $\beta 6$ model because the two models are very similar.

While scarcer, observational data for the [NeII] 12.81 µm does not indicate a clear relation with the accretion luminosity (Pascucci et al., 2020). From a theoretical standpoint, the accretion luminosity will be too soft to ionise Ne, as the first ionisation potential of Ne is 21.56 eV, where a blackbody with $T = 12000\,\mathrm{K}$ has essentially no contribution. Indeed, the models show only a small (factor of ~ 2) increase in [NeII] 12.81 µm luminosity when comparing the $\beta 4$ model to the other two. From Fig. 5.3, it is clear that [NeII] 12.81 µm in the $\beta 4$ model predominantly traces a narrow vertically extended region along the dense inner wind, where X-ray absorption is high and Ne efficiently ionised. Conversely, in the other models, the [NeII] 12.81 µm line extends to larger radii, where the temperature and density quickly drop, and line excitation becomes less efficient. In Fig. 5.5, the [OI] 6300 Å and [NeII] 12.81 µm luminosities are compared to observations. Both are consistent with the observed range, although they are closer to the lower end of the observed luminosities.

The most significant increase in line luminosity between the models is in the [NeIII] 15.55 µm line due to the favourable conditions for ionisation at the dense inner wind in this model. Data on this line is rare; however, Bajaj et al. (2024) recently detected it in T Cha with a luminosity $log(L_{\mathrm{NeIII}}/L_\odot) = -5.76$. Sellek et al. (2024) subsequently investigated it in the context of photoevaporation and collected values from two more observations, -6.54 ± 0.4 in TW Hya (Najita et al., 2010a) and -5.58 ± 0.09 in CS Cha (Espaillat et al., 2013), as well as two upper limits of < -5.75 in V 4046 Sgr (Rapson et al., 2015) and < -4.68 in RX J1615.3-3255 (Szulágyi et al., 2012). The detection in TW Hya matches the luminosity in the PE model almost exactly, while T Cha has a slightly higher luminosity. Model $\beta 4$ is only consistent with the latter upper limit.

The most significant difference in the emission regions (Fig. 5.3) can be seen in the [SII] 6730 Å line, which, as the other lines, is constrained to the innermost wind-regions in the $\beta 4$ model, but moves away from those regions and reaches deep into the wind in the other models, up to the outer radial boundary. The luminosity is small $log(L_{\mathrm{SII}}/L_\odot) < -7$ in both models. In the models by Weber et al. (2020), this line is $\sim$ 2–3 orders of magnitude brighter than it is found here. However, since the 80 % emission region is not fully contained within the computational domain, the values quoted here are only a lower limit. A quick test using the PE-1 model presented in Weber et al. (2020) reveals that $\sim 52\,\%$ of the total flux is emitted at spherical radii $r > 16\,\mathrm{au}$. This is clearly insufficient to explain the large discrepancy. Another comparison with the Weber et al. (2020) models shows that their temperatures are generally higher close to the disc surface, and the [SII] 6730 Å line emission extends down to the disc surface. This is likely due to the inner disc atmosphere being more "puffed-up" in the $\beta 6$ and even the PE model than in their models, leading to a partial screening for the lower wind regions close to the disc surface. Whether this is sufficient to explain the difference would have to be

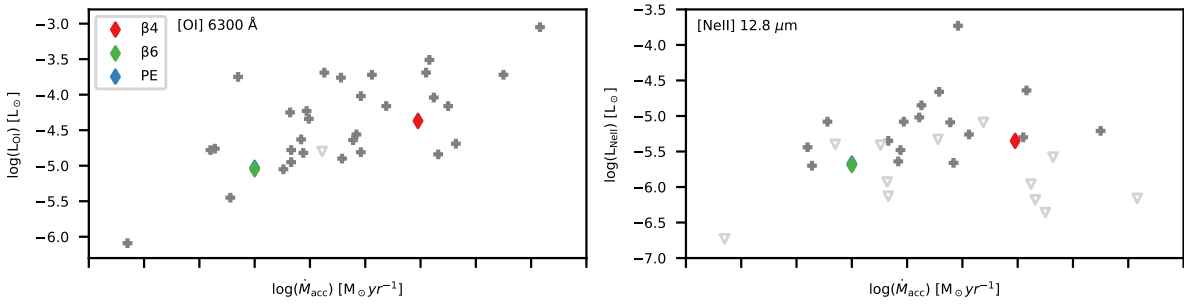

Figure 5.5: [OI] 6300 Å and [NeII] 12.81 µm luminosities against accretion rate compared to the observations. Grey plusses and triangles are observed values reported in Pascucci et al. (2020), where triangles indicate upper limits. Note that the markers for the PE model are hidden behind the $\beta 6$ model.

explored in a dedicated investigation. As pointed out by Pascucci et al. (2020), the line is very rarely detected in observations. If it is, most of the time, only an HVC is found, i.e. the bright [SII] 6730 Å emission in the Weber et al. (2020) models is likely overestimated.

5.3.3 Line ratios

As discussed in Sect. 1.3.4.1, Sellek et al. (2024) recently investigated the origin of Ne and Ar lines observed in T Cha (Bajaj et al., 2024), and they find that both are likely to trace an X-ray photoevaporative wind with a mass-loss rate $\sim 3 \cdot 10^{-8}\,\mathrm{M_\odot\,yr^{-1}}$. Their argument is partially based on the observed line ratios $L_{\mathrm{NeIII}}/L_{\mathrm{NeII}} \approx 10^{-1}$ and $L_{\mathrm{ArIII}}/L_{\mathrm{ArII}} \approx 10^{-2}$, which can only be reproduced if the degree of ionisation is low. In EUV ionised regions, line ratios of > 1 are expected. To achieve a lower degree of ionisation, the wind must be dense enough to screen from EUV, which implies high mass-loss rates.

While it it is not the intention of this work to reproduce a particular set of observations, the $\beta 6$ and PE models have $L_{\mathrm{NeIII}}/L_{\mathrm{NeII}}$ line ratios of ≈ 0.16 and ≈ 0.14, respectively, close to the value observed in T Cha and consistent with the above interpretation. However, the Ar ratios $L_{\mathrm{ArIII}}/L_{\mathrm{ArII}} \approx 10^{-1}$ are approximately an order of magnitude higher than in the observations. Conversely, the $\beta 4$ model has $L_{\mathrm{NeIII}}/L_{\mathrm{NeII}} > 1$, hinting towards a highly ionised emitting region. As discussed in the previous section, this is indeed accurate. However, the $\beta 4$ model is also that with the highest mass-loss rate ($4.2 \cdot 10^{-8}\,\mathrm{M_\odot\,yr^{-1}}$), which shows that high ionisation fractions are not necessarily indicative of an EUV wind. In the presence of an inner wind dense enough to absorb a significant amount of (hard) X-ray in a narrow region., the [NeII] 12.81 µm and [NeIII] 15.55 µm lines can trace highly ionised regions along the inner edge of that wind while more extended emission is suppressed.

5.3.4 Line profiles

Fig. 5.6 presents the spectral line profiles. Higher resolution profiles are shown in appendix 5.4. Once again, the $\beta 6$ and PE models barely differ, although the $\beta 6$ profiles are slightly more extended on the blueshifted side, especially the [NeIII] 15.55 µm profile. The $\beta 4$ profiles are the most blueshifted, which is expected, considering that the emission is predominantly concentrated at the inner edge of the wind, where the outflow is magnetically driven and reaches the highest velocities. Keplerian double peaks appear at inclinations $i \geq 60°$. Interestingly, the $\beta 6$ model exhibits slightly stronger double peaks in the [OI] 6300 Å profile, although this would likely not be distinguishable in real observations

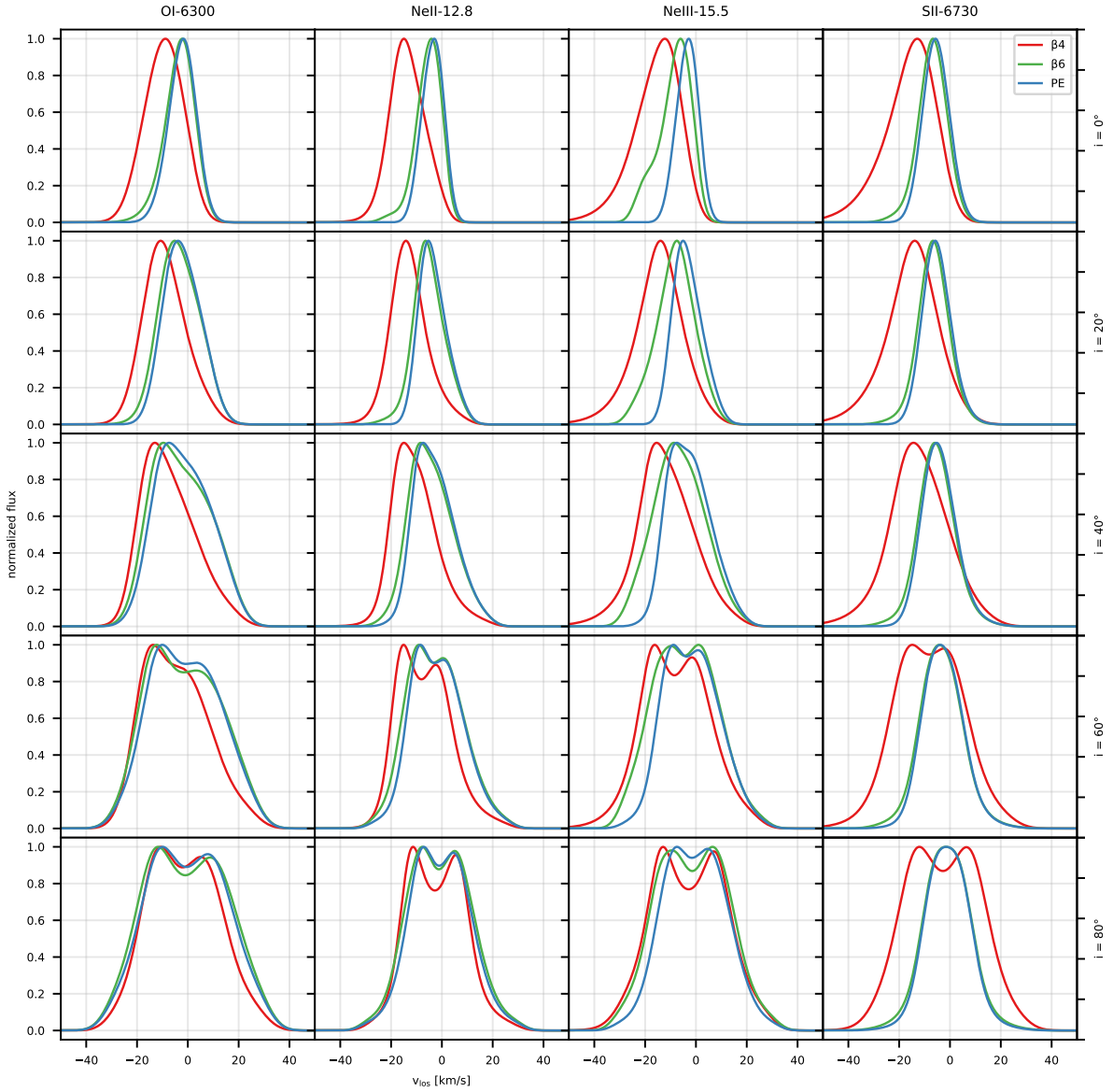

Figure 5.6: Synthetic spectral line profiles observed at different inclinations. The profiles are degraded to the resolving power $R_{\mathrm{spec,opt}} = 50000$ and $R_{\mathrm{spec,IR}} = 30000$, respectively, for the optical and IR lines.

with limited signal-to-noise ratio. The $\beta4$ model clearly has the most noticeable double peaks in all other profiles.

To facilitate the comparison to observations, the line profiles are decomposed following the typical multi-Gaussian fitting procedure, as described in Sect. 5.2.2. The centroid-velocities and FWHMs of the resulting Gaussian components are shown in Fig. 5.7. Observational data from Banzatti et al. (2019); Fang et al. (2018) for the [OI] 6300 Å line and Pascucci et al. (2020) for the [NeII] 12.81 µm is shown for comparison. The multi-Gaussian decomposition tends to fit the Keplerian double peaks, resulting in two components where one is highly blueshifted and the other redshifted, contrary to what is observed. An alternate version where the fit was restricted to a single Gaussian component is shown in the right panels. The following discussion will be focused mainly on these single-Gaussian fits. While this means that some details can get lost, it is reasonable to expect that upon the extraction of the BLVCs, they would get lost in real observations, too. Detailed studies of tailored individual models should examine the complex spectral line shapes instead of relying on the separation by Gaussian components. Nevertheless, decomposition helps describe and compare trends in the models.

In all profiles, all components are classified as NLVCs, except the $i = 80°$ [OI] 6300 Å profile in the $\beta6$ model, which, when fitted with a single component, has a width of $41.6\,\mathrm{km\,s^{-1}}$ and is thus narrowly classified as BLVC. It is nonetheless clear that BLVCs cannot be reproduced with these models, which is unsurprising, given that the inner boundary of the models is at 0.6 au. The profiles of the $\beta4$ model generally populate the parameter space at higher blueshifts. A trend is visible that leads towards smaller blueshifts and narrower components with decreasing magnetic field strength. This is most striking in the [SII] 6730 Å, where the $\beta6$ and PE models have very narrow components compared to the $\beta4$ model. The explanation is simply the big difference in the emitting regions discussed in the previous section (see also Fig 5.3).

The observed distribution of the [OI] 6300 Å NLVCs is mostly reproduced, with the $\beta4$ model reaching the high end of the blueshifts, while the other two models reach moderate blueshifts. Only the fastest components and the observations centred around 0 are narrowly missed. The latter are often SCs, which are most common in discs with inner cavities. Such components have been successfully reproduced by photoevaporation models of transition discs, where a part of the receding wind on the other side of the disc becomes visible through the cavity (Ercolano & Owen, 2010; Picogna et al., 2019). The observed [NeII] 12.81 µm NLVCs can all be roughly reproduced. However, when observed at inclinations $i \leq 60°$, the $\beta4$ model predicts components with higher blueshifts than are observed.

Fig. 5.8 shows the correlation of the centroid properties with inclination. In both lines, the $\beta4$ model has the strongest correlating centroid velocities, as expected from the fact that its lines trace the fastest outflows. The FWHMs follow the expected Keplerian broadening when the inclination is larger than 20°, where the narrower components in the $\beta4$ model correctly indicate an emission region that is radially more extended than in the other models (see Fig. 5.3). At lower inclinations, the wind's velocity gradient dominates the broadening, and the $\beta4$ components become broader than those of the other models.

5.4 Conclusions

The synthetic observations in this chapter show that even in the presence of a dense inner magnetic wind (model $\beta4$), the [NeII] 12.81 µm should be detectable. In such a scenario, unless the disc is viewed at a high inclination, the blueshifts reach values of $\sim 10\,\mathrm{km\,s^{-1}}$, which is at odds with observations. Current [NeII] 12.81 µm observations are much better reproduced by the weak magnetic field model $\beta6$, and the purely photoevaporative PE model, but the [OI] 6300 Å observations are

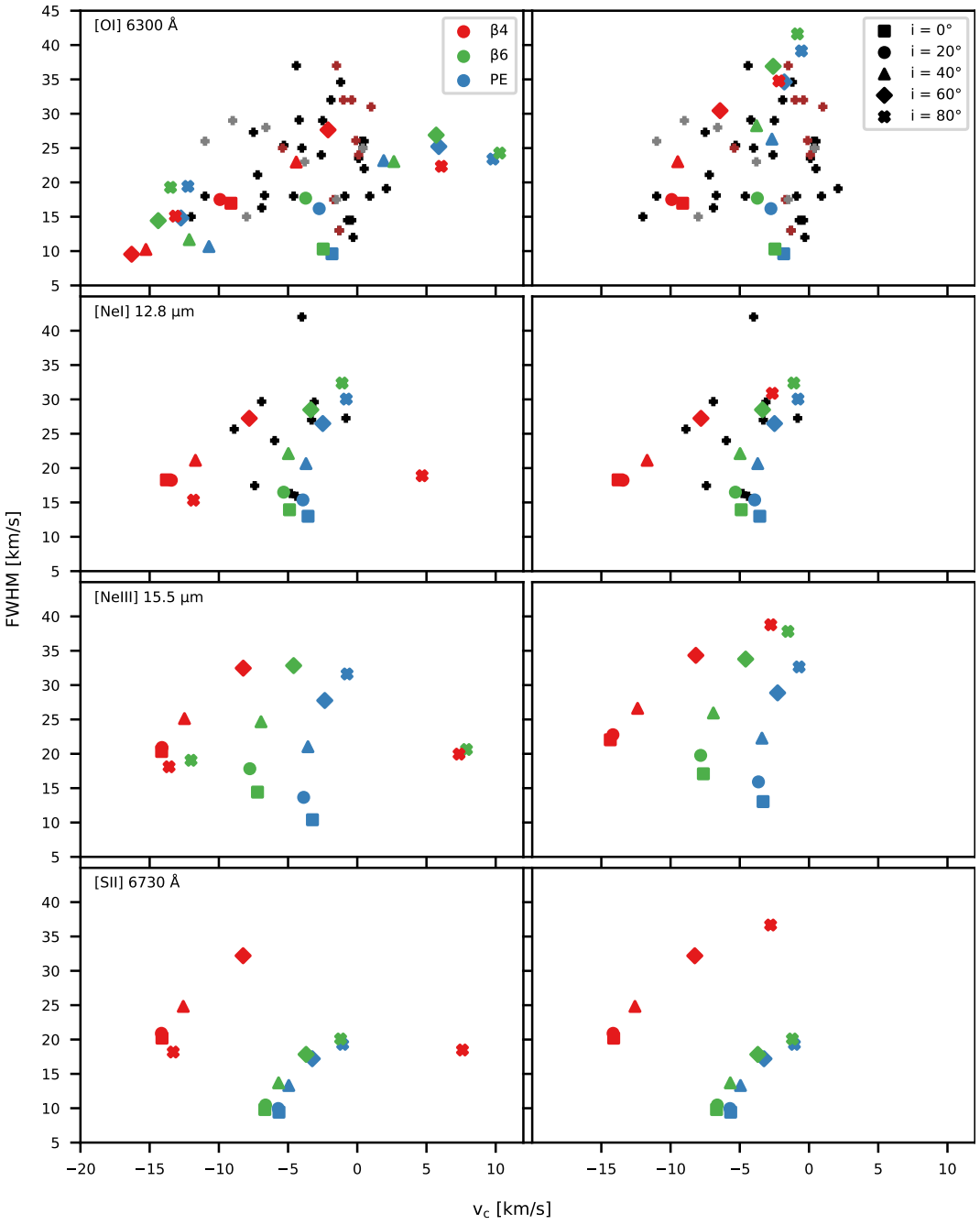

Figure 5.7: Overview of the line centroid and FWHMs of the Gaussian components that fit the profiles. The panels on the left show the results of the multi-Gaussian decomposition. The panels on the right show the properties when the profile is fit with a singular Gaussian component. For the [OI] 6300 Å line, black plusses represent the NLVCs reported by Banzatti et al. (2019); Fang et al. (2018), grey and brown plusses represent SCJ and SC components by Banzatti et al. (2019), respectively. Black plusses in the [NeII] 12.81 µm line panels are the observed components reported by Pascucci et al. (2020).

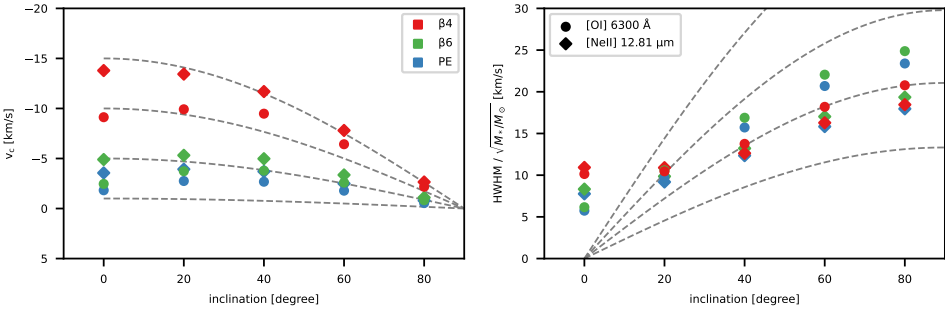

Figure 5.8: Line centroid velocities (left panel) and FWHM (right panel) vs. inclination. Squares indicate the [OI] 6300 Å components, whereas diamonds represent the [NeII] 12.81 µm line. The grey dashed lines in the left panel show the projected velocity of a vertical outflow with a speed of (from top to bottom) 15, 10, 5, and 1 km s^{-1}. In the right panel, the dashed grey lines represent the width expected from Keplerian broadening at radii (from top to bottom) 0.5, 1, 2, and 5 au.

consistent with the predictions of all models and the $\beta4$ model can reproduce the fastest observed [OI] 6300 Å components that are not predicted with lower magnetisation.

However, the observed sample of [NeII] 12.81 µm is still small, and their spectral resolution is much lower than that of recent [OI] 6300 Å observations. Nevertheless, an intriguing trend in the observations is that [NeII] 12.81 µm LVCs are predominantly detected in more evolved discs with inner dust cavities and rarely in full discs (Pascucci et al., 2020). This finding led Pascucci et al. (2020) to sketch an evolutionary scenario where discs at early stages of their evolution exhibit a strong inner magnetic wind that shields the outer regions of the wind from the hard X-ray irradiation that ionises Ne. Indeed, the strong magnetic wind in the $\beta4$ model is very effective in shielding the outer disc, but the [NeII] 12.81 µm is bright at the innermost edge of this wind. As pointed out by Pascucci et al. (2020), to explain the non-detections of the [NeII] 12.81 µm in such a scenario, the inner wind would have to be cool (T ~ few 100 K), since the excitation temperature of [NeII] 12.81 µm is only ~ 1000 K. To resolve this, they propose that the X-ray-absorbing inner wind is molecular and, therefore, is cooled much more efficiently than an atomic wind. The models presented here do not account for molecular cooling, i.e. the temperatures may indeed be overestimated if the inner MHD wind is molecular. However, at the same time, the ubiquitous detection of BLVCs in the [OI] 6300 Å line requires a hot, atomic ($T \gtrsim 5000$ K) inner wind. Their proposed wind would, therefore, be multi-layered with an innermost layer that is hot and neutral, heated by absorbing the EUV and soft X-rays. Once the soft X-rays reach an optical depth of unity, a cool, dense molecular layer that absorbs the hard X-rays would follow. In many observations, however, the [OI] 6300 Å has both an NLVC and BLVC, even when the [NeII] 12.81 µm is undetected. If the NLVC traces the more extended regions between $0.5 < R < 5$ au, as is usually believed, then the neutral, hot layer traced by [OI] would constitute a large volume. According to the models presented here, this volume would also emit a significant flux in the [NeII] 12.81 µm line since the emission regions largely overlap. This inconsistency still needs to be resolved. Magnetothermal models that include the innermost parts of the disc and wind, ideally while including detailed thermochemistry, would be invaluable to shed light on this problem. However, obtaining larger observational samples would be extremely helpful in confirming whether [NeII] 12.81 µm emission is generally suppressed in full discs.

In conclusion, this chapter shows that the predicted NLVCs from the X-ray irradiated magnetothermal models are fully consistent with observations when the magnetic component of the wind is weak. If it is strong ($\beta = 10^4$), the model predicts higher blueshifts for the [NeII] 12.81 µm line than observed.

However, the fastest [OI] 6300 Å NLVCs can only be reproduced if the magnetic wind component is strong.

Appendix

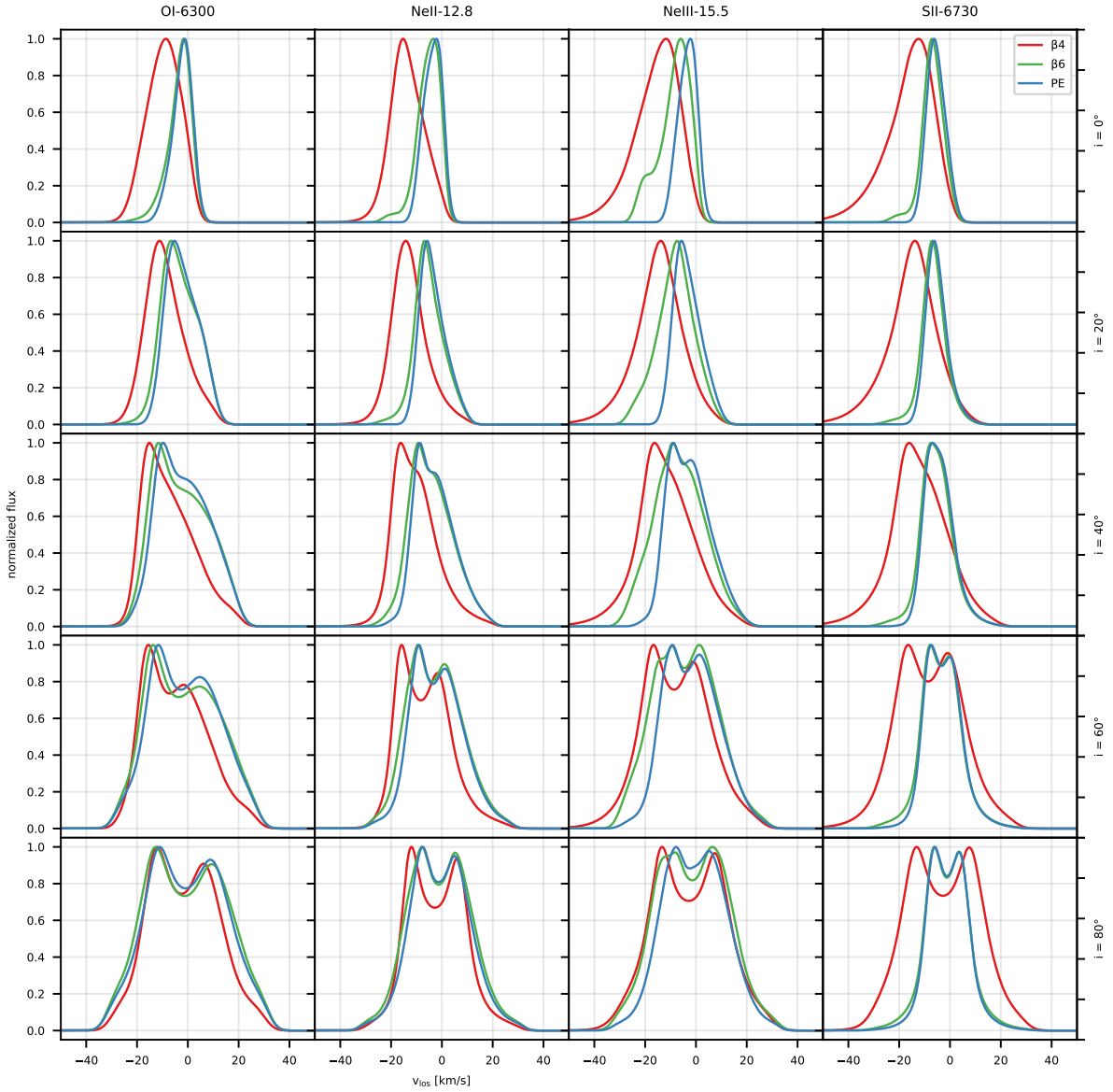

Figure 5.9: As Fig. 5.6 but with double the spectral resolution, i.e. $R_{\mathrm{spec,opt}} = 100000$ and $R_{\mathrm{spec,IR}} = 60000$, for the optical and IR lines, respectively.

Chapter 6

Summary and Outlook

The first chapter of this thesis highlighted the crucial role that protoplanetary disc winds and planet-disc interactions play in shaping the evolution of protoplanetary discs and forming planets. Building on this foundation, the subsequent chapters have investigated the complex interplay between photoevaporative disc winds, giant planets with their associated substructure, and their protoplanetary discs, uncovering new mechanisms with substantial implications for the discs, planets, and observational wind signatures. By conducting three-dimensional hydrodynamic simulations of giant-planet hosting discs under the influence of X-ray photoevaporation, it was revealed in chapter 2 that planets massive enough to open a gap in their disc will significantly alter the structure of photoevaporative winds. From within the gap, no wind can be launched, which results in a region with lower density and pressure above the gap. Consequently, a radial pressure gradient develops, such that the wind in the inner disc is launched at a flat angle towards that region, while the wind near the outer edge of the gap is driven radially inwards. Above the gap, the two flows collide and fall back into the gap if they are below a certain height, approximately ~ 1 au from the disc surface. By post-processing the models with a photoionisation and dust-radiative transfer code, forbidden emission lines commonly used as disc tracers were predicted. Since the lines predominantly trace the regions closest to the star, the changed flow structure does not leave a distinctively recognisable signature in the spectral line profiles at typical resolutions. However, asymmetries such as the spiral density waves induced by the planet can leave an imprint in the wind structure that leads to periodic variability in the line profiles during the planet's orbit. Specifically, redshifted peaks could be a characteristic signature. With high spectral resolution and signal-to-noise ratio, this variability could be observed on timescales of a quarter of the planet's orbit, providing indirect evidence of the presence of an embedded planet.

With revised models, Chapter 3 explored the feedback that the delivery of material through the wind into the gap has on the planet and the disc. It was shown that the gas delivered by the wind can significantly reduce the depth of the gap, allowing the planet to double its accretion rate. Since the planet's torque pushes the gas out of the gap, it is possible to achieve high mass transport rates across the gap. The partial recycling of the wind through the gap and the high mass flux across the gap leads to a slower dispersal of the inner disc than without a planet. This is the opposite of the previous expectation of planet-induced photoevaporation. Moreover, the changed balance between the mass of the inner and the outer discs results in a weaker torque that is acting on the planet, which will affect its migration. The exact migration behaviour, however, cannot be accurately determined from models where the planet is held in a fixed orbit. If the planet moves freely, the disc and gap usually adjust their position on the viscous timescale. However, if the wind efficiently refills the gap,

this would reduce the timescale, and the planet could migrate faster, even if the torque acting on it is weaker than in a disc with no wind. Additional modelling with a freely migrating planet is required to determine the exact outcome under such conditions. Models that follow the long-term evolution of protoplanetary discs should consider all the above effects, as they could significantly alter the outcome of, for example, population synthesis models. However, such models are generally conducted in one dimension and rely on 1D mass-loss profiles for the wind. Therefore, a set of mass-loss profiles that can account for the redistribution of gas by the wind under various conditions would be valuable. This requires a parameter-space study, which is too costly in 3D. However, imposing a gap structure in a two-dimensional photoevaporating disc model would be an exciting prospect for future studies. Lastly, it could be an interesting avenue to investigate the effect on the chemical and isotopic composition of the disc or the planet's atmosphere. The wind enables the efficient redistribution of gas from the inner to the outer disc and to the planet, which is not expected in the inner regions of purely viscous discs. Not only because the chemical composition in the inner disc is different from cooler regions at larger radii but also because the material that is transported through the wind is exposed to a hot environment with high-energy irradiation, which could enable physical or chemical or selective processes that are not possible in the interior of the disc.

The subsequent chapters of this work concentrated on generating synthetic observables for protoplanetary disc winds. In chapter 4, it was shown that state-of-the-art photoevaporation models are entirely consistent with spatial observations of the [OI] 6300 Å in TW Hya recently observed by Fang et al. (2023), who concluded that this line must trace an inner magnetic wind. By modelling the [OI] 6300 Å and [NeII] 12.81 µm emission, it was shown that not only the spatial observations are consistent, but also the spectral profiles and line luminosities, which are matched even better by the photoevaporation model than their MHD wind model, suggesting that the bulk of the wind in TW Hya is launched by photoevaporation.

Despite the photoevaporation models' success in reproducing the observed NLVCs, it is clear that they cannot be responsible for the observations of broader components. Such components are generally attributed to magnetic or magnetothermal winds. Chapter 5 explored the synthetic observables of the X-ray irradiated magnetothermal wind models by Sarafidou et al. (2024). The findings indicate that while a strong magnetic inner wind can reproduce the observed [OI] 6300 Å NLVCs, it also produces luminous [NeII] 12.81 µm NLVCs that, when the disc is not highly inclined ($i \lesssim 60°$), are more blueshifted than observed. Conversely, if the magnetic wind component is weak or the wind is purely photoevaporative, the [OI] 6300 Å and [NeII] 12.81 µm NLVCs are consistent with observations, but the observed [OI] 6300 Å NLVCs with the highest blueshifts cannot be reproduced. BLVCs cannot be reproduced with this model, which is expected, as the regions closer than $r < 0.6$ au could not be included in the model due to numerical limitations. Observational evidence suggests that in less evolved discs, where [NeII] 12.81 µm is not often detected, an inner magnetic field could shield the more extended regions from high-energy irradiation that could produce the ionised neon required for [NeII] 12.81 µm emission. The models show that a strong inner magnetic wind can indeed prohibit the emission of the [NeII] 12.81 µm at larger radii. However, luminous flux is then expected from the innermost region of the magnetic wind. Resolving this question requires a larger observational sample of [NeII] 12.81 µm detections and models that include the innermost parts of the disc as well as detailed thermochemistry to account for potentially important molecular cooling processes.

In conclusion, this work demonstrated the significant impact of the intricate interplay between photoevaporative disc winds and massive planets, laying the foundations for further exploration of its effects. Furthermore, it bolstered the confidence in photoevaporation models by reaffirming their consistency with observational constraints from forbidden emission lines while re-emphasising the need for detailed magnetothermal disc wind models that include the innermost regions of the disc.

References

ALMA Partnership et al., 2015, Astrophysical Journal Letters, 808, L3

Alarcón F., Bergin E. A., Cugno G., 2024, The Astrophysical Journal, 966, 225

Alexander R. D., 2008, Monthly Notices of the Royal Astronomical Society: Letters, 391, L64

Alexander R. D., Armitage P. J., 2009, Astrophysical Journal, 704, 989

Alexander R. D., Pascucci I., 2012, Monthly Notices of the Royal Astronomical Society, 422, L82

Alexander R. D., Clarke C. J., Pringle J. E., 2004, Monthly Notices of the Royal Astronomical Society, 354, 71

Alexander R. D., Clarke C. J., Pringle J. E., 2006a, Monthly Notices of the Royal Astronomical Society, 369, 216

Alexander R. D., Clarke C. J., Pringle J. E., 2006b, Monthly Notices of the Royal Astronomical Society, 369, 229

Alexander R., Pascucci I., Andrews S., Armitage P., Cieza L., 2014, The Dispersal of Protoplanetary Disks. eprint: arXiv:1311.1819, doi:10.2458/azu_uapress_9780816531240-ch021

André P., Di Francesco J., Ward-Thompson D., Inutsuka S. I., Pudritz R. E., Pineda J. E., 2014, From Filamentary Networks to Dense Cores in Molecular Clouds: Toward a New Paradigm for Star Formation. eprint: arXiv:1312.6232, doi:10.2458/azu_uapress_9780816531240-ch002

Andrews S. M., 2020, Annual Review of Astronomy and Astrophysics, 58, 483

Andrews S. M., Williams J. P., 2005, The Astrophysical Journal, 631, 1134

Andrews S. M., Rosenfeld K. A., Kraus A. L., Wilner D. J., 2013, The Astrophysical Journal, 771, 129

Andrews S. M., et al., 2016,] 10.3847/2041-8205/820/2/L40, 820, L40

Andrews S. M., Terrell M., Tripathi A., Ansdell M., Williams J. P., Wilner D. J., 2018a, The Astrophysical Journal, 865, 157

Andrews S. M., et al., 2018b, The Astrophysical Journal, 869, L41

Andrews S. M., Teague R., Wirth C. P., Huang J., Zhu Z., 2024, On Kinematic Measurements of Self-Gravity in Protoplanetary Disks, doi:10.48550/arXiv.2405.19574

Ansdell M., et al., 2016, The Astrophysical Journal, 828, 46

Ansdell M., et al., 2018, The Astrophysical Journal, 859, 21

Aoyama Y., Bai X., 2023, Three-Dimensional Global Simulations of Type-II Planet-disk Interaction with a Magnetized Disk Wind: I. Magnetic Flux Concentration and Gap Properties, doi:10.48550/arXiv.2302.01514

Arlt R., Urpin V., 2004, Astronomy and Astrophysics, 426, 755

Armitage P. J., 2010, Astrophysics of Planet Formation

Arulanantham N., et al., 2024, The Astrophysical Journal, 965, L13

Asplund M., Grevesse N., Sauval A. J., 2005, Cosmic Abundances as Records of Stellar Evolution and Nucleosynthesis, 336, 25
Astropy Collaboration et al., 2013,] 10.1051/0004-6361/201322068, 558, A33
Astropy Collaboration et al., 2018,] 10.3847/1538-3881/aabc4f, 156, 123
Bai X. N., 2015, Astrophysical Journal, 798, 84
Bai X.-N., 2016, The Astrophysical Journal, 821, 80
Bai X.-N., 2017, The Astrophysical Journal, 845, 75
Bai X.-N., Stone J. M., 2013, The Astrophysical Journal, 769, 76
Bai X.-N., Ye J., Goodman J., Yuan F., 2016, The Astrophysical Journal, 818, 152
Bajaj N. S., et al., 2024, The Astronomical Journal, 167, 127
Balbus S. A., Hawley J. F., 1991, The Astrophysical Journal, 376, 214
Ballabio G., Alexander R. D., Clarke C. J., 2020, Monthly Notices of the Royal Astronomical Society, 496, 2932
Bally J., Reipurth B., Davis C. J., 2007, Observations of Jets and Outflows from Young Stars
Balog Z., et al., 2016, The Astrophysical Journal, 832, 87
Banzatti A., Pascucci I., Edwards S., Fang M., Gorti U., Flock M., 2019, The Astrophysical Journal, 870, 76
Banzatti A., et al., 2022,] 10.3847/1538-3881/ac52f0, 163, 174
Banzatti A., et al., 2023, The Astronomical Journal, 165, 72
Barranco J. A., Marcus P. S., 2005, The Astrophysical Journal, 623, 1157
Baruteau C., et al., 2014, Planet-Disk Interactions and Early Evolution of Planetary Systems. eprint: arXiv:1312.4293, doi:10.2458/azu_uapress_9780816531240-ch029
Bast J. E., Brown J. M., Herczeg G. J., van Dishoeck E. F., Pontoppidan K. M., 2011, Astronomy & Astrophysics, Volume 527, id.A119, ¡NUMPAGES¿18¡/NUMPAGES¿ pp., 527, A119
Benisty M., et al., 2015, Astronomy and Astrophysics, 578, L6
Benisty M., et al., 2017, Astronomy and Astrophysics, 597, A42
Benisty M., et al., 2018, Astronomy and Astrophysics, 619, A171
Benisty M., et al., 2023,] 10.48550/arXiv.2203.09991, 534, 605
Benítez-Llambay P., Masset F. S., 2016, The Astrophysical Journal Supplement Series, 223, 11
Bertoldi F., 1989, The Astrophysical Journal, 346, 735
Béthune W., Lesur G., Ferreira J., 2017, Astronomy and Astrophysics, 600, A75
Birnstiel T., 2023, Dust Growth and Evolution in Protoplanetary Disks, doi:10.48550/arXiv.2312.13287
Birnstiel T., Ormel C. W., Dullemond C. P., 2011, Astronomy and Astrophysics, 525, A11
Blandford R. D., Payne D. G., 1982, Monthly Notices of the Royal Astronomical Society, 199, 883
Bohlin R. C., Savage B. D., Drake J. F., 1978, The Astrophysical Journal, 224, 132
Booth R. A., Clarke C. J., 2021, Monthly Notices of the Royal Astronomical Society, 502, 1569
Booth R. A., Clarke C. J., Madhusudhan N., Ilee J. D., 2017, Monthly Notices of the Royal Astronomical Society, 469, 3994
Bosman A. D., et al., 2021, The Astrophysical Journal Supplement Series, 257, 15
Bouvier J., Cabrit S., Fernandez M., Martin E. L., Matthews J. M., 1993, Astronomy and Astrophysics, 272, 176
Bradley L., et al., 2022, Astropy/Photutils: 1.5.0, Zenodo, doi:10.5281/zenodo.6825092
Burkert A., Bodenheimer P., 2000, The Astrophysical Journal, 543, 822
Churchwell E., Felli M., Wood D. O. S., Massi M., 1987, The Astrophysical Journal, 321, 516
Clarke C. J., Gendrin A., Sotomayor M., 2001, Monthly Notices of the Royal Astronomical Society, 328, 485

Coleman G. A. L., Mroueh J. K., Haworth T. J., 2024, Monthly Notices of the Royal Astronomical Society, 527, 7588
Crida A., Sándor Z., Kley W., 2008, Astronomy and Astrophysics, 483, 325
Currie T., Kenyon S. J., Balog Z., Rieke G., Bragg A., Bromley B., 2008, The Astrophysical Journal, 672, 558
D'Alessio P., Calvet N., Hartmann L., 2001, The Astrophysical Journal, 553, 321
D'Angelo G., Lubow S. H., 2008, The Astrophysical Journal, 685, 560
D'Angelo G., Kley W., Henning T., 2003, The Astrophysical Journal, 586, 540
Dale J. E., 2015, New Astronomy Reviews, 68, 1
De Val-Borro M., et al., 2006, Monthly Notices of the Royal Astronomical Society, 370, 529
Dere K. P., Landi E., Mason H. E., Monsignori Fossi B. C., Young P. R., 1997, Astronomy and Astrophysics Supplement Series, 125, 149
Dere K. P., Zanna G. D., Young P. R., Landi E., Sutherland R. S., 2019, The Astrophysical Journal Supplement Series, 241, 22
Desch S. J., Turner N. J., 2015,] 10.1088/0004-637X/811/2/156, 811, 156
Duchêne G., et al., 2024, The Astronomical Journal, 167, 77
Dullemond C. P., Hollenbach D., Kamp I., D'Alessio P., 2006, in Reipurth B., Jewitt D., Keil K., eds, Protostars and Planets V. p. 555
Dullemond C. P., Hollenbach D., Kamp I., D'Alessio P., 2007, Models of the Structure and Evolution of Protoplanetary Disks. eprint: arXiv:astro-ph/0602619, doi:10.48550/arXiv.astro-ph/0602619
Dürmann C., Kley W., 2015, Astronomy and Astrophysics, 574, A52
Dürmann C., Kley W., 2017, Astronomy and Astrophysics, 598, 80
Eisner J. A., Bally J. M., Ginsburg A., Sheehan P. D., 2016, The Astrophysical Journal, 826, 16
Elbakyan V., Wu Y., Nayakshin S., Rosotti G., 2022, Monthly Notices of the Royal Astronomical Society, 515, 3113
Emsenhuber A., Burn R., Weder J., Monsch K., Picogna G., Ercolano B., Preibisch T., 2023, Astronomy and Astrophysics, 673, A78
Ercolano B., Clarke C. J., 2010, Monthly Notices of the Royal Astronomical Society, 402, 2735
Ercolano B., Owen J. E., 2010, Monthly Notices of the Royal Astronomical Society, 406, 1553
Ercolano B., Owen J. E., 2016,] 10.1093/mnras/stw1179, 460, 3472
Ercolano B., Pascucci I., 2017, Royal Society Open Science, 4, 170114
Ercolano B., Picogna G., 2022, European Physical Journal Plus, 137, 1357
Ercolano B., Rosotti G., 2015, Monthly Notices of the Royal Astronomical Society, 450, 3008
Ercolano B., Barlow M. J., Storey P. J., Liu X. W., 2003, Monthly Notices of the Royal Astronomical Society, 340, 1136
Ercolano B., Barlow M. J., Storey P. J., 2005, Monthly Notices of the Royal Astronomical Society, 362, 1038
Ercolano B., Young P. R., Drake J. J., Raymond J. C., 2008a, The Astrophysical Journal Supplement Series, 175, 534
Ercolano B., Drake J. J., Raymond J. C., Clarke C. C., 2008b, The Astrophysical Journal, 688, 398
Ercolano B., Clarke C. J., Drake J. J., 2009, Astrophysical Journal, 699, 1639
Ercolano B., Mayr D., Owen J. E., Rosotti G., Manara C. F., 2014,] 10.1093/mnras/stt2405, 439, 256
Ercolano B., Koepferl C., Owen J., Robitaille T., 2015,] 10.1093/mnras/stv1528, 452, 3689
Ercolano B., Rosotti G. P., Picogna G., Testi L., 2017,] 10.1093/mnrasl/slw188, 464, L95
Ercolano B., Weber M. L., Owen J. E., 2018, Monthly Notices of the Royal Astronomical Society: Letters, 473, L64

Ercolano B., Picogna G., Monsch K., Drake J. J., Preibisch T., 2021, Mon. Not. R. Astron. Soc, 000, 1675
Ercolano B., Rab C., Molaverdikhani K., Edwards B., Preibisch T., Testi L., Kamp I., Thi W.-F., 2022, Monthly Notices of the Royal Astronomical Society, 512, 430
Ercolano B., Picogna G., Monsch K., 2023, Monthly Notices of the Royal Astronomical Society, 526, L105
Espaillat C., et al., 2013, The Astrophysical Journal, 762, 62
Evans II N. J., 1999, Annual Review of Astronomy and Astrophysics, 37, 311
Evans II N. J., et al., 2009, The Astrophysical Journal Supplement Series, 181, 321
Fang M., et al., 2018, The Astrophysical Journal, 868, 28
Fang M., et al., 2023, Nature Astronomy, 7, 905
Fatuzzo M., Adams F. C., 2008, The Astrophysical Journal, 675, 1361
Favre C., Cleeves L. I., Bergin E. A., Qi C., Blake G. A., 2013, The Astrophysical Journal, 776, L38
Fedele D., Van Den Ancker M. E., Henning T., Jayawardhana R., Oliveira J. M., 2010, Astronomy and Astrophysics, 510
Feigelson E. D., Montmerle T., 1999, Annual Review of Astronomy and Astrophysics, 37, 363
Flock M., Nelson R. P., Turner N. J., Bertrang G. H. M., Carrasco-González C., Henning T., Lyra W., Teague R., 2017, The Astrophysical Journal, 850, 131
Flock M., Turner N. J., Nelson R. P., Lyra W., Manger N., Klahr H., 2020, The Astrophysical Journal, 897, 155
Font A. S., McCarthy I. G., Johnstone D., Ballantyne D. R., 2004, The Astrophysical Journal, 607, 890
Frank J., King A., Raine D. J., 2002, Accretion Power in Astrophysics: Third Edition
Frank A., et al., 2014, Jets and Outflows from Star to Cloud: Observations Confront Theory. eprint: arXiv:1402.3553, doi:10.2458/azu_uapress_9780816531240-ch020
Franz R., Picogna G., Ercolano B., Birnstiel T., 2020,] 10.1051/0004-6361/201936615, 635, A53
Franz R., Picogna G., Ercolano B., Casassus S., Birnstiel T., Rab Ch., Pérez S., 2022
Fricke K., 1968, Zeitschrift fur Astrophysik, 68, 317
Fung J., Chiang E., 2016, The Astrophysical Journal, 832, 105
Furuya K., Aikawa Y., 2018, The Astrophysical Journal, 857, 105
Gaia Collaboration et al., 2021,] 10.1051/0004-6361/202039498, 649, A6
Galloway-Sprietsma M., et al., 2023, The Astrophysical Journal, 950, 147
Gangi M., et al., 2020, Astronomy and Astrophysics, 643, A32
Getman K. V., Feigelson E. D., Garmire G. P., Broos P. S., Kuhn M. A., Preibisch T., Airapetian V. S., 2022, ApJ, 935, 43
Goldreich P., Schubert G., 1967, The Astrophysical Journal, 150, 571
Goldreich P., Tremaine S., 1979, The Astrophysical Journal, 233, 857
Goldreich P., Tremaine S., 1980, The Astrophysical Journal, 241, 425
Goodman A. A., Benson P. J., Fuller G. A., Myers P. C., 1993, The Astrophysical Journal, 406, 528
Gorti U., Hollenbach D., 2009, The Astrophysical Journal, 690, 1539
Gorti U., Dullemond C. P., Hollenbach D., 2009,] 10.1088/0004-637X/705/2/1237, 705, 1237
Gorti U., Hollenbach D., Dullemond C. P., 2015, The Astrophysical Journal, 804, 29
Gressel O., Turner N. J., Nelson R. P., McNally C. P., 2015, Astrophysical Journal, 801, 84
Gressel O., Ramsey J. P., Brinch C., Nelson R. P., Turner N. J., Bruderer S., 2020, The Astrophysical Journal, 896, 126
Guillot T., Fletcher L. N., Helled R., Ikoma M., Line M. R., Parmentier V., 2022, Giant Planets from the Inside-Out, doi:10.48550/arXiv.2205.04100

Haffert S. Y., Bohn A. J., de Boer J., Snellen I. A. G., Brinchmann J., Girard J. H., Keller C. U., Bacon R., 2019, Nature Astronomy, 3, 749
Haisch Jr. K. E., Lada E. A., Lada C. J., 2001, The Astrophysical Journal, 553, L153
Hamann F., 1994, The Astrophysical Journal Supplement Series, 93, 485
Harris C. R., et al., 2020, Nature, 585, 357
Hartigan P., Edwards S., Ghandour L., 1995, The Astrophysical Journal, 452, 736
Hartmann L., Calvet N., Gullbring E., D'Alessio P., 1998, The Astrophysical Journal, 495, 385
Hartmann L., Herczeg G., Calvet N., 2016, Annual Review of Astronomy and Astrophysics, 54, 135
Haworth T. J., Facchini S., Clarke C. J., Cleeves L. I., 2017, Monthly Notices of the Royal Astronomical Society, 468, L108
Hendler N., Pascucci I., Pinilla P., Tazzari M., Carpenter J., Malhotra R., Testi L., 2020, The Astrophysical Journal, 895, 126
Hildebrand R. H., 1983, Quarterly Journal of the Royal Astronomical Society, 24, 267
Hollenbach D., Gorti U., 2009, The Astrophysical Journal, 703, 1203
Hollenbach D., Johnstone D., Lizano S., Shu F., 1994, The Astrophysical Journal, 428, 654
Hsieh C.-H., Arce H. G., Maureira M. J., Pineda J. E., Segura-Cox D., Mardones D., Dunham M. M., Arun A., 2024, The ALMA Legacy Survey of Class 0/I Disks in Corona Australis, Aquila, chaMaeleon, oPhiuchus North, Ophiuchus, Serpens (CAMPOS). I. Evolution of Protostellar Disk Radii, doi:10.48550/arXiv.2404.02809
Hunter J. D., 2007, Computing In Science & Engineering, 9, 90
Hutchison M. A., Clarke C. J., 2021, Monthly Notices of the Royal Astronomical Society, 501, 1127
Hutchison M. A., Laibe G., Maddison S. T., 2016, Monthly Notices of the Royal Astronomical Society, 463, 2725
Jankovic M. R., Owen J. E., Mohanty S., Tan J. C., 2021,] 10.1093/mnras/stab920, 504, 280
Jeans J. H., 1902, Proceedings of the Royal Society of London Series I, 71, 136
Jennings J., Ercolano B., Rosotti G. P., 2018, Monthly Notices of the Royal Astronomical Society, 477, 4131
Kamp I., Tilling I., Woitke P., Thi W.-F., Hogerheijde M., 2010,] 10.1051/0004-6361/200913076, 510, A18
Kanagawa K. D., Muto T., Tanaka H., Tanigawa T., Takeuchi T., Tsukagoshi T., Momose M., 2015, The Astrophysical Journal, 806, L15
Kanagawa K. D., Muto T., Tanaka H., Tanigawa T., Takeuchi T., Tsukagoshi T., Momose M., 2016, Publications of the Astronomical Society of Japan, 68, 1
Keppler M., et al., 2018, Astronomy and Astrophysics, 617, A44
Kimmig C. N., Dullemond C. P., Kley W., 2020, Astronomy and Astrophysics, 633, A4
Klaassen P. D., Mottram J. C., Maud L. T., Juhasz A., 2016, Monthly Notices of the Royal Astronomical Society, 460, 627
Klahr H., Hubbard A., 2014, The Astrophysical Journal, 788, 21
Klahr H., Kley W., 2006, Astronomy and Astrophysics, 445, 747
Kley W., Nelson R. P., 2012, Annual Review of Astronomy and Astrophysics, 50, 211
Kley W., Bitsch B., Klahr H., 2009, Astronomy and Astrophysics, 506, 971
Koenigl A., Ruden S. P., 1993, Origin of Outflows and Winds
Koepferl C. M., Ercolano B., Dale J., Teixeira P. S., Ratzka T., Spezzi L., 2013,] 10.1093/mnras/sts276, 428, 3327
Komaki A., Nakatani R., Yoshida N., 2021, The Astrophysical Journal, 910, 51
Krapp L., Gressel O., Benítez-Llambay P., Downes T. P., Mohandas G., Pessah M. E., 2018, The Astrophysical Journal, 865, 105

Kratter K., Lodato G., 2016, Annual Review of Astronomy and Astrophysics, 54, 271
Kudo T., Hashimoto J., Muto T., Baobab Liu H., Dong R., Hasegawa Y., Tsukagoshi T., Konishi M., 2018, The Astrophysical Journal, 868, L5
Kunitomo M., Suzuki T. K., Inutsuka S. I., 2020, Monthly Notices of the Royal Astronomical Society, pp 3849–3858
Lada C. J., 1987, 115, 1
Larson R. B., 1969, Monthly Notices of the Royal Astronomical Society, 145, 271
Larson R. B., 1981, Monthly Notices of the Royal Astronomical Society, 194, 809
Lee C.-F., Tabone B., Cabrit S., Codella C., Podio L., Ferreira J., Jacquemin-Ide J., 2021, The Astrophysical Journal, 907, L41
Lega E., et al., 2021, Astronomy & Astrophysics, 646, A166
Lesur G. R., 2021, Astronomy and Astrophysics, 650, A35
Lesur G. R. J., Latter H., 2016, Monthly Notices of the Royal Astronomical Society, 462, 4549
Lesur G., et al., 2022, arXiv e-prints, p. arXiv:2203.09821
Lesur G., et al., 2023, in Inutsuka S., Aikawa Y., Muto T., Tomida K., Tamura M., eds, Astronomical Society of the Pacific Conference Series Vol. 534, Protostars and Planets VII. p. 465
Liffman K., 2003, Publications of the Astronomical Society of Australia, 20, 337
Lin D. N. C., Papaloizou J., 1979, Monthly Notices of the Royal Astronomical Society, 186, 799
Lin D. N. C., Papaloizou J., 1986, The Astrophysical Journal, 309, 846
Lin D. N. C., Papaloizou J. C. B., 1993, On the Tidal Interaction Between Protostellar Disks and Companions
Liu S.-F., Jin S., Li S., Isella A., Li H., 2018, The Astrophysical Journal, 857, 87
Lodato G., 2008, New Astronomy Reviews, 52, 21
Lodato G., et al., 2023, Monthly Notices of the Royal Astronomical Society, 518, 4481
Long F., et al., 2018, The Astrophysical Journal, 869, 17
Louvet F., Dougados C., Cabrit S., Mardones D., Ménard F., Tabone B., Pinte C., Dent W. R. F., 2018, Astronomy and Astrophysics, 618, A120
Lubow S. H., D'Angelo G., 2006, The Astrophysical Journal, 641, 526
Lynden-Bell D., 1996, Monthly Notices of the Royal Astronomical Society, 279, 389
Lynden-Bell D., Pringle J. E., 1974, Monthly Notices of the Royal Astronomical Society, 168, 603
Lyra W., 2014, The Astrophysical Journal, 789, 77
Mamajek E. E., Usuda T., Tamura M., Ishii M., 2009, in EXOPLANETS AND DISKS: THEIR FORMATION AND DIVERSITY: Proceedings of the International Conference. AIP Conference Proceedings. AIP Publishing, pp 3–10 (arXiv:0906.5011), doi:10.1063/1.3215910
Manara C. F., Morbidelli A., Guillot T., 2018, Astronomy and Astrophysics, 618, L3
Manara C. F., et al., 2021, Astronomy and Astrophysics, 650, A196
Manara C. F., Ansdell M., Rosotti G. P., Hughes A. M., Armitage P. J., Lodato G., Williams J. P., 2023,] 10.48550/arXiv.2203.09930, 534, 539
Marcus P. S., Pei S., Jiang C.-H., Hassanzadeh P., 2013, Physical Review Letters, 111, 084501
Masset F., 2000, Astronomy and Astrophysics Supplement Series, 141, 165
Masset F. S., Papaloizou J. C. B., 2003, The Astrophysical Journal, 588, 494
Matsuyama I., Johnstone D., Hartmann L., 2003, The Astrophysical Journal, 582, 893
Mayor M., Queloz D., 1995, Nature, 378, 355
McGinnis P., Dougados C., Alencar S. H., Bouvier J., Cabrit S., 2018, Astronomy and Astrophysics, 620, A87
McKee C. F., Ostriker E. C., 2007, Annual Review of Astronomy and Astrophysics, 45, 565
Mesa D., et al., 2022, Astronomy and Astrophysics, 658

Mignone A., Bodo G., Massaglia S., Matsakos T., Tesileanu O., Zanni C., Ferrari A., 2007, The Astrophysical Journal Supplement Series, 170, 228
Milliner K., Matthews J. H., Long K. S., Hartmann L., 2019, Monthly Notices of the Royal Astronomical Society, 483, 1663
Miotello A., et al., 2017, Astronomy and Astrophysics, 599, A113
Miotello A., Kamp I., Birnstiel T., Cleeves L. C., Kataoka A., 2023,] 10.48550/arXiv.2203.09818, 534, 501
Monsch K., Ercolano B., Picogna G., Preibisch T., Rau M. M., 2019, Monthly Notices of the Royal Astronomical Society, 483, 3448
Monsch K., Picogna G., Ercolano B., Kley W., 2021a, Astronomy and Astrophysics, 646, A169
Monsch K., Picogna G., Ercolano B., Preibisch T., 2021b, Astronomy and Astrophysics, 650, A199
Morbidelli A., Szulágyi J., Crida A., Lega E., Bitsch B., Tanigawa T., Kanagawa K., 2014, Icarus, 232, 266
Muzerolle J., Hillenbrand L., Calvet N., Briceño C., Hartmann L., 2003, The Astrophysical Journal, 592, 266
Najita J. R., Carr J. S., Strom S. E., Watson D. M., Pascucci I., Hollenbach D., Gorti U., Keller L., 2010a, The Astrophysical Journal, 712, 274
Najita J. R., Carr J. S., Strom S. E., Watson D. M., Pascucci I., Hollenbach D., Gorti U., Keller L., 2010b,] 10.1088/0004-637X/712/1/274, 712, 274
Nakatani R., Hosokawa T., Yoshida N., Nomura H., Kuiper R., 2018a, The Astrophysical Journal, 857, 57
Nakatani R., Hosokawa T., Yoshida N., Nomura H., Kuiper R., 2018b,] 10.3847/1538-4357/aad9fd, 865, 75
Nakatani R., Turner N. J., Takasao S., 2024, Broadening the Canonical Picture of EUV-Driven Photoevaporation of Accretion Disks, doi:10.48550/arXiv.2406.18461
Nelson R. P., Gressel O., Umurhan O. M., 2013, Monthly Notices of the Royal Astronomical Society, 435, 2610
Nelson R. P., Lega E., Morbidelli A., 2023, Astronomy and Astrophysics, 670, A113
Nemer A., Goodman J., 2024, The Astrophysical Journal, 961, 122
Nisini B., et al., 2024, Astronomy and Astrophysics, 683, A116
Nomura H., et al., 2022, The Isotopic Links from Planet Forming Regions to the Solar System, doi:10.48550/arXiv.2203.10863
Öberg K. I., et al., 2021, The Astrophysical Journal Supplement Series, 257, 1
Ogilvie G. I., Lubow S. H., 2002, Monthly Notices of the Royal Astronomical Society, 330, 950
Owen J., 2011, PhD thesis, University of Cambridge, UK
Owen J. E., 2019, Annual Review of Earth and Planetary Sciences, 47, 67
Owen J. E., Ercolano B., Clarke C. J., Alexander R. D., 2010, Monthly Notices of the Royal Astronomical Society, 401, 1415
Owen J. E., Ercolano B., Clarke C. J., 2011, Monthly Notices of the Royal Astronomical Society, 412, 13
Owen J. E., Clarke C. J., Ercolano B., 2012, Monthly Notices of the Royal Astronomical Society, 422, 1880
Paardekooper S. J., Baruteau C., Crida A., Kley W., 2010, Monthly Notices of the Royal Astronomical Society, 401, 1950
Paardekooper S.-J., Dong R., Duffell P., Fung J., Masset F. S., Ogilvie G., Tanaka H., 2022, Planet-Disk Interactions (arXiv:2203.09595), doi:10.48550/arXiv.2203.09595
Papaloizou J., Lin D. N. C., 1984, The Astrophysical Journal, 285, 818

Pascucci I., Sterzik M., 2009,] 10.1088/0004-637X/702/1/724, 702, 724
Pascucci I., et al., 2011,] 10.1088/0004-637X/736/1/13, 736, 13
Pascucci I., Ricci L., Gorti U., Hollenbach D., Hendler N. P., Brooks K. J., Contreras Y., 2014, The Astrophysical Journal, 795, 1
Pascucci I., et al., 2016, The Astrophysical Journal, 831, 125
Pascucci I., et al., 2020, The Astrophysical Journal, 903, 78
Pascucci I., Cabrit S., Edwards S., Gorti U., Gressel O., Suzuki T., 2022, The Role of Disk Winds in the Evolution and Dispersal of Protoplanetary Disks (arXiv:2203.10068), doi:10.48550/arXiv.2203.10068
Persson M. V., 2014,] 10.6084/m9.figshare.654555.v7
Picogna G., Ercolano B., Owen J. E., Weber M. L., 2019, Monthly Notices of the Royal Astronomical Society, 487, 691
Picogna G., Ercolano B., Espaillat C. C., 2021, Monthly Notices of the Royal Astronomical Society, 508, 3611
Pinte C., et al., 2018, The Astrophysical Journal, 860, L13
Pinte C., et al., 2019, Nature Astronomy, 3, 1109
Pinte C., Teague R., Flaherty K., Hall C., Facchini S., Casassus S., 2022a, arXiv e-prints, p. arXiv:2203.09528
Pinte C., Teague R., Flaherty K., Hall C., Facchini S., Casassus S., 2022b, Kinematic Structures in Planet-Forming Disks (arXiv:2203.09528), doi:10.48550/arXiv.2203.09528
Pontoppidan K. M., Blake G. A., Smette A., 2011, The Astrophysical Journal, Volume 733, Issue 2, article id. 84, ¡NUMPAGES¿17¡/NUMPAGES¿ pp. (2011)., 733, 84
Preibisch T., et al., 2005, The Astrophysical Journal Supplement Series, 160, 401
Qi C., et al., 2004,] 10.1086/421063, 616, L11
Rab Ch., et al., 2022, Astronomy and Astrophysics, 668, A154
Rab C., Weber M. L., Picogna G., Ercolano B., Owen J. E., 2023, The Astrophysical Journal, 955, L11
Rapson V. A., et al., 2015, The Astrophysical Journal, 810, 62
Ray T. P., Ferreira J., 2021, New Astronomy Reviews, 93, 101615
Ray T. P., Mundt R., Dyson J. E., Falle S. A. E. G., Raga A. C., 1996, The Astrophysical Journal, 468, L103
Ray T., Dougados C., Bacciotti F., Eislöffel J., Chrysostomou A., 2007, Toward Resolving the Outflow Engine: An Observational Perspective. eprint: arXiv:astro-ph/0605597, doi:10.48550/arXiv.astro-ph/0605597
Ribas Á., Merín B., Bouy H., Maud L. T., 2014, Astronomy and Astrophysics, 561
Rigliaco E., Pascucci I., Gorti U., Edwards S., Hollenbach D., 2013, Astrophysical Journal, 772, 60
Robrade J., Schmitt J. H. M. M., 2006,] 10.1051/0004-6361:20054247, 449, 737
Rodenkirch P. J., Dullemond C. P., 2022,] 10.1051/0004-6361/202142571, 659, A42
Rodenkirch P. J., Klahr H., Fendt C., Dullemond C. P., 2020, Astronomy and Astrophysics, 633, A21
Rosenfeld K. A., Andrews S. M., Hughes A. M., Wilner D. J., Qi C., 2013,] 10.1088/0004-637X/774/1/16, 774, 16
Rosotti G. P., 2023, New Astronomy Reviews, 96, 101674
Rosotti G. P., Ercolano B., Owen J. E., Armitage P. J., 2013, Monthly Notices of the Royal Astronomical Society, 430, 1392
Sanchis E., Picogna G., Ercolano B., Testi L., Rosotti G., 2020, Monthly Notices of the Royal Astronomical Society, 492, 3440
Sarafidou E., Gressel O., Picogna G., Ercolano B., 2024, Monthly Notices of the Royal Astronomical Society, 530, 5131

Savage B. D., Sembach K. R., 1996, The Astrophysical Journal, 470, 893
Schneider A. D., Bitsch B., 2021, Astronomy and Astrophysics, 654, A71
Sellek A. D., Clarke C. J., Booth R. A., 2021, Monthly Notices of the Royal Astronomical Society, 506, 1
Sellek A. D., Clarke C. J., Ercolano B., 2022,] 10.1093/mnras/stac1148, 514, 535
Sellek A. D., et al., 2024, The Astronomical Journal, 167, 223
Shakura N. I., Sunyaev R. A., 1973, Astronomy and Astrophysics, 24, 337
Simon M. N., Pascucci I., Edwards S., Feng W., Gorti U., Hollenbach D., Rigliaco E., Keane J. T., 2016, The Astrophysical Journal, 831, 169
Simon J. B., Bai X.-N., Flaherty K. M., Hughes A. M., 2018, The Astrophysical Journal, 865, 10
Skrutskie M. F., Dutkevitch D., Strom S. E., Edwards S., Strom K. M., Shure M. A., 1990, The Astronomical Journal, 99, 1187
Somigliana A., Testi L., Rosotti G., Toci C., Lodato G., Tabone B., Manara C. F., Tazzari M., 2023, The Astrophysical Journal, 954, L13
Szulágyi J., 2017, arXiv
Szulágyi J., Pascucci I., Ábrahám P., Apai D., Bouwman J., Moór A., 2012, The Astrophysical Journal, 759, 47
Szulágyi J., Masset F., Lega E., Crida A., Morbidelli A., Guillot T., 2016, Monthly Notices of the Royal Astronomical Society, 460, 2853
Tarter C. B., Tucker W. H., Salpeter E. E., 1969, The Astrophysical Journal, 156, 943
Teague R., Bae J., Bergin E. A., Birnstiel T., Foreman-Mackey D., 2018, The Astrophysical Journal, 860, L12
Teague R., Bae J., Bergin E. A., 2019a, Nature, 574, 378
Teague R., Bae J., Huang J., Bergin E. A., 2019b, The Astrophysical Journal, 884, L56
Teague R., et al., 2021, The Astrophysical Journal Supplement Series, 257, 18
Testi L., et al., 2022, Astronomy and Astrophysics, 663, A98
Thanathibodee T., Molina B., Serna J., Calvet N., Hernández J., Muzerolle J., Franco-Hernández R., 2023, The Astrophysical Journal, 944, 90
Thi W.-F., Woitke P., Kamp I., 2011,] 10.1111/j.1365-2966.2010.17741.x, 412, 711
Thorngren D. P., Fortney J. J., Murray-Clay R. A., Lopez E. D., 2016, The Astrophysical Journal, 831, 64
Tripathi A., Andrews S. M., Birnstiel T., Wilner D. J., 2017, The Astrophysical Journal, 845, 44
Tychoniec Ł., et al., 2018, The Astrophysical Journal Supplement Series, 238, 19
Veronesi B., Paneque-Carreño T., Lodato G., Testi L., Pérez L. M., Bertin G., Hall C., 2021, The Astrophysical Journal, 914, L27
Virtanen P., et al., 2020, Nature Methods, 17, 261
Visser R., van Dishoeck E. F., Black J. H., 2009, Astronomy and Astrophysics, 503, 323
Wafflard-Fernandez G., Lesur G., 2023, Planet-Disk-Wind Interaction: The Magnetized Fate of Protoplanets, doi:10.48550/arXiv.2305.11784
Wagner K., et al., 2018, The Astrophysical Journal, 863, L8
Wang L., Goodman J., 2017,] 10.3847/1538-4357/aa8726, 847, 11
Wang L., Bai X.-N., Goodman J., 2019, The Astrophysical Journal, 874, 90
Ward W. R., 1991, 22, 1463
Weber M. L., Ercolano B., Picogna G., Hartmann L., Rodenkirch P. J., 2020, Monthly Notices of the Royal Astronomical Society, 496, 223
Weber M. L., Ercolano B., Picogna G., Rab C., 2022, Monthly Notices of the Royal Astronomical Society, 517, 3598

Weber M. L., Picogna G., Ercolano B., 2024, Astronomy and Astrophysics, 686, A53
Weder J., Mordasini C., Emsenhuber A., 2023, Astronomy and Astrophysics, 674, A165
Weidenschilling S. J., 1977, Astrophysics and Space Science, 51, 153
Williams J. P., Cieza L. A., 2011, Annual Review of Astronomy and Astrophysics, 49, 67
Williams J. P., McKee C. F., 1997, The Astrophysical Journal, 476, 166
Williams J. P., Cieza L., Hales A., Ansdell M., Ruiz-Rodriguez D., Casassus S., Perez S., Zurlo A., 2019, The Astrophysical Journal, 875, L9
Winter A. J., Haworth T. J., 2022, European Physical Journal Plus, 137, 1132
Winter A. J., Kruijssen J. M. D., Chevance M., Keller B. W., Longmore S. N., 2020, Monthly Notices of the Royal Astronomical Society, 491, 903
Woitke P., Kamp I., Thi W.-F., 2009,] 10.1051/0004-6361/200911821, 501, 383
Woitke P., et al., 2016,] 10.1051/0004-6361/201526538, 586, A103
Woitke P., et al., 2019,] 10.1088/1538-3873/aaf4e5, 131, 064301
Wölfer L., Picogna G., Ercolano B., van Dishoeck E. F., 2019, Monthly Notices of the Royal Astronomical Society, 490, 5596
Wölfer L., et al., 2021, Astronomy and Astrophysics, 648, A19
Wölfer L., et al., 2023, Astronomy and Astrophysics, 670, A154
Young A. K., 2023, Frontiers in Astronomy and Space Sciences, 10, 1288730
Yu H., Teague R., Bae J., Öberg K., 2021, The Astrophysical Journal, 920, L33
Zhang K., Bergin E. A., Blake G. A., Cleeves L. I., Hogerheijde M., Salinas V., Schwarz K. R., 2016, The Astrophysical Journal, 818, L16
van Boekel R., et al., 2017,] 10.3847/1538-4357/aa5d68, 837, 132
van der Marel N., et al., 2013, Science, 340, 1199

List of Figures

List of Tables

List of acronyms/abbreviations

ALMA Atacama Large Millimeter/Submillimeter Array
BLVC broad low-velocity component
COS convective overstability
DSHARP Disk Substructures at High Angular Resolution Project
EUV extreme-ultraviolet
FHSC first hydrostatic core
FUV far-ultraviolet
FWHM Full Width at Half Maximum
GMC giant molecular cloud
HST Hubble Space Telescope
HVC high-velocity component
IR infrared
ISM interstellar medium
JWST James Webb Space Telescope
LVC low-velocity component
MHD magnetohydrodynamic
MRI magnetorotational instability
NLVC narrow low-velocity component
ONC Orion Nebular Cluster
PAH polycyclic aromatic hydrocarbon
PE photoevaporation
PIPE planet-induced photoevaporation
SC single component
SCJ single component + jet
SED spectral energy distribution
SPHERE Spectro-Polarimetric High-contrast Exoplanet Research

UV ultraviolet

VLT Very Large Telescope

VSI vertical shear instability

YSO young stellar object

ZVI zombie vortex instability

List of publications

1. **Michael L. Weber**, Giovanni Picogna, Barbara Ercolano: "The interplay between forming planets and photoevaporating discs II: Wind-driven gas redistribution",
Astronomy & Astrophysics, Volume 686 (2024), A53
2. B. Nisini, M. Gangi, T. Giannini, S. Antoniucci, K. Biazzo, A. Frasca, Juan M. Alcalá, C. F. Manara, **M. L. Weber**: "GIARPS High-resolution Observations of T Tauri stars (GHOsT) V. New insights into disk winds from 3 km s^{-1} resolution spectroscopy",
Astronomy & Astrophysics, Volume 683 (2024), A116
3. Christian Rab, **Michael Weber**, Giovanni Picogna, Barbara Ercolano, James Owen: "High-resolution [OI] line spectral mapping of TW Hya consistent with X-ray driven photoevaporation",
The Astrophysical Journal Letters, Volume 955 Issue 1 (2023), L11
4. **Michael L. Weber**, Barbara Ercolano, Giovanni Picogna, Christian Rab: "The interplay between forming planets and photoevaporating discs I: forbidden line diagnostics",
Monthly Notices of the Royal Astronomical Society, Volume 517 Issue 3 (2022), 3598-3612
5. Ch. Rab, **M. L. Weber**, T. Grassi, B. Ercolano, G. Picogna, P. Caselli, W.-F. Thi, I. Kamp, P. Woitke: "Interpreting molecular hydrogen and atomic oxygen line emission of T Tauri disks with photoevaporative disk-wind models.",
Astronomy & Astrophysics, Volume 668 (2022), A154
6. Luca Ricci, Sarah K. Harter, Barbara Ercolano, **Michael Weber**: "Testing Photoevaporation and MHD Disk Wind Models through Future High-angular Resolution Radio Observations: The Case of TW Hydrae",
The Astrophysical Journal, Volume 913 Issue 2 (2021), 122
7. **Michael L. Weber**, Barbara Ercolano, Giovanni Picogna, Lee Hartmann, Peter J. Rodenkirch: "The interpretation of protoplanetary disc wind diagnostic lines from X-ray photoevaporation and analytical MHD models",
Monthly Notices of the Royal Astronomical Society, Volume 496 Issue 1 (2020), 223–244
8. Giovanni Picogna, Barbara Ercolano, James E. Owen, **Michael L. Weber**: "The dispersal of protoplanetary discs – I. A new generation of X-ray photoevaporation models",
Monthly Notices of the Royal Astronomical Society, Volume 487 Issue 1 (2019), 691–701
9. Barbara Ercolano, **Michael L. Weber**, James E. Owen: "Accreting transition discs with large cavities created by X-ray photoevaporation in C and O depleted discs",
Monthly Notices of the Royal Astronomical Society: Letters, Volume 473 Issue 1 (2018), L64–L68

Acknowledgements

I want to express my deepest gratitude to everyone who has supported and guided me throughout my journey. This thesis would not have been possible without the collective encouragement, support, and belief of many individuals.

First and foremost, I am immensely thankful to my supervisor, Prof. Barbara Ercolano, for her unwavering support, invaluable advice, and endless patience, as well as for giving me the space and freedom to steer my research in my direction. Your belief in my potential has been a constant source of motivation.

I would also like to thank all the past and present members of Barbara's and Til's groups for the many enjoyable moments we shared in meetings, (SPF) lunches, and conference trips. Special thanks to Giovanni Picogna for offering countless pieces of advice and sharing his expertise in PLUTO with me, to Christian Rab for insightful discussions and numerous sessions troubleshooting and benchmarking our synthetic observations, and to Eleftheria Sarafidou for re-running and providing their magnetothermal wind models.

I was incredibly fortunate to have lived in Munich's finest shared flat with the best flatmates for many years. I am especially grateful to Tim and Raffaela for being the best home office mates and great friends and for many unforgettable memories I will always cherish.

To my dear friends Samu, Momo, Paddy, and all other "Schwobabuaba": thank you for countless fun times, laughter, TS sessions, game nights (and days), and keeping the dialect alive.

To my parents and sister, I would never have made it this far without your constant support. Thank you for always having my back.

Finally, to Ellen: your support and encouragement mean the world to me. Thank you for everything.